CONTROLLING PATHOLOGICAL MINERALIZATION USING MOLECULAR MODIFIERS

by
Doyoung Kim

A dissertation submitted to the William A. Brookshire Department of Chemical and Biomolecular Engineering

in partial fulfillment of the requirements for the degree of

DOCTOR OF PHILOSOPHY

in Chemical Engineering

Chair of Committee: Dr. Jeffrey D. Rimer

Committee Member: Dr. Peter G. Vekilov

Committee Member: Dr. Jeremy Palmer

Committee Member: Dr. Debora Rodrigues

Committee Member: Dr. T. Randall Lee

University of Houston

AUGUST 2021

ACKNOWLEDGMENTS

First and foremost, I would like to express my sincere gratitude to my advisor Dr. Jeffrey D. Rimer. I am indebted for his constant guidance, encouragement, the tremendous support and opportunities he provided throughout my doctoral studies at University of Houston. You have motivated me, supported me, and inspired me throughout my Ph.D career. My success is your blessing, Dr. Rimer, and I will always be thankful to you.

I would also like to thank all my committee members. To Professor Peter G. Vekilov, thank you for your invaluable advice and discussions on many of my projects, and for being so kind and friendly. Thank you, Dr. Jeremy Palmer, Dr. Debora Rodrigues, and Dr. T. Randall Lee for serving as my PhD defense committee. It is an honor to present my work to you.

I thank all my collaborators, Dr, Nicola Irwin, Chara Olympiou, and Dr. Jessica Moore, who has come all the way from Northern Ireland to Houston and made this amazing collaboration possible. It was truly a pleasure to have you here and I look forward to seeing you again.

I thank each and every Rimer group members, both former and current, for the supportive and enabling environment and also for making this journey more enjoyable. I give special thanks to Ricardo for truly being through all of this with me and for all the support and encouragement.

I dedicate my work to my family who has motivated me from the start. I thank you for your unconditional love and support. To Sung, you are a treasure to me. I love

spending life with you, with all your kindness, sincerity, all the laughs, the friends and family we share, and even the long hard days. I could not have done this without you by my side. To Boyoung, my beautiful little sister, you are my favorite. Thank you for encouraging me, being my best friend, and making me proud. To mom and dad, thank you for everything. I cannot wait to go back home to you.

ABSTRACT

The development of new methods to prevent mineral scale formation can have significant impact on natural, biological, and industrial process. A ubiquitous approach to regulating crystal formation is through the use of modifiers, which are (macro)molecules that interact with crystals to inhibit nucleation and/or growth. Understanding the fundamental mechanisms of crystallization inhibitors is relevant to a broad range of fields, including their frequent use in crystal engineering and biomineralization. This dissertation focuses on two types of pathological crystals: calcium oxalate monohydrate (COM), the primary component of kidney stones, and magnesium ammonium phosphate hexahydrate (struvite). Struvite is a key constituent of infection stones (e.g., kidney stones); and it is also a common scale in water purification and transport. Despite considerable interest in this material, the fundamental understanding of struvite growth is still at its infancy due to the lack of appropriate platforms to assess growth over multiple length scales. The use of flow systems to study infection stone formation is promising, as they can simulate the flow conditions where struvite naturally forms (e.g., urinary tract systems, catheter, pipelines, etc.). This dissertation has established a new method of evaluating struvite crystal growth under flow using a combination of microfluidics and *in situ* atomic force microscopy (AFM). Through these synergistic approaches, we quantified anisotropic kinetics of crystallization over a broad range of conditions and resolved the molecular mechanism of growth and its inhibition whereby layers on crystal surfaces advance from either screw dislocations or 2-dimensional generation and spreading of islands – both of which are classical pathways.

Growth modifiers range from small ions and molecules to large macromolecules. Here, we examined the impact of bio-inspired small molecules on both struvite and COM crystallization. Several phosphate-based molecules exhibit an unparalleled dual mode of action capable of suppressing both nucleation and growth of crystals. Time-resolved AFM images of struvite surface at varying inhibitor concentration revealed a unique mode of crystal growth inhibition, wherein surfaces become laden with an amorphous layer that leads to roughened interfaces and growth succession through dynamic sequences that are not commonly witnessed for other minerals. In studies of COM, we observed that modifiers irreversibly stunt crystal growth in timescales that are relevant to pathological COM kidney stone formation. Comparisons between phosphate-based modifiers and two reference compounds previously identified as highly effective COM inhibitors, carboxylate-based hydroxycitrate and the urinary protein osteopontin, revealed that phosphate-based inhibitors suppress COM crystallization at substantially lower concentrations than both conventional modifiers, thus highlighting the unique efficacy of these newly evaluated bio-inspired molecules. In addition, the results presented in this dissertation address knowledge gaps that are beneficial to the development of effective inhibitors with the potential to replace existing therapeutics for these widespread maladies.

Collectively, this dissertation presents research efforts aimed at inhibiting the formation of pathological crystals, focusing on an understanding of crystal growth under dynamic conditions and pathways to arrest growth via modifiers (i.e., inhibitors) that may serve as model compounds for preventative drugs.

TABLE OF CONTENTS

LIST OF TABLES

LIST OF FIGURES

CHAPTER 1

1 Introduction

Crystallization is a ubiquitous process that impacts our daily lives. It is a process of atoms and molecules arranging into well-defined structure, crystals, which serve as an integral part of biology and nature in various forms, such as bones and shells of organisms. In commercial processes, this phenomenon is utilized to separate and purify specialty chemicals[3] and pharmaceuticals[4-6] as well as to produce functional materials (e.g., semiconductors[7-8], zeolites[9-10]) that can benefit a wide array of industries; however, crystallization can also be an undesirable process such as in the case of pathological diseases including gout (buildup of uric acid crystals in joints)[11], gallstones (hardened cholesterol deposits in the gallbladder)[12-13], atherosclerosis (cholesterol plaque in artery)[14], malaria (heme crystallization)[15-16], and kidney stones[17-18]. The latter is the main area of interest for this dissertation.

1.1 Kidney Stone Disease

The prevalence of urolithiasis in industrialized countries has increased significantly over the last twenty-five years.[19] It is a common chronic disorder that influences more than 10 – 15 % of U.S. population.[20] Women have seen their rate of stone disease increase disproportionally more than men; and stone rates have increased in the pediatric population as well.[21] Though many factors have been identified as potential contributors to the increase in urolithiasis, including the obesity epidemic, antibiotic usage, climate change and others, identification of these factors has not led to

societal interventions to stem the tide.[22-24] Even as urolithiasis is becoming more common, development of new pharmacologic therapies has been slow.

Kidney stones are complex aggregates of crystals comprised of a bulk of inorganic material and a minor fraction of organic compounds, such as lipids, proteins, and polysaccharides. They are classified based on the composition of the inorganic fraction. Calcium stones effect about 80% of kidney stone patients among which calcium oxalate stones are the most predominant form. Calcium oxalate stones exist in three hydrate forms: calcium oxalate monohydrate (COM) or whewellite, calcium oxalate dihydrate (COD) or weddellite, and calcium oxalate trihydrate (COT) or caoxite.[25] COM is the most thermodynamically stable hydrate and the most common component of kidney stones. COD is a more metastable hydrate and is considered to be pathologically benign. COD crystals are less prone to aggregate, thus they are primarily found in normal urine of healthy individuals and in voided urine of asymptomatic individuals as microcrystals.[26] COT is the least stable hydrate and less physiologically relevant. The development of calcium oxalate stones is often related to metabolic abnormalities including hypercalciuria (excessive amount of calcium in urine), hyperoxaluria (excessive oxalate in urine), and hypocitraturia (abnormally low excretion of urinary citrate).[25] Calcium phosphate stones, often found in alkaline urine, are not as common and is often found as a small component of calcium oxalate stones.[27] Uric acid stones occur in about 10 % of all kidney stones and can form when the urine is too acidic.[28] Improper processing of uric acid or protein intake can increase the acid level in urine. Struvite ($NH_4MgPO_4 \cdot 6H_2O$) constitutes about 10 – 15% of the urinary stones, but this form rapidly grows into large calculi that can block the kidney, ureter,

and bladder.[29] Moreover, struvite is a primary component of infectious stones,[30-32] which are the byproduct of urinary tract infections (UTIs) in which the bacteria affect the chemical balance in urine and cause the formation of irregular and jagged edged large stones.[13] Cystine is the least common form that is caused by a metabolic disorder (cystinuria) leading to an excessive amount of L-cystine in urine.[7]

Treatment for kidney stones varies depending on the type and cause of the stone. For larger stones, sound wave treatment and surgical removal are available. In cases of smaller stones, drinking water, taking pain relievers or muscle relaxation medication is recommended to relieve the pain and help pass the stone. The chance of passing decreases dramatically with the increase in stone size. Also, clinical studies have shown a high recurrence rate of 50% in 5 years and up to 80% at 10 years after the first stone. In select cases, therapeutics are available. Oral alkali therapy, particularly potassium citrate, is a commonly prescribed treatment to prevent kidney stones. Alkali therapy prevents calcium stones by increasing urine citrate, which acts by complexing urine calcium, thereby reducing ionized calcium and urine saturation of calcium salts[33-34]. Citrate also has direct crystal inhibitory effects at the crystal surface, reducing calcium oxalate crystal growth and aggregation.[35] Only a small fraction of the citrate absorbed from the intestine is excreted unchanged in the urine.[36] Citrate is metabolized to bicarbonate in the liver; this alkali load leads to a small increase in blood pH, which reduces proximal tubule citrate reabsorption, thereby increasing urine citrate excretion.[37-38] The alkali load also neutralizes metabolic acid production and reduces renal proton excretion, raising urine pH. The effect on urine pH makes potassium citrate a useful therapy for uric acid stone formers, who have acidic urine as their most common

metabolic defect[39]; however, the increase in urine pH with potassium citrate therapy may not be beneficial in all calcium stone patients. As urine pH increases, more phosphate exists in the monohydrogen form, raising calcium phosphate (CaP) supersaturation, potentially offsetting the benefit of increased citrate levels. Thus, patients with CaP stones and calcium oxalate stone patients with an alkaline urine pH are populations that could benefit the most from the development of new therapies.

1.2 Infection Stone

Infection stones are a particular subset of urinary stones that are primarily comprised of struvite combined with CaP and/or calcium oxalate.[40] These species are strictly associated with urinary tract infections by bacteria that produce the enzyme urease. The formation of infection stones is a result of complex interactions between urease positive bacteria and compounds in urine. Urease catalyzes the hydrolysis of urea to ammonia and carbon dioxide.[41] Ammonia production subsequently increases urinary pH, causing the increase phosphate^{-} ions. These ions together with magnesium ions present in urine favors precipitation of struvite ($MgNH_4PO_4 \cdot 6H_2O$) crystals. Infection stones are one of the most problematic stone diseases due to rapid growth of struvite, its high recurrence rate, and the tendency of struvite to aggregate into larger stones (staghorn calculi) that fully occupy the entire intrarenal collecting system.[31] The development of staghorn calculi can obstruct urinary tract and lead to sepsis, renal failure, and even death.

Infection stones can also be linked to medical device-associated infections.[42] Urinary catheters can serve as a route for pathogenic bacteria, allowing them to enter

into the sterile and nutrient-rich environment of the urinary tract. These bacteria colonize on the device surface potentially leading to biofilm development[32, 43], which is an amorphous matrix that provides an additional protection from the immune system. Biofilms primarily comprised of extracellular polysaccharide material, including polysaccharides, extracellular DNA, and proteins [44], commonly cause recurrent and chronic infections by shielding bacteria and allowing them to detach and cause additional infection in other parts of the urinary tract.[45-46] Catheter associated urinary tract infection is one of the most common healthcare-related infections reported in the majority of developed countries including the United States.[47] The most common microorganisms causing this are *Enterococcus spp.*, *Klebsiella spp.*, *Candida spp.*, *Escherichia coli*, *Proteus mirabilis* (*P. mirabilis*) and *Enterobacter spp*.[48] where P. mirabilis accounts for approximately 40% of all long-term catheterized patients.[30] Catheter blockage is one of the most serious complications encountered predominantly in long-term catheterized patients.[49-50] Approximately 50% of all long-term catheterized patients experience catheter blockage due to encrustation[50] that obstructs the normal drainage of urine.[51] Urinary catheter blockage can be sudden and may induce pain in the bladder. Urine retention in the bladder may cause leakage around the catheter causing urinary incontinence. Furthermore, this may cause reflux to the kidneys by urine flowing back, leading to kidney and bloodstream complications such as pyelonephritis and septicaemia.[52] The current methods for the prevention and control of this complication, apart from removal and changing of the catheter, are not effective.[50]

Treatment for infection stones involve the use of antibiotics to treat urinary tract infections, surgical and medical procedures to break up and remove stones, dissolution

therapies, as well as drugs that can inhibit urease and ease and reduce the pain and inflammation from surgery. However, emergence of antibiotic resistance, side effects of currently administered drugs, and high recurrence rate of infections has led to a decrease in the efficacy of these methods.[53-55] To this end, my research focuses on two types of biominerals: COM and struvite. This dissertation will present research efforts aimed at inhibiting the formation of these pathological crystals, focusing on understanding crystal growth in dynamic conditions and arresting growth via modifiers (i.e., inhibitors) that may serve as model compounds for preventative drugs. This chapter will provide background information on these topics. First, we will discuss the driving force of crystallization, and mechanisms governing crystal growth and inhibition. Second, a general description of COM and the review of previous research on its growth mechanism and the role of various classes of growth modifiers will be provided. Lastly, a general description of struvite and previous findings on its growth and modulation of crystallization will be presented.

1.3 Crystal Nucleation and Growth

Crystallization occurs to minimize the energy state of a system where the driving force is the free energy excess in the solvated state governed by the degree of supersaturation.[56] Crystal continues to nucleate and grow until the chemical potential (μ) of the reactants is equal to that of the final crystal product at equilibrium (i.e., $\Delta\mu = 0$). In terms of solution activities, which is a measure of the effective concentration, crystallization occurs when the actual activity product of the reactants exceeds the

equilibrium activity product of the reactants, with the latter corresponding to the equilibrium constant, K_{sp}. The change in chemical potential is defined as

$$\Delta\mu = k_B T \ln(AP/K_{sp}) \quad (1.1)$$

where k_B is the Boltzmann constant, T is the absolute temperature, and AP is the activity product of the reactants. This can be expressed in terms of supersaturation, σ, by

$$\Delta\mu = k_B T \ln(\sigma) \quad (1.2)$$

where σ is often approximated as (AP/K_{sp})-1 or even (C/C_e)-1. The term C is the actual reactant concentration in solution and C_e is the concentration at equilibrium. Solution properties including concentration, ionic strength, pH, and solvent, can affect the solubility and activity of the material. Consequently, crystallization processes can be manipulated by tuning these parameters.

The energetic landscape for each crystallization processes is distinct and depending on the complexity, they can be classified as either classical or nonclassical crystallization. All aspects of the crystals, including phase, final habit, growth kinetics, and intermediate states, can be selected based on the shape of the energy landscape; therefore, the first step to achieve control over crystallization processes is to understand the underlying mechanism of crystallization. By doing so, we can identify specific stages of crystal formation or sites on crystal surfaces that can be targeted to effectively modulate these processes.

1.3.1 Classical Nucleation Theory

Classical crystallization begins with a phase transition that occurs directly from the solution to an ordered structure identical to that of the bulk crystal. The initial step

requires the system to overcome a free energy barrier, ΔG* (Figure 1.1). This barrier is associated with the energetics involved in the formation of a nucleus. Molecules on the surface of the nucleus are bound to fewer neighboring molecules compared to the ones in the bulk of the nucleus. The difference between them is computed as the interfacial energy (σ). When the size of the nucleus is small, the contribution of surface molecules is dominant, and the interfacial free energy destabilizes the nucleus, leading to high probability of its dissolution. At the critical size (n*), the nucleus can grow or dissolve with equal probability. When the size of the nucleus exceeds this critical size, every addition of a molecule to the lattice reduces the free energy and the nucleus most likely grows. Accordingly, the probability of nucleation strongly depends on the critical size, which is a phenomenon referred to as Gibbs-Thomson effect, which can be manipulated by changing the solution composition (i.e., altering interfacial energy or the supersaturation).

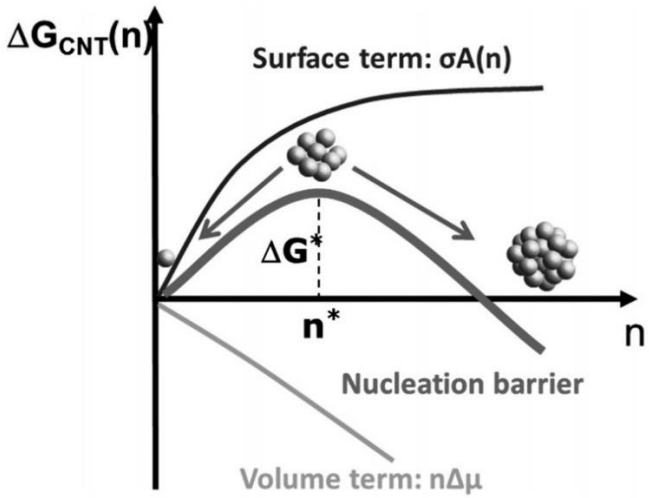

Figure 1.1. Gibbs energy landscape for nucleus formation according to Classical Nucleation Theory, $\Delta G_{CNT}(n)$. n is the number of molecules in a cluster and ΔG* is the max. Height of barrier or nucleation barrier, at critical size (n*).[57]

Indeed, strategies to control crystallization for industrial applications often utilize different regimes on the solubility curve established by the Gibbs-Thompson effect. As shown in Figure 1.2, the crystallization solubility curve can be divided into three regimes: stable, metastable, and unstable zones. The stable zone is where the solution is undersaturated. At fixed concentration, as the solution is cooled, supersaturation increases and at a certain temperature, called the "metastable limit", crystal nucleation begins. The difference between this temperature and the solubility curve is called the metastable zone. It is possible to design crystallization processes to obtain desired crystal size, shape, and purity, using this phase diagram. For instance, after an initial nucleation of crystals ("seeding") in the unstable zone, conditions can be adjusted and retained to be within the metastable zone for crystal growth until the desired size is achieved. Similar control can be accomplished by changing the concentration of the solution.

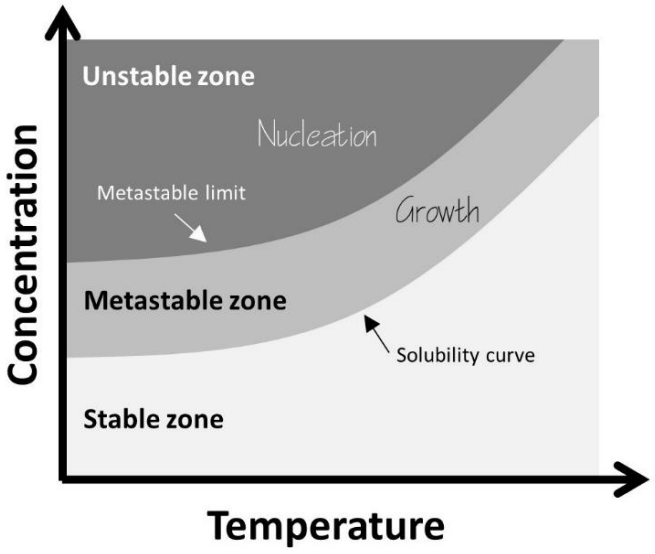

Figure 1.2. Illustration of crystallization solubility curve highlighting three regimes: Stable zone where crystals dissolve, metastable zone where crystals grow, and unstable zone where crystals spontaneously nucleate.

1.3.2 Mechanisms of Classical Crystal Growth

Classical crystal growth occurs through the attachment of monomeric units (ions or molecules) to the crystal surfaces. The three most common sites on crystal surface are terraces, steps, and kinks (Figure 1.3). Terraces are flat regions, and steps are the unfinished layers separating terraces of different heights. Steps can also be unfinished, creating kink sites that are the most favorable for solute attachment due to the high number of neighboring bonds. In addition, kink sites are unique positions that are retained after monomer attachment and do not change the surface free energy of the crystal. Growth kinetics of crystallization is determined by the kink density and the barriers to incorporation into these sites. The anisotropic bonds in crystals lead to a distinct kink density on different surfaces, which in turn contributes to anisotropic growth rates of crystals. Crystal surfaces with higher kink density can rapidly grow out of the crystal, whereas the final crystal habit is determined by large surfaces of the slowest growth directions.

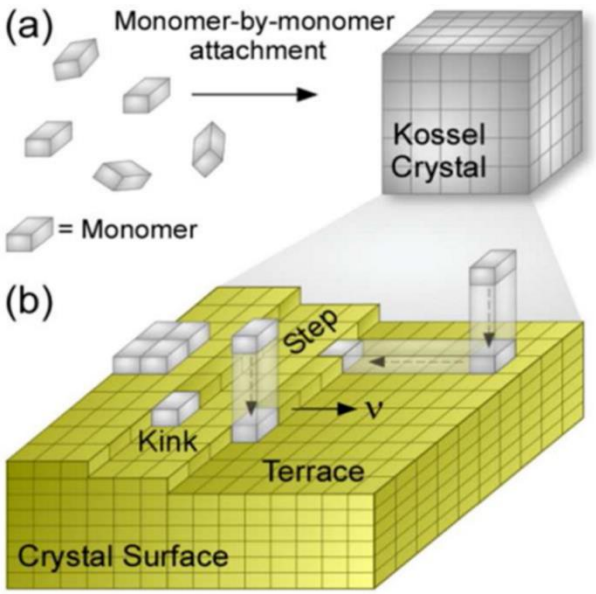

Figure 1.3. (a) Classical crystallization occurs through monomer-by-monomer attachment (b) A model Kossel crystal surface illustrating three common sites (steps, terrace, and kink) and the routes for monomer attachment.[58]

Monomers can reach growth sites either by direct incorporation from solution or by first adsorbing onto the crystal terrace and diffusing along the surface to reach the growth sites[59]. Direct incorporation involves a single barrier that considers the monomer-crystal interaction at the site as well as the displacement of the solvent from the growth sites. The surface diffusion pathway involves multiple energetic barriers for 1) the initial adsorption on terrace, 2) desorption, 3) diffusion along the surface towards the steps, and lastly, 4) the attachment to growth sites.[60-61] Indeed, the number of stages in the latter pathway offers more options to regulate crystal growth. The two mechanisms can be discerned by directly monitoring the velocities of isolated and densely packed steps on crystal surfaces using techniques such as *in situ* atomic force microscopy (AFM). For growth governed by a surface diffusion mechanism, the step

velocity has a strong dependence on step width wherein the densely packed steps grow slower due to the limited amount of solute available.

In a classical growth mechanism, steps can generate from a new layer (or 2D island) and propagate across the surface. Similar to the nucleation of crystals from solution, there is a critical size and energy barrier associated with the formation of new step edges. If the size of the nucleus is less than its critical radius, the layer will likely dissolve, whereas layers exceeding the size of critical radius will likely grow. As supersaturation increases, the critical radius decreases and becomes less than the size of the growth units resulting in barrier-free nucleation and rough surfaces, which is a phenomenon referred to as kinetic roughening. Step generation from a defect in the crystal lattice (e.g., dislocation) can bypass the energetic barrier required for nucleation of a layer and enable growth at lower supersaturation. Steps emanating from a screw dislocation center twist to form a hillock morphology, which serves as a continuous source of kink sites. The dependence of crystal growth rates on these two mechanisms will be discussed in a later chapter.

1.3.3 Nonclassical Crystallization

Nonclassical crystallization refers to relatively more complex pathways due to the involvement of various non-monomeric species. These precursors range from multi-ion complexes to fully formed nanocrystals and vary in size, shape, phase, and structure (Figure 1.4).[62] Precursors can act as growth units via attachments amongst themselves or to a crystal surface and constitute growth sites that have distinct features (i.e., 3D nuclei compared to the 2D layers generated in classical route).[10] The surfaces that grow

as a result of nonclassical routes are continuously changing. Precursors often evolve in size and structure through assembly steps and can become more ordered prior to integrating into the crystalline lattice.[63-64] There are richer set of kinetic and thermodynamic routes to consider for controlling nonclassical pathways compared to the classical growth mechanism. In many cases, classical and nonclassical pathways can occur simultaneously wherein monomer and precursor addition both contribute to the growth of the material[65-69]. The relative contribution of each pathway can vary depending on the crystallization conditions.

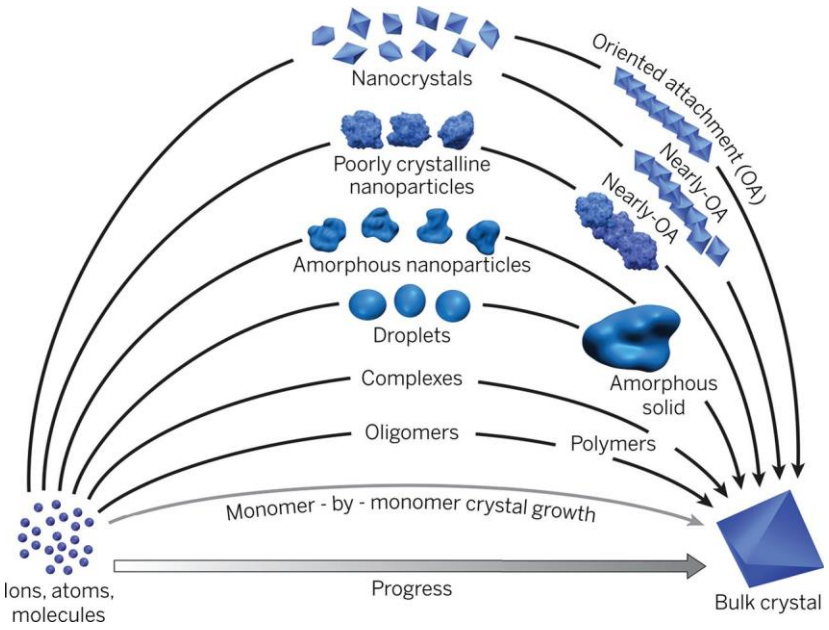

Figure 1.4. Schematic showing wide array of crystallization growth units. Growth by monomer addition is defined as classical while growth via other complex precursors is considered a nonclassical pathway.[62]

The nonclassical pathway has been observed in a diverse number of inorganic and organic materials, which include (but are not limited to) proteins[70-71], calcium carbonate[72], and zeolites (porous aluminosilicates)[63, 65, 73], where growth often involves a wide range of precursors depending on the conditions. For instance, in the synthesis

of zeolites, amorphous particles form with a range of properties based on the selection of solute (silicon and aluminum), pH, and temperature[74]. The existence and role of these precursors are gleaned from both *ex situ* and *in situ* experiments. The former often involve microscopy where images of crystals covered in deposits that resemble the size of the precursors detected via various scattering or spectroscopy techniques in growth solutions is evidence for nonclassical growth.[75-76] *In situ* techniques, such as AFM, have a spatiotemporal resolution enabling direct observation of crystallization by particle attachment[65-66].

1.3.4 Mechanisms of Crystal Growth Inhibition

Growth prevention can generally occur in two ways. Molecules may sequester free ions reducing the relative supersaturation to achieve either partial or full inhibition of crystallization depending on the inhibitor concentration. A second mechanism is kinetic in origin where crystal growth inhibition involves modifier adsorption on crystal surfaces, thereby frustrating monomer attachment to active growth sites (*i.e.*, terraces, steps, and kinks)[77-80]. This interfacial phenomenon can occur by adsorbed modifiers physically impeding solute attachment to adjacent surface sites and/or by the presence of the modifier altering localized solvent structuring[81]. The physicochemical factors governing modifier-crystal recognition include modifier structure, chemical functionality, stereochemistry, and the spatial sequencing of binder moieties;[58, 82] however, there are many unresolved questions regarding the factors governing modifier specificity.

The mechanisms of growth inhibition involve modifier interaction with a specific growth site (Figure 1.5) and characteristic dependence of step speed on supersaturation and inhibitor concentration (Figure 1.6). Modifiers can attach to terraces and impede the advancement of layers. When the layers advance and encounter an adsorbed modifier on the terrace sites, the layers can only propagate by growing around the blocked sites, developing a step curvature. According to Gibbs-Thompson equation, supersaturation is a function of curvature. Layers can only advance when the distance between the pinned sites are much greater than the critical radius of the step curvature and when the distance drops to below the critical curvature, the step movement is arrested. Accordingly, there is a dead zone, a range of concentration below the critical

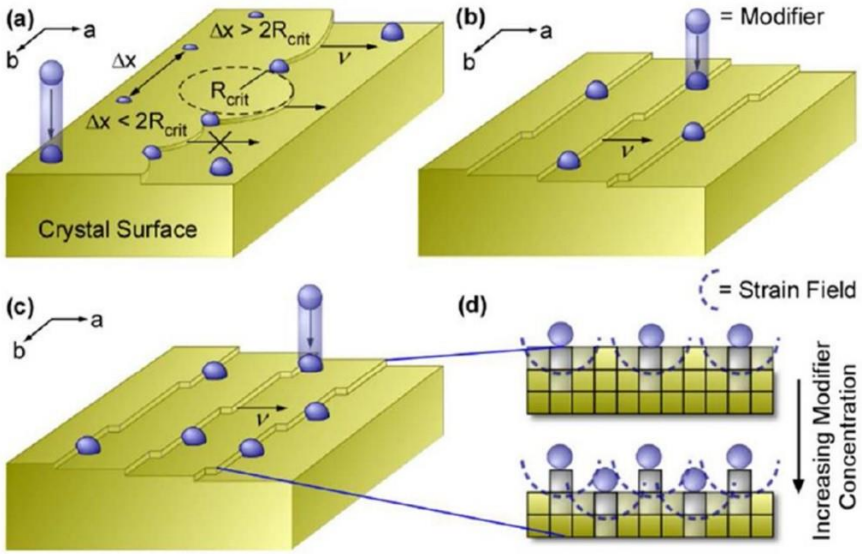

Figure 1.5. Classical mechanism of crystal growth inhibition. (a) step-pinning, (b) kink blocking, and (c and c) strain-induced dissolution.[58]

supersaturation, where no growth occurs. This region expands with inhibitor concentration in which inhibitor occupies more terrace sites. Modifiers can also attach to kink sites and reduce the effective kink density. If inhibitors occupy kink sites, they

block further attachment of solute molecules, which blocks kink propagation but cannot permanently block step advancement. Therefore, the solubility is not affected and only the kinetic coefficient is affected, reducing the slope of supersaturation versus step velocity. Modifiers can also be trapped in a kink site or within an advancing step; and this incorporation results in a distortion of the crystal lattice, which can either increase or decrease the free energy and solubility by enthalpic or entropic contributions, respectively. This only affects the effective supersaturation and does not impact the kinetics of solute attachment. Consequently, the slope of velocity versus concentration plot remains unchanged. Combinations of modifiers that interact with different sites can lead to cooperative effects that are either synergistic or antagonistic.[83] In addition to these more conventional inhibition mechanisms, a recent study by Rimer and coworkers[84] revealed that inhibitors adsorbed to step edges can induce strain and dissolve the crystals under supersaturated conditions. This mode of action is not fully resolved, and it has only been shown to work in a specific range of inhibitor concentrations and supersaturation.[2, 85-86]

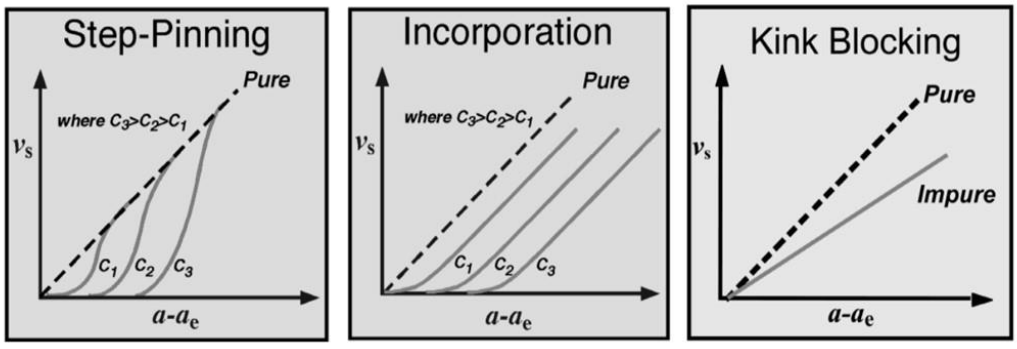

Figure 1.6. The effects of inhibitors on step kinetics (v_s: step velocity, a: activity, a_e: equilibrium activity, c_i: inhibitor concentration).[56]

In nonclassical crystallization, it is challenging to identify specific binding sites for modifier attachment. Modifiers can have indirect effects by altering the self-assembly and the structural evolution of precursors.[87] On the crystal surface, the transition from a disordered precursor to ordered species that incorporates into the underlying crystal may also be hindered. The modifier can complex with solute (e.g., monomer or oligomers in solution) or stabilize precursors to prevent their aggregation and/or attachment to crystal surfaces. Overall, owing to diversity of precursors and the complex dynamics involved in nucleation and growth, there are multiple routes where modifiers can inhibit nonclassical pathways of crystal growth.

1.4 Calcium Oxalate Monohydrate Crystals

Calcium oxalate monohydrate (COM) is the most thermodynamically stable form of calcium oxalate stones and the predominant from of physiological kidney stones.[20] It forms a hexagonal shape and has $P2_1/c$ space group with parameters a = 6.290 Å, b = 14.583 Å, c = 10.116 Å and $\beta = 109.46°$.[21] Synthetic COM crystals typically exhibit a hexagonal platelet morphology bound by (100), (010), (121), and (021) surfaces (Figure 1.7a). Each plane on COM crystal contains different densities of ions in distinct spatial orientations (Figure 1.7b). The density of calcium ions for each surface termination is in the order from highest to the lowest in (100), (121), and (010). The COM lattice contains two types of oxalate ions[88] with the long axis of oxalate ions oriented either perpendicular or parallel to the (010) plane. Both types of oxalate ions are tilted at the apical tips of the crystals, (121) and (021) surfaces.

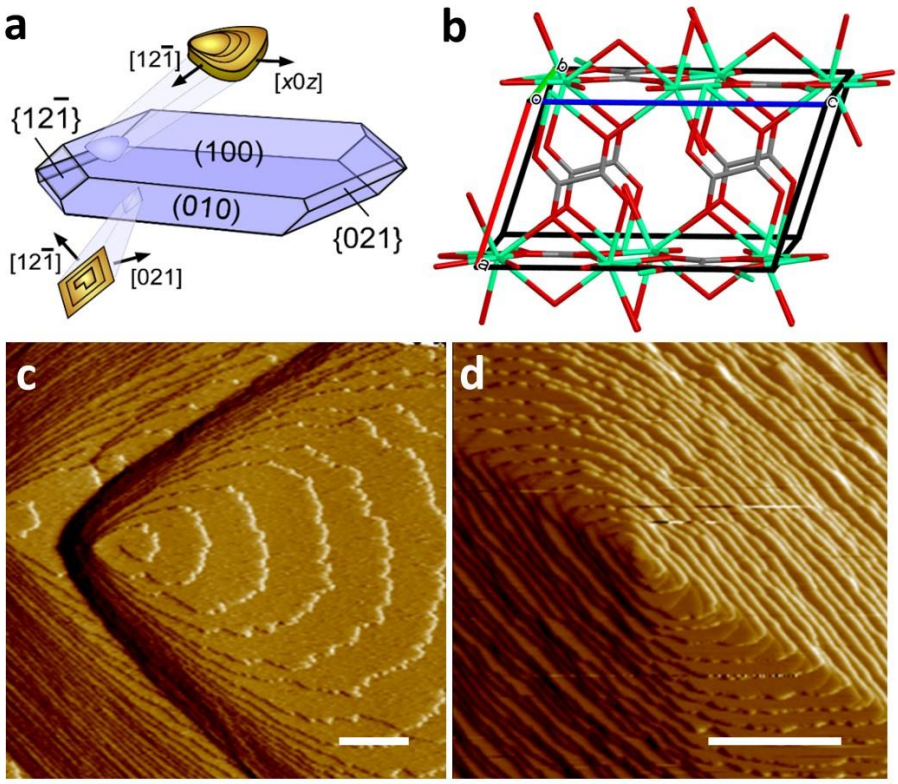

Figure 1.7. (a) COM crystal with indexed facets. (b) Unit cell showing the orientation of oxalate molecules. Hillocks on the (100) basal surface (c) and the (010) surface (d). Scale bars equal 0.5 µm.

1.4.1 Mechanism of Calcium Oxalate Crystallization

Numerous previous reports on COM growth are in consensus regarding *in situ* AFM observations on the (100) and (010) faces. The surface growth of COM adheres to the classical route wherein steps propagate through monomer-by-monomer addition on screw dislocation hillocks (Figure 1.7c). On the (100) surface, triangle hillocks are bound by crystallographically identical [12-1] and [1-2-1] steps, with step advancement predominant along the [001] direction. Growth hillocks on (010) surfaces are rhombohedral in shape and bounded by [12-1] and [021] steps (Figure 1.7d). Several recent studies[89-90] have suggested a nonclassical pathway akin to the two-step mechanism[91-93] is potentially involved in the nucleation of calcium oxalate hydrates. For

instance, Banner et al. observed amorphous clusters that go through dynamic events in the sequence of 1) growth, 2) partial dissolution 3) shape change, and 4) coalescence, to form COM crystals. Putnis and coworkers also made similar observations wherein small calcium oxalate particles that form on a mica surface aggregate into larger entities and finally develop facets resembling the morphology of calcium oxalate crystals. Notably, studies that report nonclassical routes of calcium oxalate formation either use extreme conditions[89-90, 94-96] (i.e., excessively high calcium oxalate and/or inhibitor concentrations) or growth solutions containing disproportionate ratios of calcium and oxalate. Moreover, studies have reported amorphous calcium oxalate (ACO) formation in physiologically-irrelevant media (i.e., ethanol solvent)[97]. As such, there remain many questions pertaining to the nature of clusters or amorphous phases that exist prior to nucleation, as well as the role of these clusters (if any) on COM crystallization.

1.4.2 Inhibitors of COM

In normal urine, which is often supersaturated with respect to the crystallizing material(s), many native species inhibit one of the four critical steps in stone formation: nucleation, growth, aggregation, and retention. Many small ions and molecules (e.g., citrate[98], magnesium, pyrophosphate[99]) and urinary proteins (e.g., Tamm-Horsfall protein[100] and osteopontin[101]) have been identified as inhibitors of calcium stone formation. Therefore, efforts have been made to fundamentally understand this biological control.

Polyprotic macromolecules including urinary proteins are generally the most effective inhibitors owing to the high density of binding moieties. Osteopontin (OPN)

is a well characterized crystal modulating protein. The full length of human OPN is 298 amino acid with an abundance of acidic amino acids (i.e., 48 aspartic acids and 27 glutamic acid residues), as well as 42 serines and 14 threonine residues that are susceptible to post-translational modification commonly as phosphorylation.[27-29] OPN has been shown to inhibit *in vitro* crystallization of COM, whereas animal studies are often conducted on OPN knockout mice, which have been shown to have higher susceptibility to ethylene glycol induced nephrolithiasis[30]. Molecular-scale interactions of OPN with COM surfaces has been resolved using AFM where hillocks on the (010) surface become indistinguishable with imaging time.[102] In contrast, OPN exhibits weak interactions with steps on the (100) surface showing no change in either step velocity or hillock morphology. The high population of acid-rich domains of acidic amino acid is also commonly found in OPN from other species; therefore, many studies have focused on evaluating contributions of aspartic and glutamic acid residues as well as phosphorylation of the OPN peptides[103-104]. It has been reported that short polyelectrolytes (e.g., polyaspartate) and short segments of OPN of highly anionic region can strongly effect nucleation, growth, and agglomeration processes[31-33]. These findings suggest that the entire protein is not required for maximum efficacy, and that smaller peptide domains can inhibit COM crystal growth.

Molecular modifiers offer increased flexibility to tune their specificity for different crystallographic faces and mediate the anisotropic rate of crystal growth. Inhibitors can interact with the COM surfaces via calcium bridging, COO^- (COM) … Ca^{2+} … ^-OOC (modifier), or hydrogen bonds, -COO- …HOOC-. The inhibitor's efficacy is generally improved with acid strength[86] and the addition of acidic groups[105].

Taking inspiration from natural urinary proteins, a variety of small molecules with high percentages of anionic functional groups (e.g., carboxylates) have been tested as putative inhibitors of COM crystallization. In particular, citrate, containing three carboxylic acids, revealed a maximum of 60% inhibition of COM crystallization. Hydroxycitrate (HCA), a structural analogue of citrate with an additional hydroxyl group, was found to be more potent.[84, 86] These molecules were also found capable of imparting strain and dissolving crystal surfaces. This phenomenon was observed using *in situ* AFM wherein steps receded in supersaturated solution containing a narrow concentration of citrate or HCA. Citrates, in conditions outside of this specific range, along with various other modifiers have been shown to follow a more conventional mode of action (e.g., step pinning or kink blocking), as illustrated in Figure 1.5.

Ionic modifiers were also shown to have a marked impact on COM growth with respect to the crystal size, habit, number density, and growth rate[80, 106]. Among alkali metals, Li^+ and K^+ were the most and least effective inhibitors of COM, respectively, with trends that are qualitatively consistent with Collins' theory of matching water affinities to determine their binding affinity with the COM surfaces.[80] Zinc ions had a unique ability to truncate the height of the layers on the (100) face, which had a concomitant effect of facilitating intergrowth and hindering the step growth on the surface.[107]

The role of inhibitors on alternative crystallization pathways have also been proposed. Akin et al.[108] proposed that rapid adsorption of polymeric additives can reduce the number of active growth sites on subcritical nuclei. The thermodynamically unstable nuclei eventually dissolve and prolong the induction periods. Studies have

shown different intermediates of calcium oxalate mineralization that can either be induced or altered in the presence of modifiers. Ruiz-Argudo et al.[89] identified small individual particles and a carbon-rich rim around AOC particles in the presence of citrate, suggesting the possible role of modifier as a colloidal stabilizer. Banner et al.[95] proposed citrate can prevent the stable precipitation of calcium oxalate through the formation of soluble calcium/citrate complexes. Moreover, some modifiers are found to inhibit COM formation by modulating the structure, hydration level, and solubility of amorphous precipitates and directing the formation of different calcium oxalate hydrates[89-90, 95]. However, in line with uncertainties of the role of the precursor phase(s) in calcium oxalate formation, the physiological relevance of the control over these routes is still not fully understood.

1.5 Struvite Crystals

Struvite is a transparent inorganic crystal which belongs to the non-centrosymmetric point group mm2 of the orthorhombic system with the space group *Pmn2₁*, with dimensions: a = 6.9650(2) Å, b = 6.1165(2) Å, and c = 11.2056(3) Å[1]. The basic struvite crystal habit (Figure 1.8a) is a hemimorphic coffin-like morphology composed of (001), (00-1), (101), (10-1), (011), (012), and (010) faces wherein the (001) and (00-1) faces are not related by symmetry element[109-110]. The crystal structure (Figure 1.8b) contains tetrahedral PO_4^{3-}, octahedral $Mg(H_2O)_6^{2+}$, and tetrahedral NH_4^+ groups held together by hydrogen bond network of O-H…O and N-H…O. The c-axis is a

dipolar axis with NH_4^+ groups terminating (001) surface and PO_4^{3-} and $Mg(H_2O)_6^{2+}$ groups terminating (00-1) surface.[111]

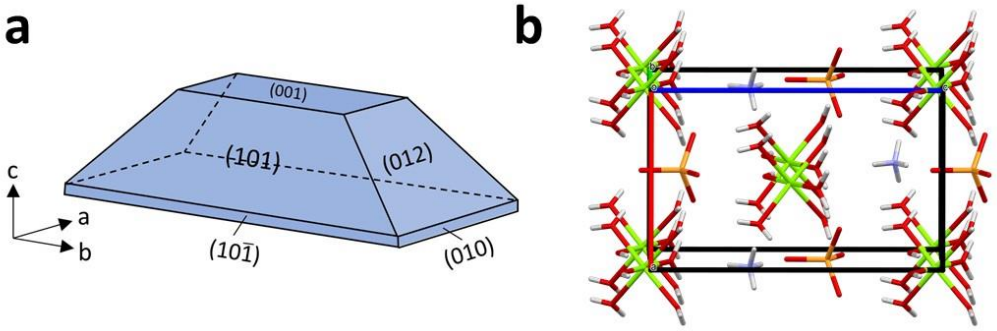

Figure 1.8: (a) Schematic of a characteristic struvite crystal with indexed facets. (b) Unit cell of struvite crystal.

1.5.1 Modulators of Struvite Crystallization

The formation and characteristics of struvite stones, known as infection stones, is heavily governed by the urinary composition and its interaction with bacteria. Owing to the acid/base chemistry of ammonia and phosphate (discussed in **Chapter 2**), both the pH change and the ion concentrations determine the supersaturation of the solution and are critical for struvite crystallization. Fundamental understandings of struvite nucleation and growth are still at their infancy. Previous studies have reported struvite nucleation and growth on brucite, $Mg(OH)_2$, surface involving particle-mediated processes, which suggest a deviation from classical crystallization[112]; however, the physicochemical properties of these particles remain elusive, as well as the exact mechanism of struvite crystallization, which could potentially involve classical pathways of ion/molecule addition.

Struvite crystals can often form twinned, branched, and dendritic structures[109, 113]. These complex structures primarily form at high pH[109-110, 114-116]; however, the

formation of these hierarchical structures is attributed to rapid rates of pH change with only a minor influence from the actual value of the pH. Solutions experiencing a gradual increase in pH have no reported dendrite-like crystals. The pH increase by chemical addition of bases is more rapid than the pH change induced by bacteria. One characteristic feature of struvite that is commonly reported in literature is the surface features that show patterned pores resembling typical structures of mesocrystal assembly[109-110, 115]. Analysis of the cross sections of these crystals do not show ordered arrangement of small units, proving otherwise.[109] Nonetheless, these external features only form in the presence of bacteria, suggesting a direct interaction between struvite crystal surfaces and the microorganisms. The interaction between bacteria and struvite crystals could be due to the anionic nature of the outermost structures of *P. mirabilius* cells, which is composed of polysaccharides. Macromolecules secreted by bacteria also contain anionic groups that can facilitate their interaction with struvite crystals. For instance, Zhao et al.[116] reported that macromolecules adsorbed to struvite surface could increase the local Mg^{2+} concentration and serve as nucleation sites for the overgrowth of struvite.

Prior studies have also identified a select number of modifiers that can inhibit struvite crystallization. Phosphocitrate reduces the size and the number of struvite crystals formed[117]. Moreover, it enhances the expression of (011) and (101) planes, presumably due to a high density of magnesium ions on those terminations that facilitate the interaction with phosphocitrate. Citrate increased the induction for struvite formation by forming complexes with ammonium and magnesium ions[118]. The observed increase (001) surface area and the corresponding reduction in *b/a* aspect ratio was

attributed to the high amount of NH_4^+ groups exposed on these surface terminations. Similarly, the presence of tetrasodium pyrophosphate caused a delay of struvite nucleation and reduced quantity of crystals by forming $MgP_2O_7^-$ complexes.[119] It also induced morphological changes that resemble overgrowth. It has also been shown that substances with chelating properties (e.g., EDTA) can inhibit struvite formation through pure chelation without apparent interaction with crystal surfaces.[120] Moreover, several natural compounds from plant extract[121-123] (e.g., Commiphora wightii, Boerhaavia diffusa Linn, and Rotula aquatic Lour) were also found to have an inhibitory effect on struvite formation.

To our knowledge, other research groups have not provided direct molecular scale observation of inhibitor interactions with struvite crystal surfaces. The majority of studies that test putative modifiers of struvite formation employ bulk crystallization assays under quiescent conditions where solute depletion is tracked by changes in solution properties (e.g., conductivity and pH), or the net change in average crystal size and morphology has been evaluated *ex situ* by optical/electron microscopy; however, these techniques have limitations that include (but are not limited to) their inability to elucidate mechanisms of growth and modifier action, and to simulate flow conditions encountered in the practical applications described above. The use of flow systems to study mineral formation is purported as a promising approach[124-127], especially for infection stone formation, as they mimic the flow conditions where struvite naturally forms (e.g., pipelines, urinary tract systems, etc.)[31, 128].

1.6 Thesis Overview

The first part of the thesis focuses on struvite. In Chapter 2, we establish a platform to evaluate struvite growth under flow and evaluate the growth rates and growth mechanisms at various conditions. In Chapter 3, we utilize this platform to evaluate the effects of a set of putative inhibitors, polyphosphates, on struvite nucleation and growth and elucidate their mechanism of action. In Chapter 4, we investigate the antimicrobial and anti-encrustation activities of tetrasodium salt form of ethylenediaminetetraacetic acid (tEDTA) to combat catheter associated urinary tract infections and the associated catheter blockages. In this work, the effect of tEDTA on struvite nucleation and growth is examined by bulk crystallization assays, microfluidics assays, as well as in vitro bladder model assays.

Among the COM growth inhibitors studied, HCA is of particular interest as a potential new therapy for calcium urolithiasis. In Chapter 5, we detail the crystal inhibition activity of HCA, review current knowledge of HCA use in humans, and identify gaps in knowledge that require appropriate research studies before HCA can be recommended as a therapy for kidney stones. In Chapter 6, we benchmark from the struvite studies and examine the effects of polyphosphates on COM crystallization. Finally, we conclude the thesis by providing a summary and future directions for the projects.

CHAPTER 2

A NEW PLATFORM TO ASSESS TIME-RESOLVED DYNAMICS OF STRUVITE CRYSTALLIZATION

2.1. Motivation

The crystallization of struvite ($MgNH_4PO_4 \cdot 6H_2O$) is relevant for nutrient (nitrogen and phosphorus)[129-130] recovery in water purification[131-136] and scale formation in pipelines[137-138], and it is a primary component of so-called *infection stones* arising from urinary tract infections[40, 50-51]. The vast majority of studies focused on struvite have overlooked fundamental aspects of crystal nucleation and growth at near molecular level. Knowledge of these processes can aid in the design of conditions that either promote or inhibit struvite formation, depending on the application. The primary motivation for this study is derived from the dearth of information regarding the factors that mediate the formation of struvite infection stones in urolithiasis, which is one of the most difficult and dangerous stone diseases due to the large size and rapid growth of the crystals, and high recurrence rate[139]. Infection by urease-positive bacteria, predominantly *Proteus mirabilis,* leads to a cascade of reactions that elevate urinary pH, as well as ammonium and phosphate ion concentrations, thus resulting in struvite formation[40, 140-141]. Struvite crystals, without proper treatment, can develop into large staghorn calculi (>2,500 mm^2), with the capacity to fill the entire intra-renal collecting system, irritating the bladder and blocking the flow of urine[142-143]. Moreover, crystalline biofilms composed of struvite complicate the care of patients undergoing long-term

catheterization due to catheter encrustation and blockage, which impacts approximately 50% of catheter users[41, 49-50, 144]. Due to the emergence of antibacterial resistance and reported recurrence rates of 50%, the standard care involving removal/replacement of catheters and the use of antibiotics is becoming less effective[145-148].

Understanding processes of crystallization is crucial for development of improved therapeutics for struvite infection stones. Several factors (e.g., saturation state, pH, and the presence of growth modifiers) can influence struvite formation[51, 117-119, 149-151]. Growth modifiers ranging from ions and small molecules to large macromolecules can impact crystal growth by altering supersaturation (i.e., forming modifier-solute complexes), physically blocking solute attachment by binding to crystal surfaces, or disrupting the local environment around crystal-solute interfaces[58]. Prior studies of modifiers in other systems, such as antimalarials used to avert hematin crystallization[152] and acids used to treat calcium oxalate kidney stones[153], have been shown to inhibit crystallization through preferential binding to crystal surfaces. In some cases, modifiers have been shown to possess the ability to dissolve crystals in supersaturated conditions[2, 84, 154]. Similarly, studies have identified a select number of modifiers (e.g., citrate[118], phosphocitrate[117], and pyrophosphate[119]) that influence struvite crystallization. The majority of studies that test putative modifiers of struvite formation employ bulk crystallization assays under quiescent conditions where solute depletion is tracked by changes in solution properties (conductivity, pH), or the net change in average crystal size and morphology is evaluated *ex situ* by microscopy; however, these techniques are typically time consuming and have limitations that include (but are not limited to) their

inability to elucidate mechanisms of growth and modifier action, and to simulate flow conditions encountered in the practical applications described above.

In this chapter, we developed a microfluidics platform for the rapid screening of struvite growth under flow at varying conditions. Our findings demonstrate the advantages of this platform over more traditional bulk crystallization assays at quiescent conditions, owing in part to the ability to capture time-resolved dynamics of crystal growth. This system also creates an environment that mimics the flow conditions where struvite forms naturally (e.g., pipelines, urinary tract systems, etc.). One of the disadvantages of bulk assays is the inability to decouple nucleation and growth, which is accomplished in the microfluidics device using crystal seeds that are grown under the continuous supply of solutions maintained at constant composition. Herein, we evaluate struvite growth under flow conditions to quantify the kinetics of crystallization and changes in morphology as a function of supersaturation. In parallel, we conducted *in situ* scanning probe microscopy measurements to elucidate the molecular mechanisms of struvite growth. These microscopic studies correlate well with macroscopic kinetic measurements showing a transition in the mode of growth from screw dislocation to two-dimensional (2D) nucleation with increased supersaturation.

2.2. Result and Discussion

2.2.1. Bulk Crystallization Assays

We first tested the effect of supersaturation on struvite crystallization using *ex situ* bulk crystallization, which is a conventional means of evaluating the independent or combined effects of different parameters by tracking the changes in overall size,

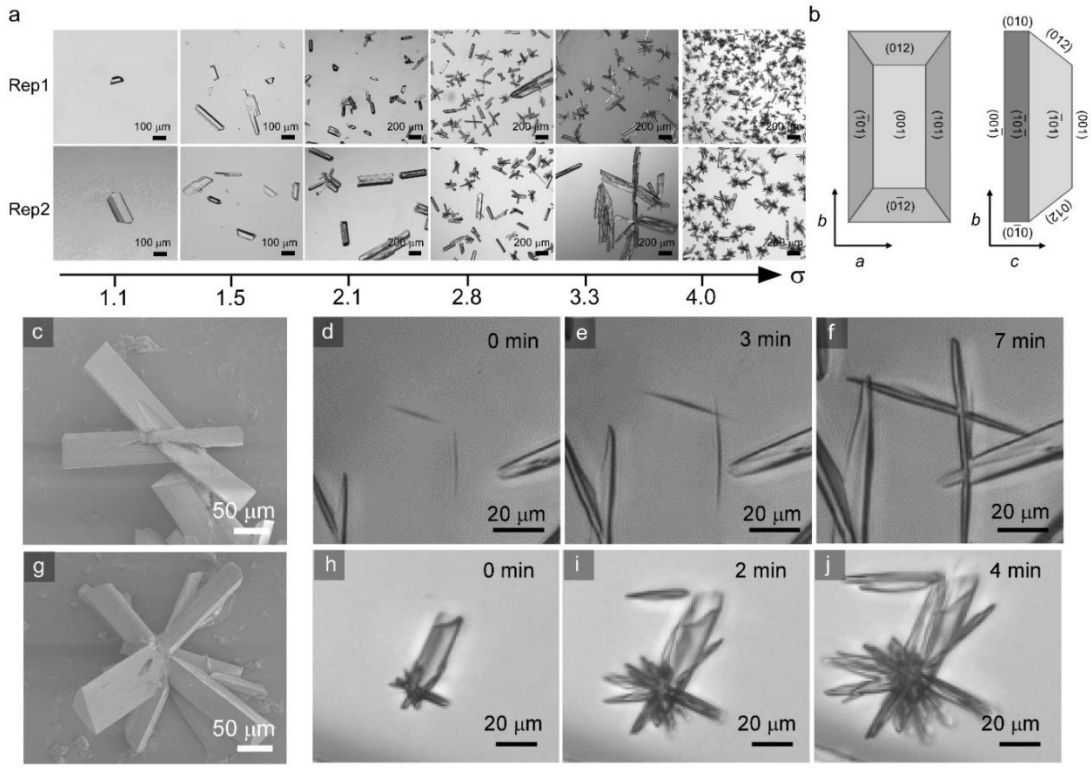

Figure 2.1. (a) Effect of σ on bulk crystallization. (b) Crystallographic faces of struvite[110]. (c) X-shaped crystal. (d-f) Overgrowth of individually nucleated crystals. (g) Spicule-like crystal. (h-j) Outward growth of crystals into (g).

morphology, and number density of crystal populations. The relative supersaturation, σ, of growth solutions was adjusted by altering the pH from 8.0 to 9.3 (Figure A1), which yields values of $1.4<\sigma<4.0$, respectively (where $\sigma = (IAP/K_{sp})^{1/3}-1$ and pK_{sp} = 13.26 at 25 °C[155]). In assays with $\sigma \leq 1.0$, there were no crystals detected within the typical timeframe of measurements (ca. 36 h). At low supersaturation ($\sigma = 1.0 – 1.5$), a small population of crystals with a coffin-like morphology, analogous of struvite crystals found in living organisms was observed[109, 113]. Scanning electron micrographs (Figure A3) revealed that the coffin-shaped crystals exhibit multiple facets with the following surface terminations (Figure 2.2.1b): $(001), (00\bar{1}), (012), (0\bar{1}2), (101),$

and $(\bar{1}01)$ faces[110]. At moderate supersaturation (σ = 1.5 – 3.0), the population of crystals was predominantly twinned and/or polycrystalline, producing x-like and star-like crystals respectively. The latter are formed by two general processes. The first involves either the agglomeration or overgrowth of individually nucleated crystals (Figure 2.2.1c). Time-resolved optical micrographs from the microfluidics analysis (Figure 2.2.1d – f) have captured the overgrowth of adjacent crystals. The second process involves the growth of spicule-like particles comprised of multiple crystals growing in random directions from an apparent common core (Figure 2.2.1g). Time-resolved images (Figure 2.2.1h – j) have been able to capture the outward growth of crystals in these hierarchical structures. Collectively, these complex features render the analysis of anisotropic crystal growth more challenging.

For all bulk crystallization assays in this study, comparisons among different batches revealed wide variations in crystal size, shape, and number density. Examples of two representative (Rep) batches are shown in Figure 2.2.1a for each supersaturation tested. In some instances (e.g., σ = 2.1), there were substantial differences between batches, whereas others were more consistent (e.g., σ = 4.0); however, at high supersaturation (σ >3.0) the frequency of hierarchical structures was increased (Figure A2). Moreover, the crystals can develop irregular morphologies, as shown in Figure 2.2.1a (Rep2, σ = 3.3), that resemble either rough growth or defective crystals (e.g., intergrowths). There are several factors that potentially contribute to the polymorphism

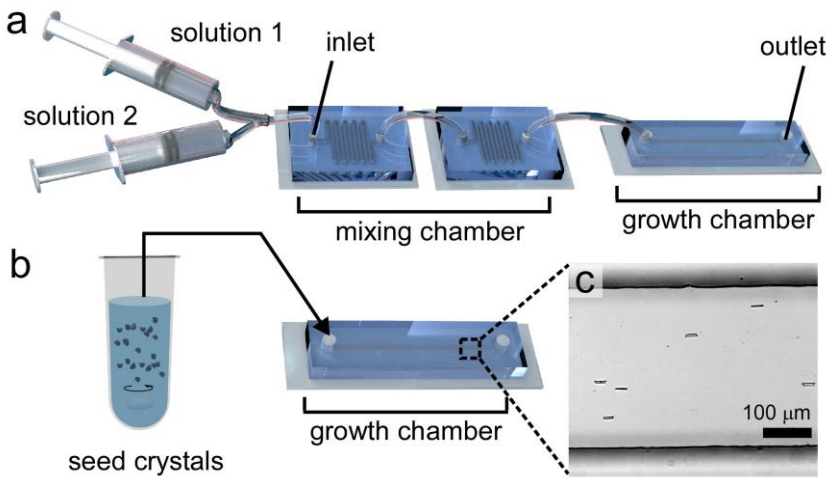

Figure 2.2. Microfluidic device set up. (a) In situ seeding method. (b) Seed transfer method. (c) Optical micrograph of a seeded channel.

and heterogeneity of struvite crystals grown in quiescent conditions. The first is a correlated reduction in pH (by 1 – 2 pH units) with struvite formation, which has a concomitant effect on supersaturation (Figure A1). In addition, the fact that struvite is composed of three ionic constituents[109] suggests that diffusion limitations in quiescent assays could lead to local variations in supersaturation. Irrespective of the causes, the resultant heterogeneity makes it difficult to quantify systematic trends in the growth and/or physical properties of struvite crystals as a function of synthesis conditions. To this end, we designed and implemented a microfluidics platform to address these limitations.

2.2.2. Microfluidic Platform for Struvite Crystallization

Microfluidics is most commonly used as a microbatch system in the form of droplet microfluidics to monitor crystal nucleation and growth in nanoliter volumes[156-158]. To our knowledge, few crystalline materials have been studied in microfluidic

devices under continuous flow of a growth medium[159-160]. In this study, we used a modified design of an established microfluidics platform[159] for measurements of struvite crystallization. The configuration used in the microfluidic system has several advantages: it delivers a growth medium at fixed pH and supersaturation to crystal surfaces, allows for the analysis of anisotropic growth in multiple crystallographic directions, and is an efficient method for gathering statistically-significant data over a range of synthesis conditions. This is a unique platform for characterizing struvite crystallization in that it mimics the flow conditions of the urinary tract system, which is relevant for biomedical applications, and provides a well-defined laminar flow profile for assessing the effects of mass transfer. Moreover, the continuous flow configuration overcomes limitations of droplet microfluidics (and quiescent bulk assays) by isolating the effects of growth from that of nucleation at fixed solute supersaturation.

The procedure for introducing crystal seeds into the microfluidics device required optimization. Our first attempt involved *in situ* seeding whereby a highly supersaturated solution was mixed in stream and flowed through a growth chamber to nucleate and retain crystals within microchannels (Figure 2.2a). In this configuration, a mixture of magnesium ammonium phosphate (solution 1) was mixed in-line with an aqueous solution of NaOH and NaCl (solution 2) in ratios that generated a combined growth solution of predetermined pH and supersaturation. An undesirable outcome of this set up was the generation of high solute concentrations at the boundaries of the two inlet solutions (prior to the generation of a homogeneous solution within the mixing chamber). This consequently led to rapid struvite crystallization that clogged the

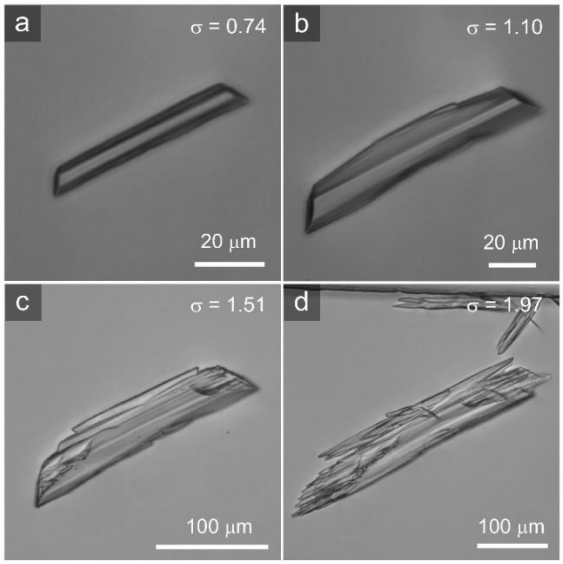

Figure 2.3. A seed crystal grown under continuous flow (24 ml min^{-1}) of solution at (a) $\sigma = 0.74$, (b) $\sigma = 1.10$, (c) $\sigma = 1.51$, and (d) $\sigma = 1.97$.

inlet tubing and the micrometer-sized channels of the mixing chamber. The preemptive formation of seed crystals led to their random and scattered deposition on glass interfaces throughout the microfluidics device. An interesting observation was also made when attempting to conduct secondary growth of seeds at lower supersaturations. Notably, a significant fraction of seed crystals would not grow, which we attribute to potential defects leading to strain. For instance, it is reported that crystal defects can strain the lattice, increase the free energy of crystal and reduce supersaturation, thereby facilitating growth cessation[161]. We posit that the unusually high local concentrations at the point of in-line mixing increases the probability of generating highly defective seed crystals. This effect was not observed in our previous study of barite ($BaSO_4$)[159], which was used as a reference for our initial design of the microfluidics device for this study.

Among the fraction of seed crystals that were observed to grow within the microchannels when placed into contact with a secondary growth solution (Figure 2.3a), higher supersaturation led to abnormal phenomena. This included asymmetrical growth

along particular crystallographic directions (Figure 2.3b), and the formation of crystals that resemble those in Figure 2.2.1a ($\sigma = 3.3$) when the growth solution introduced

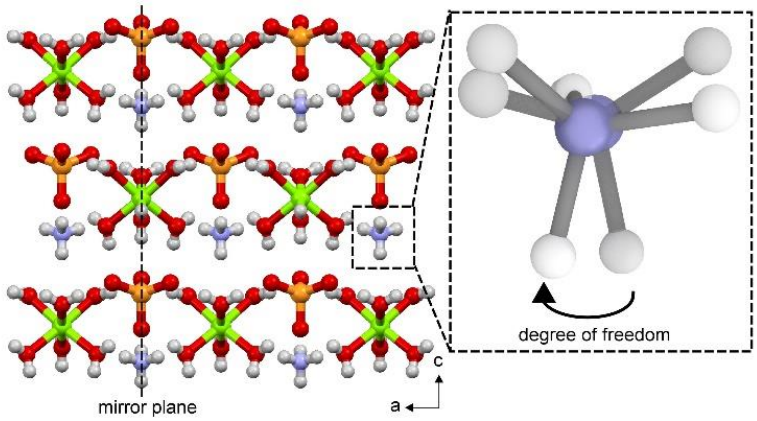

Figure 2.4. Structure of struvite along the [010] zone axis[1], where the dashed line indicates the mirror plane. Left is an ordered arrangement and the right illustrates disorder of ammonium groups.

into the microfluidics device reached $\sigma \geq 1.5$ (Figure 2.3c and d). The purportedly defective seed crystals retained within the growth chamber tended to be one of two general types: those that appeared to lack defects (similar to Figure 2.3a) and those that had notable irregularities (similar to Figure 2.3c). Our studies of varying supersaturation were intended to assess our hypothesis that local increases in solute concentration increased the probability of generating irregular (or defective) seed crystals. Indeed, our findings indicate that higher supersaturation does result in these apparent features; therefore, based on these observations, all *in situ* growth measurements reported herein were performed at lower supersaturations ($\sigma < 1.1$).

We performed structural analysis to look for possible signatures that may make struvite prone to defects. Several crystal structure determinations of struvite have been published, based on X-ray and neutron diffraction data[1, 111, 162-164]. While clues of subtle disorder are present in each of the published results, in every case except one it was not

reported. Whitaker *et al*. proposed that the ammonium ion was partially disordered, but they lacked the technology in 1970 to conclusively prove it[162]. In order to verify inherent disorder in the structure, we collected our own high resolution X-ray data. Our data are consistent with the previous studies and confirm that the ammonium group truly is disordered across a mirror plane (Figure 2.4). There is also strong evidence that several of the water molecules are disordered as well. The various ionic species comprising solid struvite do not quite fit together in an orderly fashion. Such structural characteristics can predispose the crystals to growth defects, especially under a highly supersaturated solution. Since all room temperature and very low temperature studies to date show the same evidence of internal disorder, the method by which the crystals are grown would not seem to be a factor in removing this disorder within individual single crystals; however, changing the growth conditions could conceivably alter the thermodynamics of crystallization and significantly reduce the tendency of twinning and fracturing.

Using the microfluidic configuration in Figure 2.2a, we tested a range of supersaturations ($1.5 < \sigma < 4.0$) for seeding by two different routes: altering pH (pH 7 - 9) and directly adjusting solute concentration (2.1 – 7 mM). In all cases heterogeneity among seed crystals with respect to their size and apparent defects, which manifested in a broad range of growth rates were observed. This confirmed the necessity of utilizing an alternative seeding method. Previously, Jensen and coworkers[160] reported a process whereby they seeded glycine crystals in a microfluidics device by first synthesizing seed crystals in a continuously stirred system and then delivering them into the device using pressure-driven flow. Herein we adopted a similar approach (Figure 2.2b) using seed

crystals prepared by stirring a supersaturated solution ($\sigma = 1.5$) with a stir bar at 600 rpm for 15 sec. This relatively short timeframe limits the nucleation density and results in mostly single crystals of approximately homogeneous size. This solution was then immediately transferred to a syringe and delivered directly to the growth channels of the microfluidic device. With this method, we were able to introduce ca. 20 to 30 well-faceted crystals (35 – 45 μm in length) along the channel (Figure 2.2b, callout). This approach also circumvented the problem of uncontrolled precipitation in Figure 2.2a that led to clogged microchannels and crystal heterogeneity. Another advantage of the direct injection of seeds is an observed uniformity of growth rates among populations of crystals (as illustrated in the following sections).

2.2.3. Analysis of Struvite Growth under Flow

Seed crystals orient along the microchannels in one of two configurations with their faces normal to either the $\vec{a}$ direction (Figure 2.5a) or $\vec{c}$ direction (Figure 2.5b). An approximate equal percentage of both configurations enables the tracking of struvite growth along all three principal crystallographic directions.

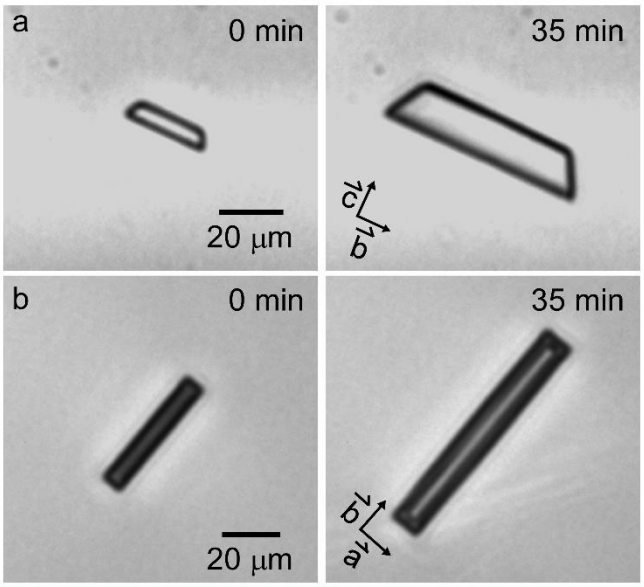

Figure 2.5. Struvite growth under flow of supersaturated solution (σ = 0.95) at room temperature. Struvite crystals lying normal to the (a) $\vec{a}$ direction and (b) $\vec{c}$ direction. Images are shown at time 0 min (left) and 35 min (right).

Prior experimental and computational fluid dynamics analyses[159] of the microfluidic device have shown that the mixing chamber results in complete mixing of solutes without detectable gradients along the width of the microchannels in the growth chamber. For all measurements reported herein, the supersaturated solutions used for growth studies were set below the metastability limit (σ <1.1) to eliminate the possibility of nucleation within the solution.

Struvite crystals were grown under both quiescent and flow conditions. Struvite grows fastest in the $\vec{b}$ direction, thus leading to its characteristic coffin-like shape with a truncated rectangular pyramid morphology (Figure 2.2.1b). Under quiescent conditions, struvite crystals increase only slightly in size before reaching a plateau (Figure 2.6) due to the rapid depletion of solution, thus reducing the driving force for struvite growth. Furthermore, struvite precipitation causes a reduction of pH which

accelerates the drop in supersaturation. These effects restrict bulk crystallization analyses to measurements of final crystal size and morphology. Conversely, a continuous flow of supersaturated solution maintains a constant driving force (supersaturation) that allows for kinetic studies of struvite growth in all crystallographic directions. As shown in Figure 2.6, measurements of crystal length in the $\vec{b}$ direction under flow result in a linear advancement with time. Using this data, we can then extract the growth rate, *r*, from the slope of the line.

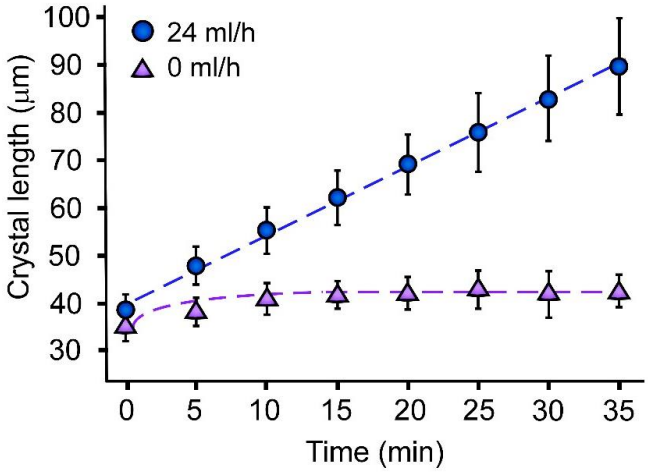

Figure 2.6. Temporal change in struvite crystal length, $\vec{b}$, in the microchannels at quiescent and flow conditions (flow rate = 24 ml/h).

The microfluidics platform allows for facile analysis of parameters such as supersaturation, solution pH, and flow rate with statistical certainty. It is well established that crystal growth can be either transport or kinetically limited[165]. The former is dominated by the mass transport of solute from the solution to the crystal solid-liquid interface, whereas the latter is limited by the energetics of solute incorporation into the crystal lattice. The relative importance of each rate limiting step can be tuned by varying the flow rate. An increasing flow rate results in a decreasing

boundary layer thickness surrounding the crystal interface, thereby reducing the time for solute to diffuse through the solution to the crystal surface. In a purely kinetic regime, the crystal growth rate reflects the rate of solute (ion or molecule) adsorption/desorption at the crystal surface, which is tuned by the supersaturation. Here, we investigated the relative importance of transport versus surface kinetics by varying the flow rate in the microfluidic device. For these measurements we focused exclusively on the fastest growing direction ($\vec{b}$ axis). As shown in Figure 2.7, the rate of crystal growth increases linearly with flow rate when the flow rate is less than 24 ml h^{-1}, which corresponds to the region of transport limitations. At flow rates higher than 24 ml h^{-1}, struvite growth rate is approximately constant (i.e., plateaus at 0.9 μm h^{-1}), thus signifying the onset of the kinetic regime. For measurements reported herein, we operate at flow rates within the kinetic regime to minimize the effects of mass transport limitations.

Growth kinetics were examined over a range of supersaturations. A unique aspect of the microfluidic platform is the ability to track macroscopic growth along all principal dimensions of a crystal, which is not possible with techniques such as AFM or ellipsometry, which are limited to specific interfaces (i.e., often faces with the largest

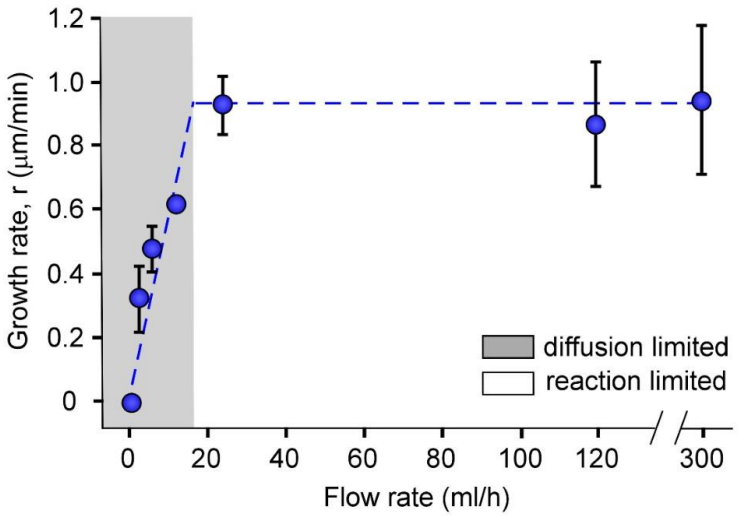

Figure 2.7. Effect of flow rate on the seeded growth of struvite measured by linear regression of crystal length, $\vec{b}$, versus time in a growth solution at σ = 0.89.

surface area). Struvite growth rates along the $\vec{a}$, $\vec{b}$, and $\vec{c}$ directions showed a superlinear dependence over the range of supersaturations investigated (Figure 2.8). This dependence is indicative of surface growth by layer generation and spreading where models predict a power law behavior. It is generally established that the growth of faceted crystal surfaces proceeds layer by layer through spiral growth triggered by screw dislocations, and/or nucleation and growth of 2D islands[56]. The normal growth rate (R) of a face resulting from a screw dislocation is related to step velocity *v* and mean step density, *h/l*, where *l* is the characteristic spacing between steps and *h* is the step height

$$R = (h/l)v. \tag{2.1}$$

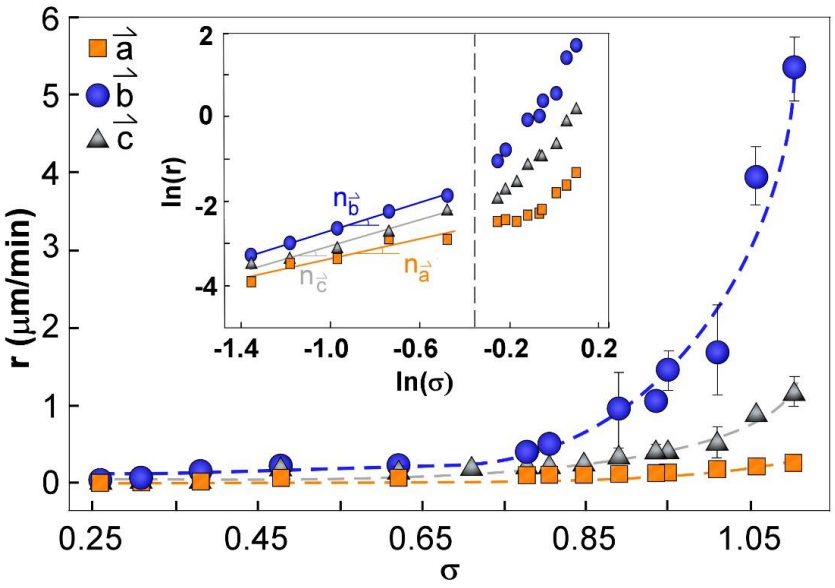

Figure 2.8: Growth rate, r, in the $\vec{a}$ (orange), $\vec{b}$ (blue), and $\vec{c}$ (grey) directions measured in microchannels at a fixed flow rate (24 ml/h) as a function of relative supersaturation, σ.

When the separation between the turns of spirals is sufficient (i.e., when the diffusion fields of the turns do not overlap), the relationship between normal growth rate and supersaturation is $R \sim \sigma^2$. For overlapping or dense hillocks,[59, 166] this dependence is reduced to $R \sim \sigma$. The growth rate of faces with 2D nucleation is determined by the size of the nuclei and their rates of formation. According to classical nucleation theory (CNT), the rate of 2D nucleation of new layers (J_{2D}) is determined by the free-energy barrier for formation of the 2D critical nucleus, ΔG^*_{2D}

$$J_{2D} = \exp(-\Delta G^*_{2D}/k_B T). \quad (2.2)$$

Estimates of the barrier for nucleation, $\Delta G^*_{2D} = \pi R_c h \gamma$, are dependent upon the critical radius of the nucleus, $R_c(\sigma)$, which is governed by the Gibbs-Thompson relation, $R_c = \Omega\gamma/k_B T\sigma$ (where h is the layer thickness; γ is the surface free energy of the layer edge; and Ω is the volume of a formula unit). Based on the decrease in R_c with increasing σ,

the resulting growth rate for the 2D nucleation regime is expected to follow an exponential dependence upon σ.

Replotting the growth rate data as *ln r* versus *ln σ* (Figure 2.8, inset) reveals a linear region corresponding to the quasiparabolic rate law of screw dislocations with the expected power law dependency in the range 1<n<2 (i.e., $n_{\vec{a}} = 1.1,\ n_{\vec{b}} = 1.6,\ n_{\vec{c}} = 1.5$). At higher supersaturation, the reaction order increases to n >2 indicating an exponential dependence that is commensurate with the transition to 2D nucleation (the corresponding linearized plot is provided in Figure A4 with $n_{\vec{a}} = 5.6,\ n_{\vec{b}} = 8.2,\ and\ n_{\vec{c}} = 6.3$). In order to validate the transition between these two modes of growth, we monitored struvite crystallization at a microscopic length scale using *in situ* AFM to capture layer-by-layer growth in real time, as described in the following section.

2.2.4. Analysis of Struvite Surface Growth

In situ AFM has proven to be a valuable technique for elucidating structural and dynamic characteristics of crystal growth mechanisms[10, 61, 102]. Previously, it has been observed that struvite nucleation and growth on a brucite, $Mg(OH)_2$, surface occurs *via* a particle-mediated process suggesting a deviation from classical crystallization[112]; however, the physicochemical properties of these particles remain elusive, as is the exact mechanism of struvite crystallization, which could potentially involve classical pathways of ion/molecule addition. In order to gain a fundamental understanding of various modes of growth, we used AFM to track the dynamics of growing struvite surfaces. The liquid cell used for *in situ* AFM measurements is equipped with

inlet/outlet ports to allow growth solution to be delivered at a constant flow rate, analogous to the design of the microfluidics platform.

Struvite crystals with their (101) surfaces oriented normal to the plane of imaging were placed in the AFM liquid cell in contact with growth solutions prepared with low supersaturation ($\sigma = 0.43$). From time-resolved images extracted from Movie S1 we observed a classical growth mechanism wherein spirals of trapezoidal morphology bound by (012), $(0\bar{1}2)$, (001), and $(00\bar{1})$ steps initiate from dislocation sources (Figure 2.9a and b). The average height of steps forming hillocks (Figure 2.9c, $h = 0.59 \pm 0.02$ nm) is approximately equal to the unit cell dimension (0.58 nm, Figure 2.9d). Identical measurements performed with growth solutions at higher supersaturation ($\sigma = 1.38$) showed the transition to 2D layer nucleation and spreading (Figure 2.9e). Snapshots taken from Movie S2 show the nucleation of new layers (arrows in Figure 2.9f) occurring at random locations on the substrate surface. The advancement of layers on the (101) surface is associated with growth along the $\vec{a}$ direction. Based on the macroscopic growth rates obtained from the

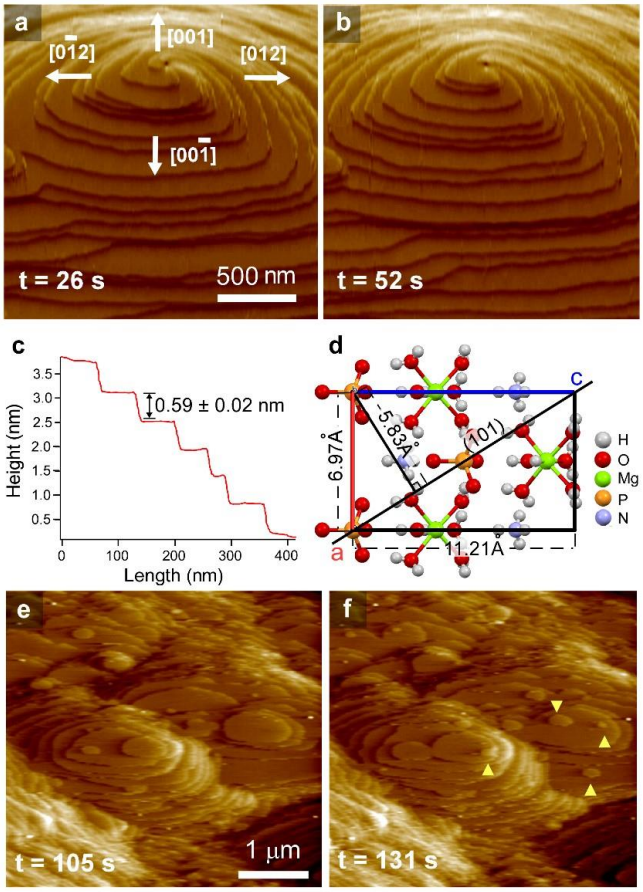

Figure 2.9. Layered growth on (101) surfaces at (a) 26 sec and (b) 52 sec at σ = 0.39. (c) Height along the growth hillock in panel a. (d) Unit cell of struvite. Images taken at (a) 105 sec and (b) 131 sec at σ = 1.38.

microfluidics device (Figure 2.8), the transition to 2D layer generation and spreading occurs around σ = 0.86, which is consistent with AFM measurements conducted at supersaturations below and above this threshold.

The classical modes of layer growth in Figure 2.9 do not show evidence of the particle-mediated process that was postulated by Hövelmann and Putnis[112]; however, it is important to note that the system being analyzed in their study is markedly different from the one presented here. For instance, the source of Mg^{2+} in the study by Putnis is derived from the dissolution of a brucite ($MgOH_2$) surface in contact with a $NH_4H_2PO_4$ solution. The exact supersaturation that mediates heterogeneous nucleation and growth

of struvite on the brucite surface is unknown, while the 100 mM $(NH_4)_2HPO_4$ solution (pH 8.5) employed in their crystallization assays is significantly more concentrated than those used in our study (<10 mM). Our attempts to perform microfluidic and AFM studies at higher supersaturation were unsuccessful owing to the rapid rate of struvite nucleation and growth, which led to the plugging of inlet/outlet ports as well as the deposition of crystallites (from solution) to the surfaces of growing crystal substrates. However, it is evident from our studies that struvite growth can occur *via* a classical mechanism.

2.3. Conclusions

In summary, we demonstrated a new method of evaluating the growth of struvite using a microfluidics device to recreate the flow conditions that are often encountered in practical cases, such as catheters used to treat kidney disease and waste water treatment. In the absence of flow, our findings reveal that bulk crystallization leads to a heterogeneous distribution of crystal size with populations of crystals that often differed from batch to batch. Single crystal X-ray diffraction of struvite crystals reveals an inherent disorder attributed to the ammonium ions, which explained our observation of crystal defects (particularly at high supersaturation).

A switch from quiescent to flow conditions allowed for the analysis of struvite growth along all major crystallographic planes. The resulting kinetics of crystal growth mirror the bulk habit in that the growth along the b-direction is

much faster. Characterization of bulk growth rates in the microfluidic channels as a function of solute supersaturation resulted in a typical profiles corresponding to distinct modes of growth. This was confirmed by time-resolved *in situ* AFM measurements that reveal a switch from growth by spiral dislocations at low supersaturation to 2D generation and spreading of layers at high supersaturation. Based on our observations, we posit that growth predominantly occurs by a classical pathway involving monomer addition.

The microfluidics device used for these analyses is a versatile platform for evaluating struvite crystallization under conditions of flow, which is most relevant for environments where struvite mineralization occurs naturally. The microfluidics platform also offers the unprecedented ability to rapidly screen and visualize crystal growth at macroscopic length scales while maintaining a constant supersaturation (i.e., driving force for crystal growth), which is difficult to achieve by most conventional methods. Ongoing work in our group is focused on expanding this platform to include studies of struvite growth in the presence of additives that function as modifiers to inhibit the rate of crystallization. Collectively, these studies aim to elucidate new routes to control, and ultimately suppress, struvite formation in diverse growth media.

2.4. Experimental Section

2.4.1. Material

The following reagents were purchased from Sigma Aldrich (St. Louis, MO, USA): magnesium chloride hexahydrate (BioXtra, ≥99.0%), ammonium dihydrogen phosphate (99.999% trace metals basis), and sodium hydroxide (≥98.0%). Sodium chloride (ACS reagent, ≥99.9%) was purchased from Alfa Aesar (Heysham, UK). Millex 0.22 μm membrane filters were purchased from Millipore Ltd (Cork, Ireland). Deionized water used in all experiments was purified with an Aqua Solutions RODI water purification system (18.2 MΩ). All reagents were used as received without further purification.

2.4.2. Bulk Crystallization.

Batch crystallization was performed in 20-ml glass vials by dissolving NaCl in deionized water, then adding 1.4 ml filtered equimolar stock solutions of each solute: 50 mM $NH_4H_2PO_4$ and 50 mM $MgCl_2{\cdot}6H_2O$. A clean glass slide was placed at the bottom of each vial to collect crystals. The pH of the growth solution was adjusted to values ranging from pH 7.5 to 9.3 by the addition of appropriate volumes of 1 M NaOH solution. The vials were vortexed for 5 sec followed by a subsequent pH measurement. The final composition of the growth solution was 7 mM $MgCl_2{\cdot}6H_2O$:7 mM $NH_4H_2PO_4$:150 mM NaCl. Crystallization was performed at room temperature (20˚C) for 36 h at static conditions (without stirring or agitation). Crystals grown on glass slides were analyzed with a Siemens D5000 X-ray powder diffractometer using a CuKα source (40 kV, 30 mA). Struvite formation was confirmed using X-ray diffraction (XRD)

reference patterns provided by the database of the RRUFF^{TM} project with ID: R050540.1. In addition, the final crystals were observed in the solution by optical microscopy using a Leica DMi8 instrument and scanning electron microscopy (SEM) using a FEI 235 dual-beam focused ion beam instrument. SEM samples were prepared by attaching glass slides to carbon tape and coated with 15-20 nm gold to reduce electron beam charging.

2.4.3. In situ Characterization of Growth.

A microfluidics device was used to examine struvite growth at macroscopic length scale. The device (poly-di-methyl-siloxane (PDMS) on glass) was fabricated in house using a reported protocol[159]. The device contains microchannels with a 400 × 200 μm^2 cross-sectional area and a length of 4.4 cm. The device used for these experiments was designed with one inlet and one outlet on each end of the channel. This system was monitored under continuous supply of a growth solution using a semi-automatic inverted light microscope (Leica DMi8 equipped with PL Fluotar 5x, 10x, 20x, and N Plan L 50x objectives).

Struvite seed crystals were prepared in a 20 ml vial containing a solution of composition 4 mM $MgCl_2 \cdot 6H_2O$:4 mM $NH_4H_2PO_4$ (pH 8.5). The order of reagent addition was identical to the procedure described above, using continuous stirring (600 rpm). The solution was mixed with a stir bar for a short time (ca. 30 sec) to minimize nucleation, followed by its immediate transfer (by syringe) to the growth chamber of the microfluidics device.

Growth solutions for microfluidics studies were prepared with molar concentrations of 2.3 mM $MgCl_2 \cdot 6H_2O$:2.3 mM $NH_4H_2PO_4$ and a chosen range of pH 8.0 – 9.0 to selectively control the supersaturation. The growth solution was delivered to the microchannel at flow rates of 0 – 60 ml/hr using a dual syringe pump (Chemyx, Fusion 200) and two syringes (plastic BD syringe, 30 ml) with an in-line mixing configuration. Solution 1 contained magnesium chloride mixed with ammonium dihydrogen phosphate, and Solution 2 contained sodium hydroxide. Combinations of the two solutions resulted in a final concentration of 2.3 mM of each component and the desired pH after exiting a mixing chamber placed prior to the entrance of the growth chamber (refer to Figure 2.2). For *in situ* time-resolved studies, images were acquired every 5 min at multiple positions along the microfluidics channel. Optical micrographs of crystals were analyzed using ImageJ (NIH) for the average length along the $\vec{a}, \vec{b}$, and $\vec{c}$ directions. The growth rate was measured by linear regression of crystal length versus time data.

In situ atomic force microscopy (AFM) was performed to examine the temporal changes in topographical features on struvite crystal surfaces. Struvite crystals prepared by the bulk crystallization method described above were mounted on an AFM specimen disk (Ted Pella) covered with a thin layer of thermally curable epoxy (Loctite, China). The epoxy was first partially cured in an oven for about 6 min at 60°C prior to gently pressing the glass slide collected from bulk crystallization to the specimen disk to immobilize struvite crystals on the partially-cured epoxy. The sample was then dried in air overnight to completely cure the epoxy. All AFM measurements were performed in a Cypher ES instrument (Asylum Research, Santa Barbara, CA) using silicon nitride

probes with gold reflex coating and a spring constant of 0.15 N/m (Olympus, TR800PSA). The liquid cell (ES-CELL-GAS) contained two ports for inlet and outlet flow to maintain constant supersaturation during AFM measurements. Several concentrations of magnesium chloride and dihydrogen ammonium phosphate ranging from 1.9 to 2.3 mM, as well as pH values spanning pH 8 – 10, were used to test a range of supersaturations. The growth solution was delivered to the liquid cell using an in-line mixing configuration where the two solute solutions were combined immediately before being introduced into the cell (similar to the microfluidics configuration). Freshly prepared growth solutions were used for each experiment (within an hour of their preparation). Continuous imaging was performed at ambient temperature in contact mode with a scan rate of 10 – 78 Hz at 256 lines per scan.

CHAPTER 3

ENGAGING A BATTLE ON TWO FRONTS: DUAL ROLE OF POLYPHOSPHATES AS POTENT INHIBITORS OF STRUVITE NUCLEATION AND CRYSTAL GROWTH

3.1. Motivation

The formation of inorganic scale, such as struvite ($MgNH_4PO_4 \cdot 6H_2O$), is often an unwanted outcome that negatively impacts the efficiency of commercial processes, such as water treatment[1-11], and is implicated in pathological diseases, such as infection stones[12,13]. Management of patients with infection stones is challenging due to the high recurrence rates, and without appropriate treatment can result in death from sepsis.[14] Scale is particularly problematic in wastewater where high levels of magnesium, ammonia, and phosphate create supersaturated media that promotes struvite crystallization. Precipitation of inorganic scale often compromises the operation and longevity of commercial equipment, while its accumulation in pipes leads to constrictions that restrict flow, leading to reduced treatment capacity and higher energy costs for the transport of water. Many efforts have been made to effectively control struvite formation to bypass the need for mechanical removal. For example, it has been shown that induced precipitation in flow by either maintaining mildly acidic conditions or using pulses of electric energy can avoid buildup on the surfaces of pipes[15,16]. Metal ions in solution can be removed by chelating agents, although this approach requires excessive volumes of the latter[17,18]. Preventative measures also include the use of chemicals that interact with the surface of scale and inhibit crystal growth. It is reported that growth modifiers, or so-called “threshold” inhibitors, can be effective at trace concentrations (e.g., < 1% of the solute)[19]. While commercial inhibitors have been used

to prevent struvite formation, few studies in literature have examined the mechanism by which these molecules selectively bind to crystal facets and impede surface growth.

A common functional moiety of inorganic crystal growth inhibitors is carboxylic acids[20,2122]; however, there have been numerous studies reporting that molecules containing phosphates can be more potent inhibitors[23–26]. Phosphorylated organic molecules such as phytate[27], phosphoproteins (e.g., osteopontin[28,29]), and peptides[30–33] derived from proteins have been shown to effectively regulate mineralization. Phytate (or phytic acid) is a natural compound comprised of a cyclohexane backbone decorated with six phosphates. It is found in most plant foods and is a reported inhibitor of calcification[34]. More generally, it has been shown that polyphosphates (PolyPs) are effective inhibitors of inorganic scales[24,35,36] and biominerals[23]. In select cases, PolyPs can impede the transformation of amorphous precursors (e.g., amorphous calcium carbonate or amorphous calcium phosphate) to crystalline products[37–39], whereas other examples have demonstrated the ability of PolyPs to alter crystal habit (size and morphology) via their putative adsorption on discrete growth sites of crystal surfaces[23,38,40].

Previous studies of struvite crystallization have identified a select number of compounds (i.e., pyrophosphate[41,42], phosphocitrate[43], and hexametaphosphate[24]) that inhibit mineral formation[39–42]; however, the exact mode of action for all reported struvite growth inhibitors has remained elusive. Understanding the mechanisms of inhibitor-crystal interactions and their impact on the kinetics of crystallization is critical for developing more efficient scale inhibitors. Similar knowledge has been used to design inhibitors for a broad range of crystals. For instance, our group has previously

shown that adsorption of certain inhibitors leads to the dissolution of calcium oxalate monohydrate in supersaturated media by inducing strain on the crystal lattice[44].

Herein, we present a comprehensive investigation of struvite crystallization at both macroscopic and microscopic length scales in the absence and presence of various PolyP inhibitors. *In situ* measurements of bulk crystal growth by microfluidics were used to track changes in anisotropic growth rates, whereas time-resolved atomic force microscopy (AFM) was used to elucidate the modes of inhibition at near molecular level. Our findings reveal unique mechanisms of struvite crystal growth inhibition, including the ability of PolyPs to function as dual inhibitors of nucleation and crystal growth.

3.2. Results and Discussion.

3.2.1. Inhibitors of Struvite Crystallization

We screened a series of PolyP (macro)molecules as potential inhibitors of struvite crystallization, restricting our selection to six commercially-available compounds listed in Figure 3.1A. These compounds include five PolyPs containing different numbers of phosphate groups and distinct structures (linear or cyclic): pyrophosphate (PP), trimetaphosphate (TMP), triphosphate (TP), hexametaphosphate (HMP), and polyphosphate type 45 (P45). We also examined the effect of phytic acid (PA). Bulk crystallization assays were conducted using identical weight percentages of

each compound (i.e., similar number of total phosphate groups) for direct comparison of efficacy.

Struvite crystallization was carried out in supersaturated solutions with a starting pH of 8.6, where HPO_4^{2-} is the dominant phosphate species (Figure B1). The incorporation of each phosphate into the crystal results in the release of a proton[10],

$$Mg^{2+} + NH_4^+ + HPO_4^{2-} + 6H_2O \leftrightarrow MgNH_4PO_4 \cdot 6H_2O + H^+. \quad (3.1)$$

The corresponding decrease in pH during crystallization allows for the extent of reaction to be monitored as a function of time (for more details refer to the Supporting Information, SI). Using the final pH of solutions as an estimate of the thermodynamic equilibrium (i.e., relative to control samples in the absence of additives), we compared the extent of reaction for each putative inhibitor (Figure 3.1B) using a fixed concentration of 50 μg mL^{-1} PolyP. Our findings reveal three categories of growth inhibitors. The first is those having very little impact on struvite crystal growth, which are PP, TP, and TMP. All of these compounds contain three or fewer phosphates. Prywer *et al*.[45] reported that PP is an effective inhibitor of struvite formation; however, the concentration of PP used in their study was an order of magnitude higher than the one used in our study, which likely explains the difference in performance. When the concentration of inhibitor approaches that of the solute, it is possible to observe thermodynamic effects as a result of phosphate sequestration of free Mg^{2+} ions, which lowers supersaturation and reduces the rate of crystallization. For all experiments reported herein, we intentionally used much lower concentrations of PolyPs in relation to solute concentration to avoid the potential effects of ion sequestration. The second class of modifiers, which demonstrate moderate inhibition (i.e., <40% reduction in the

extent of reaction), include HMP and P45. The third class is a single outlier, PA, which is the most effective among all phosphates assayed. There is an approximate 15 min delay in the induction time for nucleation of solutions containing HMP and P45, as

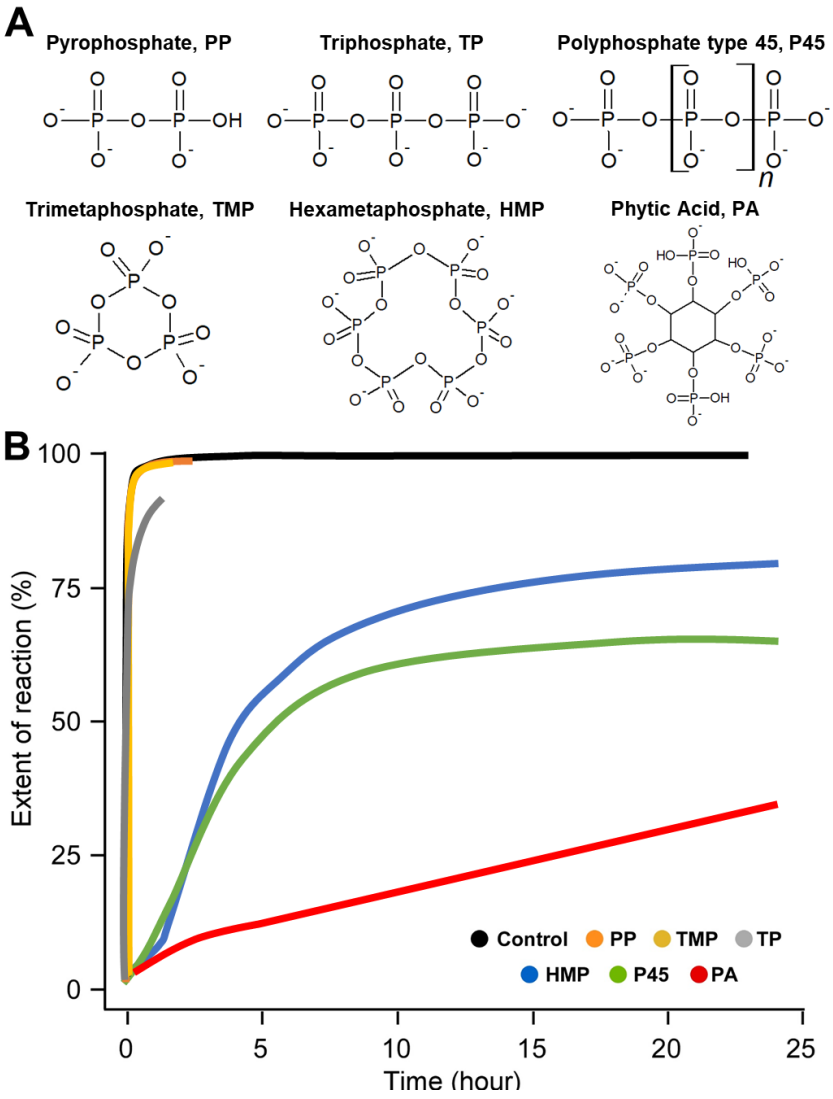

Figure 3.1. (A) Structures of the phosphate-based compounds tested in bulk crystallization assays. (B) Screening the efficacy of polyphosphates to inhibit struvite crystallization.

indicated by a stable solution pH. The same effect was observed for PA; however, the onset of a gradual increase in the extent of reaction (Figure 3.1B) for PA is not seemingly associated with the nucleation and growth of struvite, but is the result of an

amorphous precipitate. Evidence for the complete suppression of struvite nucleation by PA is gleaned from polarized optical micrographs indicating the lack of crystallinity (and absence of distinct morphology) of collected solids under conditions of stirring (Figure B2) and under quiescent conditions (Figure 3.2A and B) compared to the birefringence of control crystals (Figure 3.2C and D). The quantity of amorphous precipitate is minute, such that attempts to extract sufficient material (even with scale up) for *ex situ* characterization was not possible; however, our observation of an amorphous phase is qualitatively consistent with previous studies. For example, Prywer *et al.* detected the formation of residual amorphous material during struvite crystallization[46] and showed that its formation was promoted by (-)-epicatechin.[47] Moreover, Hövelmann *et al.*[5] showed that cobalt ions (Co^{2+}) in excess of 0.5 mM resulted in the formation of an amorphous (Mg-)Co-phosphate precursor. The exact mechanism by which PA inhibits struvite nucleation is not well understood. It has been speculated[2] that struvite formation (under certain conditions) may involve crystallization by particle attachment, or CPA[48]. Although it is unclear whether struvite grows by classical (monomer addition) and/or nonclassical (CPA) pathways, our findings identify phytate (PA) as a potent inhibitor of struvite formation. Most notably, it is rare to encounter molecules capable of completely suppressing crystal nucleation, even among the most effective modifiers of mineralization[49].

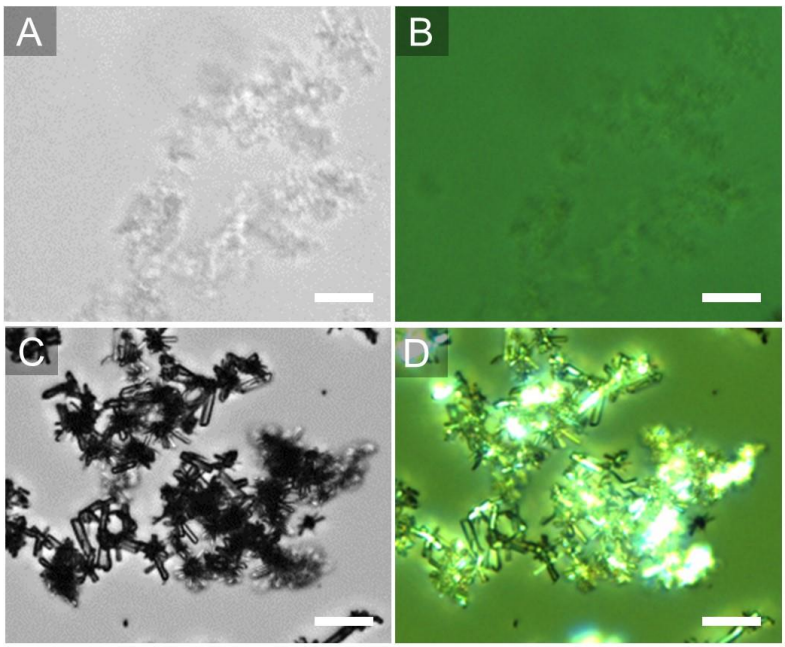

Figure 3.2. Optical (A,C) and polarized (B,D) micrographs of materials formed in the presence of 50 μg mL^{-1} PA (A,B) and in the absence of an inhibitor (C,D) under quiescent conditions. Scale bars are equal to 25 μm.

Bulk crystallization assays in Figure 3.1 were conducted under constant stirring. A parallel study under quiescent conditions using identical supersaturation and inhibitor concentration (50 μg mL^{-1}) was performed to assess the effect of each PolyP on struvite nucleation (Figure B3). Crystallization in the absence of any additives resulted in layers of crystals collected at the bottom of synthesis vials (Figure B3A). Experiments performed with the three weak inhibitors identified in Figure 3.1 (i.e., PP, TMP, and TP) revealed similar populations of crystals, consistent with the extent of reaction measurements confirming their negligible effect on struvite nucleation (Figure B3, B-D). Interestingly, the PolyPs identified as moderately effective inhibitors in Figure 3.1 (i.e., HMP and P45) were found to suppress nucleation under quiescent conditions. This was evident by the lack of visible precipitate at the bottom of the crystallization vials as well as optical micrographs showing only a few crystals (Figure B3E and F). Nucleation

suppression was also observed for growth solutions containing PA under both quiescent (Figures 3.2A and B3G) and stirring (Figures 3.1 and B2A) conditions. One notable difference among inhibitors was the formation of amorphous precipitate, which was only observed for PA while both HMP and P45 maintained a supersaturated (metastable) solution. Collectively, these results reveal distinct differences in the effect of inhibitors under stirring and quiescent conditions. Indeed, switching from a dynamic growth environment to one that is static increases the number of potent nucleation inhibitors from one (PA) to three (HMP, P45, and PA), respectively.

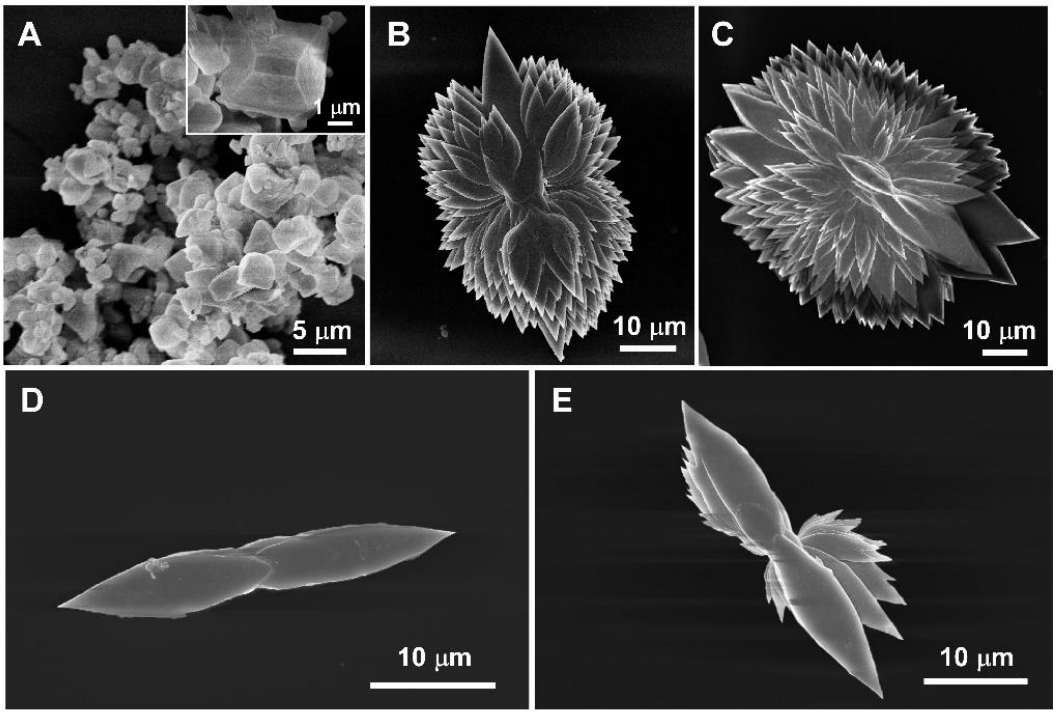

Figure 3.3. SEM of struvite synthesized in solutions containing 50 μg mL^{-1} of (A) TP, (B) P45, and (C) HMP. (D and E) Time-elapsed images of struvite crystals from growth solutions containing HMP after (D) 4 h and (E) 8 h.

Here we compare the effects of PolyPs on struvite crystal growth using a combination of electron and optical microscopy to examine time-resolved evolution of crystal size and habit. In the presence of PP and TMP, struvite crystals exhibit an

elongated tabular habit (Figure B4B and C, respectively) that is indistinguishable from that of the control (Figure B4A). On the contrary, TP had a significant effect on struvite morphology despite having only a marginal impact on the extent of reaction (compared to TMP and PP). Notably, scanning electron microscopy (SEM) images of crystals prepared with TP indicate its preferential binding to surfaces growing in the *b* direction (i.e., the fastest growth direction of struvite), leading to a reduction in the *a/c* and *b/c* aspect ratios (Figure 3.3A). There is also a net reduction in the size of struvite crystals (*b* direction) from 7 ± 4 μm (control) to 2.4 ± 0.9 μm in the presence of TP. This outcome is highly uncommon for crystal growth modifiers exhibiting such weak effects on the kinetics of crystallization. It also highlights the subtle differences in the number of phosphate groups (TP has three compared to two for PP), and the altered arrangement of three phosphate groups from a linear motif for TP to a cyclic one for TMP.

Increasing the number of phosphate groups from 3 (TP) to 45 (P45) results in a significant reduction in the number of crystals collected in the final product (Figure B3F) as well as a morphology that is quite unusual (Figure 3.3B). The crystals formed in the presence of P45 have a shape resembling a spiral leaf, and a structure that was confirmed to be struvite based on its powder X-ray diffraction pattern (Figure B5). Interestingly, the same crystal morphology was directed by HMP (Figure 3.3C), which was unexpected in view of the distinct differences in HMP and P45 structures (i.e., ring vs. linear chain). Time-resolved SEM images of struvite crystals grown in 50 μg mL^{-1} HMP reveal the initial formation of a "seed" with a distinctive and highly reproducible shape (Figure 3.3D), consistent with images of early-stage crystals extracted from solutions containing P45 (Figure B6). The evolution of these features involves

sequential branching (Figure 3.3E) and growth of individual platelets (or *leaves*) that encompass the initial seed to form a symmetrical (Figure 3.3B and C), or sometimes asymmetrical (Figure B7), hierarchical struvite crystal. The preferential binding of HMP and P45 to facets of struvite is difficult to discern; however, it is interesting to note that seeds (Figure 3.3D) appear elongated in the *c* direction, which is the opposite of naturally grown struvite that exhibits preferential growth in the *b* direction (Figure B8).

3.2.2. Microfluidics Analysis of Crystal Growth Inhibition

The extent of crystallization measured in Figure 3.1B cannot distinguish between the effects of nucleation and crystal growth inhibition. To this end, we assessed struvite growth at a macroscopic level using a microfluidics device (Figure B9) where channels were seeded with struvite crystals to bypass nucleation and focus solely on quantifying anisotropic growth under a constant flow of supersaturated solution with or without inhibitors. Sequential images from time-resolved optical microscopy were used to assess changes in crystal dimensions in all three principal growth directions by statistically sampling multiple crystals oriented (normal to the plane of imaging) in both the *c*- and *a*-directions. We first analyzed the dependence of struvite growth on inhibitor concentration for two mildly effective modifiers: PP and TP. The percent inhibition of struvite in the presence of PP (Figure 3.4A) exhibits the following trend (from highest to lowest): $\vec{b}$, $\vec{c}$, and $\vec{a}$. The preferential inhibition by PP in the *b*-direction is evident in time-elapsed images (Figure 3.4C) showing an increased *c/b* aspect ratio. Comparison with TP reveals a more pronounced effect on struvite growth (Figure 3.4B) with the

following trend (from highest to lowest): $\vec{b}$, $\vec{a}$, and $\vec{c}$. Indeed, TP almost fully suppresses growth in the *b*-direction (ca. 90 ± 9 % inhibition), which is apparent in micrographs extracted

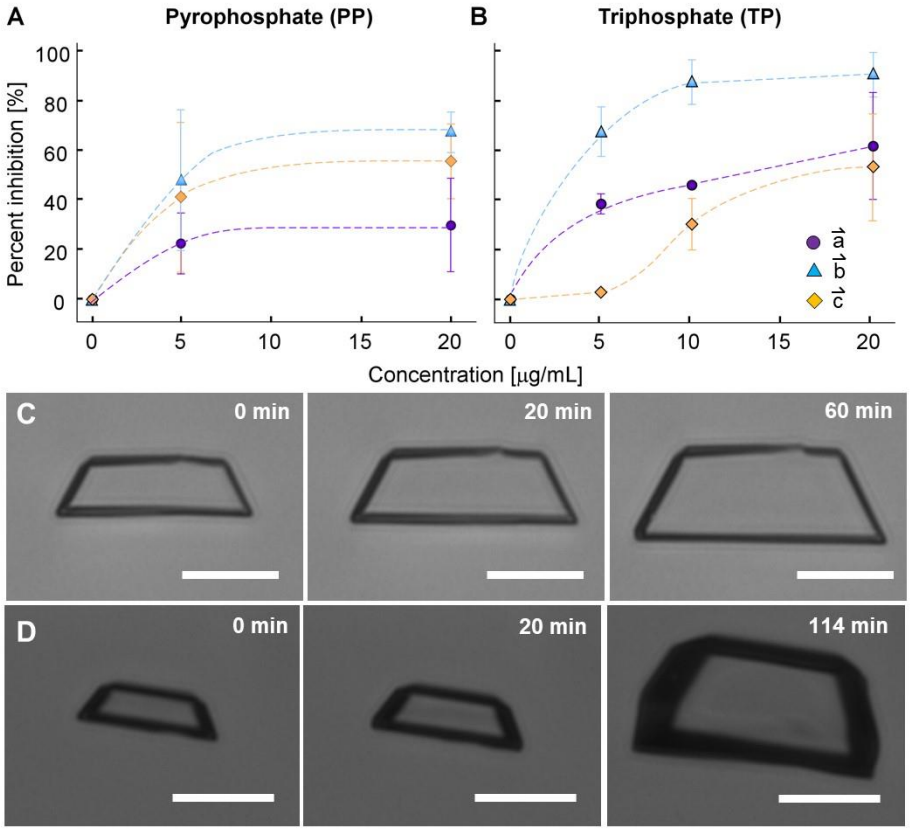

Figure 3.4: (A-B) Percent inhibition of struvite growth as a function of (A) PP and (B) TP concentration. (C and D) Effects of 5 µg mL^{-1} (C) PP and (D) TP on struvite growth under solution flow (24 mL h^{-1}). The scale bars, 20 µm.

from Movie S1 at periodic times (Figure 3.4D) showing much larger *c/b* aspect ratio for TP compared to that with PP. These changes in struvite crystal morphology observed during microfluidics analysis of TP and PP are consistent with bulk crystallization assays under quiescent conditions (Figures 3.2A and Figure B4,B).

For microfluidics studies we selected a range of inhibitor concentrations (1 – 20 µg mL^{-1}) to avoid any potential reduction in supersaturation due to inhibitor

complexation of free Mg^{2+} ions in solution (i.e., molar ratio of inhibitor/Mg^{2+} < 0.03). The monotonic change in percent crystal inhibition with increasing inhibitor concentration exhibits a Langmuir-like behavior, which is characteristic of most inhibitor-crystal adsorption profiles.[21,44] The percent inhibition reaches a plateau at some threshold inhibitor concentration, beyond which further addition of either PP or TP has little added effect on the rate of struvite growth. Interestingly, the profile for TP in the *c*-direction exhibits a sigmoidal shape that deviates from other profiles, which seems to indicate a higher tolerance for struvite growth on these facets at low coverage of TP. In the Supporting Information we provide the time-resolved analysis of TMP, the least effective inhibitor, and show that the percent inhibition is less than 25% without any observable specificity for TMP adsorption on struvite crystals (Figure B10).

In Figure 3.5A we compare the maximum percent inhibition at 20 μg mL^{-1} of PP, TP, and TMP. Similar measurements performed with HMP, P45, and PA resulted in complete suppression of crystal growth, even at much lower inhibitor concentration (1 μg mL^{-1}). This is evident from Movie S2 showing a single struvite crystal in a microfluidic channel where growth is unhindered in the absence of inhibitor (Figure 3.5B, control) and is completely stunted in all directions for potent inhibitors (e.g., Figure 3.5C for PA). It is interesting to note that under conditions of flow it is possible to fully inhibit struvite growth, whereas under constant stirring (Figure 3.1B) growth is only partially hindered. Conversely, under both conditions the most potent inhibitor, PA, fully suppresses nucleation and crystal growth. We are not aware of examples in the literature where a crystal growth modifier functions in a dual manner with such

efficacy. Hereafter, we focus exclusively on the most potent inhibitors to investigate the underlying mechanism governing their ability to fully arrest struvite growth.

3.2.3. In situ AFM Characterization of Surface Dynamics

It has been suggested by others that PolyPs inhibit struvite growth either by chelating free Mg^{2+} ions[24,35] or by interacting with crystal surfaces[42]; however, until now PolyPs have been shown to have a moderate effect on struvite formation while their specific impact on crystal growth has been gleaned from bulk techniques limited in their ability to provide molecular-level information regarding inhibitor-crystal interactions and their impact on surface growth. To this end, we used *in situ* AFM to elucidate the mechanism of inhibitory action that leads to the full suppression of crystal growth. AFM has proven to be a powerful technique for characterizing the growth of crystal surfaces in the absence and presence of inhibitors. We recently used *in situ* AFM to establish that struvite crystal growth follows a classical mechanism whereby new layers nucleate on crystal surfaces and advance by the incorporation of solute molecules at steps[50]. Indeed, a snapshot of a (101) surface during growth in supersaturated solution (Figure 3.6A) shows the presence of layers emanating from the bottom left (outside the frame of imaging) with heights equivalent to a single unit cell (h = 0.58 nm). After a period of growth in the presence of 0.3 μg mL^{-1} HMP, we observe a sequence of topographical changes in snapshots from Movie S3 showing an initial decrease in step density with 2-dimensional islands more visible (Figure 3.6B). This is then followed by a return to a

higher step density, but with steps advancing from the bottom right that are comprised of corrugated edges (Figure 3.6C). According to classical

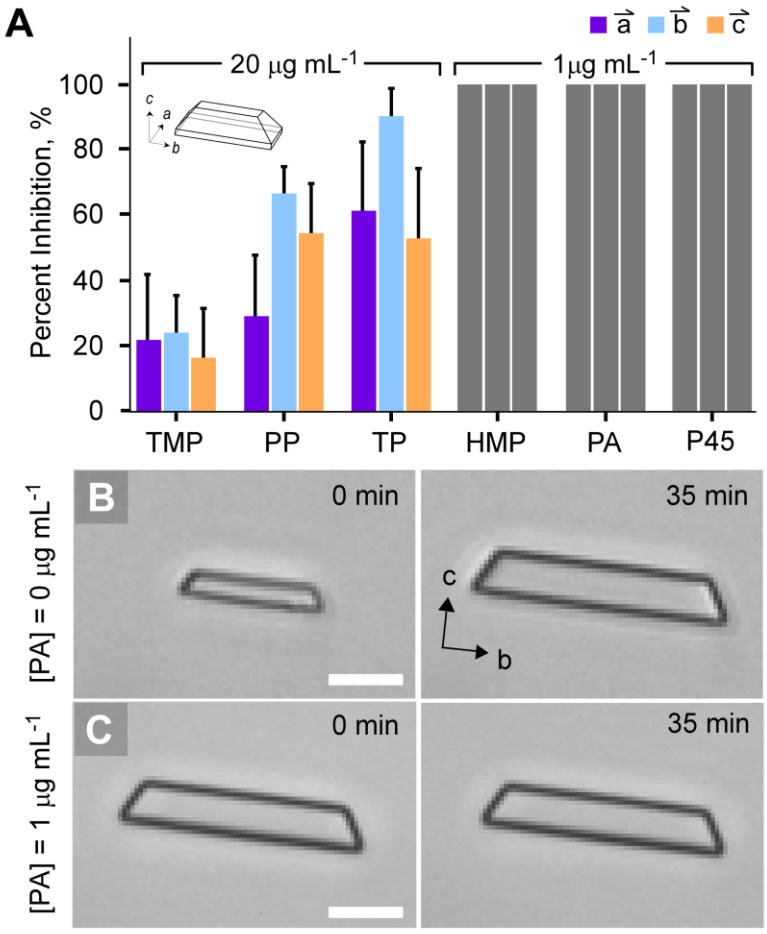

Figure 3.5. (A) Percent inhibition of struvite in the presence of inhibitors (B and C) Optical micrographs at times 0 and 35 min showing the same crystal in the absence (B) and presence (C) of 1 μg mL^{-1} PA. Scale bars are 10 μm.

nucleation theory, the free energy of the system is governed by the solution supersaturation and the free energy of the step edge[51–54]. At the conditions used for *in situ* AFM, the concentration of HMP is too small to lower supersaturation via its sequestration of free Mg^{2+} ions (i.e., Mg^{2+}:HMP > 500 in growth media). This suggests adsorbed HMP on struvite surfaces may alter the step edge energy; however, it is also

possible that HMP alters the kinetics of layer advancement owing to specific interactions with growth sites. Traditionally the mechanism of inhibition is identified by monitoring changes in step velocity as a function of inhibitor concentration where the resulting shape of the velocity profile indicates either kink blocking or step pinning[55–57]. The dramatic changes in struvite surface topography (Figure 3.6A–D) make it difficult to track step velocity and identify the mechanism of HMP inhibition; although, the presence of corrugated steps is consistent with step pinning.

Prolonged exposure of struvite surfaces to growth media containing HMP leads to roughening and the disappearance of visible layers (Figure 3.6D). Measurement of the root-mean squared (RMS) roughness for a fixed surface area during continuous scanning yields values of 0.43 nm for layered surfaces (Figure 3.7A) and 1.57 nm for rough interfaces exposed to HMP (Figure 3.7B). The rough features correspond to protrusions with step heights ranging from 0.5 to 7 nm, which are much larger than those of single steps (Figure 3.7C). The topography of crystal surfaces exposed to equivalent concentrations of P45 and PA also show similar

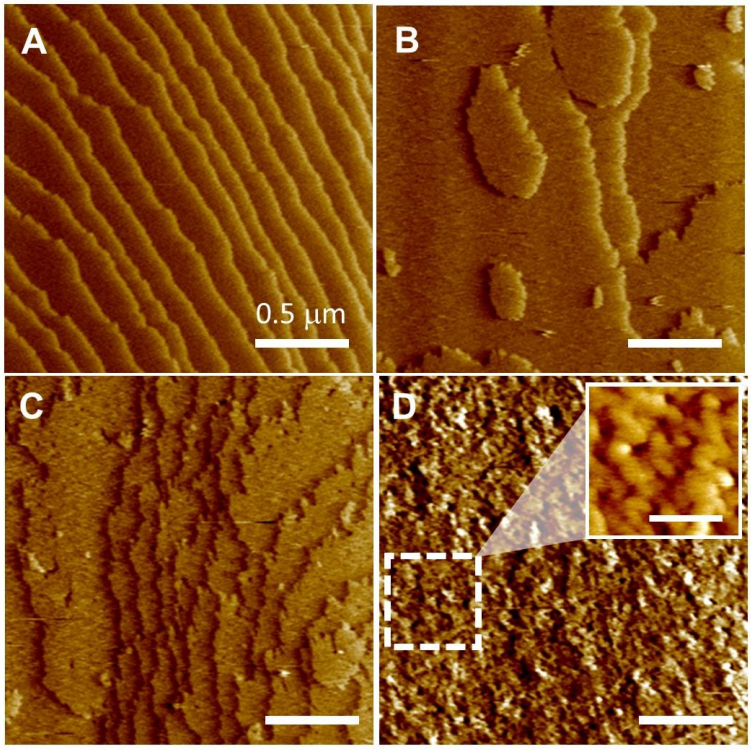

Figure 3.6. Time-resolved *in situ* AFM deflection mode images at a fixed scan area of a struvite (101) surface at (a) t = 0 min, (b) t = 10 min, (c) t = 17 min, and (d) t = 32 min. Scale bar in inset equals 100 nm.

characteristics wherein the layers are indiscernible owing to a high coverage of surface protrusions (Figure B12, A and B, respectively). The exact origin of surface roughness is unknown. Dynamic light scattering (DLS) of growth solutions show no trace of particulates, which does not exclude the possibility that particles exist in low concentrations that fall below the detection limit of DLS. *In situ* chemical force microscopy (CFM) measurements were performed according to a previous study[58] using growth solutions with and without HMP to record approach and retraction curves of an AFM silicon nitride tip impinged upon control (pristine) and rough crystal surfaces, respectively. CFM tip deflection profiles of the former (Figure 3.7D) exhibit a typical curve for hard surfaces where an attractive tip-crystal interaction yields an adhesion (or unbinding) force of 2.3 ± 0.5 nN. Conversely, the profile of the surface exposed to HMP

is characteristic of materials lacking strong tip-surface interactions. Likewise, the profile for rough surfaces resembles those reported for soft materials, such as polymers[59], whereas CFM profiles for even softer gel-like surfaces exhibit two signature features that are absent in Figure 3.7D: a nonlinear approach curve (yield stress) with hysteresis upon retraction[58].

Ex situ X-ray photon spectroscopy (XPS) measurements of rough surfaces extracted from growth solutions reveal peaks of Mg and P with no apparent difference in composition (Mg/P ≈ 1) relative to control crystals with layered crystalline surfaces; thus, the exact structure of rough protrusions is difficult to establish. Kato *et al.*[60] showed similar rough features on hydroxyapatite, $Ca_5(PO_4)_3(OH)$, plates treated with PolyP solutions and suggested these features may be surface-adsorbed PolyPs bound with Ca^{2+} ions. Moreover, it is interesting to point out that previous studies have demonstrated the presence of particles in solutions comprised of PolyPs and cationic species (e.g., Mg^{2+} ions). Similar types of particulates containing PolyPs and inorganic divalent cations have also been observed in nature, such as granules in mitochondria, while synthetic analogues can be prepared in alkaline solutions with excess cations[61–64] for use in applications of bone regeneration[65] and cartilage repair[64], among others.

CFM measurements are highly suggestive that roughened interfaces have a different structure than a pristine crystal surface. More definitive proof that these layers are a soft material is derived from AFM images in contact mode (harder engage) where areas under continuous scanning (or rastering) of the AFM

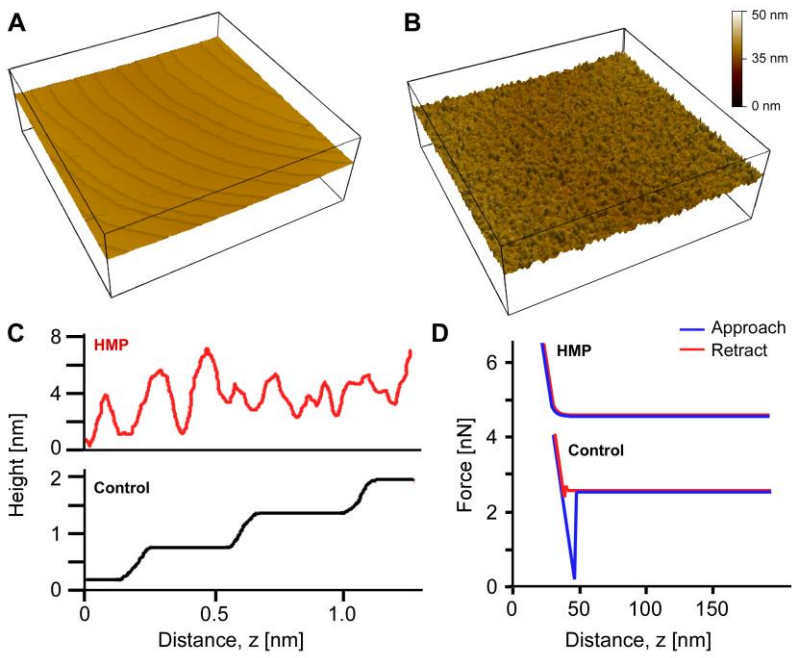

Figure 3.7. Effect of HMP on struvite surface topography.

tip are markedly different than those of surrounding (non-imaged) regions. Indeed, enlarged scanning areas of a rough struvite (101) surface after a period of *in situ* imaging shows a notable difference between the scanned and surrounding regions (Figure 3.8A). Continuous imaging of a fixed area of a crystal substrate with periodic enlargements of the scanning area reveal a monotonic increase in the height of the imaged region (Figure 3.8B); thus, continued growth occurs in areas of tip rastering while growth in regions unperturbed by the movement of the tip is suppressed. Confirmation of fully inhibited growth in non-imaged regions is difficult to extract from AFM owing to the lack of a reference point (i.e., constant baseline); however, microfluidics experiments under identical conditions confirmed that struvite growth is completely suppressed. Thus, we posit that the AFM tip temporarily disrupts or removes rough features to allow growth in the [101] direction, normal to the plane of imaging, which is reflected by the temporal

increase in the height profile (Figure 3.8B). While the exact structure of the rough features cannot be discerned from these measurements, we hypothesize they are amorphous in nature, which is qualitatively consistent with their facile removal as a result of AFM tip rastering, unlike layered crystal surfaces (control) that are unaffected by imaging with harder engage. Moreover, the observation that rough features fully suppress struvite surface growth is another indication that their structure is distinct relative to the underlying crystal lattice. Interestingly, the regions where growth occurs in the presence of HMP as a result of AFM tip movement reveal changes in both the size and morphology of rough features (Figure 3.8C–F). This phenomenon was observed over a broad range of HMP concentrations (0.3 – 3 $\mu g\ mL^{-1}$). The rough protrusions are initially globular in shape (Figure 3.8C and E), but after 60 min of imaging the average size of protrusions increases (Figure 3.8D and F). Time-resolved AFM images also indicate changes in feature shape, such as the anisotropic morphology observed at lower HMP concentration where features seemingly align in the [012] direction (Figure 3.8D). In surrounding regions not under continuous scanning, there is no apparent change in surface topography (Figure B13), which is consistent with

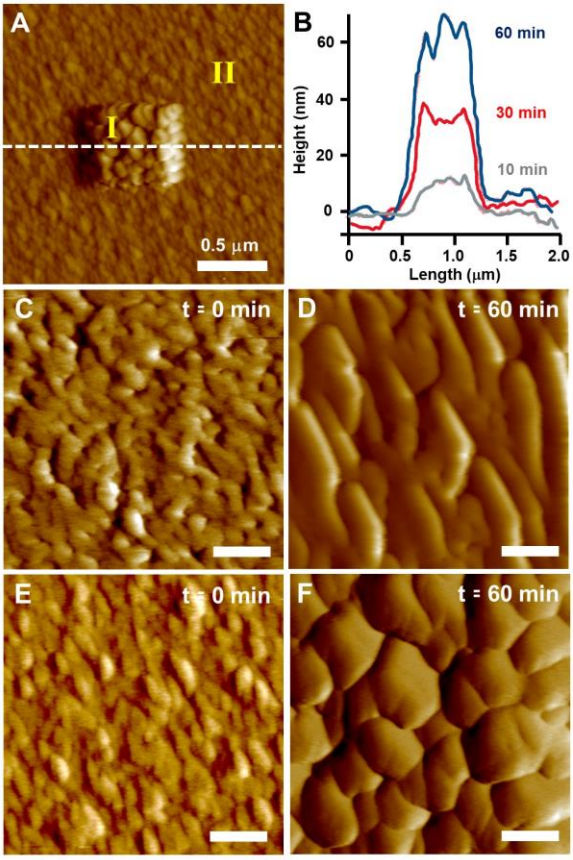

Figure 3.8. (A) Enlarged scan area of a crystal surface in a solution containing 3 μg mL^{-1} HMP showing (I) an area after 30 min of continuous scanning and (II) the non-scanned region. (B) Time-resolved height profiles.

microfluidics showing fully arrested growth in all crystallographic directions. At concentrations below 0.3 μg mL^{-1} HMP, we do not observe roughened interfaces and struvite surface growth is inhibited through a classical route involving HMP-crystal interactions. Indeed, AFM measurements of (101) step advancement in growth solutions containing 0.25 μg mL^{-1} HMP result in step corrugation and reduced step velocity (Figure B14), suggesting a critical level of HMP (around HMP/Mg ~ 0.02 %) triggering the onset of surface roughness and growth succession. AFM studies with moderately-effective inhibitors (PP, TMP, and TP) at concentrations as high as 10 μg mL^{-1} do not

result in surface roughening (Figure B15). For modifiers that induce surface roughening (i.e., HMP, P45, and PA), we observe that layered growth of struvite surfaces is recovered by exposing crystals with roughened interfaces to fresh growth solutions in the absence of inhibitor (see Figure B16). Thus, inhibition by this unique mechanism is a reversible phenomenon.

3.3. Conclusion

In summary, we evaluated six commercially available PolyPs as potential inhibitors of struvite scale formation. Bulk crystallization assays were performed under two different operating conditions. Stirring was used to assess the extent of crystallization where the compounds tested were classified into three categories based on their efficacy as crystallization inhibitors: ineffective (i.e., PP, TMP, and TP), moderately effective (i.e., HMP and P45), and highly effective (i.e., PA). Similar studies were performed under quiescent conditions in which it was observed that the efficacy of HMP and P45 was similar to that of PA. Under these conditions, all three PolyPs fully suppress struvite nucleation. Among these potent inhibitors, PA facilitates the precipitation of amorphous solids while the other two inhibitors stabilize highly supersaturated solutions.

On the basis of these observations, systematic *in situ* measurements were conducted using highly effective inhibitors that did not promote precipitation. The efficacy of HMP and P45 did not diminish in microfluidics studies, indicating that low flow rates do not impede their effect, as was observed under more severe conditions of stirring. Indeed, time-resolved measurements of struvite crystal growth by microfluidics

revealed that all three potent inhibitors of nucleation also act as efficient inhibitors of crystal growth. An interesting observation when comparing the list of PolyPs examined in this study (Figure 3.1A) is the impact of structure and size of the inhibitor. For example, three phosphates arranged in a linear chain (TP) are slightly more effective than their arrangement in a ring (TMP); however, when the size of the ring is increased from 3 to 6 phosphates (HMP) the efficacy is dramatically enhanced. Moreover, when comparing HMP to another ring bearing 6 phosphates (PA), but with a carbon backbone, the efficacy of the latter is more robust over all of the conditions tested (i.e., quiescent, stirred, and flow). These findings highlight a ubiquitous observation among numerous crystal growth inhibitors, which is that subtle variations in molecule structure and composition can lead to marked differences in their efficacy.

The mechanism by which HMP, P45, and PA inhibit struvite surface growth via the generation of a roughened interface is unique, but not well understood. Although the composition of the layer is comprised of stoichiometric magnesium and phosphorus, the physical properties of the layer are distinctly different from those of crystalline struvite. The absence of a tip-substrate pull-off profile in CFM measurements and the ability of the tip to perturb the roughened layer during *in situ* AFM imaging are two aspects not observed during similar measurements on layered (or pristine) struvite crystal surfaces. We hypothesize that the layers may be comprised of disordered (or amorphous) material facilitated by interactions with PolyPs; however, the exact composition and structure of the roughened features remains elusive. Irrespective of their physicochemical properties, the roughened interface is highly effective in suppressing struvite crystal growth. One unique aspect of PolyPs is their affinity to suppress the growth of all

principal crystallographic surfaces: [101] (or $\vec{a}$ direction), [010] and [012] (or $\vec{b}$ direction), and [001] (or $\vec{c}$ direction). This enables PolyPs to completely suppress crystallization in all directions at relatively low concentrations. To our knowledge, few growth inhibitors reported in literature exhibit such broad affinity for crystal surfaces. It is far more common to observe an inhibitor that targets one or two surfaces, leading to inhibition of bulk crystal growth in the range of 60 – 80%. Macromolecules tend to be more effective and can inhibit crystal growth in the 80 – 100% range; however, it is rare to observe modifiers with an efficiency leading to full suppression.

It is also uncommon to observe (macro)molecules capable of fully suppressing crystal nucleation. The exact mechanism by which HMP, P45, and PA achieve this is a subject of ongoing investigation. A more frequent observation in literature is an inhibitors ability to perturb the rate of nucleation, leading to fewer, albeit larger, crystals. These cases typically involve the use of high inhibitor concentration. For the PolyPs examined in this study, HMP and P45 yield only a few observable crystals in bulk assays at low inhibitor concentration. Under conditions of stirring, HMP and P45 are less effective nucleation inhibitors in comparison to PA, which fully inhibits nucleation under all conditions tested in this study. The stochastic nature of nucleation, in accordance with classical nucleation theory, would seemingly imply that this process is unlikely to be fully suppressed. Exceptions would apply to inhibitors that function as sequestering agents capable of removing ions (e.g., free Mg^{2+}) from solution, thus lowering supersaturation to levels that fall within the limit of metastability where nucleation is prevented. In this study, the amount of PolyP required to inhibit nucleation is orders of magnitude smaller than the solute; therefore, sequestration is not a factor

contributing to the observed effect. Another possible explanation may be a deviation from classical nucleation owing to the formation of pre-nucleation clusters wherein inhibitor-cluster interactions may be responsible for the full suppression of nucleation. To our knowledge, this nonclassical pathway has not been confirmed and remains a subject for future investigation.

Despite their unknown mechanism(s) of action, our discovery of the dual modes by which PolyPs inhibit both nucleation and crystal growth reveal a level of efficiency for modifiers of struvite that is rarely observed across a broad range of inorganic and organic crystallization. Indeed, *in situ* formation of amorphous surface coating is a unique mechanism that deviates from the classical inhibitory mechanism and facilitates complete suppression of layered growth. This holds a potentially broader applicability to other minerals that involve various cationic species in the formation environment.

3.4. Material and Methods

3.4.1. Materials

The following reagents were purchased from Sigma Aldrich (St. Louis, MO, USA): magnesium chloride hexahydrate (BioXtra, ≥99.0%), ammonium dihydrogen phosphate (99.999% trace metals basis), sodium hydroxide (≥98.0%), trisodium trimetaphosphate (≥ 95%), sodium triphosphate pentabasic (≥ 98%), sodium pyrophosphate tetrabasic (≥ 95%), sodium hexametaphosphate (96 %), sodium phosphate glass (type 45), sodium chloride (BioXtra, ≥ 99.5%), and sodium hydroxide solution (1.0 N). Phytic acid dipotassium salt was purchased from Boc Sciences. Filter papers were purchased from Whatman. Deionized water used in all experiments was

purified with an Aqua Solutions RODI water purification system (18.2 MΩ). All reagents were used as received without further purification.

3.4.2. Bulk Crystallization.

Batch crystallization was performed by adding stock solutions into a 20-mL glass vial in the following order: DI water, $NaCl_{(aq)}$, and aliquots of 50 mM $NH_4H_2PO_{4,(aq)}$, 50 mM $MgCl_2{\cdot}6H_2O_{(aq)}$, and 1000 μg mL^{-1} inhibitor solutions. The final growth solutions with a total volume of 10 mL had a composition of 7 mM $MgCl_2{\cdot}6H_2O$:7 mM $NH_4H_2PO_4$:150 mM NaCl:*x* μg mL^{-1} inhibitor, and the pH of the growth solution was adjusted to pH 8.6 by the addition of appropriate volumes of 1 M NaOH solution. The sample vials were first stirred for 15 minutes at 1200 rpm using a magnetic stir bar and were then left undisturbed at 22 (±1) °C for 72 h. The final crystals were observed in the solution by optical microscopy using a Leica DMi8 instrument. Crystals were than collected by vacuum filtration and dried in air overnight before further analysis. Crystals were analyzed with a Siemens D5000 X-ray diffractometer (XRD) using a CuKα source (40 kV, 30 mA) and were confirmed using struvite XRD reference patterns provided by the database of the RRUFF project with ID: R050540.1. *Ex situ* microscopy measurements were obtained by using FEI 235 dual-beam focused ion beam scanning electron microscopy (SEM). SEM samples were coated with 15-20 nm gold to reduce electron beam charging.

Kinetic measurements of struvite formation were performed by tracking the pH of the bulk crystallization solution under constant stirring at 600 rpm. The pH of growth solutions was measured at 30 sec intervals using an Orion 3-Star Plus pH benchtop meter equipped with a ROSS Ultra electrode (8102BNUWP).

3.4.3. In situ Characterization of Growth

A microfluidics device was used to examine struvite growth at macroscopic length scale. The device (poly-di-methyl-siloxane (PDMS) on glass) used for these experiments followed the same set up and fabrication protocol as reported in previous work[50,66]. This system was monitored under continuous supply of a growth solution using a semi-automatic inverted light microscope (Leica DMi8 equipped with PL Fluotar 5x, 10x, 20x, and N Plan L 50x objectives).

Struvite seed crystals were prepared in a 20 mL vial containing a solution of composition 7 mM $MgCl_2 \cdot 6H_2O$:7 mM $NH_4H_2PO_4$: 150 mM NaCl (pH 8.5). The order of reagent addition was identical to the procedure described above, using continuous stirring (600 rpm). The solution was mixed with a stir bar for a short time (ca. 30 sec) to minimize nucleation, followed by its immediate transfer (by syringe) to the growth chamber of the microfluidics device.

Growth solutions for microfluidics studies containing x μg mL^{-1} inhibitor were prepared with molar concentrations of 2.5 mM $MgCl_2 \cdot 6H_2O$:2.5 mM $NH_4H_2PO_4$. An appropriate volume of 1 M NaOH was added to adjust solution pH to 8.6. The growth solution was delivered to the microchannel at flow rates of 24 mL h^{-1} using a dual syringe pump (Chemyx, Fusion 4000) and two syringes (plastic BD syringe, 30 mL) with an in-line mixing configuration. Solution 1 contained magnesium chloride mixed with ammonium dihydrogen phosphate, and Solution 2 contained sodium hydroxide and inhibitor. Combinations of the two solutions resulted in a final concentration of 2.5 mM of each component, the desired inhibitor concentration and a pH of 8.6 after exiting a mixing chamber placed prior to the entrance of the growth chamber. For *in situ* time-

resolved studies, images were acquired every 5 min at multiple positions along the microfluidics channel. Optical micrographs of crystals were analyzed using ImageJ (NIH) for the average length along the $\vec{a}, \vec{b},$ and $\vec{c}$ directions. The growth rate was measured by linear regression of crystal length versus time data. The efficacy of struvite growth inhibitors was quantitatively assessed through calculation of the percent inhibition, defined as:

$$\mathrm{x} = \left(1 - \frac{r_{inhibitor}}{r_{control}}\right) \times 100\% \tag{3.2}$$

where $r_{control}$ and $r_{inhibitor}$ are the growth rates in the absence and presence of inhibitor, respectively.

In situ atomic force microscopy (AFM) was performed to examine the temporal changes in topographical features on struvite crystal surfaces. Struvite crystals were prepared by directly placing an AFM specimen disk (Ted Pella) into a bulk crystallization vial overnight. The sample was removed from the vial and dried in air immediately before use. All AFM measurements were performed in a Cypher ES instrument (Asylum Research, Santa Barbara, CA) using silicon nitride probes with gold reflex coating and a spring constant of 0.15 N/m (Olympus, TR800PSA). The liquid cell (ES-CELL-GAS) contained two ports for inlet and outlet flow to maintain constant supersaturation during AFM measurements. Solutions used for AFM experiments were the same as the solutions used for the microfluidics experiments. The growth solution was delivered to the liquid cell using an in-line mixing configuration where the two solute solutions were combined immediately before being introduced into the cell (similar to the microfluidics configuration). Combinations of the two solutions resulted in a final concentration of 2.5 mM of each component, the desired inhibitor

concentration and a pH of 8.6 after exiting a mixing chamber placed prior to the entrance of the AFM liquid cell. Freshly prepared growth solutions were used for each experiment (within one hour of their preparation). Continuous imaging was performed at ambient temperature in contact mode with a scan rate of 0.5 – 10 Hz at 256 lines per scan.

3.4.4. Chemical Force Microscopy

We used the Cypher ES instrument to measure the unbinding force between an AFM tip and struvite crystal surfaces. All measurements were carried out using non-functionalized silicon nitride probes with gold reflective coating and a spring constant of 0.08 N m^{-1} (Olympus, PNP-TR). The cantilever was calibrated in air to verify the spring constant using an algorithm provided by the vendor. Force measurements were performed on struvite surfaces in the absence and presence of inhibitors (HMP, P45, and PA) under identical conditions as *in situ* AFM growth experiments. We first imaged struvite crystal surfaces in contact mode to locate regions for CFM measurements. We selected a tip speed of 1.98 μm s^{-1} and trigger points of 1.00 V. Surface areas of 2 × 2 μm^2 were analyzed to gather more than 50 data points for statistical analysis.

CHAPTER 4

TETRASODIUM EDTA FOR THE PREVENTION OF URINARY CATHETER INFECTIONS AND BLOCKAGES

4.1. Motivation

Urinary catheters, either for intermittent or long-term use, are one of the most frequently employed medical devices in clinical care.[167-168] Bacterial colonisation of catheters, however, leads to the development of catheter-associated urinary tract infections (CAUTIs), which represent the most common healthcare-associated infection and account for up to 80% of all nosocomial UTIs.[167, 169-170] CAUTIs not only increase patient morbidity but, if left untreated, can lead to serious, life-threatening complications such as pyelonephritis and urosepsis.[171]

Understanding the pathogenesis of CAUTIs and the cascade of events that lead to catheter blockage are important in order to tackle this global healthcare issue. Despite aseptic measures employed during catheter insertion, microbial contamination may be considered inevitable, with the introduction of pathogens into the typically sterile urinary tract.[171] Of the range of microbes that colonise the catheter surface, urease-producing bacteria such as *Proteus mirabilis* are particularly problematic due to the formation of crystalline biofilms and subsequent encrustation of the catheter. Urease-induced hydrolysis of urea in the urine to ammonia and carbon dioxide causes elevation of urinary pH with resultant precipitation of polyvalent ions.[171-172] This can lead to the formation of an amorphous carbonate apatite ($Ca_{10}(PO_4)6CO_3$) precipitate and the nucleation of magnesium ammonium phosphate hexahydrate ($MgNH_4PO_4.6H_2O$),

struvite, crystals which can agglomerate together to form infectious urinary stones.[120, 172] Struvite crystals can grow into large staghorn calculi which cause significant trauma to the bladder and disrupt the flow of urine.

Ethylenediaminetetraacetic acid (EDTA) and its salt forms are well-established hexadentate chelating agents which have been used in a wide range of both clinical and non-clinical applications, including treatment of heavy metal poisoning and for preservation and stabilisation purposes in food, cosmetic, pharmaceutical, dental and ophthalmic products.[173-175] In addition, the chelating abilities of EDTA impart this agent with antimicrobial and antibiofilm properties. EDTA chelates cations present in bacterial cell walls, as well as Ca^{2+}, Mg^{2+}, Fe^{2+} and Zn^{2+} ions present in biofilm matrices, leading to their destabilisation. A further mechanism by which EDTA can adversely affect bacterial viability is through chelation of cations essential for bacterial survival and growth.[174, 176-178] EDTA has been investigated both as an individual antimicrobial/antibiofilm agent, and as an agent that can potentiate the activity of other antimicrobials.[174-176] From the selection of EDTA salts available, the tetrasodium salt form of EDTA (tEDTA), as shown in Figure 1, in particular, has been shown to exhibit effective antimicrobial and antibiofilm activities.[174, 179] A 4% tEDTA catheter lock solution, marketed as KiteLock, is employed to maintain patency of central venous access devices (CVADs) as a result of its antimicrobial, antibiofilm and anticoagulant properties.[179]

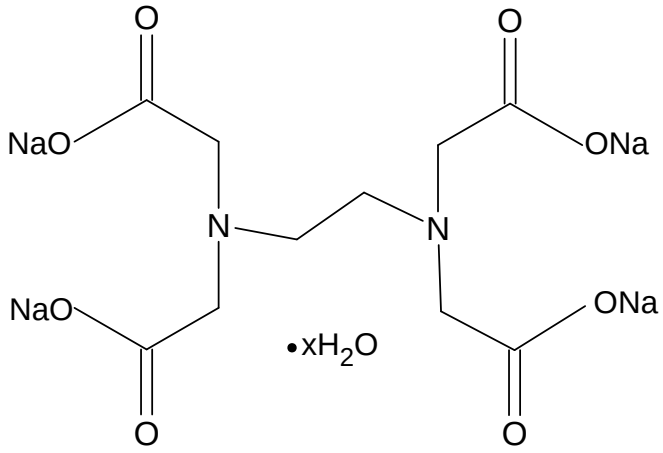

Figure 4.1. Chemical structure of ethylenediaminetetraacetic acid (EDTA).

In addition to the antimicrobial and antibiofilm properties of EDTA, this agent demonstrates promising capacity for the prevention of struvite crystallisation and urinary catheter encrustation through the chelation of Ca^{2+} and Mg^{2+} ions in the urine and resultant reduction in crystal formation.[120, 180-181] Herein we investigate the antimicrobial and anti-encrustation activities of tEDTA against uropathogens to evaluate the dual efficacy of this agent for combatting CAUTIs and associated catheter blockages. The antimicrobial activity of tEDTA against uropathogens commonly implicated in CAUTIs was assessed by determination of minimum inhibitory concentration (MIC) and minimum bactericidal concentration (MBC) values, and time kill assays performed in artificial urine (AU). The effect of tEDTA on struvite nucleation and growth, and subsequent catheter encrustation and blockage, was examined in crystallisation studies and *in vitro* bladder model assays, respectively.

4.2. Results and Discussion

4.2.1. MIC and MBC values

MIC and MBC values of tEDTA were determined against the Gram-positive *S. aureus* and Gram-negative *P. mirabilis* and *E. coli* since these pathogens commonly colonise the urine and catheters of long-term catheterised patients.[50-51, 182] The MIC and MBC values are presented in Table 1.

Table 4.1. MIC and MBC values of tEDTA against uropathogens.

	tEDTA	
	MIC mg/mL (mM)	MBC mg/mL (mM)
P. mirabilis ATCC 51286	0.47 (1.24)	30 (78.9)
E. coli NSM59	3.75 (9.86)	15 (39.5)
S. aureus ATCC 29213	0.23 (0.60)	>80 (211)

tEDTA displayed a bacteriostatic effect against *S. aureus* and *P. mirabilis* at lower respective concentrations of 0.23 and 0.47 mg/mL compared to *E. coli*, with an MIC of 3.75 mg/mL. The MIC values obtained for tEDTA against these microbes are in agreement with previous reports.[176, 179, 183-186] MIC values of 0.63, 5 and 0.63 mg/mL have previously been reported for tEDTA at pH 10.5 against *S. aureus*, *E. coli* and *P. mirabilis*, respectively [176, 183-184], while Khazandi *et al.* reported respective MIC values for the disodium salt (dEDTA) of 0.23 mg/mL and 3.80 mg/mL against *P. mirabilis* and *E. coli*.[185] Furthermore, tEDTA exhibited bactericidal activity against the Gram-negative pathogens with MBC values against *E. coli* and *P. mirabilis* of 15 mg/mL and

30 mg/mL, respectively. Conversely, tEDTA displayed no bactericidal activity against *S. aureus* up to the highest tested concentration of 80 mg/mL. Liu *et al.*[179] have previously reported MBC values for tEDTA of 20 mg/mL, 10 mg/mL and 10 mg/mL against *P. mirabilis*, *S. aureus* and *E. coli*, respectively, however, the MIC/MBC assays were performed in alkaline conditions (pH 10.5). This enhanced bactericidal activity of tEDTA could be attributed to the maximised chelation efficiency of tEDTA in alkaline conditions (pH $\geq$10.3) due to ionisation of the molecule's four carboxylate groups, resulting in greater affinity for divalent cations.[174, 179, 187] Another study reported the absence of biocidal activity of EDTA (salt not stated) against *S. aureus* and *E. coli* with tested concentrations up to 170 mg/mL.[184]

The increased susceptibility of Gram-negative bacteria to EDTA than their Gram-positive counterparts has previously been attributed to differences in the bacterial cell wall structures.[174, 176] The cell walls of Gram-negative bacteria are comprised of two lipid bilayers surrounding a thin peptidoglycan layer.[188-189] The outer membrane of Gram-negative bacteria contains divalent cations which stabilise the negatively-charged oligosaccharide chains of lipopolysaccharides (LPS) attached to the phospholipid bilayer.[174, 190] Chelation of these cations by EDTA destabilises the outer membrane causing release of LPS and subsequent solute leakage from the periplasmic space.[174, 176] In contrast, Gram-positive bacteria do not contain LPS or the associated divalent cations in their cell walls.[176, 184] While the mechanism of action of EDTA against Gram-positive bacteria remains poorly understood, Root *et al.* reported that the target site for EDTA activity against *S. epidermidis* is intracellular after SEM analysis revealed no evidence of damage to bacterial cell walls after treatment with dEDTA.[191-192] Other reports

suggest that the bacteriostatic activity of EDTA against Gram-positive bacteria may be due to chelation of ions required for biological processes and reactions essential for bacterial growth and survival.[177-178] For example, the catalytic activity of bacterial metalloproteases, which hydrolytically degrade proteins in the surrounding environment to nutrients for bacterial growth, requires the presence of Zn^{2+} ions at their active centres.[177, 193]

4.2.2. tEDTA kill kinetics

In vitro time kill kinetics of tEDTA against *P. mirabilis, S. aureus* and *E. coli* were investigated in biologically relevant AU media. tEDTA displays strong affinity to chelate divalent ions present in AU, with chelation of Ca^{2+} or Mg^{2+} in a 1:1 molar ratio.[120, 180] This chelation of divalent Ca^{2+} and Mg^{2+} ions consequentially reduce the concentration of tEDTA molecules available for interaction with bacteria therefore tEDTA concentrations of 7.63 mM (2.90 mg/mL), representing the total concentration of Ca^{2+} or Mg^{2+} ions present in the urine, and 28 mM (10.65 mg/mL), to provide excess tEDTA molecules to interact with the bacteria, were tested. At each time point, bacterial samples removed for analysis were neutralised with an excess of Ca^{2+} to ensure inactivation of tEDTA molecules through chelation.[191, 194] Preliminary studies confirmed the neutraliser solution effectively neutralised tEDTA without affecting bacterial viability.

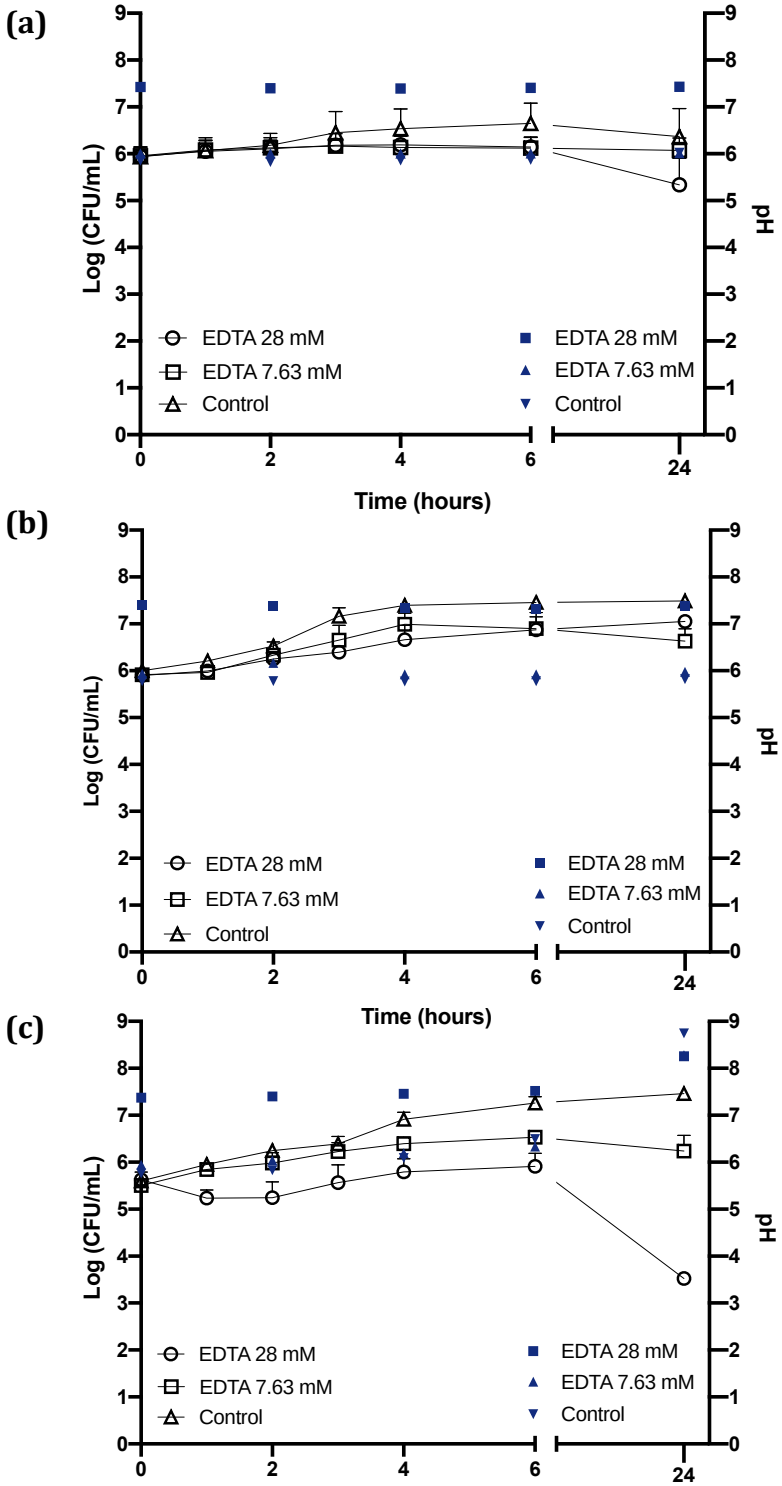

Figure 4.2. The pH (coloured symbols) and viability (open symbols) of (a) S. aureus, (b) E. coli and (c) P. mirabilis in AU in the absence (control) and presenc e of tEDTA (7.63 or 28 mM).

As shown in Figure 4.2a, no statistically significant reductions in *S. aureus* viability were observed following 24 h exposure to 7.63 or 28 mM tEDTA. Similarly, tEDTA had little antibacterial effect on *E. coli* viability (Figure 4.2b). Conversely, as seen in Figure 4.2c, *P. mirabilis* demonstrated higher susceptibility to tEDTA compared to *S. aureus* and *E. coli*, with a 2.10 ± 0.24 $\log_{10}$ reduction in *P. mirabilis* viability compared to the starting inoculum following 24 h exposure to 28 mM tEDTA. Statistically significant ($p \leq 0.05$) reductions of *P. mirabilis* compared to the control were observed in the presence of 28 mM tEDTA at 6 h and 24 h. The increased susceptibility of Gram-negative bacteria to EDTA than Gram-positive bacteria has previously been attributed to differences in the bacterial cell wall structures[174, 176], as discussed in 4.2.1.

The lack of bactericidal activity observed with tEDTA concentrations of 7.63 mM, representing the total concentration of Ca^{2+} and Mg^{2+} ions present in the AU, was due to the absence of sufficient free tEDTA molecules to interact with the bacteria. While the higher concentration of 28 mM tEDTA, in contrast, provided excess molecules for antibacterial activity, this was not sufficient for bactericidal activity against the challenge uropathogens, as defined by a ≥ 3 $\log_{10}$ reduction in bacterial density after 24 h exposure to tEDTA, relative to the starting inoculum.[195] The significant reductions in viability of *P. mirabilis*, the main causative pathogen causing crystalline biofilm formation and catheter encrustation, in the presence of tEDTA relative to control suspensions with no tEDTA, however, are promising with regards to use of this agent for prevention of CAUTIs and associated catheter blockages.[50]

The pH of the *P. mirabilis*-infected control AU in the absence of tEDTA increased from pH 5.8 to pH 6.49 ± 0.26 and pH 8.74 ± 0.15 by 6 h and 24 h, respectively, as a result of the urease-catalysed hydrolysis of urea to ammonia and carbon dioxide.[141, 180] Conversely, despite the higher initial pH of the AU containing 7.63 mM and 28 mM tEDTA, due to the basic nature of this compound, the rate of increase in pH was slower than the control. The pH of AU containing 0, 7.63 and 28 mM tEDTA increased by 0.73, 0.38 and 0.15 units over 6 h, respectively. This was attributed to interactions of tEDTA and the urease enzyme, with EDTA previously reported to chelate the Ni^{2+} ions of urease and retard the enzymatic activity.[180] The statistically similar final pH values of the control and EDTA-containing AU at 24 h suggests that EDTA does not inhibit, but instead slows, urease activity, as previously reported by Prywer *et al.*[180]

tEDTA was also observed to have a significant effect on precipitation within the AU. As displayed in Figure 4.3, precipitation was observed in the *P. mirabilis*-infected control AU after 24 h incubation, with carbonate apatite and struvite previously reported to precipitate at pH values exceeding pH 6.8 and 7.2, respectively.[120] In contrast, counterpart *P. mirabilis*-infected AU solutions containing 7.63 mM and 28 mM tEDTA remained clear despite the AU reaching values of pH 8.28 due to chelation of the precipitating Ca^{2+} and Mg^{2+} ions. Similarly, Prywer *et al*. reported prevention of both carbonate apatite and struvite formation due to chelation of all Ca^{2+} and Mg^{2+} in AU with a 10 mM dEDTA solution, whereas struvite formation was not completely inhibited when a 5 mM concentration was tested due to non-chelated Mg^{2+} ions.[120] This inhibition of crystallisation observed in the presence of both concentrations of tEDTA

is promising with regards to use of this agent for combatting catheter encrustation due to crystalline biofilm formation.

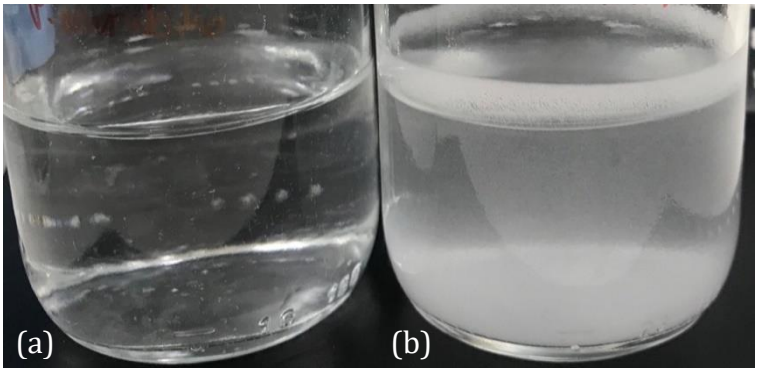

Figure 4.3. Images of P. mirabilis-inoculated AU after 24 h incubation at 37°C in an orbital incubator in the presence of **(a)** 7.63 mM tEDTA and **(b)** 0 mM EDTA.

4.2.3. Struvite Crystallisation Studies

4.2.3.1 Bulk Crystallization Assays

Bulk crystallisation studies to assess the effect of varying concentrations of tEDTA on struvite nucleation and growth were performed in a simple growth solution consisting of equimolar concentrations of $NH_4H_2PO_4$ and $MgCl_2 \cdot 6H_2O$, and with NaCl to maintain ionic strength at 150 mM. The calcium-containing components naturally present in urine were omitted to avoid precipitation of amorphous carbonate apatite.

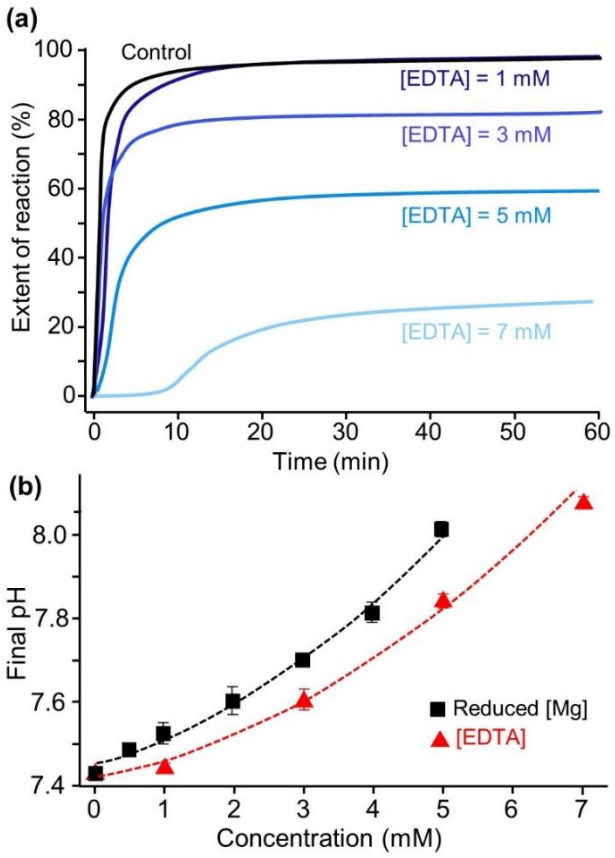

Figure 4.4. (a) Extent of reaction of struvite formation in the absence (control) and presence of 1, 3, 5, 7 mM of tEDTA. **(b)** Final pH of the samples after complete crystallization in the absence of EDTA while varying the [Mg].

Rates of struvite crystallisation can be determined by monitoring the change of absorbance (optical density/turbidity), pH or conductivity of the growth solution over time.[120, 150, 196-198] As shown in Equation 4.1, precipitation of struvite results in the release of protons, causing a decrease of solution pH[150, 196, 198], according to the following equation,

$$Mg^{2+} + NH_4^+ + H_2PO_4^- \longrightarrow MgNH_4PO_4.6H_2O + 2H^+. \quad (4.1)$$

The decrease in pH indicates the start of struvite nucleation and the rate of change in pH can provide insight to the rate of struvite formation. The corresponding decrease in

pH during crystallization allows for the extent of reaction (EOR) to be monitored as a function of time.

As shown in Figure 4.4a, crystallization occurs almost instantaneously in growth solutions containing 0, 3, and 5 mM tEDTA. In the presence of 7 mM tEDTA, however, there was approximately 10 min delay before a more gradual progression of crystallization, indicating an equivalent concentration of tEDTA to that of the concentration of Mg^{2+} ions in solution (7mM) is required to impede struvite nucleation. Similarly, Prywer *et al.*[120] have shown that dEDTA impedes struvite formation at near stoichiometric amount compared to the Ca^{2+} and Mg^{2+} ions available in solution. Doyle *et al.*[199] have previously reported the requirement for a 2:1 molar ratio of EDTA to magnesium to control struvite scale formation on stainless steel impellers used for mixing sludge liquor.[199] In contrast, potent inhibitors such as polyphosphates were shown to be effective at delaying or even completely suppressing struvite crystallization processes at approximately two orders of magnitude less than the concentration of Mg^{2+} ions.[200] At a minute level, the inhibition is attributed to surface interaction. However, when concentration of inhibitor equivalent to or exceeding that of the solute is required, the inhibition is a thermodynamic effect wherein inhibitor-divalent ion complexation sequesters free Mg^{2+} ions in solution which lower the supersaturation and reduce the rate of crystallization.[201]

One more characteristic change in the presence of tEDTA is the final pH of the solution. The reduction in the magnitude of total decrease in pH indicates the inhibitory effect of tEDTA on struvite crystallisation. With increasing concentration of tEDTA, the solution equilibrates at a higher pH corresponding to 0, 20, 40% reduction in the

extent of reaction in the presence of 1, 3, and 5 mM EDTA, respectively. In the presence of 7 mM EDTA, the solution does not completely equilibrate over the extended screen time of 600 minutes but only shows a gradual change in pH with over 70% reduction in the EOR.

In order to evaluate the thermodynamic contribution of the observed inhibition, equivalent measurements were performed at reduced magnesium concentrations in the absence of tEDTA. As shown in Figure 4.4b, as the magnesium concentration is reduced, the solution equilibrates at a higher pH, indicating a reduction in proton release, therefore a reduction in crystallization capacity. The final pH as a function of reduced magnesium concentration (Figure 4.4b, black line) closely align with the final pH as a function of tEDTA concentration. This indicates that the inhibitory effect is achieved mainly through sequestration of magnesium ions. The slightly higher final pH induced by reduction in magnesium concentration compared to final pH at the equivalent amount tEDTA, indicates that the chelation ratio of Mg^{2+} to EDTA is between 1 and 2 under this crystallisation conditions, which is slightly higher than the known 1:1 chelation ratio.[120, 180]

Representative optical micrographs of struvite crystals are presented in Figure 4.5. Typically, net change in average crystal size, number density, and morphology of crystals obtained from bulk crystallisation assays serve as an indicator of the effects of crystal growth inhibitors. As shown in Figure 4.5a, without tEDTA, struvite crystals form an elongated tabular habit.[201] With tEDTA, the characteristic morphology does not

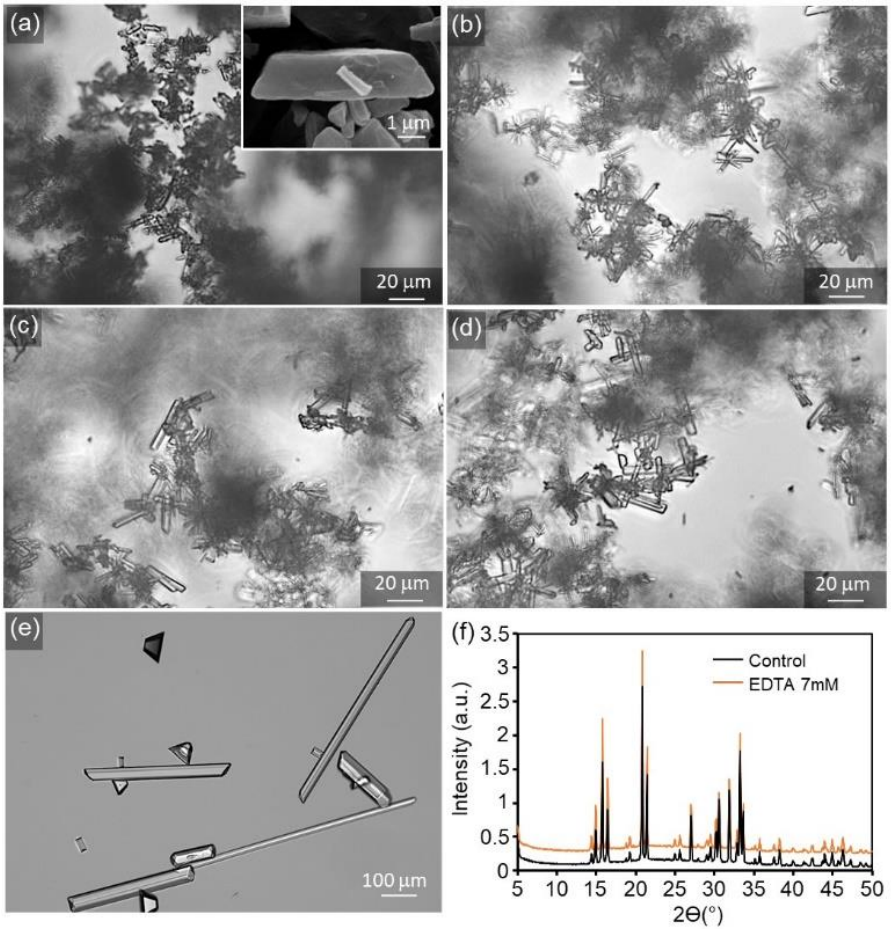

Figure 4.5. Struvite crystals formed in the absence (control) (a) and presence of 1 mM (b), 3 mM (c), 5 mM (d), and 7 mM tEDTA (e) (N=6). (f) Powder XRD patterns for the control and EDTA 7 mM samples.

change and comparison of the X-ray diffractograms of the crystals formed in the absence (control) and presence of tEDTA (displayed in Figure 4.5f) with XRD reference patterns provided by the database of the RRUFF project (ID:R050540.1) confirmed the crystals formed were struvite. However, there is a wide distribution of *b/c* and *b/a* aspect ratio in all samples which restricts the bulk crystallisation analysis. Furthermore, fewer and larger crystals formed in the presence of 7 mM tEDTA. The increase in size is typically attributed to two factors which are growth promotion or reduction in nucleation density and a concomitant increase in size due to mass balance. In the presence of 7 mM

tEDTA, it is most likely the latter case which is consistent with the significant reduction (>70%) in EOR observed in Figure 4.4. Overall, it is difficult to distinguish between the effects on nucleation and crystal growth inhibition and the heterogeneity in aspect ratio of crystals make it difficult to quantify systematic trends in growth of struvite crystals as a function of tEDTA concentration. In addition, batch to batch variation of the struvite crystals formed was observed during bulk crystallisation studies, which is a recognised disadvantage of bulk crystallisation studies compared to monitoring crystal growth under flow conditions. [201] To this end, we implemented microfluidics platform to address these limitations.

4.2.3.2 Microfluidics analysis of crystal growth inhibition.

Using microfluidics platform, we seed the channels with struvite crystals to bypass nucleation and focus solely on quantifying growth rates under a constant flow of supersaturated solution. The growth solutions consisted of 2.5 mM $NH_4H_2PO_4$ and 2.5 mM $MgCl_2 \cdot 6H_2O$ which was a metastable condition selected to avoid nucleation of new crystals and only induce crystal growth. Sequential images from time-resolved optical microscopy were used to assess multiple crystals oriented (normal to the plane of imaging) in both the *c* and *a* direction.

First, we analyzed the dependence of struvite growth on tEDTA concentration (Figure 4.6a). The reduction in growth rate of struvite increases with tEDTA concentration in all three principal directions. This monotonic change in growth

reduction with increasing tEDTA concentration indicates that this agent does not bind to the crystal surface and instead impedes struvite growth through chelation of Mg^{2+}

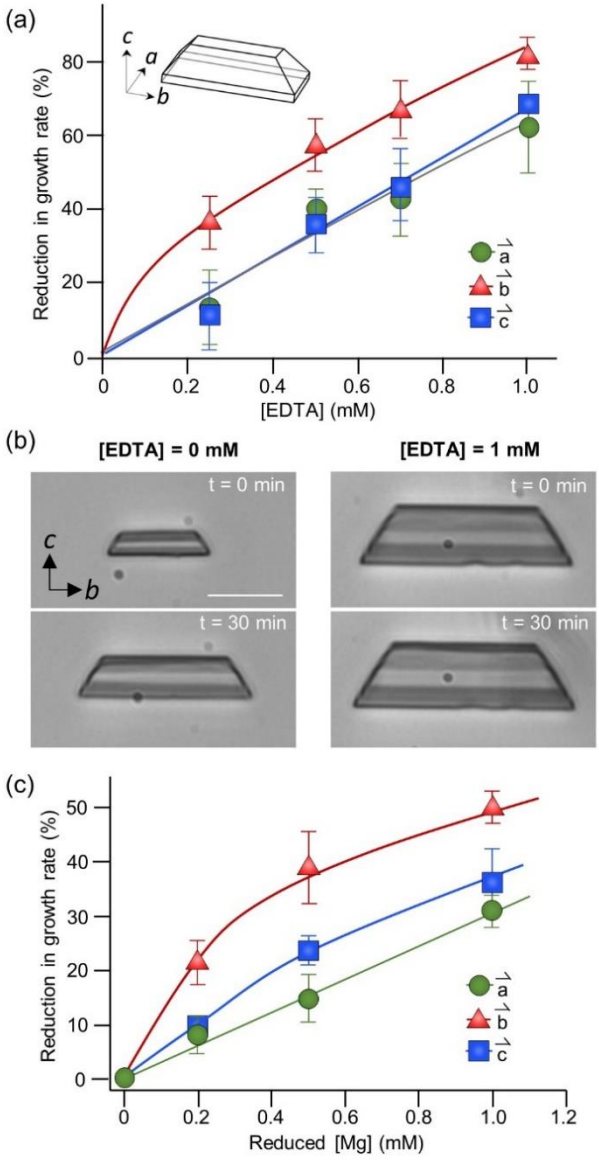

Figure 4.6. (a) Reduction in growth rate. (b) Effects of 1 mM EDTA on struvite growth. Scale bar = 20 μm. (c) Reduction in growth rate as a function of reduced [Mg] with respect to the [Mg] in control (2.5 mM).

ions. A typical inhibitor-crystal adsorption profile would exhibit a Langmuir-like behaviour wherein the reduction in growth rate reaches a plateau at some threshold inhibitor concentration, beyond which further addition of the inhibitors do not affect the

rate of crystal growth.[84, 202-203] Moreover, the close to stochiometric amount of tEDTA required for a significant reduction in crystal growth rate also confirms that the primary mode of inhibition is through ion sequestration from solution. Interestingly, the reduction in growth profile exhibits the following trend: b > c ≈ a. We performed a parallel experiment in the absence of tEDTA at a reduced magnesium concentration to check if the characteristics of the profile is consistent. Similar to the case of increasing concentrations of tEDTA, as the magnesium concentration reduces the reduction in growth monotonically increased (shown in Figure 4.6b). In addition, the reduction profile exhibits the same trend of b > c ≈ a with minimal difference in reduction for c and a direction of growth. Therefore, the anisotropic reduction in growth rate in different direction of growth is most likely induced by decreasing Mg^{2+} rather than preferential binding of tEDTA to specific surfaces.

4.2.4. In vitro bladder model assays

The findings from the crystallisation studies indicate that tEDTA concentrations equal to or exceeding those of the precipitating metal ions in solution can effectively impede struvite formation, suggesting the potential of tEDTA to be exploited in the prevention of urinary catheter encrustation and blockage. *In vitro* bladder model assays were herein performed with *P. mirabilis*-infected AU to investigate the effect of tEDTA on corresponding encrustation and blockage of urinary catheters.

Literature reports mean silicone catheter blockage times of between 36-45 h when supplied with *P. mirabilis*-inoculated AU in *in vitro* bladder models.[181, 204-205]

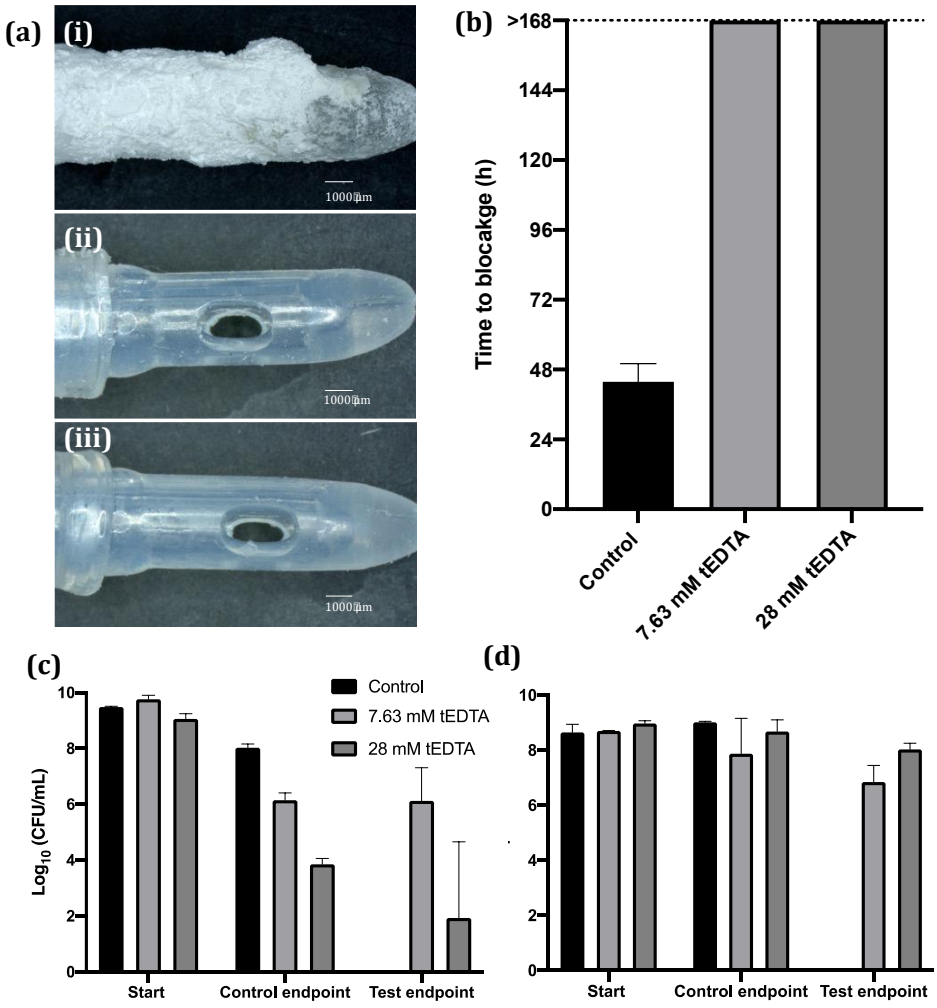

Figure 4.7. (a) Catheters supplied with infected AU in the (i) absence and (ii) presence of 7.63 mM and (iii) 28 mM tEDTA, at (i) 43.8h ± 6.3 or (ii, iii) 168 h. (b) Time of blockage. (c) P. mirabilis viability and (d) pH of urine.

Similarly, as shown in Figure 4.7b, the control silicone catheter supplied with *P. mirabilis*-infected urine, without tEDTA, blocked at 43.8 h ± 6.3 due to the encrustation of the catheter and occlusion of the eyehole with a crystalline biofilm (Figure 4.7a,i). In contrast, the catheters exposed to tEDTA drained freely for 168 h at which point the

experiment was stopped, with no crystalline deposits present (Figure 4.7a,ii and a,iii). With a total of 7.63 mM Ca^{2+} and Mg^{2+} present in the AU media, tEDTA concentrations ≥7.63 mM tEDTA were sufficient to chelate these polyvalent ions within the urine, preventing the formation of calcium apatite and struvite crystals.

SEM images of catheter cross-sections directly below the catheter eyeholes, presented in Figure 9, further demonstrate the effect of tEDTA on catheter blockage. Figure 4.8a,i shows the lumen of the encrusted control catheter at time of blockage (43.8 h ± 6.3) with the presence of crystalline deposits. Furthermore, Figure 4.8a,ii shows a magnified area of this material, displaying struvite crystals of faceted morphology surrounded by spherical carbonate apatite particles.[206] As shown in Figure 8d, the pH of residual urine within the control bladders exceeded pH 6.8 and 7.2, which is required for the formation of carbonate apatite and struvite crystals in urine, respectively.[120] Catheters exposed to 7.63 mM (b) and 28 mM (c) tEDTA were free from encrustation at 168 h. A high ~9 $\log_{10}$ (CFU/mL) inoculum was used to inoculate the bladder models in order to emulate an established, high level of infection.[204, 207] *P. mirabilis* viability within the control bladders maintained a high bacterial density (>7 $\log_{10}$(CFU/mL)) throughout, up to time of blockage. In the presence of 7.63 mM tEDTA, *P. mirabilis* viability remained ~6 $\log_{10}$ (CFU/mL) throughout the 168-h experiment. Conversely, 28 mM tEDTA had a bactericidal effect on *P. mirabilis*-infected urine, reducing

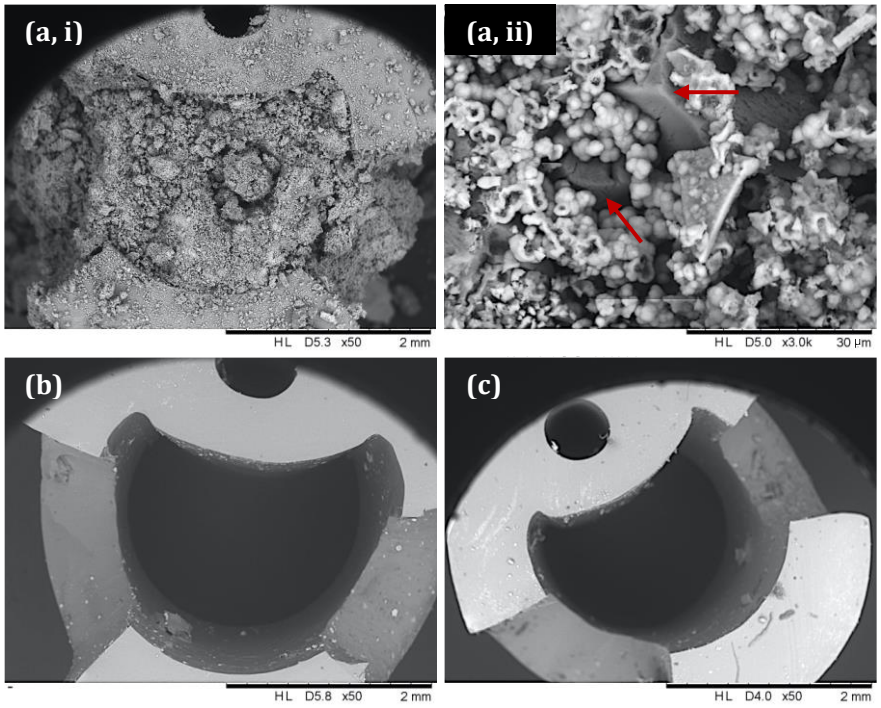

Figure 4.8. (a) A catheter supplied with control AU, removed from the bladder model at 43.8 h, and catheters supplied with AU containing (b) 7.6 mM tEDTA and (c) 28 mM tEDTA at t=168 h.

bacterial density to 2–3 $\log_{10}$ (CFU/mL) within 48 h. Overall, tEDTA concentrations of ≥7.63 mM were capable of preventing encrustation and blockage of the catheters through chelation of Mg^{2+} and Ca^{2+} ions within the urine, preventing the formation of carbonate apatite and struvite. Moreover, the higher concentration of tEDTA also had a bactericidal effect against *P. mirabilis* within the bladders, which may provide further benefit in preventing infection over longer periods, with indwelling catheters typically changed every 4-6 weeks.[208]

Using a similar bladder model set-up, Percival *et al.* found daily catheter instillations of an 80 mg/mL tEDTA solution decreased the rate of crystalline *P. mirabilis* biofilm formation and encrustation of Foley catheters, with mean catheter

blockage time delayed by ~22 h compared to the control (67 h vs 45 h). This delay was attributed to dissolution of magnesium and calcium precipitates present in the catheter lumens during the 30 min daily instillation with tEDTA.[181] Although our study employed a different approach to Percival *et al*., Figure 4.8b confirms the absence of these precipitates within catheters continuously exposed to a ~27-fold lower concentration of tEDTA, with no evidence of catheter encrustation or blockage after 168 h. We envisage the development of a urinary catheter or catheter coating which allows for controlled, continual release of low tEDTA concentrations, will have the potential to prevent encrustation and blockage of indwelling catheters.

4.3. Conclusion

Overall, tEDTA has shown to exert a bacteriostatic effect against *P. mirabilis*, a particularly problematic pathogen in the pathogenesis of catheter encrustation, as well as preventing precipitation of urinary salts. Struvite crystallisation assays confirmed the mechanism by which tEDTA impedes struvite growth is *via* chelation of Mg^{2+} in solution, with tEDTA concentrations equal to or greater than the Mg^{2+} required to prevent struvite formation. *In vitro* bladder model assays revealed a concentration of 7.63 mM tEDTA, equimolar to the concentration of divalent cations in urine, prevented encrustation and blockage of Foley catheters for over 168 h. With further research and optimisation, these promising initial findings suggest the clinical potential of this chelating agent to delay or prevent indwelling catheter blockage.

4.4. Materials and methods

4.4.1. Materials

Ethylenediaminetetraacetic acid tetrasodium salt hydrate ≥99.0% (tEDTA), calcium chloride dihydrate, magnesium chloride hexahydrate ≥99.0%, sodium chloride ≥99.0%, sodium sulfate ≥99.0%, trisodium citrate dihydrate ≥99.0%, potassium chloride ≥99.0%, ammonium chloride ≥99.5% and urea were obtained from Sigma-Aldrich (Dorset, UK). Creatinine 98%, sodium oxalate ≥99.5% and potassium dihydrogen phosphate ≥98.0% were purchased from Alfa Aesar (Heysham, UK). Quarter-strength Ringer's solution (QSRS), phosphate-buffered saline (PBS), tryptone soya broth (TSB), Mueller-Hinton broth (MHB) and agar were purchased from Oxoid Ltd. (Hampshire, UK). All chemicals were used as received. Millex 0.22 µm membrane filters were purchased from Millipore Ltd. (Cork, Ireland). BARD® silicone, 14 channel male catheters and URIPLAN® 2 L drainable bed bags (98 cm inlet) were purchased from BARD Ltd. (Crawley, UK). *Proteus mirabilis* ATCC 51286 and *Staphylococcus aureus* ATCC 29213 were purchased from LGC Standards (Middlesex, UK), and *Escherichia coli* NSM59 was obtained from Dr. Brian Jones (University of Bath, UK). The bacterial strains were preserved on cryopreservative beads (VWR, UK) in 10% glycerol at −80 °C. Deionised water used in bulk crystallisation assays was purified with an Aqua Solutions RODI-C-12A purification system (18.2 MΩ).

4.4.2. Determination of MIC and MBC Values of tEDTA

A broth microdilution method, based on the Clinical and Laboratory Standards Institute (CLSI) guidelines, was employed to determine the MIC and MBC values of

tEDTA against *S. aureus*, *P. mirabilis* and *E. coli*. Briefly, serial two-fold dilutions of tEDTA in MHB were performed in a microtiter plate. The inoculum was prepared by adjusting the turbidity of an overnight bacterial culture in logarithmic phase of growth to an optical density at 550 nm equivalent to 1 x 10^8 CFU/mL, as verified by viable count. The suspension was subsequently diluted to provide a final inoculum density of ~5 x 10^5 CFU/mL in each well. Following addition of the inoculum to each well of the plate, plates were incubated at 37°C in an orbital incubator at 100 rpm for 24 h. Positive and negative controls were included. The lowest tEDTA concentration that completely inhibited microbial growth was recorded as the MIC. 20 µL aliquots from wells exhibiting no visible growth were transferred onto nutrient agar (NA) or low swarm agar (LSWA) for *P. mirabilis*. The MBC was determined following 24 h incubation of the agar plates at 37°C as the lowest tEDTA concentration required to kill 99.9% of the inoculum. This assay was repeated on at least three independent occasions with triplicates of all concentrations and controls included on each occasion.

4.4.3. Determination of tEDTA Kill Kinetics

Time kill assays were performed in AU to assess the kinetics of tEDTA activity against *S. aureus*, *P. mirabilis* and *E. coli* in biologically relevant media. The AU composition, displayed in Table 4.2, was based on the recipe described by Griffith *et al.* and the time kill method was performed according to CLSI guidelines. Two tEDTA concentrations of 7.63 mM (2.90 mg/mL) and 28 mM (10.65 mg/mL) were tested. The required mass of tEDTA was dissolved in 49.75 mL AU immediately prior to the start of the experiment to minimise premature chelation of Ca^{2+} and Mg^{2+} ions in the AU,

and the solution filter sterilised using a 0.45 µm syringe filter. Control flasks were similarly prepared without tEDTA. The inoculum, in the logarithmic growth phase, was prepared as detailed in 2.1, and adjusted to an optical density at 550 nm in AU equivalent to 1 x 10^8 CFU/mL, as verified by viable count. Aliquots (0.25 mL) were added to the flasks to give a final inoculum density of ~5 x 10^5 CFU/mL. Flasks were incubated at 37°C in an orbital incubator and samples removed after 0, 1, 2, 3, 4, 6 and 24 h of exposure. Ten-fold serial dilutions were performed in a neutraliser solution containing 3.20 mM Ca^{2+} to prevent drug carry-over. Specifically, the neutraliser was composed of 2.66 mM calcium chloride dihydrate dissolved in QSRS (contains 0.54 mM Ca^{2+}). 20 µL of the diluted samples were plated onto LSWA or NA, and the colonies enumerated following 24 h incubation at 37°C. The pH of the media was recorded at t=0, 2, 4, 6 and 24 h with a Hanna HI 5221 pH meter and micro HI1083B electrode (Hanna Instruments Ltd. UK). Assays were repeated on at least three independent occasions. Bacteriostatic and bactericidal activity were respectively defined as a <3 $\log_{10}$ reduction and a ≥3 $\log_{10}$ reduction in bacterial density after 24 h exposure to tEDTA, relative to the starting inoculum.

Table 4.2. AU composition.

Chemical	g/L
Calcium chloride dihydrate	0.65
Magnesium chloride hexahydrate	0.65
Sodium chloride	4.60
Sodium sulfate	2.30
Trisodium citrate dihydrate	0.65

Table 4.3. AU composition based on the recipe reported by Griffith et al. (21)*.

Sodium oxalate	0.02
Potassium dihydrogen phosphate	2.80
Potassium chloride	1.60
Ammonium chloride	1.00
Urea	25.00
Creatinine	1.10
Tryptone soya broth	0.01

*****pH of the AU was adjusted to pH 5.7-5.8 using 1 M sodium hydroxide solution and filter sterilised (0.45 µm filter).

4.4.4. Bulk Struvite Crystallisation Studies

4.4.4.1. Analysis of Crystal Formation and Morphology

Struvite nucleation, growth and morphology in the presence of tEDTA were evaluated using a method modified from the bulk crystallisation protocol reported by Kim *et al.* (2020) (8). Briefly, stock solutions of 1.2 M NaCl, 50 mM $NH_4H_2PO_4$, 50 mM $MgCl_2 \cdot 6H_2O$, 1 M NaOH and 26.3 mM tEDTA were prepared in deionised water and filtered using 0.22 µm pore size syringe filters. The effect of tEDTA concentrations (0, 1, 3, 5 and 7 mM) were investigated in growth solutions (10 mL) with final composition of 7 mM $MgCl_2 \cdot 6H_2O$:7 mM $NH_4H_2PO_4$:150 mM NaCl: X mM tEDTA and adjusted to a final pH of 8.60 (±0.03) using 1 M NaOH. Solutions were stirred for 15 min at 1200 rpm and then left at static conditions and ambient temperature (20°C) for 24 h before analysis by optical microscopy using a Leica DMi8 instrument. The

crystals formed were retrieved from solutions using a Büchner filtration method. Scanning electron microscopy (SEM) using a FEI 235 dual-beam focused ion beam instrument was employed to analyse the dried crystals. SEM samples were prepared by gently placing onto carbon tape and coating with 15–20 nm gold to reduce electron beam charging. Additionally, the dried crystals were analysed with a Siemens D5000X-ray powder diffractometer using a $Cu_{K\propto}$ source (40kV, 30 mA). Struvite formation was confirmed using XRD reference patterns provided by the database of the RRUFF project with ID:R050540.1. Crystals from a minimum of six growth solutions were analysed.

4.4.4.2. Analysis of Crystallisation Kinetics

pH of the growth solutions was recorded over time to enable assessment of the effect of tEDTA concentration on the rate of struvite nucleation. The 10 mL growth solution with initial pH of 8.60 (±0.03) was prepared as described in **4.4.4.1.** and stirred continuously. The pH was automatically recorded at 0.5 min intervals up to 600 min by an Orion 3-Star Plus pH benchtop meter equipped with a ROSS Ultra electrode (8102BNUWP). The pH change in the growth solution was used as an indicator of struvite crystallization (including the effects of both nucleation and crystal growth). The extent of reaction (EOR) was assessed according to the following equation[200],

$$EOR = \frac{(pH_i - pH_t)}{(pH_i - pH_{c,eq})} \times 100 \quad (4.2)$$

where pH_i is the initial pH (8.6), pH_t is the pH at time t, and $pH_{c,eq}$ is the final equilibrium pH (pH 7.42) achieved by struvite formation free of additive (control). Equivalent kinetics measurements were performed for various concentrations of magnesium in the

absence of tEDTA. The growth solution composition was X mM $MgCl_2 \cdot 6H_2O$:7 mM $NH_4H_2PO_4$:150 mM NaCl (X = 6.5, 6, 5, 4, 3, 2) with a final pH of 8.60 (±0.03) using 1 M NaOH.

4.4.5. Struvite Microfluidics Growth Analysis

A microfluidics device was used to examine struvite growth. The device (poly-di-methyl-siloxane (PDMS) on glass) used for these experiments followed the same set up and fabrication protocol as reported in previous work.[159, 201] This system was monitored under continuous supply of growth solution using a semi-automatic inverted light microscope (Leica DMi8 equipped with PL Fluotar 5x, 10x, 20x, and N Plan L 50x objectives). Struvite seed crystals were prepared in a 20 mL vial containing a solution of composition 7 mM $MgCl_2 \cdot 6H_2O$:7 mM $NH_4H_2PO_4$: 150 mM NaCl (pH 8.5). The solution was mixed with a stir bar at 600 rpm for a short time (ca. 30 sec) and immediately transferred (by a syringe) to the growth chamber of the microfluidics device. Growth solutions for microfluidics studies were prepared with molar concentrations of 2.5 mM $MgCl_2 \cdot 6H_2O$:2.5 mM $NH_4H_2PO_4$: *X* mM tEDTA . An appropriate amount of 1 M NaOH was added to adjust solution pH to 8.6. The growth solution was delivered to the microchannel at flow rates of 24 mL h^{-1} using a dual syringe pump (Chemyx, Fusion 4000) and two syringes (plastic BD syringe, 30 mL) with an in-line mixing configuration. Solution 1 contained magnesium chloride mixed with ammonium dihydrogen phosphate, and Solution 2 contained sodium hydroxide and tEDTA. Combinations of the two solutions resulted in a final concentration of 2.5 mM of each component, the desired tEDTA concentration and a pH of 8.6 after exiting a

mixing chamber placed prior to the entrance of the growth chamber. For *in situ* time-resolved studies, images were acquired every 5 min at multiple positions along the microfluidics channel. Optical micrographs of crystals were analyzed using ImageJ (NIH) for the average length along the $\vec{a}, \vec{b},$ and $\vec{c}$ directions. The growth rate was measured by linear regression of crystal length versus time data. The effects of various concentrations of tEDTA was quantitatively assessed through calculation of the reduced growth rate, RGR, defined as

$$\text{RGR} = \left(1 - \frac{r}{r_{control}}\right) \times 100\% \tag{4.3}$$

where $r_{control}$ is the growth rate in the absence of tEDTA.

Equivalent measurements were performed for various concentrations of magnesium in the absence of tEDTA. The growth solution composition was X mM $MgCl_2 \cdot 6H_2O$:2.5 mM $NH_4H_2PO_4$ (X = 2.5, 2.3, 2.0, and 1.5) with a final pH of 8.60 (±0.03) adjusted using 1 M NaOH. The RGR was computed with respect to the control growth solution containing 2.5 $MgCl_2 \cdot 6H_2O$:2.5 mM $NH_4H_2PO_4$.

4.4.6. In vitro Bladder Model Assays

The assembly of the *in vitro* bladder model, as illustrated in Figure 4.9, was similar to that first described by Stickler *et al.*[209] and, more recently, by Nzakizwanayo *et al.*[210]. The composition of AU prepared is displayed in Table 1, however, the TSB concentration was increased from 0.001 %w/v to 0.1 %w/v to maintain viability of the high *P. mirabilis* inoculum within the flow model. Filter sterilised solutions of 7.63 mM and 28 mM tEDTA were added to urine immediately prior to the start of the experiment to minimise premature chelation of ions. Control urine contained no tEDTA. *P.*

mirabilis inoculum, in the logarithmic growth phase, was prepared as detailed in 2.1. The inoculum was centrifuged at 3000 rpm for 12 min, after which the supernatant was discarded, and the bacterial pellet resuspended in AU. The suspension was adjusted to an optical density equivalent to ~1 x 10^9 CFU/mL, as verified by viable count, and represented a high level of infection. 10 mL of this inoculum was aseptically added to each bladder using a sterile graduated pipette 1 h before starting the flow of urine (t=0 h) to allow the bacterial inoculum to establish within the bladder models. The urine flow to each bladder was maintained at a rate of 0.75 mL/min for 168 h or until catheter blockage. 1 mL samples were taken from the bladders at the start of the experiment (t=0 h), daily, following catheter blockage, and at t=168 h, if blockage had not occurred, for measurement of urinary pH and determination of bacterial viability. The total volume of urine collected in the drainage bags was used to calculate the time of blockage for each catheter per

$$Time\ to\ blockage\ (\text{min}) = \frac{Volume\ of\ urine\ collected\ in\ draining\ bag\ (mL)}{Flow\ rate\ (\frac{mL}{min})}. \qquad (4.4)$$

At time of catheter blockage, or at 168 h if not blocked, the catheters were removed from the bladder models. Segments, 1 cm in length, were cut directly below the catheter eyehole and attached to aluminium holders using carbon tape. The lumens of the catheters were imaged using a Hitachi TM-3030 Tabletop SEM operated at 5 – 15 kV.

4.4.7. Statistical Analysis

Statistical analysis was performed with Graph Pad Prism 8.0 (GraphPad Software Inc., San Diego, USA). A Kruskal-Wallis test and *post hoc* analysis using Dunn's multiple comparisons test were performed to assess the effect of tEDTA on bacterial viability in AU and urinary pH after contact periods of 6 and 24 h. In all cases $n \geq 3$ and a p value <0.05 was used to denote significance.

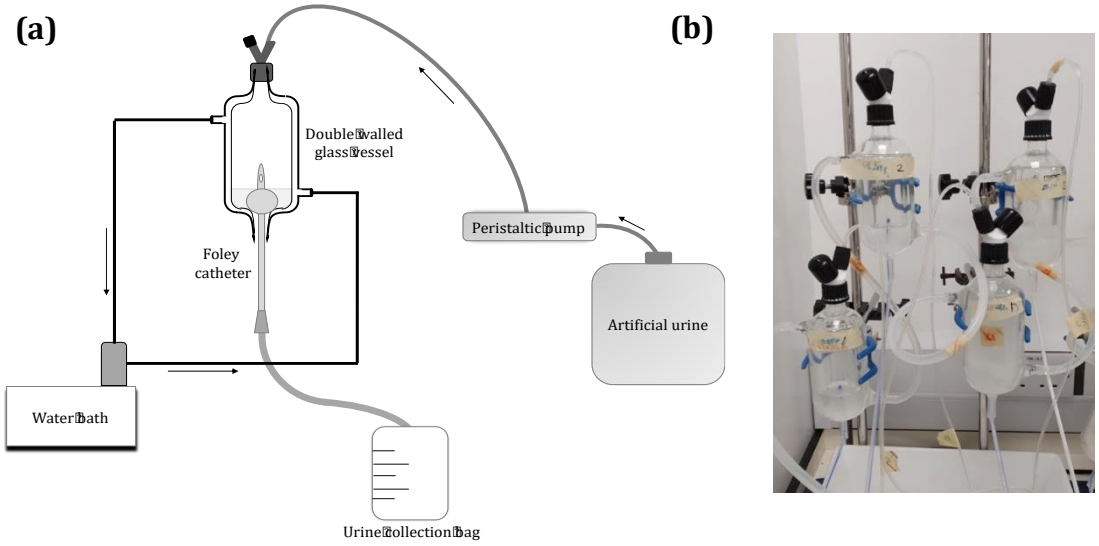

Figure 4.9: a) Schematic diagram of the in vitro bladder model assembly. (b) A photograph of the in vitro bladder model set-up.

CHAPTER 5

HYDROXYCITRATE: A POTENTIAL NEW THERAPY FOR CALCIUM UROLITHIASIS

5.1. Motivation

In 1965, HCA was identified as the acidic component of the rind of the fruit from *Garcinia Cambogia* (GC)[211], which is grown in southern India and is used as a spice as well as a curing agent in food preparation. In 1969 Watson et al. reported that HCA extracted from GC was an effective inhibitor of ATP citrate lyase, making it a useful probe for the investigation of metabolic pathways [212]. ATP citrate lyase is a cytosolic enzyme that converts citrate into oxaloacetate and acetyl CoA. Acetyl CoA is a building block of fatty acids, thus ATP citrate lyase is a key regulator of lipogenesis [213]. This biological function attracted interest in HCA as a potential weight loss supplement. A large body of literature has been produced investigating the effectiveness of HCA [214-217]**.** Indeed, HCA has been purported to reduce lipogenesis, lower appetite, and produce early satiety; however, human studies of HCA have shown conflicting results in regards to weight reduction [218-219]. Nonetheless, HCA is a common ingredient in over the counter (OTC) weight loss supplements, either as pure GC extract or as part of multicomponent weight loss pills. The ready availability of HCA makes it an attractive target for other therapeutic uses.

In addition to the structural similarities to citrate that make it a promising crystal inhibitor, HCA may have an additional mechanism for stone prevention based on its activity as an ATP citrate lyase inhibitor. Melnick et al. reported the effect of HCA

administration in rats who were made hypocitraturic by either chronic acid loading or via a potassium-deficient diet [220]. HCA significantly increased urinary citrate levels (four-fold for the rats that were acidotic and three-fold for the rats that were hypokalemic). Urine pH was not reported in this study.

Despite being on the supplement market for over three decades, little is known about the pharmacokinetics of HCA. Loe et al. measured HCA levels in people who had either taken an oral load of 2 g HCA or a placebo [221]. HCA was not detected in plasma from the placebo group. In subjects given HCA, peak plasma HCA levels were found two to three hours post ingestion and varied from 4.7 to 9 μg/ml (22 to 43 μM). HCA was detectable for up to nine hours after ingestion. The authors estimated that absorption of HCA was about 10-20% of the oral dose. Additionally, Loe et al. reported detectable levels of HCA in the urine, although no quantitative data was provided. Van Loon et al. measured plasma HCA after subjects were given 18 g of HCA in four divided doses over a two hour time period [219]. The peak plasma levels were found to be 390 μM, but no estimate of the percent absorption was provided. We measured HCA urine excretion in seven healthy subjects ingesting 2700 mg/d of HCA for three days; and 24 hr urine HCA excretion was 229 ± 125 mg/d, approximately 8.5% of the daily dose provided (Figure 5.5c) [84].

Though HCA is already marketed for human consumption, one must still consider the issue of potential toxicity before recommending for clinical use. As noted above, GC is a common dietary component in some cuisines with no apparent adverse effects noted, though the amount of HCA consumed would likely be less than when being used as a pharmaceutical. Soni et al. reported that over a 10 year period,

approximately 5 billion doses of single HCA supplement had been sold without negative side effects being noted [222]. Multiple trials of HCA in humans have reported HCA to be well tolerated, with no significant adverse events . However, there have been sporadic case reports of adverse events, particularly liver toxicity, associated with HCA consumption [223]**.** In 2009 the FDA issued a notice against the weight loss supplement Hydroxycut. There were multiple formulations of Hydroxycut, all of which were multicomponent supplements, and only some of which contained HCA. The Health and Hazard Evaluation Board concluded that it was likely Hydroxycut could cause idiosyncratic liver disease, but did not feel it could identify which ingredient(s) was responsible [224]. This ruling has generated considerable push back in support of HCA and the safety of GC extracts [225-226]. More recently, two case reports have been published implicating a GC supplement as a cause of liver toxicity, with one patient requiring a liver transplant [227-228]. As with any case report, the association is not proof of cause and effect, but it does highlight the need for continued surveillance to help determine the risk of HCA use. Of note, most trials in humans have been 12 weeks or less. If HCA is to be used to prevent kidney stone formation, it would be prescribed over the course of years, not months. Because of this, studies focused on stone patients and chronic ingestion must be done before recommendations are made regarding use in stone patients. Herein, we detail the crystal inhibition activity of hydroxycitrate, review current knowledge of hydroxycitrate use in humans, and identify gaps in knowledge that require appropriate research studies before hydroxycitrate can be recommended as a therapy for kidney stones.

5.2. Physicochemical Studies of HCA

5.2.1 HCA as a calcium complexing agent

An important aspect of citrate inhibition of kidney stones is via complexation of calcium ions, i.e., lowering ionized calcium concentration and supersaturation of calcium salts. For HCA to be of equal or greater efficacy as citrate as a stone prevention therapy, calcium binding would need to be of similar magnitude. We compared the calcium binding capacity of HCA and citrate *in vitro* at pH ranging from 5 to 7, mimicking the range commonly found in urine. Figure 5.1 shows the expected concentration dependent fall in ionized calcium as either HCA or citrate are added to solution. There is not a significant difference between HCA and citrate in lowering ionized calcium, particularly at a concentration for maximum inhibitory effect (denoted by the dashed line) during *in vitro* bulk crystallization assays.

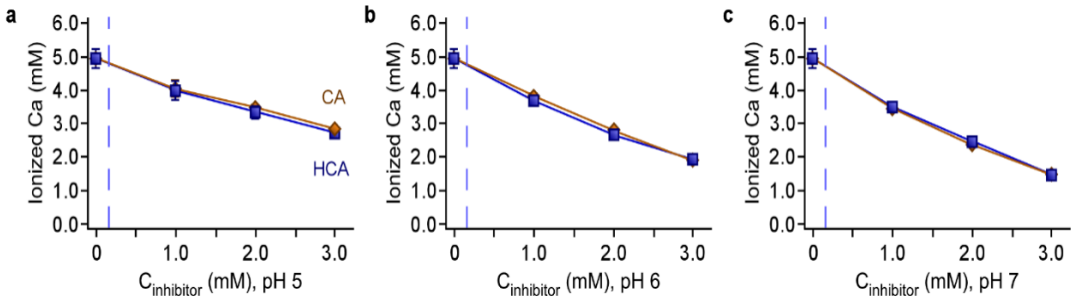

Figure 5.1. Ionized Ca measured using a calcium specific electrode at **(a)** pH 5, **(b)** pH 6, and **(c)** pH 7. A 5 mM $CaCl_2$ solution was used and was spiked with varying amounts of low molecular weight inhibitor, from 0 to 3 mM final concentration.

5.2.2. HCA as a crystal growth inhibitor

Kidney stone formation can also be inhibited through direct interaction between a modifier and a surface of a growing crystal. We examined the effect of citrate and

HCA as modifiers of calcium oxalate monohydrate (COM) crystallization through molecular and macroscopic observations [84]. In vitro bulk crystallization assays of COM growth in 150 mM salt solutions revealed that HCA is more potent than citrate, with both modifiers imparting a maximum of 60% inhibition of crystal growth rate at concentrations above ca. 0.18 mM. A molecular level understanding of crystal growth inhibition in the presence of HCA was obtained from *in situ* atomic force microscope (AFM) imaging of COM surfaces in real time. These studies revealed that HCA can dissolve crystal surfaces in supersaturated media (supersaturation ratio S = 4). To our knowledge, this was the first observation of crystal dissolution in concentrated CaOx solutions. Time-resolved images showed steps on COM (010) surfaces receding toward to the center of screw dislocations (Figure 5.2a) while layers on COM (100) surfaces developed etch pits (Figure 5.2b) with exposure to growth solutions containing HCA at a narrow range of concentrations. At concentrations below a critical range for dissolution, the velocity of advancing steps on COM surfaces is reduced with increasing HCA concentration, similar to common modes of growth modifier action [58]. Dissolution occurs within a relatively narrow range of concentrations wherein further increase in HCA content once again leads to growth inhibition (Figure 5.2c). The exact mechanism for this concentration dependence is unknown; however, density functional theory (DFT) calculations of HCA-COM interactions shows that adsorbed HCA molecules at surface sites (Figure 5.2d and e) can introduce strain in the crystal lattice, thus creating

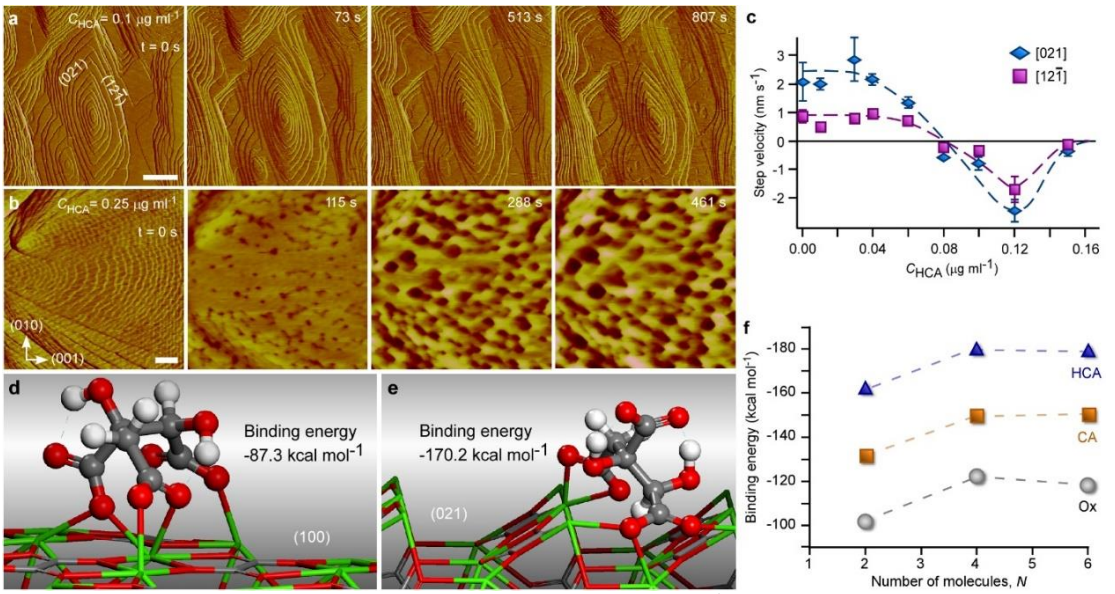

Figure 5.2. (a) Steps receding in the presence of 0.10 µg ml^{-1} HCA. **(b)** Etch pit formation on COM (100) surface at 0.25 µg ml^{-1} HCA**. (c)** Step velocity with [HCA]. **(d and e)** DFT calculations showing the conformation (d) and (e) binding energies [84].

a driving force for the release of oxalate (Ox) and calcium ions into solution to alleviate the strain – a result that is qualitatively consistent with AFM experiments showing COM surface dissolution.

The phenomenon of strain-induced dissolution was also demonstrated by Li et al. [2] for brushite ($CaHPO_4 \cdot 2H_2O$), another kidney stone constituent. In situ AFM images of brushite (010) surface growth in supersaturated calcium phosphate solutions (S = 1.357) revealed that HCA induces the formation of etch pits along the [101] direction that increase in depth with continuous imaging (Figure 5.3) [102]. Analogous to the study of COM, Li et al. showed that this effect is observed over a narrow range of HCA concentration. Moreover, they attribute brushite dissolution to localized strain in the crystal lattice as a result of HCA-brushite interactions. Their study also includes DFT calculations to quantify the relative binding affinity of HCA and citrate with brushite surfaces and showed that HCA preferentially binds to [101] steps whereas citrate

exhibits a stronger affinity for binding to [$\bar{1}$00] steps. These differences explain the results of bulk crystallization assays and AFM studies showing distinct effects of HCA and citrate on the anisotropic rates of growth and surface step density, respectively. Specific interactions between modifiers and crystal surfaces can have a concomitant effect on bulk crystal habit. For example, the interaction between citrate and HCA with brushite crystals transform the nominal triangular habit into needle-like and quadrilateral shapes, respectively (Figure 5.4c and d) [2]. For COM crystallization (Figure 5.4e), citrate binds to [001] steps and blunts the apical tips (Figure 5.4f) [102], whereas HCA binds to the apical tips (i.e., the fastest growth direction) to generate diamond-shaped crystals (Figure 5.4g).

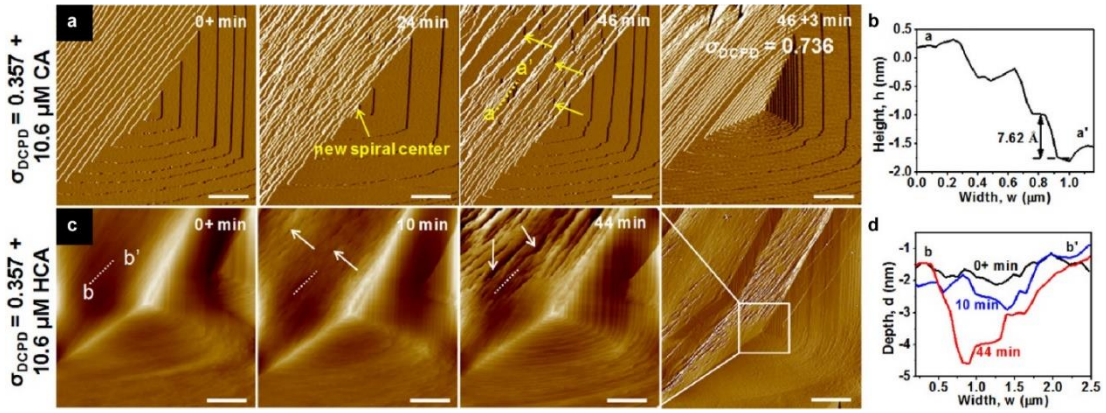

Figure 5.3. Brushite (010) surface growth at S = 1.357 in the presence of 10.6 μM citrate or HCA.[2]

5.2.3. Factors that govern modifier efficacy

The unique inhibitory mode of action exerted by HCA on calcium mineralization opens a new avenue for developing potential therapies. To this end, understanding the physicochemical factors underlying strain-induced dissolution is critical to predicting new molecules with greater efficacy than HCA. A ubiquitous characteristic of COM

crystal growth inhibitors is the presence of acid groups, which interact with crystal surfaces via calcium bridges, $COO^{-}_{(Ox)}\ldots Ca^{2+}\ldots {}^{-}OOC_{(modifier)}$, or hydrogen bonds, $COO^{-}\ldots HOOC$. Polyprotic acids decorated with numerous carboxylic acids are generally more effective inhibitors. For example, amino acids (e.g., Glu and Asp) inhibit the rate of COM crystal growth by ca. 35%, whereas polyamino acids comprised of the same monomers achieve ca. 85% inhibition [105]. Cody et al. [229] showed that at least two carboxylic acid groups are required for inhibitors to effectively reduce the rate of COM crystallization and/or precipitate its metastable counterparts, calcium oxalate dihydrate (COD) or trihydrate (COT); however, the formation of di- and trihydrates were only observed at physiologically irrelevant ionic strength (below 0.5 mM). We have assessed COM growth in the presence of a large number of polycarboxylic acids that share structural features with citrate, reporting an approximately linear correlation between COM growth inhibition and the second dissociation constant of polyprotic acids (pKa_2) [86]. This indicates an enhanced efficacy with increased acid strength, although deviations from this linear trend were observed for citrate analogues (HCA, isocitrate, and citrate) owing to the presence of alcohol groups, which enhance the inhibition of COM crystal growth. Among the common (small molecule) polyprotic acids tested in bulk crystallization assays, HCA was the most potent inhibitor of COM formation.

HCA is a molecular analog of citrate that differs only by a single alcohol group (Figure 5.4a). The improved performance of HCA highlights how a subtle difference in the molecular structure of modifiers can markedly alter their effect on crystal growth [2, 84]. DFT calculations show that the additional alcohol group of HCA increases intramolecular hydrogen bonding, thereby imparting a more rigid structure compared to

citrate [84]. This change in molecular mobility allows HCA to establish energetically favorable interactions with COM crystal surfaces, as well as more strongly bind to free calcium ions in solution (Figure 5.2f). These general effects have been observed by other groups when changing the number and/or position of alcohols along the carbon backbone of dicarboxylic acid modifiers used to dissolve minerals in undersaturated media (S = 0). For example, Qin et al. [230] reported that brushite dissolution is significantly enhanced in the presence of tartaric acid (2 alcohol groups) compared to either malic acid (1 alcohol group) or succinic acid (0 alcohol groups). They posit that crystal-modifier interactions are enhanced when one alcohol group on the modifier is bound to a calcium on the crystal surface and a second alcohol group on the modifier hydrogen bonds to a phosphate group on the brushite surface. More generally, the positive impact of hydrogen bonding in modifier-crystal interactions has been demonstrated for other minerals, such as calcium carbonate (calcite) [231]. Indeed, the judicious selection of carboxyl and hydroxyl groups on modifiers has a significant impact on their ability to inhibit crystal growth (or enhance crystal dissolution).

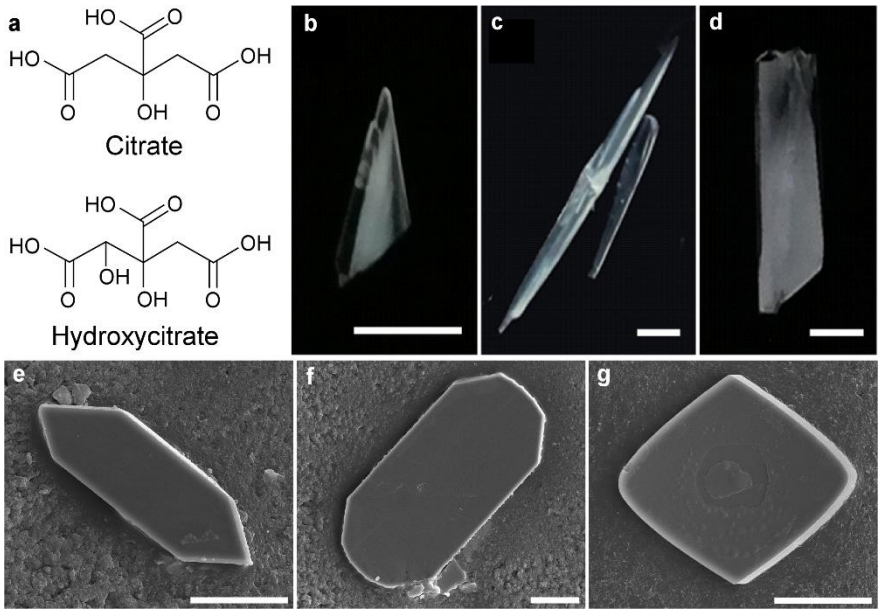

Figure 5.4. (a) Citrate and HCA. **(b**–**d)** Brushite in the absence and (b) presence of (c) 1.25 mM citrate and (d) 1.25 mM HCA**.** Scale bars, 2 μm^2. **(e-g)** COM in the absence (e) and presence of (f) 20 μg ml^{-1} citrate and (g) 20 μg ml^{-1} HCA. Scale bars, 20 μm [84].

5.2.4. Effects on early stages of crystallization

There is evidence to suggest that HCA (and other inhibitors) are able to partially suppress the nucleation of COM. Inferences of crystal nucleation are often made from bulk crystallization data showing differences in crystal number density with and without the addition of modifier. We have shown that there is a 39 ± 17% and 62 ± 15% reduction in COM number density in solutions containing 0.06 mM citrate and HCA, respectively (Figure 5.5a) [84]. This seems to indicate that HCA is a more effective inhibitor of COM nucleation, although differences are within the error of measurement. Additional evidence of nucleation suppression is gleaned from studies comparing the upper limit of metastability (ULM) of urine samples from eight patients with kidney stone disease to the untreated urine control (Figure 5.5b) in the presence of HCA and citrate. ULM represents a solute concentration limit that, when exceeded, leads to

instantaneous nucleation; therefore, the observed increase in ULM is evidence that inhibitors influence COM nucleation, although the exact mechanism for this mode of action remains elusive.

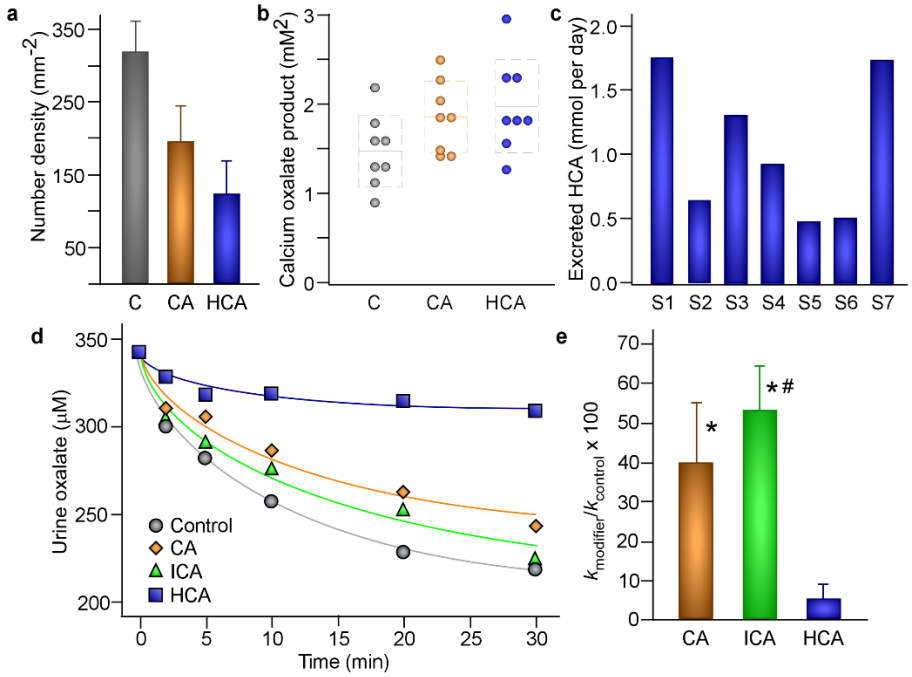

Figure 5.5. Effect of CA and HCA on **(a)** COM number density, **(b)** the upper limit of metastability at 2 mM inhibitor, **(c)** urinary excretion of orally administered HCA[84], **(d)** urine oxalate concentration, and **(e)** relative growth constants [232].

The uncertainties of COM crystallization pathway(s) complicates our fundamental understanding of nucleation and its inhibition. It is possible that nucleation occurs directly from ion/molecule association or through a two-step process involving the initial formation of clusters. Biominerals such as $CaCO_3$ and CaP frequently nucleate from solutions containing amorphous precursors [233-235]. It was recently suggested that CaOx follows a similar mechanism [89, 96]. For example, Ihli *et al.* [96] identified amorphous particles that are 10 – 50 nm in size with equimolar compositions of CaC_2O_4:H_2O that precipitate along with crystalline particles from aqueous solution.

In this study, they found that amorphous particles can be stabilized by the presence of polyprotic macromolecules, such as poly(acrylic acid). Observations by Ruiz-Agudo *et al*. [89] suggest that COM crystallizes from a suspension of polynuclear complexes that aggregate into amorphous calcium oxalate (ACO) clusters. Citrate was found to stabilize these metastable intermediate species via the generation of negative surface charge exerted by the bound carboxylates of citrate, which presumably halts the aggregation of ionic clusters and stabilizes ACO nanoparticles. Similar effects have been reported for $CaCO_3$ in the presence of silica [236], amino acids [237], and surfactants [238]. It has also been suggested that modifier-cluster interactions impact cluster solubility. For instance, it is posited that citrate alters the solubility of citrate-bearing ACO (relative to citrate-free species), which may concomitantly impact the dissolution-precipitation transition from ACO to COM crystals [89]. It is important to note, however, that evidence for clusters and amorphous phases is derived solely from *in vitro* observations, and that confirmation of their existence *in vivo* remains to be determined.

An alternative (and more commonly invoked) mechanism is heterogeneous nucleation from papillary lesions, known as Randall's plaque. Many stones are found attached to a renal papilla at the time of endoscopy and the retrieved stones exhibit concavity that matches the shape of the papillary surface [239]. Moreover, the surface of the concavity as well as deeper layers of the stone are often found to contain CaP, similar to interstitial Randall's plaque. In vitro studies have shown that CaP interfaces are capable of nucleating COM crystals [240]. Indeed, Randall's plaque is thought to be the nidus of calcium-based stones and thus, the site of heterogeneous nucleation [239]. Stoller et al. [241] was able to capture intratubular mineralization of the renal medullary tissue

that may serve as a precursor for the formation of Randall's plaque. It is, therefore, feasible that all of these pathways are putative targets for therapeutic intervention, though the precise mechanism by which HCA and other modifiers inhibit CaOx nucleation is unknown.

5.2.5. Physiological relevance of HCA

There are no studies reporting the effect(s) of HCA on renal stone formation. Although *in vitro* assays of COM crystallization have proven to be effective methods for evaluating the efficacy and mechanism of putative therapeutic agents, the results cannot be directly translated to performance *in vivo*. The growth solutions employed in most laboratory tests lack the complexity of urine to mimic native environments for stone formation. Notably, urine consists of an estimated 3,100 small molecules and about 2,000 proteins [242-243]. These molecules may influence the development of kidney stones, or potentially interfere with modifiers designed to prevent stone formation. To this end, we have evaluated HCA efficacy in human urine samples. Intriguingly, our results revealed significantly enhanced inhibition (i.e., 96 ± 3 %) compared to measurements in salt solution (i.e., 60% inhibition), as shown in Figure 5.5e [86]. This indicates a synergistic effect between HCA and urinary constituents that leads to an additional 36% inhibition – an outcome that is not encountered for citrate, which reduces the rate of COM crystallization by a maximum of 60% in human urine and salt solution.

Despite the promise of HCA as a preventative therapy of kidney stones, its potential to serve as a treatment for existing stones remains to be determined. While *in vitro* assays reveal that HCA is capable of dissolving COM and brushite crystals, this

phenomenon was observed under specific conditions – namely under continuous flow of a growth solution containing a relatively narrow range of HCA concentration without rigorous tests at varying solute supersaturation [2, 84]. In the case of brushite, etch pits formed only in ranges of $1.36 \leq S \leq 1.40$ and low concentrations of HCA (8.5 – 10.6 μM) [2]. For studies of COM, layer dissolution and etch pit formation were similarly observed under a narrow set of conditions: S = 4.1 and 0.24 – 0.73 μM HCA [84]. AFM experiments of HCA dissolution of COM crystal surfaces were performed at a fixed flow rate of 0.2 ml min^{-1} [84]. It is well established that changes in flow rate around this value can lead to distinct differences in growth being kinetically limited (at high flow rates) or diffusion limited (at low flow rates) [244]. Currently, the sensitivity of COM dissolution to these parameters is unknown; and thus, it is difficult to predict if these conditions will be achieved *in vivo* to induce dissolution of an existing stone. Moreover, *in vitro* studies utilized clean crystal surfaces (i.e., devoid of adsorbed organics), which may not be representative of renal calculi. For example, it has been proposed in related systems that rough crystal surfaces may not contain the preferred adsorption sites for drugs, thereby allowing crystallization to proceed uninhibited [245]. To this end, more tests are required to bridge the gap between *in vitro* and *in vivo* evidence of HCA efficacy, and its unique ability to dissolve COM crystals over a broader range of conditions – particularly in urine where crystals rapidly become coated with proteins and glycosaminoglycans, and HCA would have to compete with other small molecules such as citrate and pyrophosphate. It is uncertain whether strain-induced dissolution will occur in such a complex environment.

5.3. Future Direction

Despite promising *in vitro* data showing HCA a potent COM inhibitor, considerable research needs to be done to define the role of HCA in treatment of kidney stones. Here is a partial list of issues waiting to be addressed:

1. The pharmacokinetics of HCA needs to be better understood. What is the optimal dose which delivers adequate HCA to the urine with minimal adverse effects? What is the appropriate number of doses per day and how should the drug be taken in relation to meals? Current recommendations of available products are to consume HCA 30 to 60 minutes before meals, but we have no knowledge if taking with food or on an empty stomach maximizes intestinal absorption. What role does the accompanying cation affect the absorption and gastrointestinal tolerance of HCA? Is HCA metabolized by humans or is the low renal excretion rate a reflection of poor intestinal absorption?

2. HCA has two chiral centers and therefore four enantiomers [246]. HCA extracted from GC is the (2S,3S) enantiomer and this is the isomer used in all published animal and human studies. Whether all the enantiomers possess equivalent efficacy has not been investigated. Might the different enantiomers have affinity for different crystal faces, perhaps making a mix of enantiomers is preferable over a single molecule to maximize crystal inhibition? One also needs to consider whether there are differences in intestinal absorption and renal excretion amongst the enantiomers, making the pharmacokinetic profile of each compound just as important as crystal inhibition activity.

3. The *in vitro* crystallization work needs to be complemented with *in vivo* studies. To this point, the proof that HCA is excreted in human urine was a necessary first step to justify further investigation. We have initiated two studies that should provide much greater insight into the potential of HCA as a kidney stone therapy. The first is a short term trial (1 week) of an OTC HCA supplement in non-stone forming healthy subjects and in patients with calcium kidney stones. The key end-points are urinary excretion of HCA, citrate and urine pH. Though we have previously quantified HCA urine excretion, we need to expand the number of subjects in which it has been measured. In addition, patients with kidney stones will be included, as it is vital to ensure there is not a difference in intestinal or renal handling between healthy subjects and the patients. Whether urine pH changes will help determine if HCA might be of particular use in patients with calcium stones and a high urine pH. Finally, we will determine if HCA increases urine citrate, as shown in the rat model reported by Melnick et al. [220]. In our second study we will use the Genetic Hypercalciuric Stone-Forming (GHS) rat to determine if calcium stones can be prevented *in vivo*. The GHS rats spontaneously form CaP stones when fed standard rat chow [247], but will form CaOx stones when fed a diet enriched with hydroxyproline [248]. The rat studies will allow us to address both types of calcium stones and use kidney stone formation as an end-point in a time frame much shorter than feasible in a human study. Data from these two studies should provide a strong foundation for further research of HCA in stone disease.

5.4. Conclusion

Despite promising *in vitro* work, definitive studies of the efficacy and safety of HCA need to be performed. If our proposed human and animal studies are promising, a prospective trial in kidney stone patients with stone formation as an outcome would be a logical next step. Optimally, studies of both CaOx and CaP stone formers would be performed. Though readily available in OTC formulations, there have been some safety concerns with HCA use. To this end, the use of HCA for stone prevention, which would be a therapy expected to be used for years in an individual, should not be undertaken until there is clinical evidence of effectiveness and studies clearly defining the risk of adverse effects with long term use.

CHAPTER 6

BIO-INSPIRED DISRUPTORS OF PATHOLOGICAL CALCIUM OXALATE CRYSTALLIZATION

6.1. Motivation

A common and effective method of regulating synthetic, biological, and natural crystallization is growth modification using foreign species ranging from ions to (macro)molecules that interact with crystal surfaces to either inhibit or promote the incorporation of growth units.[102-104, 203, 249-251] The vast majority of studies on crystal growth modification report classical modes of action wherein modifiers bind to crystal growth sites (i.e., kinks, steps, or terraces) and either physically impede solute attachment or alter local solvent ordering.[56, 83-84, 152, 252] The emergence of nonclassical crystallization has led to alternative mechanisms of modifier action that include (but are not limited to) the disruption of cluster formation and alterations in the self-assembly and/or evolution of amorphous precursors.[253] In applications where crystallization is an undesirable outcome, such as scale formation (e.g., oil/gas pipelines and water treatment) or pathological human diseases (e.g., malaria, atherosclerosis, gallstones, kidney stones, gout, etc.), the use of modifiers can be an effective tool to inhibit or fully suppress crystal growth.

The vast majority of studies examine the effects of modifiers on crystal growth where the maximum efficacy rarely exceeds 80 – 90% growth inhibition. Relatively fewer studies examine the impact of modifiers on nucleation, and even less report examples where modifiers function in a dual manner to inhibit both nucleation and

growth.[200] Nucleation can be challenging to suppress owing to its stochastic nature and the probability of fluctuations in solution composition (i.e., non-ergotic characteristics) that promote clusters of critical size for nucleation (in accordance with classical nucleation theory).[254-256] The search for nucleation inhibitors is of interest to many of the aforementioned applications as a means of fully suppressing crystallization.[257-261]

Calcium mineralization is essential to the formation of bone and teeth of vertebrates, among other physiological processes. Several calcium minerals are also involved in pathological diseases, such as calcium oxalate monohydrate (COM), the most common constituent of human kidney stones. There are several urinary proteins that function as native inhibitors of kidney stone formation.[262-266] One of the most widely studied protein inhibitors of COM crystallization is osteopontin (OPN),[101-102, 267-269] which also functions as a regulator of bone formation (i.e., calcium phosphate crystallization).[270] The inhibitory effect of OPN on COM crystal growth is attributed to the presence of peptide sequences rich in aspartic acids. For example, OPN amino acids 62 to 85 are comprised of 54% acidic residues (aspartic and glutamic acid)[103] in its primary sequence (Figure 6.1). This has inspired numerous studies of the spatial positioning and number of acidic residues on macromolecules (e.g., peptides) to elucidate the role of these functional moieties in regulating biomineralization.[79, 102-104] Another characteristic feature of OPN is its abundance of serine and threonine residues that are susceptible to post-translational phosphorylation. Previous reports have shown general correlations between the number of phosphate groups in OPN peptide sequences and their efficacy as COM crystal growth inhibitors[269, 271]; however, exploiting these

elements in the design of small molecules capable of serving as potential therapeutics is lacking.

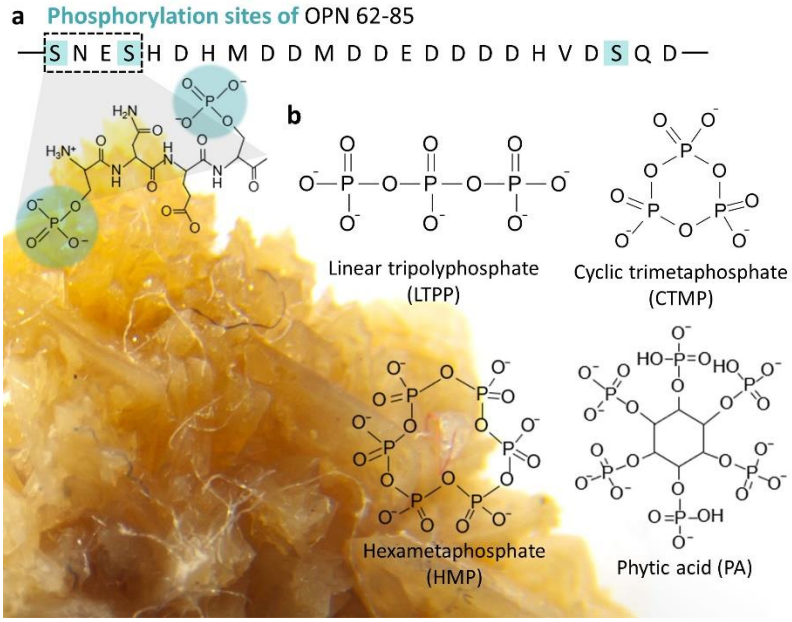

Figure 6.1. (a) Peptide sequence of OPN highlighting serines (cyan) as sites for phosphorylation. **(b)** Molecular structures of polyphosphates and phosphonate PA tested as putative inhibitors of COM crystallization.

Polyphosphates, whose backbone is composed of tetrahedral phosphates (PO_4) linked together through shared oxygen atoms, are effective molecules that can influence crystallization in many processes.[272-274] They are found in living organisms in extreme environments[275] and are used in dentistry[276-277] to treat teeth (i.e., hydroxyapatite). An advantage of polyphosphates over more conventional carboxylate-based modifiers (e.g., citrate and its derivatives)[84, 86] is their biocompatibility and hydrophilicity, which make them ideal candidates for biological applications.[278-280] Polyphosphates can be synthetically modified with different functional moieties and/or condensed to form long-chain or highly branched macromolecules.[281-286] The effectiveness of these molecules are often rationalized by their ability to complex with calcium ions, which

lowers supersaturation and concomitantly inhibits crystal growth; however, this mechanism requires high concentrations of polyphosphates,[287-288] and is inconsistent with evidence supporting a classical mechanism involving modifier interactions with crystal surfaces.

Herein, we investigate three polyphosphates with distinct linear and cyclic structures along with one phosphonate (phytate), which has been reported to be an effective growth inhibitor of COM and other minerals.[258, 287] We show that subtle differences in the structure of phosphate-based modifiers have a profound impact on their ability to inhibit COM crystallization. Interestingly, we have identified a molecule that can fully suppress COM nucleation and irreversibly stunt the growth of COM crystals. To our knowledge, irreversible growth inhibition is a rare phenomenon in the broader field of crystallization. Specific insights from this work may aid future development of more effective therapeutics for pathological COM formation.

6.2. Results and Discussion

6.2.1. Impact of Polyphosphates on COM Crystallization.

Here we screened the four polyphosphates (Figure 6.1b) using bulk crystallization assays to assess their relative impact on COM crystallization. Scanning electron microscopy (SEM) images of crystals grown in the presence of modifiers revealed significant differences in crystal habit. CTMP, a cyclic trimer, produced COM crystals with an elongated hexagonal shape (Figure 6.2a) similar to that of the control (i.e., absence of any additives). In the presence of LTPP, which is a linear analogue of CTMP, crystals form an ovoid habit (Figure C1, b and c) with a size that reduces with

increasing LTPP concentration. The absence of distinct facets on crystals in favor of curved surfaces is often attributed to the incorporation of the additives, which alters the crystal lattice.[289] HMP, a larger cyclic polyphosphate, also generates COM crystals with curved surfaces (ovoid habit) at higher HMP concentrations (30 μg mL^{-1}), whereas the original facets are retained at lower concentrations with significant reduction in (010) surfaces (Figure C1, d-f). The ovoid habit generated by LTPP and HMP is consistent with the morphology of COM crystals observed in urine sediments. In physiological environments, urinary proteins are known to modulate crystal formation by binding to specific crystal surfaces or incorporating into the urinary stone matrix.[290-291] Elemental analysis of COM crystals recovered from bulk crystallization assays in the presence of polyphosphates show evidence of modifier accumulation (≤ 0.07 P/Ca ratio, Supplementary Figure 6.2), although it is uncertain to what degree the modifiers are bound to the surface or incorporated into crystals as defects (*vide infra*).

Above a certain threshold concentration, LTPP and HMP induced a phase change to calcium oxalate dihydrate (COD) crystals (Figure 6.2c). COD is more thermodynamically metastable than COM and is considered a benign form of calcium oxalate in pathological crystallization.[26] Indeed, COD is primarily found in normal urine of healthy individuals and in voided urine of asymptomatic individuals where prior studies report that COD is less prone to aggregation and/or adhesion to cellular membranes in the kidney.[26, 292-293] It has also been reported that modifiers can inhibit COM crystallization and stabilize COD.[101, 263, 271, 294-298] Putative mechanisms for this phenomenon include the generation of high supersaturation favoring COD nucleation[299], the role of modifiers as templates to promote COD formation[300-301], and

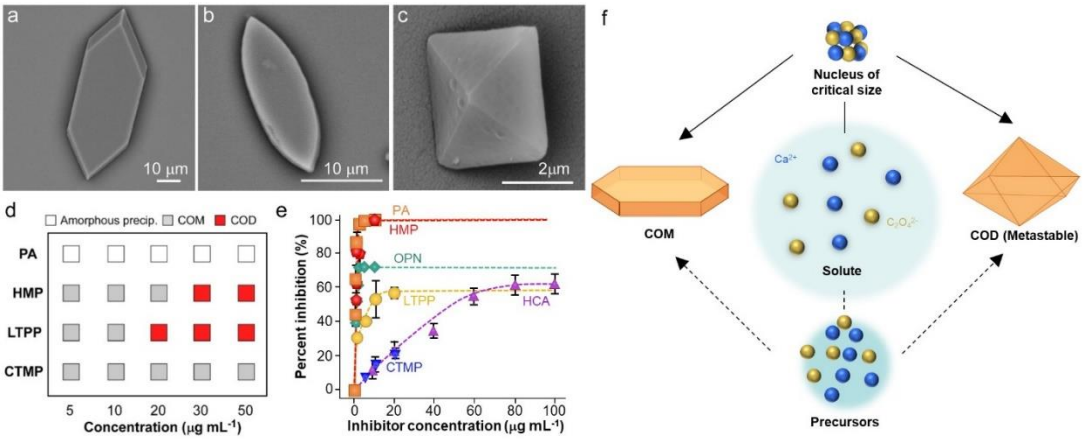

Figure 6.2. (a-c) Crystals prepared with 20 μg mL^{-1} of **(a)** CTMP and **(b)** HMP, and **(c)** 30 μg mL^{-1} HMP. **(d)** Phase of CaOx product with modifier concentration. **(e)** Percent inhibition from ISE measurements. **(f)** Idealized schematic of CaOx crystallization.

the potential for modifiers to alter the structure, hydration level, and/or solubility of amorphous precipitates that seemingly precede the nucleation of calcium oxalate hydrates[89-90, 95].

We observed that both LTPP and HMP inhibit COM formation in favor of metastable COD crystallization (Figure 6.2d) at modifier concentrations of 20 and 30 μg mL^{-1}, respectively. Among the phosphates tested, the most potent inhibitor of COM crystallization was phytate (PA). Bulk crystallization assays revealed that 5 μg mL^{-1} PA was sufficient to completely suppress COM nucleation without any observed shift to COD. Optical micrographs of glass slides placed at the bottom of bulk crystallization vials showed no evidence of crystals or any amorphous precipitate (Figure C3). To our knowledge, this is the first demonstration of a modifier capable of completely suppressing calcium oxalate nucleation; however, we previously reported that PA has a similar inhibitory effect on both nucleation and growth of struvite crystals (a minor component of human kidney stones).[200]

The influence of polyphosphates on the kinetics of COM crystallization was assessed by *in situ* ion selective electrochemical (ISE) measurements to track the temporal removal of Ca^{2+} ions from supersaturated growth solutions with and without the addition of modifiers (Figure C4). Here, we use two natural modifiers as references owing to their reported high efficacy as COM growth inhibitors: OPN and hydroxycitrate (HCA). The latter is a molecular analogue of citrate and has proven to be a more potent inhibitor of COM crystallization compared to other small molecule carboxylate-based polyprotic acids.[79] The performance of the modifiers (Figure 6.2e) follows a Langmuir-like behavior wherein the percent inhibition of calcium oxalate crystallization plateaus at some concentration of inhibitor (a trend in ISE data that is typical of numerous inhibitors of crystal growth[84, 200, 203]). Our findings reveal that OPN is more potent than HCA with a higher percent inhibition. Macromolecules tend to be more effective inhibitors of crystallization compared to small molecules owing to a higher percentage of proximal anionic functional moieties that can cooperatively bind to crystal surfaces.[105] In the case of phosphates tested in this study, we observed distinct efficacy (Figure 6.2e). CTMP was comparable to HCA; LTPP was also comparable to HCA (maximum of ca. 60% inhibition) but with higher potency; and HMP and PA surprisingly outperformed OPN with 100% inhibition observed at low modifier concentration.

HMP and PA are reported metal chelators[273, 302-303] and disruptors of mineralization[258, 276, 304-308] in various applications. The specific role of HMP as a crystal growth inhibitor is rationalized in literature on the basis of thermodynamic effects (i.e., the formation of complexes or chelation of ions)[306, 309-310]; however, the quantity of

HMP (and PA) used in bulk crystallization assays is two orders of magnitude less than the concentration of calcium, suggesting kinetic factors are more likely involved in the observed inhibition of COM crystallization. To test this hypothesis, measurements were performed over a range of supersaturation (in the absence of modifier) where the concentration of oxalate was fixed and that of calcium was reduced relative to the control (Figure 6.5). As expected, a reduction in calcium concentration concomitantly reduced the rate of Ca^{2+} ion consumption. If we assume HMP or PA has the capacity to sequester Ca^{2+} in a ratio of 6:1 (Ca:modifier), we estimate a 10% reduction in COM crystallization (i.e., corresponding to 0.466 mM Ca^{2+} in Figure C5). Given that this reduction is well below the 100% inhibition observed in ISE measurements, we posit that HMP and PA impede crystallization via kinetic pathways; however, ISE cannot distinguish between a modifier's impact on nucleation and crystal growth (these effects are decoupled in later sections).

The exact mechanism by which modifiers inhibit COM nucleation is not well understood. Akin et al.[108] proposed that rapid adsorption of polymeric additives can reduce the number of active growth sites on subcritical nuclei, creating a thermodynamic driving force for particle dissolution and a concomitant extension of the induction period. It is alternatively proposed that modifiers influence calcium oxalate intermediates. For example, Ruiz-Argudo et al.[89] reported the formation of small clusters (ca. 2 nm) and larger amorphous calcium oxalate (ACO) particles (30 – 100 nm) in the presence of citrate. More recently, Banner et al.[95] reported a counter observation wherein amorphous clusters form only in the absence of citrate. Collectively, these studies suggest that nonclassical pathways akin to the two-step

mechanism[93] are potentially involved in the nucleation of calcium oxalate hydrates (Figure 6.2f, top pathway) in addition to classical nucleation theory (Figure 6.2f, bottom pathway).

Here we explored the potential nonclassical route of COM nucleation for the experimental conditions used in our study. We employed oblique illumination microscopy (OIM), which is a light scattering technique used to identify the presence of particles (or clusters) through Brownian dynamics.[70] We prepared solutions with fixed ionic strength (150 mM NaCl) and a range of calcium oxalate concentrations to test three regimes: supersaturation (S = 1 – 4), saturation (S = 1), and undersaturaration (S = 0.8). In each regime, we did not detect any particles or clusters in the absence or presence of polyphosphates (Table C1). One possible scenario is that clusters may form with a number density and/or size (< 20 nm) below the detection limit of OIM. To this end, we performed atomic force microscopy (AFM) measurements using an adapted protocol by Putnis and coworkers[94] that visualized small clusters (< 10 nm) in COM growth media. In these measurements we used mica surfaces as a flat substrate for the adsorption of calcium oxalate clusters; however, the set of conditions tested in this study (Table C2) showed no evidence of precursor formation, even at prolonged times of measurement (ca. 10 h), in solutions with and without modifiers. It should be noted that prior studies reporting nonclassical routes for calcium oxalate nucleation use growth media at conditions far from physiological relevance[89-90, 95-96] (i.e., calcium oxalate concentrations that exceed 100 mM and modifier concentrations orders of magnitude higher than those used in our study). Others have observed cluster formation when using disproportionate molar ratios of calcium and oxalate[94] or when substituting water with

an alternative solvent (e.g., ethanol)[97]. There remain many questions pertaining to the nature of cluster formation and its role in COM (or COD) nucleation, and to what extent modifiers influence these processes. It is evident, however, for the conditions tested in this study that nucleation and its inhibition by polyphosphates involve classical pathways.

6.2.2. Impact of Polyphosphates on COM Growth

We used a combination of microfluidics and *in situ* AFM to evaluate the effects of polyphosphates on COM growth at a macroscopic and microscopic level, respectively. The design and testing of a microfluidic device was previously reported by our group for studies of other minerals (e.g., barite[159] and struvite[201]). Here we used the same device to monitor time-resolved changes in COM crystal size and morphology under conditions where growth solution (with or without modifier) is continuously flowed over seed crystals in a microfluidic channel. The random orientations of seed crystals on either the basal (100) or side (010) facets enables the evaluation of growth along the three principal directions: [100], [010], and [001]. Measurements in the presence of LTPP reveals its preferential binding in the order of COM (100) > (121) > (010), which leads to a decreased thickness in the [100] direction (Figure 6.3b) as well as a decrease in the length-to-width ratio (*c/b*, Figure 6.3c) with increased exposure to LTPP-containing solutions (Figure 6.3a). Microscopic evaluation of LTPP growth inhibition using *in situ* AFM revealed a significant reduction of layer advancement in the c-direction with the generation of corrugated step edges that is characteristic of a step pinning mode of action (Figure 6.3d and Movie C1).

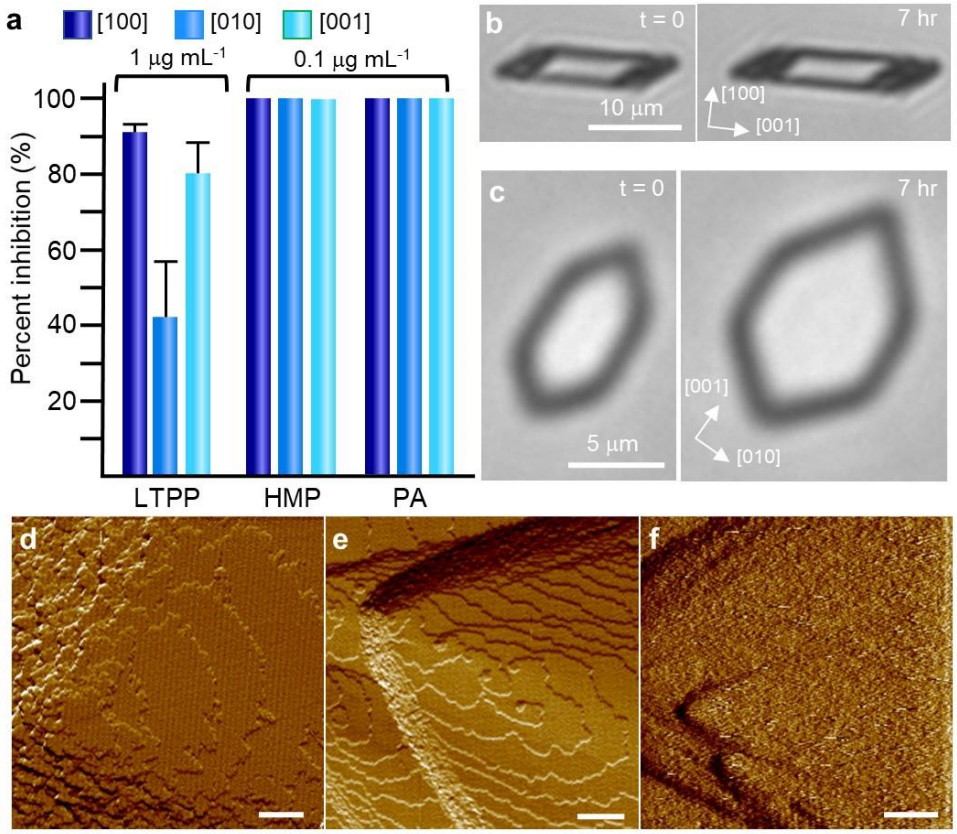

Figure 6.3. (a) Percent inhibition of COM crystal growth. **(b and c)** COM crystals grown in solution (S = 4.1) containing 1 μg mL^{-1} LTPP. **(d-f)** COM100) surfaces in solutions containing 1 μg mL^{-1} of **(d)** LTPP, **(e)** HMP, and **(f)** PA. Scale bars equal 500 nm.

Our findings revealed that the two most effective nucleation inhibitors, HMP and PA, were also able to fully suppress COM growth. Microfluidic assays using solutions containing HMP or PA (0.1 μg mL^{-1}) showed no change in any crystal dimension (Figure 6.3a). Similarly, *in situ* AFM measurements on basal (100) surfaces revealed that step advancement is completely arrested shortly after HMP was introduced into the sample cell (Figure 6.3e and Movie C2). In the presence of PA, we observed a slightly different phenomenon wherein the entire surface is covered by rough features that gradually obscures the underlying layers (Figure 6.3f). AFM imaging revealed that step

growth is completely suppressed prior to the formation of rough surfaces and the eventual disappearance of steps (Figure C6). It is important to note that these effects occur at very low modifier concentration (0.1 μg mL^{-1}), nearly three orders of magnitude less than the concentration of calcium; therefore, these findings are consistent with the proposed kinetic mechanism of crystal growth inhibition.

6.2.3. Regeneration of Surface Growth after Exposure to Polyphosphates

Here we assessed the ability to regenerate COM (100) surface growth after complete suppression by HMP and PA. Nominal layer advancement on this surface occurs by screw dislocations (Figure 6.4a) where triangular hillocks are generated by the anisotropic advancement of layers in the [001] direction at velocities that are approximately 10-times faster than those in the [121] direction. Steps with (010), (0-10), (0-21), and (021) faces are not expressed. After surface growth is completely arrested by exposure to HMP, we tested whether layer advancement could be restored to its original rate under continuous supply of growth solution containing no inhibitor (i.e., same condition as Figure 6.4a). Continuous AFM imaging for upwards of 10 h showed that step edges remained frozen, indicating irreversible inhibition; however, we did observe two-dimensional nucleation and growth of islands on the terraces between steps (Figure 6.4b). To our knowledge, this is the first observation of 2D birth and spreading on COM crystal surfaces in any growth medium among the numerous published studies of COM crystallization.[86, 102, 107, 311-314] These islands that appear during surface regeneration are initially rounded (Figure 6.4c) single layers with heights

of ca. 0.6 nm, which is equivalent to the expected dimension of (100) step edges (Figure 6.4d).

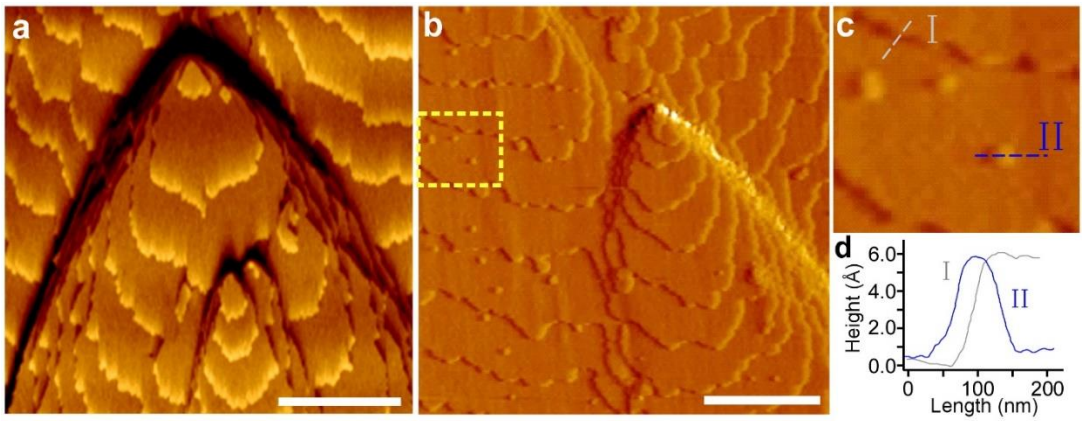

Figure 6.4. (a) COM (100) surface growing in control growth. **(b)** Surface growing in control solution after 149 min exposure to HMP. Scale bars equal 1 μm. **(c)** Arrested step edge (I) and 2D islands (II). **(d)** Height profiles across the dashed lines in (c).

Evidence for irreversible inhibition was obtained by monitoring changes in surface features after first arresting growth in the presence of HMP and then introducing a fresh growth solution (without modifier) to regenerate surface growth. Under nominal growth conditions, step advancement is difficult to track owing to the fast kinetics of surface growth (i.e., steps advance out of the frame of imaging within 1 min). After exposure to HMP, steps could be tracked over much longer periods of time (> 5 h) intermittent imaging revealed that the original steps do not advance during regeneration. *In situ* AFM imaging of COM crystal surfaces capture 2D nucleation of islands in real time, but even more interestingly time-elapsed images reveal that these islands grow in a unique way (Figure 6.5a). Notably, 2D islands do not propagate in the [001] direction, which is the predominant direction of growth for crystals that have not been exposed to HMP (Figure 6.4a). Growth of 2D islands occurs in the opposite [00-1] direction where their advancement leads to a gradual change in layer morphology and the appearance of

a hexagonal shape (Figure 6.5b). Analysis of the COM crystal structure (Figure 6.5c) shows that the steric presentation of oxalates causes the steps to form acute angles with the underlying terrace in one direction, and obtuse angles in the opposite direction. Solute attachment preferentially occurs at acute steps; however, 2D island growth involves solute attachment to obtuse steps. The exact mechanism for this irregular growth pattern is not fully understood, but we posit that residual HMP in COM crystals is responsible for the observed effects (*vide infra*).

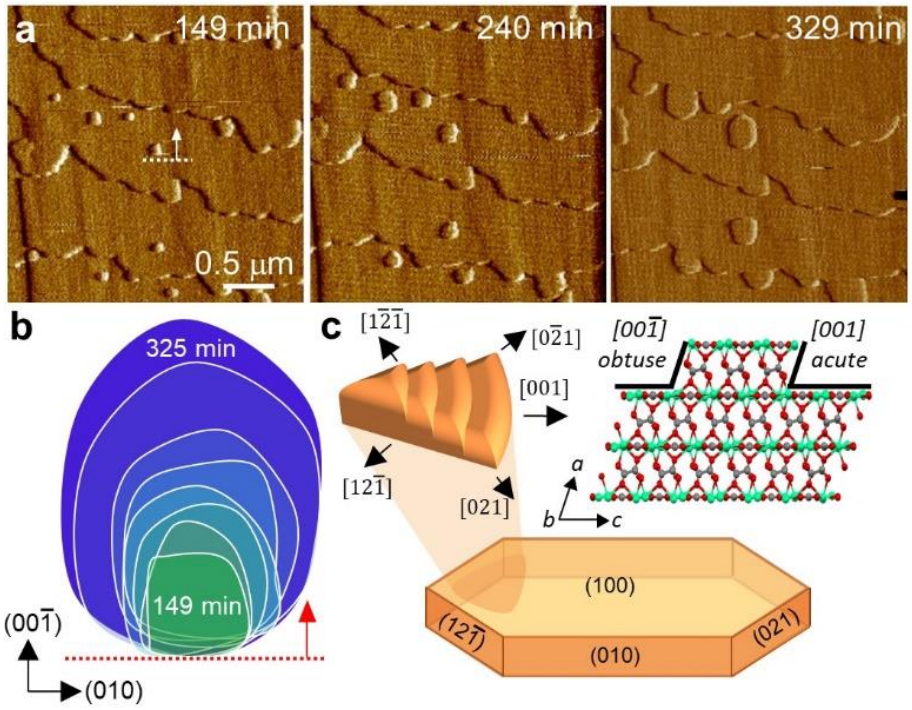

Figure 6.5. (a) COM (100) surface previously exposed to HMP that is subjected to a continuous flow of control growth solution (modifier free). **(b)** Contours of a growing 2D island highlighted in (a). **(c)** Schematic of the COM crystal habit with indexed facets.

Detailed analysis of AFM images from *in situ* growth and regeneration measurements was performed to extract the distance of step and 2D island advancement with time in the [001] and [00-1] directions, respectively. We observed that the rate of

island advancement is reduced by more than 97% relative to step advancement (Figure 6.6a). This indicates that HMP can not only suppress layer growth via its adsorption on COM (100) surfaces and steps, but seemingly imparts a strain on 2D islands that slows their advancement while hindering growth in the [001] direction. Arrested step advancement was unexpected since growth inhibition is typically a reversible process. Prior studies have demonstrated this for COM as well as other crystalline materials such as struvite and calcite[104, 200, 203, 315] where regeneration with inhibitor-free growth solutions leads to a return to normal rates of step advancement, often after an initial delay that is either related to the time required for modifier desorption from the crystal surface or overlayers to reduce strain imposed by modifiers that are occluded within the crystal (as defects). Growth may resume via the generation of macrosteps while elementary (or single layer) steps remain pinned or immobilized.[316-317] In terms of irreversible inhibition, we are only aware of one reported case – a study by Ma et al.[252] on an organic crystal (hematin) where nanocrystals in solution deposit on crystal surfaces and reduce the rate of layer advancement with the original rate of layered growth unable to be recovered during regeneration.

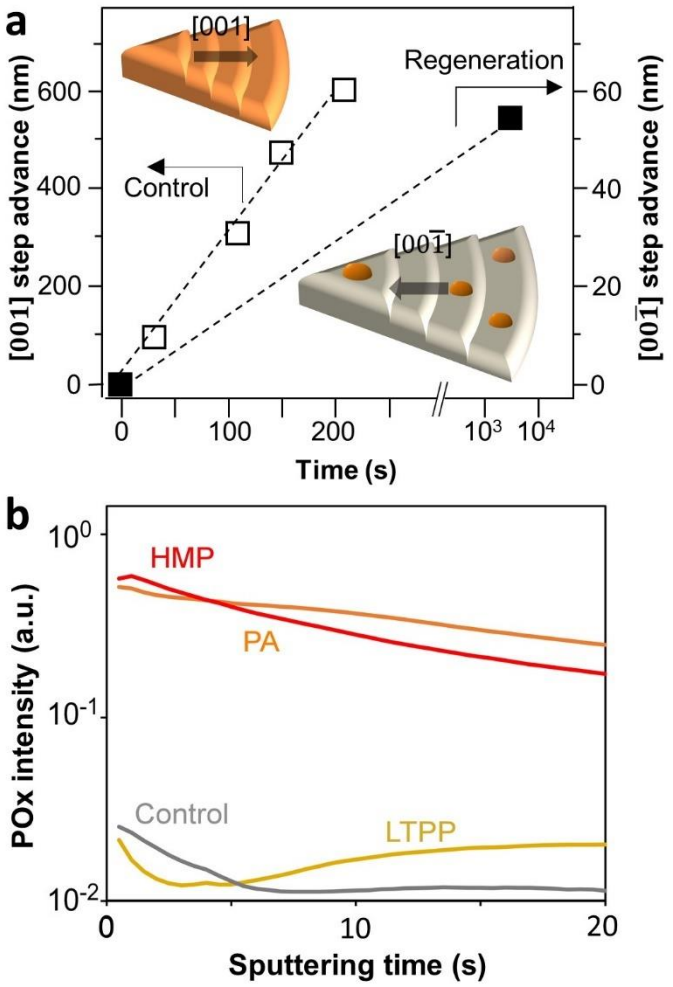

Figure 6.6. (a) Step advancement as a function of time during in situ AFM measurements of (left) step growth ([001] direction) and (right) island growth ([00-1] direction) during regeneration. **(b)** ToF-SIMS intensity profiles of phosphate (PO_x).

To assess whether phosphate adsorption on (or incorporation in) COM crystal surfaces is irreversible, we performed time of flight secondary ion mass spectrometry (ToF-SIMS) for samples after 2-h of regeneration (Figure 6.6b). The control represents a zero baseline given that this sample was not exposed to any phosphorus-containing compounds. Samples exposed to HMP and PA retain a notably high amount of phosphate on (or within) COM crystal surfaces compared to the control. It is difficult to extract information from ToF-SIMS regarding the location of phosphates on either

external surface sites or within the outermost layer(s) of COM given that the crystals prepared on substrates do not lay flat, leading to a monotonic reduction in intensity with sputtering time (Figure 6.6b). This observation indicates that phosphates irreversibly adsorb on (or incorporate in) the outermost layer of COM crystals, such that residual modifier is putatively responsible for suppressed, irreversible step growth observed during *in situ* AFM and microfluidics measurements. Likewise, adsorbed phosphates may facilitate 2D island nucleation, while also acting as stoppers to hinder 2D island advancement in the [001] direction, which is consistent with the preferential binding of HMP and PA to acute steps on COM (100) surfaces.

ToF-SIMS data also revealed that the sample exposed to LTPP has slightly higher intensity than the control with increased sputtering time, indicating a small quantity of LTPP irreversibly accumulates on COM crystal surfaces. Regeneration of these crystals reveals a reversible process with growth occurring without appreciable delay (Figure C7). Time-resolved AFM images reveal that layered growth resumes through the propagation of macrosteps that form shortly after the replacement of LTPP-containing solution with fresh (modifier-free) growth solution (Figure C8). Pinned steps where residual LTPP is presumably adsorbed advance slowly and are quickly overtaken by much faster advancing macrosteps. These macrosteps have heights (Figure C9) nearly two orders of magnitude greater than the elementary step height of COM (100) layers.

The effects of residual HMP and PA were further investigated by evaluating macroscopic changes in crystal dimensions during regeneration. Time-resolved optical micrographs of COM crystals in a microfluidic channel (Figure 6.7, a and b) reveal no

observable change crystal size after exposure to HMP and over the course of 10 h regeneration. This is consistent with *in situ* AFM measurements showing that 2D island growth during regeneration is relatively slow. Continued imaging beyond 10 h revealed a sudden change in crystal size and morphology (Figure 6.7a) that corresponds to the emergence of crystalline protrusions. SEM images of the crystals retrieved during the regeneration process provides a closer look at these abnormal features. The protrusions resemble new crystals that nucleate on either basal surfaces or apical tips (Figure 6.7b) with apparent crystallographic registry. SEM images also capture protrusions overtaking (i.e., growing around and engulfing) areas of the crystal that were immobilized by HMP (Figure 6.7c). This is qualitatively consistent with our hypothesis that residual phosphates serve as possible nucleation sites that can enhance local supersaturation. The timescale required for these features to nucleate during regeneration is relatively long, but once formed there is no phosphate bound to their surfaces to hinder outward growth. Experiments with PA show similar trends as HMP during regeneration wherein COM crystals remain stunted for ca.10 h and regeneration leads to analogous protrusions (Movie C5).

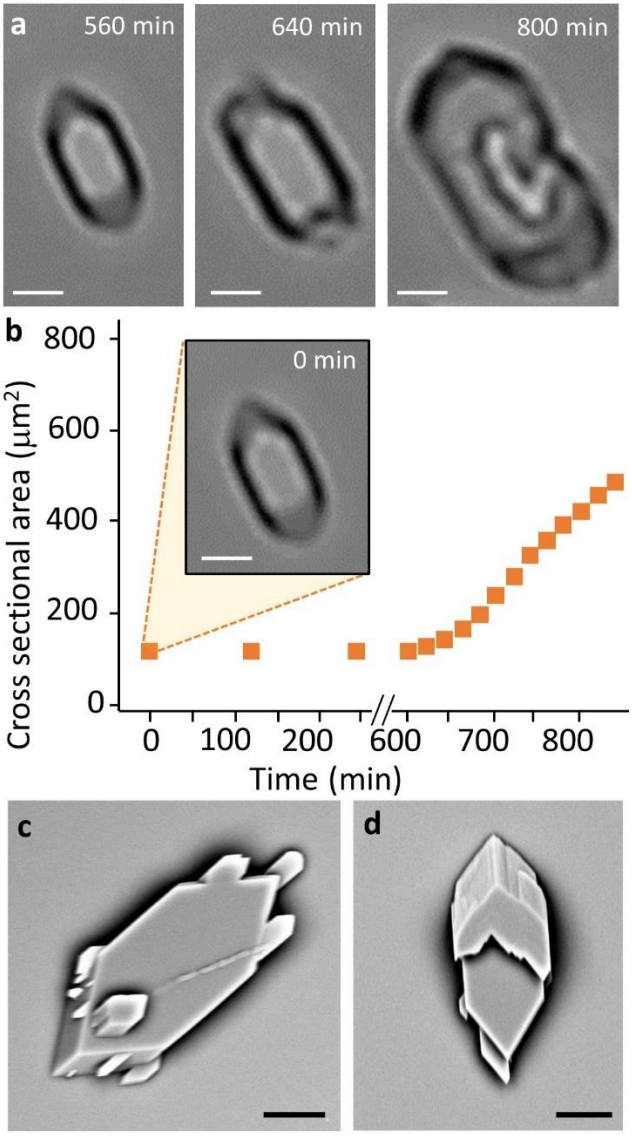

Figure 6.7. (a) COM crystal that was exposed to HMP, imaged during regeneration over a 13-h period. (**b**) Cross-sectional area of COM crystals during a period of growth following initial exposure to HMP. **(c and d)** SEM images regenerating crystals.

6.3. Summary

Polyphosphates are an interesting group of molecular modifiers that can be an effective nucleation and/or crystal growth inhibitor. We have identified that a cyclic polyphosphate, HMP, is an effective nucleation inhibitor, but is a weak to moderate crystal growth modifier. Conversely, the linear polyphosphate, LTPP, is effective at

inhibiting growth, but not nucleation. Secondly, modifiers that are effective nucleation inhibitors demonstrated high potency and efficacy in bulk crystallization assays compared to crystal growth inhibitors. The exact mechanism(s) in which polyphosphates operate in COM crystallization remains to be elucidated; however, our findings have opened a new area in biomineralization for exploring the effect of modifiers on nucleation, which to our knowledge is a subject that has received little attention and few examples exist.

6.4. Methods

6.4.1. Materials

Reagents for all experiments were obtained from Sigma Aldrich (St. Louis, MO) and used without further purification: calcium chloride dehydrate (ACS Reagent, 99+%), sodium oxalate ($Na_2C_2O_4$, >99%), sodium citrate dihydrate (>99%), sodium chloride (>99.5%), sodium triphosphate pentabasic (>98%, linear tripolyphosphate or LTPP), trisodium trimetaphosphate (>95%, cyclic trimetaphosphate or CTMP), and sodium hexametaphosphate (96%, hexametapshophate or HMP). Phytic acid dipotassium salt (98 %, phytate or **PA**) was purchased from Boc Sciences. All experiments were used deionized (DI) water (18.2 MΩ) purified by an Aqua Solutions RODI-C-12A system.

6.4.2. COM Crystallization

COM crystals were prepared using a previously reported protocol.[318] Stock solutions of calcium chloride and sodium oxalate were prepared at 10 mM concentration

by dissolving corresponding quantities of each reagent in deionized water. 1000 μg mL^{-1} of polyphosphate (LTPP, HMP, CTMP, and PA) solutions and 1.2 M sodium chloride stock solutions were prepared as well. Batch crystallization was performed in a 20-mL glass vial by making a 10 mL solution of composition 0.7 mM $CaCl_2$:0.7 mM $Na_2C_2O_4$: 150 mM NaCl: X μg mL^{-1} PolyP (pH = 6.1 ± 0.2). The pH of the growth solutions was measured with Orion 3-Star Plus benchtop meter equipped with a ROSS Ultra electrode (8102BNUWP). All samples were incubated for 1 hour at 60 °C prior to the drop wise addition of 10 mM $Na_2C_2O_4$, 1000 μg mL^{-1} polyphosphate, and appropriate amount of $NaOH_{(aq)}$ to adjust the pH to 6.1 ± 0.2. All solutions were placed in the incubator at 60 °C for three days. The final crystals were observed in the solution by optical microscopy using a Leica DMi8 instrument.

6.4.3. Scanning Electron Microscopy

SEM was performed using Phenom Pharos (Thermo Scientific). As-synthesized crystals were gently rinsed with DI water, and dried in air prior to analysis. SEM samples were prepared by attaching the glass slides to the SEM studs (Ted Pella) using carbon tape and were coated with a layer of gold (about 20 nm thick) to reduce the effects of electron beam charging.

6.4.4. Kinetic Studies of Crystallization

The kinetics of COM crystallization was measured *in situ* using a calcium ion-selective electrode (ISE) from Orion (model 9720BNWP). COM growth was analyzed at 23 ± 2 °C under constant stirring (1200 rpm) using solutions with a supersaturation

ratio S ~ 4.0 prepared with compositions 0.5 mM $CaCl_2$, 0.5 mM $Na_2C_2O_4$, 150 mM NaCl, and X mM modifier. Solutions were prepared using the same procedure outlined above, with modifiers added prior to the addition of $Na_2C_2O_4$ stock solution. The supersaturation ratio was calculated using the relationship IAP/K_{sp}, where IAP is the ion activity product ($aCa^{2+} \cdot aC_2O_4^{2-}$) and K_{sp} is the solubility product for COM reported in literature at 25 °C. [319]

6.4.5. Oblique illumination microscopy (OIM)

Brownian microscopy was employed to investigate the presence of precursors (clusters) in COM solutions. For these experiments, solutions were prepared according to the aforementioned procedure for COM crystallization with the calcium oxalate concentrations adjusted to achieve conditions ranging undersaturation to slightly supersaturated. OIM measurements were performed using a Nanosight LM10-HS device where calcium oxalate solutions with or without modifier were illuminated using a specifically designed laser beam. Scattered light was collected from a liquid cell of dimensions 120 x 80 x 5 μm^3 (length x width x height) containing the sample.

6.4.6. Microfluidics Growth.

A microfluidics device was used to examine COM growth at macroscopic length scale. The device (poly(dimethylsiloxane) (PDMS) on glass) used for these experiments followed the same set up and fabrication protocol as reported in previous work.[159] This system was monitored under continuous supply of growth solution using a semiautomatic inverted light microscope (Leica DMi8 equipped with PL Fluotar 5X, 10X, 20X, and N plan L 50X objectives). For in situ crystallization studies, the

microchannels were first flushed thoroughly with DI water. The conditions to prepare COM seed crystals were optimized to obtain at least 50 COM crystals well dispersed along the channel. First, a solution containing 0.85 mM Ca^{2+} was mixed through a y-connector with a second solution component containing 0.85 mM $C_2O_4^{2-}$ and 300 mM NaCl and delivered into the channels using a dual syringe pump (CHEMYX Fusion 200) for 100 min at a flow rate of 12 mL h^{-1}. Subsequently, these solutions were replaced by a slightly lower concentration solutions to reduce nucleation and grow the seed crystals to an appropriate size (approx. 20 – 30 μm in size) for observation. 0.8 mM Ca^{2+} and a second solution containing 0.8 mM $C_2O_4^{2-}$ and 300 mM NaCl was mixed in line and delivered into the channels for 800 min.

Time-resolved imaging of COM crystal growth and inhibition using an inverted optical microscope was performed to quantify the kinetics of COM crystallization. Two solution components were prepared in individual syringes: one solution contained 0.36 mM $CaCl_{2,(aq)}$ and the second solution contained 0.36 mM $Na_2C_2O_4$. The two solutions were mixed using an inline flow configuration that produced a final composition of 0.18 mM $CaCl_2$ and 0.18 mM $Na_2C_2O_4$. The fully mixed growth solution was introduced into seeded PDMS chips at a combined rate of 12 mL h^{-1} using a dual syringe pump. For inhibition studies, appropriate amount of inhibitor was added to the syringe containing $Na_2C_2O_4$.

6.4.7. Atomic Force Microscopy (AFM)

COM crystals were collected on AFM specimen disks (Ted Pella, Inc.) by placing the specimen disks in the synthesis vial prior to the addition of reagents used

for COM crystallization. After synthesis, the solution was cooled down and disks containing COM crystals were retrieved, rinsed thoroughly in DI water, and air-dried prior to AFM analysis. COM crystals were anchored with either the (100) or (010) surface oriented in the plane of imaging.

AFM measurements were performed using a Cypher ES instrument (Santa Barbara, CA) in contact mode (256 lines/scan) with scanning rates of 2 Hz and 11 - 25 Hz for *ex situ* and *in situ* studies, respectively. Topographical images were collected using Asylum TR800PSA cantilevers. Solutions used for *in situ* measurements of COM surface were the same as the solutions used for the microfluidics experiments. The growth solution was delivered to the liquid cell using an in-line mixing configuration, where the two solute solutions were combined immediately before being introduced into the cell (similar to the microfluidics configuration).

6.4.8. Time of Flight Secondary Ion Mass Spectrometry (ToF-SIMS)

Negative high mass resolution depth profiles were performed using a ToF-SIMS NCS instrument, which combines a TOF.SIMS5 instrument (ION-TOF GmbH, Münster, Germany) and an *in situ* scanning probe microscope (NanoScan, Switzerland) in the Shared Equipment Authority at Rice University. Samples were prepared by subjecting COM crystals to a sequence of treatments: (i) growth in a supersaturated solution without modifier for 2 h; (ii) growth in the same solution containing 1 μg mL^{-1} of modifiers for 1 h; and (iii) for all samples exposed to modifiers the last step involved regeneration for 2 h in a supersaturated solution without modifier. Samples were dried in air before analysis. A bunched 30 keV Bi^{3+} ion source (with a measured current of

0.2 pA) was used as primary probe for analysis (scanning area of 80 × 80 μm^2), and sputtering was performed using Ar1500+ ions at 1 keV with a typical current around 25 nA and a rastered area of 500 × 500 μm^2. The beams were operated in non-interlaced mode, alternating 4 analysis cycles and 0.5 s of a sputter cycle followed by a pause of 3 s for the charge compensation with an electron flood gun. An adjustment of the charge effects was operated using a surface potential. During depth profiling, the cycle time was fixed to 90 µs (corresponding to a mass-to-charge ratio of m/z = 0 – 737 a.m.u.). Ion intensities were normalized by point-to-point normalization using the total ion intensity for a standardization of data to be able to compare depth profiles. Data was binned using 15 points adjacent averaging for improving the signal-to-noise ratio.

CHAPTER 7

SUMMARY AND FUTURE STUDIES

7.1. Summary

Crystallization plays a critical role in the function of living organisms; however, it can be an undesirable process associated with pathological diseases. For this dissertation, we selected two types of pathological minerals, struvite and COM, with the goals to (1) understand struvite growth under flow conditions, (2) identify effective inhibitors of COM and struvite, and (3) elucidate the underlying mechanisms of crystal nucleation and growth inhibition.

The first step to achieve control over crystallization processes is to understand the underlying mechanism of crystallization to identify specific stages of crystal formation or specific sites on crystal surfaces that can be targeted to effectively modulate these processes. In Chapter 2, we established a new method for evaluating struvite crystal growth under flow based on microfluidics with more detailed insight provided by complementary *in situ* AFM. Through these synergistic approaches, we quantified anisotropic kinetics of crystal growth over a broad range of conditions and resolved the molecular mechanism of growth, which predominantly occur by classical pathways involving layer generation and advancement from either screw dislocations or 2-dimensional islands.

A ubiquitous approach to regulating crystal formation is the use of modifiers, which are (macro)molecules that interact with crystals or crystallization precursors to inhibit nucleation and/or growth. Understanding the fundamental mechanisms of crystallization inhibitors is relevant to a broad range of fields, including their frequent

use in crystal engineering and biomineralization. In Chapter 3, we examined the effects of phosphate-based molecules on struvite crystallization processes. We identified several phosphate-based molecules that exhibit an unparalleled dual mode of action capable of suppressing both nucleation and growth of crystals. Molecular level characterization of inhibitor-crystal interactions revealed a unique mechanism of crystal growth inhibition wherein surfaces become laden with an amorphous layer that leads to roughened interfaces and growth succession through dynamic sequences that are not commonly witnessed for other minerals. In Chapter 4, we performed a comprehensive evaluation of tEDTA against infection stone formation where we showed the tEDTA is effective against *P. mirabilis*, a particularly problematic pathogen in urinary tract infections, as well as struvite formation. Bulk crystallization studies revealed that, in contrast to the polyphosphates, tEDTA impedes struvite growth via chelation of Mg^{2+} in solution, at concentrations equal to or greater than Mg^{2+} in struvite growth solutions. Similarly, *in vitro* bladder model assays revealed tEDTA of equimolar concentration to that of the divalent cations in urine is required to prevent encrustation and blockage of catheters.

Among the COM growth inhibitors studied, hydroxycitrate (HCA) is of particular interest as a potential new therapy for calcium urolithiasis. In Chapter 5, we reviewed the crystal inhibition activity of HCA, current knowledge of HCA use in humans, and provided a list of issues that need to be addressed to define the role of HCA in treatment of kidney stones. The considerations listed in this chapter (e.g., dosage, enantiomeric compound, *in vivo* studies) are beneficial to the development of effective inhibitors with the potential to replace existing therapeutics (e.g., citrate) for kidney

stones. In Chapter 6, we tested the effects of phosphate-based modifiers on COM and showed that hexametaphosphate (HMP) and phytate (PA), which demonstrated a dual inhibitory role against struvite formation, has a similar effect on COM crystallization by fully suppressing both nucleation and growth. Moreover, we observed that both modifiers irreversibly stunt COM crystal growth within timescales that are relevant to pathological COM kidney stone formation. In this chapter, we compared phosphate-based modifiers against two reference compounds previously identified as highly effective COM inhibitors: carboxylate-based HCA and the urinary protein osteopontin. Our findings reveal that HMP and PA suppress COM crystallization at substantially lower concentrations than both references, thus highlighting the unique efficacy of these bio-inspired molecules.

Collectively, the discovery of potent inhibitors that operate by unparalleled dual modes of action capable of suppressing both nucleation and crystal growth has potential implications for their use in the prevention of pathological mineralization and development of therapeutics. Moreover, the fundamental mechanisms of inhibitors identified in this dissertation may prove to be relevant for other inorganic crystals given the ubiquitous use of inhibitors in processes spanning from biomineralization to crystal engineering.

7.2. Future Studies

7.2.1. Redetermination of Struvite Crystal Structure

In Chapter 2, we examined struvite growth under varying flow rates and solution supersaturation. An interesting behavior was observed wherein a significant fraction of

struvite seed crystals did not grow; and among the fraction of struvite crystals that grew it was observed that higher supersaturation led to noticeable defects. We posited that the incorporation of high amounts of defects imposed strain on the crystal to either suppress further growth or generate irregularities (e.g., fracturing or twinning). A similar hypothesis has been proposed for protein crystallization[320]; however, we are not aware of such effects being reported for inorganic crystals grown under flow (e.g., a recent study on barite, $BaSO_4$, showed no evidence of defect formation). [159] These preliminary observations of struvite suggest there are inherent features of the crystal structure that predispose it to the formation of growth defects, which prompted a structural analysis of struvite to search for signatures of disordered features. Several crystal structure determinations of struvite have previously been published based on X-ray and neutron diffraction data performed at room temperature (ca. 298 K) [111, 162-164] and most recently at 90 K.[1] The material was determined to consist of tetrahedral PO_4^{3-}, octahedral $Mg(H_2O)_6^{2+}$, and tetrahedral NH_4^+ groups held together by hydrogen bonds. To our knowledge, all prior reports have focused on periodic three-dimensional arrangements within this structure, but have failed to resolve the apparent disorder of several molecular species that under certain conditions could markedly impact crystal growth behavior.

7.2.1.1 Preliminary Data

The crystal structure of the struvite is determined using data collected at 293 K (the experimental method for this work is provided in the Appendix D). The common method for detecting any disorder in crystal structures is via examination of the

displacement parameters. Whilst large values of the displacement parameters in the crystal structure are a clear indication of disorder, in some cases, careful examination of the displacement parameters may be needed to rule out the possibility of subtle disorder. The material struvite crystallizes in space group Pmn2(1), with magnesium, phosphorous, nitrogen and few oxygens occupying mirror planes perpendicular to the *a* axis. Molecules situated on this mirror will have half of their atoms related by symmetry to the other half, with the displacement parameters constrained to be equal. If any atom constrained to lie on the mirror plane shows unusual displacement parameters in the direction perpendicular to the mirror, this would indicate that the atom may not actually be on the mirror, but is instead disordered in a position slightly off of the mirror. Similarly, if any atom not constrained to the mirror plane exhibits unusually large displacement, this may indicate that the atom does not correspond in position to its mirror and is disordered. All previous reports of the crystal structure of struvite clearly show such anomalies. In the 1970 report by Whitaker et al., the N atom has a very large B23 component compared to P and Mg, and a large B11 component as well. Water O(W1) has B11 about twice as large as all other O atoms, and O(W2) has very large B22 and B23 components of the atomic displacement parameters (ADP). Initial refinement of B(iso) (essentially IDP) for the various H atoms showed a quite unreasonable range of values, which forced the authors to hold these parameters at fixed theoretical values.[162] In the 1973 report by Ferraris et al., the N atom has B11 three times that of both P and Mg. Moreover, B11 of O(W1) and B23 and B33 of O(W2) are also very large, and B(iso) of several H atoms are markedly high.[163] In the 1984 report by Abbona et al., U(eq) for N is double that of both P and Mg, while O(W1) and O(W2)

have very large U(eq) values compared to other O atoms. Many of the H atoms also show large values.[111] In the 1986 neutron study by Ferraris et al., B(eq) of N is double that of both P and Mg, B(eq) for O(W1) and O(W2) are large, and some of the values for H atoms are much larger than the others, most notably for H(N2) and H(N3) within the ammonium molecule.[164] Finally, in the 2019 report by Prywer et al., very little true thermal motion of atoms in the crystal structure would be expected since all measurements were made at 90 K; however, the principal ADP axes (U11, U22, U33) for N are still almost double the corresponding values for P and Mg, U(iso) for H9 in the ammonium group is extremely large compared to all other H atoms, and U11 for O4 is almost three times that of the other oxygen atoms of water.[1] In all previous studies of struvite there is evidence of disorder in the ammonium group and two of the water molecules. In the earlier works, disorder was proposed and partially investigated; however, later reports conclusively ruled out such disorder. Additionally, previous studies did not propose any disorder model for the water molecules. Neutron diffraction is very sensitive to hydrogen parameters, yet the authors of the prior neutron study claimed that disorder of the ammonium group was not detected, contrary to their figures which show obvious disorder of the entire ion, including the N atom itself.[164]

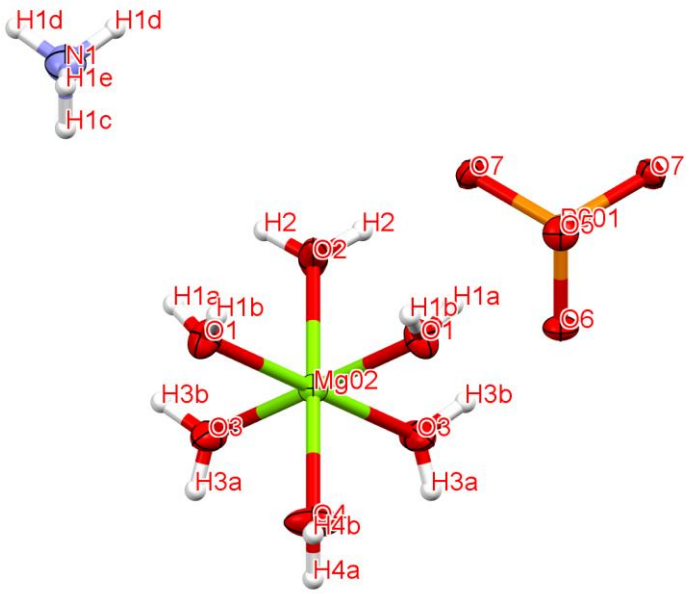

Figure 7.1. View of the molecules showing the atom numbering scheme. Thermal ellipsoids are 50% probability level, with hydrogen atoms as spheres. The disorder is not shown in the structure.

Our room temperature data collection shows result quite similar to all previous reports. The numbering scheme and the observable ADP is shown in Figure 7.1. The bond distances and bond angles observed in struvite are shown in Table D2 and Table D3, respectively. When an ordered model was employed, careful examination of the isotropic displacement parameters of the ammonium nitrogen indicates significantly larger values of isotropic thermal parameters of nitrogen when compared to phosphorus and the oxygens attached to phosphorous, indicating disorder in the nitrogen (Table 7.1). The protons attached to nitrogen also exhibited unusually larger displacement parameters compared to that of the hydrogens of water molecules. In our initial models of refinement, we explored the possibility that the nitrogen of ammonium group may not be restricted to the mirror plane, thereby refining the entire ammonium group freely without being restricted to the mirror plane. However, the refined coordinates of the

nitrogen always returned with values where the nitrogen was occupying a mirror plane. Since the partial hydrogen positions on the ammonium nitrogen could not be refined accurately, the disordered ammonium cation had to be restricted as an ideal tetrahedral rigid body with disordered nitrogen atoms. The final refined model of the ammonium group, with subtle disorder in the nitrogen along the mirror plane and their hydrogen bonding arrangement is shown in

Figure 7.2. H-bonding (dashed lines) between both ammonium cation to neighboring

phosphate and magnesium hexahydrate groups. Similar H-bonding

arrangement was observed in both disordered and non-disordered models.

. Two hydrogens of the ammonium cation are hydrogen bonded to the water molecules while one of the protons of the ammonium ion is hydrogen bonded to the phosphate oxygen.

Table 7.1. Fractional Atomic Coordinates ($\times 10^4$) and Equivalent Isotropic Displacement Parameters ($Å^2 \times 10^3$) for struvite.

Atom	***x***	***y***	***z***	**U(eq)**
P001	10000	5065.4(3)	6057.3(3)	13.06(4)
O7	8180.2(7)	3863.1(8)	6475.7(5)	19.69(9)
O6	10000	7379.6(11)	6592.0(7)	20.52(12)
O5	10000	5222.9(13)	4682.5(7)	20.71(13)
Mg02	5000	8766.5(6)	4776.2(3)	16.30(6)
O1	2818.0(9)	7631.9(11)	3675.3(5)	25.13(11)
O3	7106.3(10)	9850.0(10)	5910.8(7)	30.52(15)
O2	5000	5785.7(18)	5698.7(11)	39.2(3)
O4	5000	11828.1(16)	3917.4(8)	36.4(3)
N1	0	1344(2)	3388.8(11)	31.6(2)

In the crystal structure presented here, one of the hydrogens (H1e) of the ammonium cation is not involved in a conventional hydrogen bonding arrangement but participates in several weak H-bonding interactions. The average isotropic displacement parameter of the four hydrogen atoms is considerably larger than the values for some of the hydrogens of water molecules. Therefore, it is possible that the true disorder in this group is more complicated that what is accounted for in the current model.

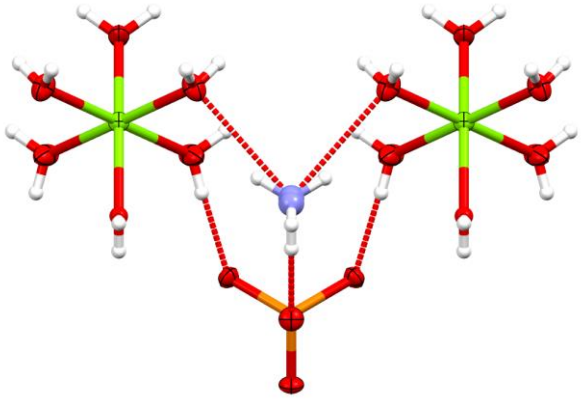

Figure 7.2. H-bonding (dashed lines) between both ammonium cation to neighboring phosphate and magnesium hexahydrate groups. Similar H-bonding arrangement was observed in both disordered and non-disordered models.

Two of the water oxygen atoms (O2 and O4) showed relatively large anisotropic displacement parameters compared to other two water molecules (O1 and O3) (Table 7.2). The U33 component of atom O2 was quite large, indicating disorder along the *c* direction. Additionally, the U11 component of atom O4 was also significantly larger, indicating disorder along the *a* direction perpendicular to the mirror plane along *a*.

Table 7.2. Anisotropic Displacement Parameters (Å2×103) for struvite.

Atom	U_{11}	U_{22}	U_{33}	U_{12}	U_{13}	U_{23}
P001	14.69(8)	11.80(7)	12.69(7)	-0	-0	0.31(6)
O7	17.16(18)	19.43(18)	22.5(2)	-3.35(15)	1.11(16)	3.63(17)
O6	25.7(3)	14.0(3)	21.8(3)	-0	-0	-3.1(2)
O5	25.9(3)	23.7(3)	12.5(3)	-0	-0	0.5(2)
Mg02	17.66(13)	16.30(13)	14.95(12)	-0	-0	-0.03(10)
O1	24.6(3)	32.9(3)	17.8(2)	-6.0(2)	-0.34(19)	-4.2(2)
O3	29.5(3)	20.6(2)	41.5(4)	2.5(2)	-17.3(3)	-8.3(2)
O2	17.0(3)	33.9(4)	66.7(8)	-0	-0	30.5(5)
O4	69.4(8)	18.9(4)	20.9(4)	-0	-0	4.7(3)
N1	33.9(5)	30.2(5)	30.6(5)	-0	-0	-5.5(4)

The disorder in atoms O2 and O4 were modelled by slitting each of the atomic positions separately into two separate positions and allowing the positional and occupancy factors to refine freely. Since both the O2 and O4 atoms occupy the mirror symmetry, the combined occupancy of the two atoms was restricted to 0.5. The final disordered model of the structure is shown in Figure 7.3.

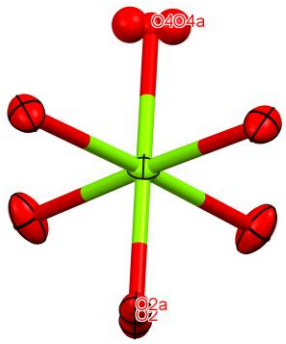

Figure 7.3. View of the most highly disordered model of water oxygen atoms O4 and O5.

7.2.1.2 Conclusion

This new investigation of struvite was initially undertaken in order to determine if some internal characteristics of the crystal structure might account for observed defects in crystal growth patterns. While previous reports on struvite have described it as an ordered arrangement of ionic species, the true crystal structure is now found to be quite disordered in a subtle manner not easily modeled. The possibility of disorder was proposed very early[162, 321] and clues are present in all subsequent published data, but later investigators either ignored or dismissed these indicators. By focusing on the relative values of the atomic displacement parameters rather than the absolute values, it has now been possible to determine with a high degree of certainty that the ammonium ion and some of the water molecules in struvite are in fact disordered. This new model shows significant improvements over the non-disordered model in displacement parameters and bonding geometries. These revelations demonstrate that the individual components of struvite do not actually comprise the ordered arrangement which has always been assumed, and it is possible that such structural variations could lead to dislocations during crystal growth which favor defects and twinning.

7.2.2 Polyprotic Acids as Demineralizing Agents for COM and Struvite

This dissertation demonstrates the effect of polyprotic acids (e.g., carboxylates, polyphosphates) as highly effective inhibitors of pathological crystallization for potential utilization as preventative treatments. An alternative remedy for these conditions may be dissolution. For uric acid and cystine stones, alkalization of urine is the most effective way to induce dissolution *in vivo*. In contrast, acidic irrigating agents

have been used to dissolve struvite crystals. For instance, “Renacidin”, a currently available commercial irrigating solution, is composed of citric acid, glucono delta-lactone, and magnesium carbonate. This is used within the lower urinary tract for the dissolution of bladder calculi of the struvite or apatite variety and operates by exchanging the magnesium in Renacidin for the calcium contained in the apatite formation and by utilizing the acidic pH to solubilize struvite crystals. COM is extremely resistant to dissolution therapies owing to its solubility, which is almost constant over the pH range of 3 to 8; thus, simple acidic or basic solutions are ineffective, and complete dissolution of calcium oxalate stones typically requires several hundred hours, which is infeasible; however, combined with other treatments that can break up the stone into little fragments (e.g., extracorporeal shock wave lithotripsy), dissolution therapy may be more amenable for COM.

Preliminary studies reveal that dissolution of COM crystals is enhanced in the presence of various polyprotic acids (Figure 7.4). The most notable effect is seen in the presence of HMP (Figure 7.4f), wherein the bulk of the crystals were dissolved within 48 hours compared to the crystals that are mostly intact after at an equivalent amount of exposure time to solutions containing no additive or those containing other additives (reported for tests using HCA, pyrophosphate (PP), cyclic trimetaphosphate (CTMP), and PA).

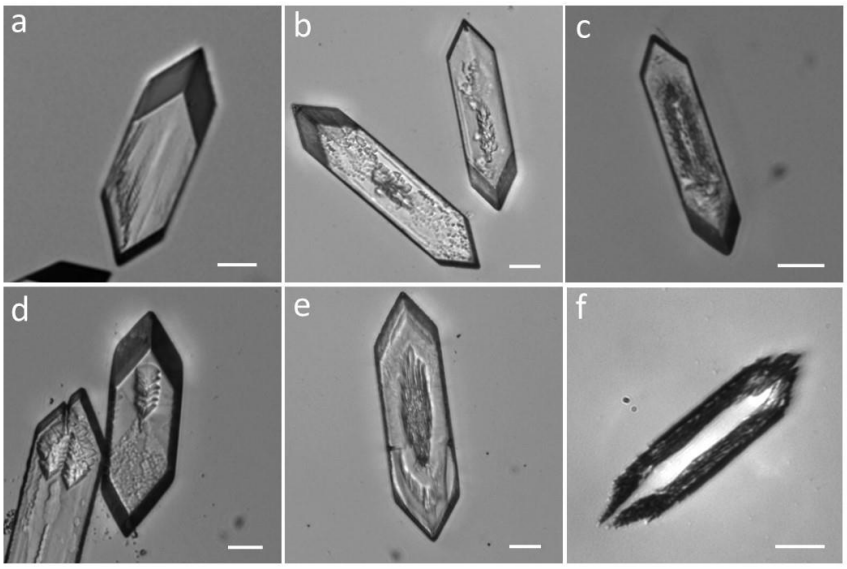

Figure 7.4. COM crystals dissolved for 48 hours in solutions adjusted to pH 6.1 in the absence (a) and the presence of 1000 μg mL^{-1} of CTMP (b), PP (c), HCA (d), PA (e), and HMP (f). Scale bars equal 25 μm.

In situ AFM measurements reveal distinct features and mechanisms that facilitate these dissolution processes. In the absence of additives, COM (100) surface dissolves through the formation of etch pits (Figure 7.5a) with morphologies seemingly consistent with a previous report.[105] These etch pits contain layers, which indicates dissolution occurs layer by layer with receding steps dissolving by a dissolution mechanism that appears to be governed by monomer detachment. In the presence of HMP, the COM (100) surface exhibits an altered etch pit habit (Figure 7.5b). The etch pits are equilateral triangular shapes and these eventually connect to form elongated faults. In the presence of PA, the mechanism of dissolution is completely altered (Figure 7.5c), leading to crystal surfaces completely covered by globular features. Time-resolved images show the disappearance of these individual particles at different timeframes (not shown), suggesting that the detachment of these nanoparticulate features may be facilitating the dissolution.

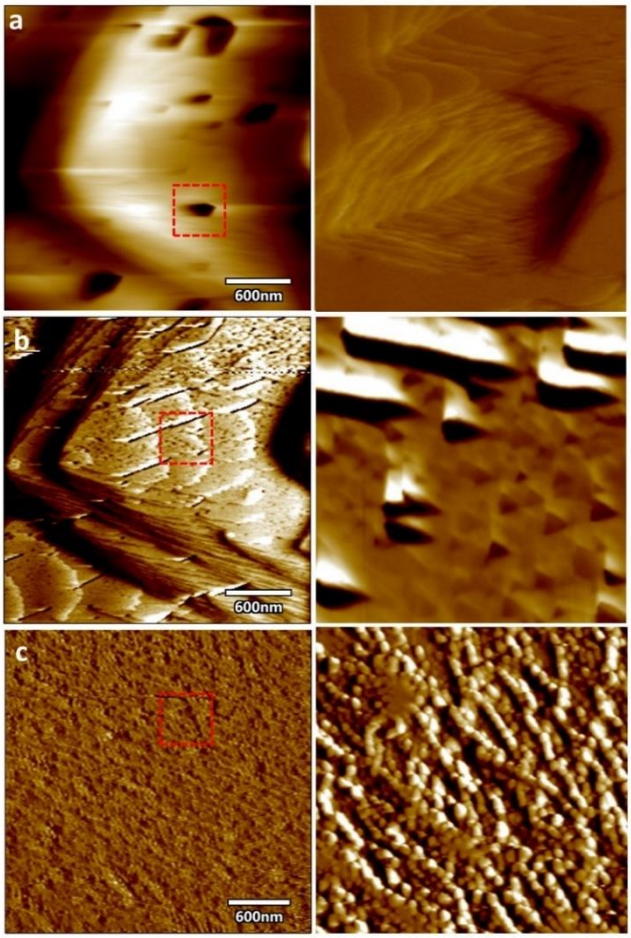

Figure 7.5. In situ AFM images of COM (100) surfaces dissolving in the absence (a) and the presence of 100 μg mL^{-1} HMP (pH 6.1) (b), and 1 μg mL^{-1} P45 (pH 7.0).

Future studies could be conducted to establish correlations between the molecular structure of acids and their efficacy as demineralizing agents. Moreover, their effects at varying solution conditions (e.g., pH, concentration, etc.) could be systematically evaluated. For instance, a prior study by Sosa et al.[322] showed that a combination of additives exhibited synergistic or antagonistic effects depending on the pH of the solution. Accordingly, experiments could be conducted using binary mixtures of additives to understand their cooperative action on crystal surface dissolution.

REFERENCES

1. Prywer, J.; Sieroń, L.; Czylkowska, A., Struvite grown in gel, its crystal structure at 90 K and thermoanalytical study. *Crystals* **2019,** *9* (2), 89.
2. Li, M.; Zhang, J.; Wang, L.; Wang, B.; Putnis, C. V., Mechanisms of Modulation of Calcium Phosphate Pathological Mineralization by Mobile and Immobile Small-Molecule Inhibitors. *J. Phys. Chem. B* **2018,** *122* (5), 1580-1587.
3. Myerson, A., *Handbook of industrial crystallization*. Butterworth-Heinemann: 2002.
4. Abu Bakar, M. R.; Nagy, Z. K.; Saleemi, A. N.; Rielly, C. D., The impact of direct nucleation control on crystal size distribution in pharmaceutical crystallization processes. *Cryst. Growth Des.* **2009,** *9* (3), 1378-1384.
5. Tung, H., Industrial perspectives of pharmaceutical crystallization. *Org. Process Res. Dev.* **2013,** *17* (3), 445-454.
6. Chen, J.; Sarma, B.; Evans, J. M.; Myerson, A. S., Pharmaceutical crystallization. *Cryst. Growth Des.* **2011,** *11* (4), 887-895.
7. Liu, G.; Jimmy, C. Y.; Lu, G. Q. M.; Cheng, H., Crystal facet engineering of semiconductor photocatalysts: motivations, advances and unique properties. *ChemComm* **2011,** *47* (24), 6763-6783.
8. Feinleib, J.; DeNeufville, J.; Moss, S. C.; Ovshinsky, S., Rapid reversible light-induced crystallization of amorphous semiconductors. *Appl. Phys. Lett.* **1971,** *18* (6), 254-257.
9. Rimer, J. D.; Kumar, M.; Li, R.; Lupulescu, A. I.; Oleksiak, M. D., Tailoring the physicochemical properties of zeolite catalysts. *Catal. Sci. Technol* **2014,** *4* (11), 3762-3771.
10. Kumar, M.; Choudhary, M. K.; Rimer, J. D., Transient modes of zeolite surface growth from 3D gel-like islands to 2D single layers. *Nat. Commun* **2018,** *9* (1), 2129.
11. Seegmiller, J. E.; Grayzel, A. I.; Laster, L.; Liddle, L., Uric acid production in gout. *J. Clin. Investig.* **1961,** *40* (7), 1304-1314.
12. Holan, K. R.; Holzbach, R. T.; Hermann, R. E.; Cooperman, A. M.; Claffey, W. J., Nucleation time: a key factor in the pathogenesis of cholesterol gallstone disease. *Gastroenterology* **1979,** *77*, 611–617.
13. Lamont, J. T.; Carey, M. C., Cholesterol gallstone formation. 2. Pathobiology and pathomechanics. *Prog. Liver Dis.* **1992,** *10*, 165–191.
14. Dorozhkin, S. V., Calcium orthophosphates: occurrence, properties, biomineralization, pathological calcification and biomimetic applications. *Biomatter* **2011,** *1* (2), 121-164.
15. Francis, S. E.; Sullivan, D. J., JR.; Goldberg, D. E., Hemoglobin metabolism in the malaria parasite Plasmodium falciparum. *Annu. Rev. Microbiol.* **1997,** *51*, 97-123.
16. Pagola, S.; Stephens, P. W.; Bohle, D. S.; Kosar, A. D.; Madsen, S. K., The structure of malaria pigment beta-haematin. *Nature* **200,** *404* (6775), 307-310.
17. Selvam, R.; Kalaiselvi, P., Oxalate binding proteins in calcium oxalate nephrolithiasis. . *Urol. Res.* **2003,** *31* (4), 242-256.

18. Asplin, J. R., Hyperoxaluric calcium nephrolithiasis. *Endocrinol. Metab. Clin. North Am.* **2002,** *31* (4), 927-949.
19. Scales Jr, C. D.; Smith, A. C.; Hanley, J. M.; Saigal, C. S.; Project, U. D. i. A., Prevalence of kidney stones in the United States. *Eur. Urol.* **2012,** *62* (1), 160-165.
20. Pearle, M. S.; Calhoun, E. A.; Curhan, G. C.; Project, U. D. o. A., Urologic diseases in America project: urolithiasis. *J. Urol.* **2005,** *173* (3), 848-857.
21. Sas, D. J., An update on the changing epidemiology and metabolic risk factors in pediatric kidney stone disease. *Clin. J. Am. Soc. Nephrol.* **2011,** *6* (8), 2062-2068.
22. Taylor, E. N.; Stampfer, M. J.; Curhan, G. C., Obesity, weight gain, and the risk of kidney stones. *JAMA* **2005,** *293* (4), 455-462.
23. Brikowski, T. H.; Lotan, Y.; Pearle, M. S., Climate-related increase in the prevalence of urolithiasis in the United States. *Proc. Natl. Acad. Sci. U.S.A* **2008,** *105* (28), 9841-9846.
24. Tasian, G. E.; Jemielita, T.; Goldfarb, D. S.; Copelovitch, L.; Gerber, J. S.; Wu, Q.; Denburg, M. R., Oral antibiotic exposure and kidney stone disease. *J. Am. Soc. Nephrol.* **2018,** *29* (6), 1731-1740.
25. Millan, A., Crystal Growth Shape of Whewellite Polymorphs: Influence of Structure Distortions on Crystal Shape. *Cryst. Growth Des.* **2001,** *1* (3), 245-254.
26. Sheng, X.; Ward, M. D.; Wesson, J. A., Crystal surface adhesion explains the pathological activity of calcium oxalate hydrates in kidney stone formation. *J. Am. Soc. Nephrol.* **2005,** *16* (7), 1904-1908.
27. Parks, J. H.; Worcester, E. M.; Coe, F. L.; Evan, A. P.; Lingeman, J. E., Clinical implications of abundant calcium phosphate in routinely analyzed kidney stones. *Kidney Int.* **2004,** *66* (2), 777-785.
28. Sakhaee, K., Epidemiology and clinical pathophysiology of uric acid kidney stones. *J. Nephrol.* **2014,** *27* (3), 241-245.
29. Griffith, D. P., Struvite stones. *Kidney Int.* **1978,** *13* (5), 372-382.
30. Warren, J. W., The catheter and urinary tract infection. *Med. Clin. N.* **1991,** *75* (2), 481-493.
31. Espinosa-Ortiz, E. J.; Eisner, B. H.; Lange, D.; Gerlach, R., Current insights into the mechanisms and management of infection stones. *Nat. Rev. Urol.* **2019,** *16* (1), 35-53.
32. Trautner, B. W., Management of catheter-associated urinary tract infection (CAUTI). *Curr. Opin. Infect. Dis.* **2010,** *23* (1), 76.
33. Nicar, M. J.; Hill, K.; Pak, C. Y., Inhibition by citrate of spontaneous precipitation of calcium oxalate in vitro. *J. Bone Miner. Res.* **1987,** *2* (3), 215-220.
34. Tiselius, H.; Berg, C.; Fornander, A.; Nilsson, M., Effects of citrate on the different phases of calcium oxalate crystallization. *Scanning Microsc.* **1993,** *7* (1), 381-9.
35. Tiselius, H.-G.; Fornander, A.-M.; Nilsson, M.-A., The effects of citrate and urine on calcium oxalate crystal aggregation. *Urol. Res.* **1993,** *21* (5), 363-366.
36. Hamm, L. L., Renal handling of citrate. *Kidney Int.* **1990,** *38* (4), 728-735.
37. Simpson, D. P., Citrate excretion: a window on renal metabolism. *Am. J. Physiol. Renal Physiol.* **1983,** *244* (3), F223-F234.

38. Brennan, S.; Hering-Smith, K.; Hamm, L., Effect of pH on citrate reabsorption in the proximal convoluted tubule. *Am. J. Physiol. Renal Physiol.* **1988,** *255* (2), F301-F306.
39. Rimer, J. D.; Sakhaee, K.; Maalouf, N. M., Citrate therapy for calcium phosphate stones. *Curr. Opin. Nephrol. Hypertens.* **2019,** *28* (2), 130-139.
40. Bichler, K. H.; Eipper, E.; Naber, K.; Braun, V.; Zimmermann, R.; Lahme, S., Urinary infection stones. *Int. J. Antimicrob. Agents* **2002,** *19* (6), 488-498.
41. Milo, S.; Thet, N. T.; Liu, D.; Nzakizwanayo, J.; Jones, B. V.; Jenkins, A. T. A., An in-situ infection detection sensor coating for urinary catheters. *Biosens. Bioelectron.* **2016,** *81*, 166-172.
42. Weinstein, R. A.; Darouiche, R. O., Device-associated infections: a macroproblem that starts with microadherence. *Clin. Infect. Dis.* **2001,** *33* (9), 1567-1572.
43. Wang, R.; Neoh, K. G.; Shi, Z.; Kang, E.; Tambyah, P. A.; Chiong, E., Inhibition of Escherichia coli and Proteus mirabilis adhesion and biofilm formation on medical grade silicone surface. *Biotechnol. Bioeng.* **2012,** *109* (2), 336-345.
44. Stickler, D. J.; Morgan, S. D., Modulation of crystalline Proteus mirabilis biofilm development on urinary catheters. *J. Med. Microbiol* **2006,** *55* (5), 489-494.
45. Andersen, R.; Loebel, N.; Hammond, D.; Wilson, M., Treatment of periodontal disease by photodisinfection compared to scaling and root planing. *J Clin Dent.* **2007,** *18* (2), 34.
46. Sadekuzzaman, M.; Yang, S.; Mizan, M.; Ha, S., Current and recent advanced strategies for combating biofilms. *Compr. Rev. Food Sci. Food Saf.* **2015,** *14* (4), 491-509.
47. Tambyah, P. A., Catheter-associated urinary tract infections: diagnosis and prophylaxis. *Int. J. Antimicrob. Agents* **2004,** *24*, 44-48.
48. Nicolle, L. E., Catheter associated urinary tract infections. *Antimicrob. Resist. Infect. Control* **2014,** *3* (1), 1-8.
49. Holling, N.; Lednor, D.; Tsang, S.; Bissell, A.; Campbell, L.; Nzakizwanayo, J.; Dedi, C.; Hawthorne, J.; Hanlon, G.; Ogilvie, L., Elucidating the genetic basis of crystalline biofilm formation in Proteus mirabilis. *Infect. Immun.* **2014,** *82* (4), 1616-1626.
50. Stickler, D., Clinical complications of urinary catheters caused by crystalline biofilms: something needs to be done. *J. Intern. Med.* **2014,** *276* (2), 120-129.
51. Broomfield, R. J.; Morgan, S. D.; Khan, A.; Stickler, D. J., Crystalline bacterial biofilm formation on urinary catheters by urease-producing urinary tract pathogens: a simple method of control. *J. Med. Microbiol* **2009,** *58* (10), 1367-1375.
52. Fisher, L. E.; Hook, A. L.; Ashraf, W.; Yousef, A.; Barrett, D. A.; Scurr, D. J.; Chen, X.; Smith, E. F.; Fay, M.; Parmenter, C. D., Biomaterial modification of urinary catheters with antimicrobials to give long-term broadspectrum antibiofilm activity. *J. Control Release* **2015,** *202*, 57-64.
53. Griffith, D. P.; Gleeson, M. J.; Lee, H.; Longuet, R.; Deman, E.; Earle, N., Randomized, Double-Blind Trial of Lithostat™(Acetohydroxamic Acid) in the Palliative Treatment of Infection-Induced Urinary Calculi. *Eur. Urol.* **1991,** *20*, 243-247.

54. Williams, J. J.; Rodman, J. S.; Peterson, C. M., A randomized double-blind study of acetohydroxamic acid in struvite nephrolithiasis. *N. Engl. J. Med.* **1984,** *311* (12), 760-764.
55. Chomarat, M., Resistance of bacteria in urinary tract infections. *Int. J. Antimicrob. Agents* **2000,** *16* (4), 483-487.
56. De Yoreo, J. J.; Vekilov, P. G., Principles of crystal nucleation and growth. *Rev. Mineral. Geochem.* **2003,** *54* (1), 57-93.
57. Reguera, D.; Rubí, J. M., Non-equilibrium thermodynamics for nucleation kinetics. In *Experimental Thermodynamics Volume X*, 2015; pp 314-337.
58. Olafson, K. N.; Li, R.; Alamani, B. G.; Rimer, J. D., Engineering Crystal Modifiers: Bridging Classical and Nonclassical Crystallization. *Chem. Mater.* **2016,** *28* (23), 8453-8465.
59. Vekilov, P. G., What Determines the Rate of Growth of Crystals from Solution? *Cryst. Growth Des.* **2007,** *7* (12), 2796-2810.
60. Vekilov, P. G.; Kuznetsov, Y. G.; Chernov, A. A., Interstep interaction in solution growth; (101) ADP face. *J. Cryst. Growth* **1992,** *121* (4), 643-655.
61. Olafson, K. N.; Ketchum, M. A.; Rimer, J. D.; Vekilov, P. G., Molecular Mechanisms of Hematin Crystallization from Organic Solvent. *Cryst. Growth Des.* **2015,** *15* (11), 5535-5542.
62. De Yoreo, J. J.; Gilbert, P. U. P. A.; Sommerdijk, N. A. J. M.; Penn, R. L.; Whitelam, S.; Joester, D.; Zhang, H.; Rimer, J. D.; Navrotsky, A.; Banfield, J. F.; Wallace, A. F.; Michel, F. M.; Meldrum, F. C.; Cölfen, H.; Dove, P. M., Crystallization by particle attachment in synthetic, biogenic, and geologic environments. *Science* **2015,** *349* (6247), aaa6760.
63. Kumar, M.; Li, R.; Rimer, J. D., Assembly and Evolution of Amorphous Precursors in Zeolite L Crystallization. *Chem. Mater.* **2016,** *28* (6), 1714-1727.
64. Rimer, J. D.; Vlachos, D. G.; Lobo, R. F., Evolution of Self-Assembled Silica−Tetrapropylammonium Nanoparticles at Elevated Temperatures. *J. Phys. Chem. B* **2005,** *109* (26), 12762-12771.
65. Choudhary, M. K.; Jain, R.; Rimer, J. D., In situ imaging of two-dimensional surface growth reveals the prevalence and role of defects in zeolite crystallization. *Proc. Natl. Acad. Sci. U.S.A* **2020,** *117* (46), 28632-28639.
66. Lupulescu, A. I.; Rimer, J. D., In Situ Imaging of Silicalite-1 Surface Growth Reveals the Mechanism of Crystallization. *Science* **2014,** *344* (6185), 729.
67. Henzler, K.; Fetisov, E. O.; Galib, M.; Baer, M. D.; Legg, B. A.; Borca, C.; Xto, J. M.; Pin, S.; Fulton, J. L.; Schenter, G. K., Supersaturated calcium carbonate solutions are classical. *Sci. Adv.* **2018,** *4* (1), eaao6283.
68. Sear, R. P., The non-classical nucleation of crystals: microscopic mechanisms and applications to molecular crystals, ice and calcium carbonate. *Int. Mater. Rev.* **2012,** *57* (6), 328-356.
69. Raiteri, P.; Gale, J. D., Water is the key to nonclassical nucleation of amorphous calcium carbonate. *J. Am. Chem. Soc.* **2010,** *132* (49), 17623-17634.
70. Safari, M. S.; Wang, Z.; Tailor, K.; Kolomeisky, A. B.; Conrad, J. C.; Vekilov, P. G., Anomalous Dense Liquid Condensates Host the Nucleation of Tumor Suppressor p53 Fibrils. *iScience* **2019,** *12*, 342-355.

71. Vekilov, P. G., Phase transitions of folded proteins. *Soft Matter* **2010,** *6* (21), 5254-5272.
72. Nielsen, M. H.; Aloni, S.; De Yoreo, J. J., In situ TEM imaging of CaCO3 nucleation reveals coexistence of direct and indirect pathways. *Science* **2014,** *345* (6201), 1158.
73. Ren, N.; Subotić, B.; Bronić, J.; Tang, Y.; Dutour Sikirić, M.; Mišić, T.; Svetličić, V.; Bosnar, S.; Antonić Jelić, T., Unusual Pathway of Crystallization of Zeolite ZSM-5 in a Heterogeneous System: Phenomenology and Starting Considerations. *Chem. Mater.* **2012,** *24* (10), 1726-1737.
74. Oleksiak, M. D.; Soltis, J. A.; Conato, M. T.; Penn, R. L.; Rimer, J. D., Nucleation of FAU and LTA Zeolites from Heterogeneous Aluminosilicate Precursors. *Chem. Mater.* **2016,** *28* (14), 4906-4916.
75. Yucelen, G. I.; Choudhury, R. P.; Vyalikh, A.; Scheler, U.; Beckham, H. W.; Nair, S., Formation of Single-Walled Aluminosilicate Nanotubes from Molecular Precursors and Curved Nanoscale Intermediates. *J. Am. Chem. Soc.* **2011,** *133* (14), 5397-5412.
76. Aerts, A.; Kirschhock, C. E. A.; Martens, J. A., Methods for in situ spectroscopic probing of the synthesis of a zeolite. *Chem. Soc. Rev.* **2010,** *39* (12), 4626-4642.
77. Rimer, J. D.; An, Z.; Zhu, Z.; Lee, M. H.; Wesson, J. A.; Goldfarb, D. S.; Ward, M. D., Crystal Growth Inhibitors for the Prevention of L-Cystine Kidney Stones Through Molecular Design. *Science* **2010,** *330* (337), 337-341.
78. Sizemore, J. P.; Doherty, M. F., A new model for the effect of molecular imposters on the shape of faceted molecular crystals. *Cryst. Growth Des.* **2009,** *9* (6), 2637-2645.
79. Chung, J.; Sosa, R.; Rimer, J. D., Elucidating the effects of polyprotic acid speciation in calcium oxalate crystallization. *Cryst. Growth Des.* **2017,** *17* (8), 4280-4288.
80. Farmanesh, S.; Alamani, B. G.; Rimer, J. D., Identifying alkali metal inhibitors of crystal growth: a selection criterion based on ion pair hydration energy. *Chem. Commun.* **2015,** *51*, 13964.
81. Weissbuch, I.; Addadi, L.; Lahav, M.; Leiserowitz, L., Molecular Recognition at Crystal Interfaces. *Science* **1991,** *253* (5020), 637-645.
82. Alamani, B. G.; Rimer, J. D., Molecular modifiers of kidney stones. *Curr. Opin. Nephrol. Hypertens.* **2017,** *26* (4), 256-265.
83. Ma, W.; Lutsko, J. F.; Rimer, J. D.; Vekilov, P. G., Antagonistic cooperativity between crystal growth modifiers. *Nature* **2020,** *577* (7791), 497-501.
84. Chung, J.; Granja, I.; Taylor, M. G.; Mpourmpakis, G.; Asplin, J. R.; Rimer, J. D., Molecular modifiers reveal a mechanism of pathological crystal growth inhibition. *Nature* **2016,** *536* (7617), 446-450.
85. Kim, D.; Rimer, J. D.; Asplin, J. R., Hydroxycitrate: a potential new therapy for calcium urolithiasis. *Urolithiasis* **2019,** *47* (4), 311-320.
86. Chung, J.; Taylor, M. G.; Granja, I.; Asplin, J. R.; Mpourmpakis, G.; Rimer, J. D., Factors differentiating the effectiveness of polyprotic acids as inhibitors of calcium

oxalate crystallization in kidney stone disease. *Cryst. Growth Des.* **2018,** *18* (9), 5617-5627.
87. Choudhary, M. K.; Kumar, M.; Rimer, J. D., Regulating Nonclassical Pathways of Silicalite-1 Crystallization through Controlled Evolution of Amorphous Precursors. *Angew. Chem. Int.* **2019,** *58* (44), 15712-15716.
88. Sheng, X.; Jung, T.; Wesson, J. A.; Ward, M. D., Adhesion at calcium oxalate crystal surfaces and the effect of urinary constituents. *Proc. Natl. Acad. Sci. U.S.A* **2005,** *102* (2), 267-272.
89. Ruiz-Agudo, E.; Burgos-Cara, A.; Ruiz-Agudo, C.; Ibañez-Velasco, A.; Cölfen, H.; Rodriguez-Navarro, C., A non-classical view on calcium oxalate precipitation and the role of citrate. *Nat. Commun.* **2017,** *8* (1), 1-10.
90. Li, S.; Tang, W.; Li, M.; Wang, L.; Yang, Y.; Gong, J., Understanding the role of citric acid on the crystallization pathways of calcium oxalate hydrates. *Cryst. Growth Des.* **2019,** *19* (6), 3139-3147.
91. Vekilov, P. G., Dense Liquid Precursor for the Nucleation of Ordered Solid Phases from Solution. *Cryst. Growth Des.* **2004,** *4* (4), 671-685.
92. Vekilov, P. G., Nucleation. *Cryst. Growth Des.* **2010,** *10* (12), 5007-5019.
93. Vekilov, P. G., The two-step mechanism of nucleation of crystals in solution. *Nanoscale* **2010,** *2* (11), 2346-2357.
94. Zhang, J.; Wang, L.; Zhang, W.; Putnis, C. V., Role of Hyperoxaluria/Hypercalciuria in Controlling the Hydrate Phase Selection of Pathological Calcium Oxalate Mineralization. *Cryst. Growth Des.* **2020**.
95. Banner, D. J.; Firlar, E.; Rehak, P.; Phakatkar, A. H.; Foroozan, T.; Osborn, J. K.; Sorokina, L. V.; Narayanan, S.; Tahseen, T.; Baggia, Y., In Situ Liquid-Cell TEM Observation of Multiphase Classical and Nonclassical Nucleation of Calcium Oxalate. *Adv. Funct. Mater.* **2021**, 2007736.
96. Ihli, J.; Wang, Y.-W.; Cantaert, B.; Kim, Y.-Y.; Green, D. C.; Bomans, P. H.; Sommerdijk, N. A.; Meldrum, F. C., Precipitation of amorphous calcium oxalate in aqueous solution. *Chem. Mater.* **2015,** *27* (11), 3999-4007.
97. Hajir, M.; Graf, R.; Tremel, W., Stable amorphous calcium oxalate: synthesis and potential intermediate in biomineralization. *Chem. Commun.* **2014,** *50* (49), 6534-6536.
98. Sakhaee, K.; Nicar, M.; Hill, K.; Pak, C. Y.; Sakhaee, K., Contrasting effects of potassium citrate and sodium citrate therapies on urinary chemistries and crystallization of stone-forming salts. *Kidney Int.* **1983,** *24* (3), 348-352.
99. Fleisch, H., Inhibitors and promoters of stone formation. *Kidney Int.* **1978,** *13* (5), 361-371.
100. Mo, L.; Huang, H.-Y.; Zhu, X.-H.; Shapiro, E.; Hasty, D. L.; Wu, X.-R., Tamm-Horsfall protein is a critical renal defense factor protecting against calcium oxalate crystal formation. *Kidney Int.* **2004,** *66* (3), 1159-1166.
101. Wesson, J. A.; Johnson, R. J.; Mazzali, M.; Beshensky, A. M.; Stietz, S.; Giachelli, C.; Liaw, L.; Alpers, C. E.; Couser, W. G.; Kleinman, J. G., Osteopontin is a critical inhibitor of calcium oxalate crystal formation and retention in renal tubules. *J. Am. Soc. Nephrol.* **2003,** *14* (1), 139-147.

102. Qiu, S. R.; Wierzbicki, A.; Orme, C. A.; Cody, A. M.; Hoyer, J. R.; Nancollas, G. H.; Zepeda, S.; De Yoreo, J. J., Molecular modulation of calcium oxalate crystallization by osteopontin and citrate. *Proc. Natl. Acad. Sci. U.S.A* **2004,** *101* (7), 1811-1815.
103. Hoyer, J. R.; Asplin, J. R.; Otvos Jr, L., Phosphorylated osteopontin peptides suppress crystallization by inhibiting the growth of calcium oxalate crystals. *Kidney Int.* **2001,** *60* (1), 77-82.
104. Nene, S. S.; Hunter, G. K.; Goldberg, H. A.; Hutter, J. L., Reversible inhibition of calcium oxalate monohydrate growth by an osteopontin phosphopeptide. *Langmuir* **2013,** *29* (21), 6287-6295.
105. Guo, S.; Ward, M. D.; Wesson, J. A., Direct visualization of calcium oxalate monohydrate crystallization and dissolution with atomic force microscopy and the role of polymeric additives. *Langmuir* **2002,** *18* (11), 4284-4291.
106. Meyer, J. L.; Thomas, W. C., Trace metal-citric acid complexes as inhibitors of calcification and crystal growth. II. Effects of iron(III), chromium(III) and aluminum(III) complexes on calcium oxalate crystal growth. *J. Urol.* **1982,** *128*, 1376.
107. Alamani, B. G.; Gale, J. D.; Rimer, J. D., Zinc Ions Modify Calcium Oxalate Growth by Distinct Transformation of Crystal Surface Termination. *Cryst. Growth Des.* **2021**.
108. Akın, B.; Öner, M.; Bayram, Y.; Demadis, K. D., Effects of carboxylate-modified,"green" inulin biopolymers on the crystal growth of calcium oxalate. *Cryst. Growth Des.* **2008,** *8* (6), 1997-2005.
109. Prywer, J.; Torzewska, A.; Płociński, T., Unique surface and internal structure of struvite crystals formed by Proteus mirabilis. *Urol. Res.* **2012,** *40* (6), 699-707.
110. Prywer, J.; Torzewska, A., Bacterially induced struvite growth from synthetic urine: experimental and theoretical characterization of crystal morphology. *Cryst. Growth Des.* **2009,** *9* (8), 3538-3543.
111. Abbona, F.; Calleri, M.; Ivaldi, G., Synthetic struvite, MgNH4PO4. 6H2O: correct polarity and surface features of some complementary forms. *Acta Crystallogr., Sect. B: Struct. Sci* **1984,** *40* (3), 223-227.
112. Hövelmann, J. r.; Putnis, C. V., In situ nanoscale imaging of struvite formation during the dissolution of natural brucite: implications for phosphorus recovery from wastewaters. *Environ. Sci. Technol.* **2016,** *50* (23), 13032-13041.
113. Abbona, F.; Boistelle, R., Growth morphology and crystal habit of struvite crystals (MgNH4PO4· 6 H2O). *J. Cryst. Growth* **1979,** *46* (3), 339-354.
114. Bazin, D.; André, G.; Weil, R.; Matzen, G.; Emmanuel, V.; Carpentier, X.; Daudon, M., Absence of bacterial imprints on struvite-containing kidney stones: a structural investigation at the mesoscopic and atomic scale. *Urology* **2012,** *79* (4), 786-790.
115. Prywer, J.; Torzewska, A., Biomineralization of struvite crystals by Proteus mirabilis from artificial urine and their mesoscopic structure. *Cryst. Res. Technol* **2010,** *45* (12), 1283-1289.
116. Zhao, T.-L.; Li, H.; Jiang, H.-F.; Yao, Q.-Z.; Huang, Y.; Zhou, G.-T., Morphogenesis and evolution mechanisms of bacterially-induced struvite. *Sci. Rep.* **2021,** *11* (1), 1-11.

117. Wierzbicki, A.; Sallis, J.; Stevens, E.; Smith, M.; Sikes, C., Crystal growth and molecular modeling studies of inhibition of struvite by phosphocitrate. *Calcif. Tissue Int.* **1997,** *61* (3), 216-222.
118. Prywer, J.; Mielniczek-Brzóska, E.; Olszynski, M., Struvite crystal growth inhibition by trisodium citrate and the formation of chemical complexes in growth solution. *J. Cryst. Growth* **2015,** *418*, 92-101.
119. Olszynski, M.; Prywer, J.; Mielniczek-Brzóska, E., Inhibition of struvite crystallization by tetrasodium pyrophosphate in artificial urine: chemical and physical aspects of nucleation and growth. *Cryst. Growth Des.* **2016,** *16* (6), 3519-3529.
120. Prywer, J.; Olszynski, M., Influence of disodium EDTA on the nucleation and growth of struvite and carbonate apatite. *J. Cryst. Growth* **2013,** *375*, 108-114.
121. Muryanto, S.; Sutanti, S.; Kasmiyatun, M. In *Inhibition of struvite crystal growth in the presence of herbal extract orthosiphon aristatus BL. MIQ*, MATEC web of conferences, EDP Sciences: 2016; p 01013.
122. Chauhan, C. K.; Joshi, M. J., In vitro crystallization, characterization and growth-inhibition study of urinary type struvite crystals. *J. Cryst. Growth* **2013,** *362*, 330-337.
123. Chauhan, C.; Joshi, M.; Vaidya, A., Growth inhibition of struvite crystals in the presence of herbal extract Commiphora wightii. *J. Mater. Sci. Mater. Med.* **2009,** *20* (1), 85.
124. Zeng, Y.; Cao, J.; Wang, Z.; Guo, J.; Zhou, Q.; Lu, J., Insights into the confined crystallization in microfluidics of amorphous calcium carbonate. *Cryst. Growth Des.* **2018,** *18* (11), 6538-6546.
125. Li, L.; Sanchez, J. R.; Kohler, F.; Røyne, A.; Dysthe, D. K., Microfluidic control of nucleation and growth of CaCO3. *Cryst. Growth Des.* **2018,** *18* (8), 4528-4535.
126. Giri, G.; Yang, L.; Mo, Y.; Jensen, K. F., Adding crystals to minimize clogging in continuous flow synthesis. *Cryst. Growth Des.* **2018,** *19* (1), 98-105.
127. Kelland, M. A.; Mady, M. F.; Lima-Eriksen, R., Kidney stone prevention: dynamic testing of edible calcium oxalate scale inhibitors. *Cryst. Growth Des.* **2018,** *18* (12), 7441-7450.
128. Hobbs, T.; Schultz, L. N.; Lauchnor, E. G.; Gerlach, R.; Lange, D., Evaluation of biofilm induced urinary infection stone formation in a novel laboratory model system. *J. Urol.* **2018,** *199* (1), 178-185.
129. Yilmazel, Y. D.; Demirer, G. N., Nitrogen and phosphorus recovery from anaerobic co-digestion residues of poultry manure and maize silage via struvite precipitation. *Waste Manag. Res.* **2013,** *31* (8), 792-804.
130. Lu, X.; Shih, K.; Li, X.-y.; Liu, G.; Zeng, E. Y.; Wang, F., Accuracy and application of quantitative X-ray diffraction on the precipitation of struvite product. *Water Res.* **2016,** *90*, 9-14.
131. Ueno, Y.; Fujii, M., Three years experience of operating and selling recovered struvite from full-scale plant. *Environ. Technol.* **2001,** *22* (11), 1373-1381.
132. Le Corre, K. S.; Valsami-Jones, E.; Hobbs, P.; Parsons, S. A., Phosphorus recovery from wastewater by struvite crystallization: A review. *Crit. Rev. Environ. Sci. Technol.* **2009,** *39* (6), 433-477.

133. Desmidt, E.; Ghyselbrecht, K.; Zhang, Y.; Pinoy, L.; Van der Bruggen, B.; Verstraete, W.; Rabaey, K.; Meesschaert, B., Global phosphorus scarcity and full-scale P-recovery techniques: a review. *Crit. Rev. Environ. Sci. Technol.* **2015,** *45* (4), 336-384.
134. Kataki, S.; West, H.; Clarke, M.; Baruah, D. C., Phosphorus recovery as struvite: Recent concerns for use of seed, alternative Mg source, nitrogen conservation and fertilizer potential. *Resour. Conserv. Recy.* **2016,** *107*, 142-156.
135. Kataki, S.; West, H.; Clarke, M.; Baruah, D. C. J. W. M., Phosphorus recovery as struvite from farm, municipal and industrial waste: Feedstock suitability, methods and pre-treatments. *Waste Manage.* **2016,** *49*, 437-454.
136. Yetilmezsoy, K.; Ilhan, F.; Kocak, E.; Akbin, H. M., Feasibility of struvite recovery process for fertilizer industry: A study of financial and economic analysis. *J. Clean. Prod.* **2017,** *152*, 88-102.
137. Doyle, J. D.; Parsons, S. A., Struvite formation, control and recovery. *Water Res.* **2002,** *36* (16), 3925-3940.
138. Huang, H.; Zhang, P.; Zhang, Z.; Liu, J.; Xiao, J.; Gao, F., Simultaneous removal of ammonia nitrogen and recovery of phosphate from swine wastewater by struvite electrochemical precipitation and recycling technology. *J. Clean. Prod.* **2016,** *127*, 302-310.
139. Kennedy, E. H.; Greene, M. T.; Saint, S., Estimating hospital costs of catheter-associated urinary tract infection. *J. Hosp. Med.* **2013,** *8* (9), 519-522.
140. McLean, R. J.; Nickel, J. C.; Cheng, K.-J.; Costerton, J. W.; Banwell, J. G., The ecology and pathogenicity of urease-producing bacteria in the urinary tract. *CRC Crit. Rev. Microbiol.* **1988,** *16* (1), 37-79.
141. Armbruster, C. E.; Mobley, H. L.; Pearson, M. M., Pathogenesis of Proteus mirabilis infection. *EcoSal Plus* **2018,** *8* (1).
142. Diri, A.; Diri, B., Management of staghorn renal stones. *Ren. Fail.* **2018,** *40* (1), 357-362.
143. Lam, H. S.; Lingeman, J. E.; Barron, M.; Newman, D. M.; Mosbaugh, P. G.; Steele, R. E.; Knapp, P. M.; Scott, J. W.; Nyhuis, A.; Woods, J. R., Staghorn calculi: analysis of treatment results between initial percutaneous nephrostolithotomy and extracorporeal shock wave lithotripsy monotherapy with reference to surface area. *J. Urol.* **1992,** *147* (5), 1219-1225.
144. Getliffe, K. A., The characteristics and management of patients with recurrent blockage of long-term urinary catheters. *J. Adv. Nurs.* **1994,** *20* (1), 140-149.
145. Wassil, S. K.; Crill, C. M.; Phelps, S. J., Antimicrobial impregnated catheters in the prevention of catheter-related bloodstream infection in hospitalized patients. *J. Pediatr. Pharmacol. Ther.* **2007,** *12* (2), 77-90.
146. Savage, V. J.; Chopra, I.; O'Neill, A. J., Staphylococcus aureus biofilms promote horizontal transfer of antibiotic resistance. *Antimicrob. Agents Chemother.* **2013,** *57* (4), 1968.
147. Omar, M.; Abdulwahab-Ahmed, A.; Chaparala, H.; Monga, M., Does stone removal help patients with recurrent urinary tract infections? *J. Urol.* **2015,** *194* (4), 997-1001.

148. Lorente, L., Antimicrobial-impregnated catheters for the prevention of catheter-related bloodstream infections. *World J. Crit. Care Med.* **2016,** *5* (2), 137.
149. Sadowski, R. R.; Prywer, J.; Torzewska, A., Morphology of struvite crystals as an evidence of bacteria mediated growth. *Cryst. Res. Technol.* **2014,** *49* (7), 478-489.
150. Le Corre, K. S.; Valsami-Jones, E.; Hobbs, P.; Parsons, S. A., Impact of calcium on struvite crystal size, shape and purity. *J. Cryst. Growth* **2005,** *283* (3-4), 514-522.
151. Li, H.; Yao, Q.-Z.; Wang, Y.-Y.; Li, Y.-L.; Zhou, G.-T., Biomimetic synthesis of struvite with biogenic morphology and implication for pathological biomineralization. *Sci. Rep.* **2015,** *5* (1), 1-8.
152. Olafson, K. N.; Ketchum, M. A.; Rimer, J. D.; Vekilov, P. G., Mechanisms of hematin crystallization and inhibition by the antimalarial drug chloroquine. *Proc. Natl. Acad. Sci. U.S.A* **2015,** *112* (16), 4946-4951.
153. De Yoreo, J. J.; Qiu, S. R.; Hoyer, J. R., Molecular modulation of calcium oxalate crystallization. *Am. J. Physiol. Renal Physiol.* **2006,** *291* (6), F1123-F1132.
154. Kim, D.; Rimer, J. D.; Asplin, J. R., Hydroxycitrate: a potential new therapy for calcium urolithiasis. *Urolithiasis* **2019**, 1-10.
155. Kofina, A.; Koutsoukos, P., Spontaneous precipitation of struvite from synthetic wastewater solutions. *Cryst. Growth Des.* **2005,** *5* (2), 489-496.
156. Li, L.; Du, W.; Ismagilov, R. F., Multiparameter screening on slipchip used for nanoliter protein crystallization combining free interface diffusion and microbatch methods. *J. Am. Chem. Soc.* **2010,** *132* (1), 112-119.
157. Perry, S. L.; Roberts, G. W.; Tice, J. D.; Gennis, R. B.; Kenis, P. J., Microfluidic generation of lipidic mesophases for membrane protein crystallization. *Cryst. Growth Des.* **2009,** *9* (6), 2566-2569.
158. Gerdts, C. J.; Tereshko, V.; Yadav, M. K.; Dementieva, I.; Collart, F.; Joachimiak, A.; Stevens, R. C.; Kuhn, P.; Kossiakoff, A.; Ismagilov, R. F., Time-controlled microfluidic seeding in nL-volume droplets to separate nucleation and growth stages of protein crystallization. *Angew. Chem. Int.* **2006,** *118* (48), 8336-8340.
159. Sosa, R. D.; Geng, X.; Reynolds, M. A.; Rimer, J. D.; Conrad, J. C., A microfluidic approach for probing hydrodynamic effects in barite scale formation. *Lab Chip* **2019,** *19* (9), 1534-1544.
160. Sultana, M.; Jensen, K. F. J. C. g.; design, Microfluidic continuous seeded crystallization: extraction of growth kinetics and impact of impurity on morphology. *Cryst. Growth Des.* **2012,** *12* (12), 6260-6266.
161. Weber, P. C., Cessation of growth and crystal disorder. In *Advances in protein chemistry*, Anfinsen, C. B.; Edsall, J. T.; Richards, F. M.; Eisenberg, D. S., Eds. Acadmic press, lnc: 1991; Vol. 41, pp 19-20.
162. Whitaker, A.; Jeffery, J., The crystal structure of struvite, MgNH4PO4. 6H2O. *Acta crystallogr., B Struct. crystallogr. cryst. chem.* **1970,** *26* (10), 1429-1440.
163. Ferraris, G.; Franchini-Angela, M., Hydrogen bonding in the crystalline state. Refinement of the crystal structure of MgNH4AsO4. 6H2O, arsenstruvite. *Acta crystallogr., B Struct. crystallogr. cryst. chem.* **1973,** *29* (4), 859-863.

164. Ferraris, G.; Fuess, H.; Joswig, W., Neutron diffraction study of MgNH4PO4. 6H2O (struvite) and survey of water molecules donating short hydrogen bonds. *Acta. Crystallogr. B. Struct. Sci.* **1986,** *42* (3), 253-258.
165. Gilmer, G.; Ghez, R.; Cabrera, N., An analysis of combined surface and volume diffusion processes in crystal growth. *J. Cryst. Growth* **1971,** *8* (1), 79-93.
166. Chernov, A. A., The Spiral Growth of Crystals. *Sov. Phys. Usp.* **1961,** *4*, 116.
167. Cortese, Y. J.; Wagner, V. E.; Tierney, M.; Devine, D.; Fogarty, A., Review of catheter-associated urinary tract infections and in vitro urinary tract models. *J. Healthc. Eng.* **2018,** *2018*.
168. Irwin, N. J.; Bryant, M. G.; McCoy, C. P.; Trotter, J. L.; Turner, J., Multifunctional, Low Friction, Antimicrobial Approach for Biomaterial Surface Enhancement. *ACS Appl. Bio Mater.* **2020,** *3* (3), 1385-1393.
169. Saint, S.; Chenoweth, C. E., Biofilms and catheter-associated urinary tract infections. *Infect Dis Clin North Am* **2003,** *17* (2), 411-432.
170. Lo, E.; Nicolle, L.; Classen, D.; Arias, K. M.; Podgorny, K.; Anderson, D. J.; Burstin, H.; Calfee, D. P.; Coffin, S. E.; Dubberke, E. R., Strategies to prevent catheter-associated urinary tract infections in acute care hospitals. *Infect. Control Hosp. Epidemiol.* **2008,** *29* (S1), S41-S50.
171. Jacobsen, S.; Stickler, D.; Mobley, H.; Shirtliff, M., Complicated catheter-associated urinary tract infections due to Escherichia coli and Proteus mirabilis. *Clin. Microbiol. Rev.* **2008,** *21* (1), 26-59.
172. Prywer, J.; Torzewska, A., Impact of bacteria on aggregation of crystalline and amorphous components of infectious urinary stones. *J. Cryst. Growth* **2019,** *506*, 71-78.
173. Prachayasittikul, V.; Isarankura-Na-Ayudhya, C.; Tantimongcolwat, T.; Nantasenamat, C.; Galla, H.-J., EDTA-induced membrane fluidization and destabilization: biophysical studies on artificial lipid membranes. *Acta Biochim Biophys Sin* **2007,** *39* (11), 901-913.
174. Finnegan, S.; Percival, S. L. J. A. i. w. c., EDTA: an antimicrobial and antibiofilm agent for use in wound care. *Adv Wound Care* **2015,** *4* (7), 415-421.
175. Lanigan, R.; Yamarik, T., Final report on the safety assessment of EDTA, calcium disodium EDTA, diammonium EDTA, dipotassium EDTA, disodium EDTA, TEA-EDTA, tetrasodium EDTA, tripotassium EDTA, trisodium EDTA, HEDTA, and trisodium HEDTA. *Int. J. Toxicol.* **2002,** *21*, 95-142.
176. Hamoud, R.; Zimmermann, S.; Reichling, J.; Wink, M., Synergistic interactions in two-drug and three-drug combinations (thymol, EDTA and vancomycin) against multi drug resistant bacteria including E. coli. *Phytomedicine* **2014,** *21* (4), 443-447.
177. Dos Santos, M. H. B.; Da Costa, A. F. E.; Da Silva Santos, G.; Dos Santos, A. L. S.; Nagao, P. E., Effect of chelating agents on the growth, surface polypeptide synthesis and interaction of Streptococcus agalactiae with human epithelial cells. *Mol. Med. Rep.* **2009,** *2* (1), 81-84.
178. Howell, K.; Yan, F.; Tokich, A.; Ng, K., Iron sequestration is not the main mechanism in the inhibition of Staphylococcus aureus growth by cranberry phytochemicals. *Integr Food Nutr Metab*

2015, *2* (3), 184-8.
179. Liu, F.; Hansra, S.; Crockford, G.; Köster, W.; Allan, B. J.; Blondeau, J. M.; Lainesse, C.; White, A. P., Tetrasodium EDTA is effective at eradicating biofilms formed by clinically relevant microorganisms from patients' central venous catheters. *Msphere* **2018,** *3* (6).
180. Prywer, J.; Olszynski, M.; Torzewska, A.; Mielniczek-Brzóska, E., Comparative in vitro studies on disodium EDTA effect with and without Proteus mirabilis on the crystallization of carbonate apatite and struvite. *J. Cryst. Growth* **2014,** *395*, 123-131.
181. Percival, S. L.; Sabbuba, N. A.; Kite, P.; Stickler, D. J., The effect of EDTA instillations on the rate of development of encrustation and biofilms in Foley catheters. *Urol. Res.* **2009,** *37* (4), 205-209.
182. Macleod, S. M.; Stickler, D. J., Species interactions in mixed-community crystalline biofilms on urinary catheters. *J. Med. Microbiol.* **2007,** *56* (11), 1549-1557.
183. Chan, W. Y.; Khazandi, M.; Hickey, E. E.; Page, S. W.; Trott, D. J.; Hill, P. B., In vitro antimicrobial activity of seven adjuvants against common pathogens associated with canine otitis externa. *Vet. Dermatol.* **2019,** *30* (2), 133-e38.
184. El-Sharif, A. A.; Hussain, M. H., Chitosan–EDTA new combination is a promising candidate for treatment of bacterial and fungal infections. *Curr. Microbiol.* **2011,** *62* (3), 739-745.
185. Khazandi, M.; Pi, H.; Chan, W. Y.; Ogunniyi, A. D.; Sim, J. X. F.; Venter, H.; Garg, S.; Page, S. W.; Hill, P. B.; McCluskey, A., In vitro antimicrobial activity of robenidine, ethylenediaminetetraacetic acid and polymyxin B nonapeptide against important human and veterinary pathogens. *Front. microbiol.* **2019,** *10*, 837.
186. Sim, J.; Khazandi, M.; Pi, H.; Venter, H.; Trott, D.; Deo, P., Antimicrobial effects of cinnamon essential oil and cinnamaldehyde combined with EDTA against canine otitis externa pathogens. *J. Appl. Microbiol.* **2019,** *127* (1), 99-108.
187. Ma, R.; Liu, Z.; Zhu, C., A comparative study of root smear layer removal using different pH EDTA salts. *Shanghai Kou Qiang Yi Xue* **2003,** *12* (3), 197-199.
188. Demidova, T. N.; Hamblin, M. R., Effect of cell-photosensitizer binding and cell density on microbial photoinactivation. *Antimicrob Agents Chemother* **2005,** *49* (6), 2329-2335.
189. Alves, E.; Faustino, M.; Neves, M.; Cunha, A.; Tome, J.; Almeida, A., An insight on bacterial cellular targets of photodynamic inactivation. *Future Med. Chem.* **2014,** *6* (2), 141-164.
190. Marvin, H.; Ter Beest, M.; Witholt, B., Release of outer membrane fragments from wild-type Escherichia coli and from several E. coli lipopolysaccharide mutants by EDTA and heat shock treatments. *J. Bacteriol. Res.* **1989,** *171* (10), 5262-5267.
191. Al-Bakri, A. G.; Othman, G.; Bustanji, Y., The assessment of the antibacterial and antifungal activities of aspirin, EDTA and aspirin–EDTA combination and their effectiveness as antibiofilm agents. *J. Appl. Microbiol.* **2009,** *107* (1), 280-286.
192. Root, J. L.; McIntyre, O.; Jacobs, N.; Daghlian, C., Inhibitory effect of disodium EDTA upon the growth of Staphylococcus epidermidis in vitro: relation to infection prophylaxis of Hickman catheters. *Antimicrob Agents Chemother* **1988,** *32* (11), 1627-1631.

193. Wu, J.-W.; Chen, X.-L., Extracellular metalloproteases from bacteria. *Appl. Microbiol. Biotechnol.* **2011,** *92* (2), 253-262.
194. Arias-Moliz, M. T.; Ferrer-Luque, C. M.; Espigares-Rodríguez, E.; Liébana-Ureña, J.; Espigares-García, M., Bactericidal activity of phosphoric acid, citric acid, and EDTA solutions against Enterococcus faecalis. *Oral Surg Oral Med Oral Pathol Oral Radiol Endod* **2008,** *106* (2), e84-e89.
195. Irwin, N.; McCoy, C.; Carson, L., Effect of pH on the in vitro susceptibility of planktonic and biofilm-grown P roteus mirabilis to the quinolone antimicrobials. *J. Appl. Microbiol.* **2013,** *115* (2), 382-389.
196. Kofina, A. N.; Demadis, K. D.; Koutsoukos, P. G., The effect of citrate and phosphocitrate on struvite spontaneous precipitation. *Cryst. Growth Des.* **2007,** *7* (12), 2705-2712.
197. Fattah, K.; Mavinic, D., Investigating techniques to determine magnesium addition requirements for the operation of a struvite crystallization process. *Int J Environ Sci Technol* **2015,** *12* (2), 473-478.
198. Muryanto, S.; Bayuseno, A., Influence of Cu2+ and Zn2+ as additives on crystallization kinetics and morphology of struvite. *Powder Technol.* **2014,** *253*, 602-607.
199. Doyle, J. D.; Oldring, K.; Churchley, J.; Price, C.; Parsons, S. A., Chemical control of struvite precipitation. *J. Environ. Eng.* **2003,** *129* (5), 419-426.
200. Kim, D.; Moore, J.; McCoy, C. P.; Irwin, N. J.; Rimer, J. D., Engaging a Battle on Two Fronts: Dual Role of Polyphosphates as Potent Inhibitors of Struvite Nucleation and Crystal Growth. *Chem. Mater.* **2020,** *32* (19), 8672-8682.
201. Kim, D.; Olympiou, C.; McCoy, C. P.; Irwin, N. J.; Rimer, J. D., Time-Resolved Dynamics of Struvite Crystallization: Insights from the Macroscopic to Molecular Scale. *Chem. Eur. J.* **2020,** *26* (16), 3555-3563.
202. Ilevbare, G. A.; Liu, H.; Edgar, K. J.; Taylor, L. S., Inhibition of solution crystal growth of ritonavir by cellulose polymers–factors influencing polymer effectiveness. *CrystEngComm* **2012,** *14* (20), 6503-6514.
203. Farmanesh, S.; Ramamoorthy, S.; Chung, J.; Asplin, J. R.; Karande, P.; Rimer, J. D., Specificity of Growth Inhibitors and their Cooperative Effects in Calcium Oxalate Monohydrate Crystallization. *J. Am. Chem. Soc.* **2014,** *136* (1), 367-376.
204. Burns, J.; McCoy, C. P.; Irwin, N. J., Weak organic acid synergy towards the prevention of catheter blockages. *J. Hosp. Infect.* **2021**.
205. Stickler, D.; Morgan, S., Observations on the development of the crystalline bacterial biofilms that encrust and block Foley catheters. *J. Hosp. Infect.* **2008,** *69* (4), 350-360.
206. Khan, S. R.; Pearle, M. S.; Robertson, W. G.; Gambaro, G.; Canales, B. K.; Doizi, S.; Traxer, O.; Tiselius, H.-G., Kidney stones. *Nat. Rev. Dis. Primers* **2016,** *2* (1), 1-23.
207. Nzakizwanayo, J.; Scavone, P.; Jamshidi, S.; Hawthorne, J. A.; Pelling, H.; Dedi, C.; Salvage, J. P.; Hind, C. K.; Guppy, F. M.; Barnes, L. M., Fluoxetine and thioridazine inhibit efflux and attenuate crystalline biofilm formation by Proteus mirabilis. *Sci. Rep* **2017,** *7* (1), 1-14.

208. Palka, M. A., Evidenced based review of recommendations addressing the frequency of changing long-term indwelling urinary catheters in older adults. *Geriatric Nursing* **2014,** *35* (5), 357-363.
209. Stickler, D. J.; Morris, N. S.; Winters, C. J. M. i. e., [35] Simple physical model to study formation and physiology of biofilms on urethral catheters. *Method. Enzymol.* **1999,** *310*, 494-501.
210. Nzakizwanayo, J.; Pelling, H.; Milo, S.; Jones, B. V., An In Vitro Bladder Model for Studying Catheter-Associated Urinary Tract Infection and Associated Analysis of Biofilms. In *Proteus mirabilis*, Springer: 2019; pp 139-158.
211. Lewis, Y.; Neelakantan, S., (−)-Hydroxycitric acid—the principal acid in the fruits of Garcinia cambogia desr. *Phytochemistry* **1965,** *4* (4), 619-625.
212. Watson, J. A.; Fang, M.; Lowenstein, J. M., Tricarballylate and hydroxycitrate: Substrate and inhibitor of ATP: Citrate oxaloacetate lyase. *Arch. Biochem. Biophys.* **1969,** *135*, 209-217.
213. Lowenstein JM, B. H. H. M. E.-. Hydroxycitrate. *Methods Enzymol.* **1981,** *72* (486), 97.
214. Louter-van de Haar, J.; Wielinga, P. Y.; Scheurink, A. J.; Nieuwenhuizen, A. G., Comparison of the effects of three different (-)-hydroxycitric acid preparations on food intake in rats. *Nutr. Metab.* **2005,** *2* (1), 1-9.
215. Chuah, L. O.; Ho, W. Y.; Beh, B. K.; Yeap, S. K., Updates on antiobesity effect of garcinia origin (−)-HCA. *Evid. Based Complementary Altern. Med.* **2013,** *2013*.
216. Fassina, P.; Adami, F. S.; Zani, V. T.; Machado, I. C. K.; Garavaglia, J.; Grave, M. T. Q.; Ramos, R.; Dal Bosco, S. M., The effect of Garcinia cambogia as coadjuvant in the weight loss process. *Nutr. Hosp.* **2015,** *32* (6), 2400-2408.
217. Sripradha, R.; Magadi, S. G., Efficacy of garcinia cambogia on body weight, inflammation and glucose tolerance in high fat fed male wistar rats. *J. Clin. Diagn. Res.* **2015,** *9* (2), BF01.
218. Heymsfield, S. B.; Allison, D. B.; Vasselli, J. R.; Pietrobelli, A.; Greenfield, D.; Nunez, C., Garcinia cambogia (hydroxycitric acid) as a potential antiobesity agent: a randomized controlled trial. *JAMA* **1998,** *280* (18), 1596-1600.
219. van Loon, L. J.; van Rooijen, J. J.; Niesen, B.; Verhagen, H.; Saris, W. H.; Wagenmakers, A. J., Effects of acute (−)-hydroxycitrate supplementation on substrate metabolism at rest and during exercise in humans. *Am. J. Clin. Nutr.* **2000,** *72* (6), 1445-1450.
220. Melnick, J. Z.; Srere, P. A.; Elshourbagy, N. A.; Moe, O. W.; Preisig, P. A.; Alpern, R. J., Adenosine triphosphate citrate lyase mediates hypocitraturia in rats. *J. Clin. Investig.* **1996,** *98* (10), 2381-2387.
221. Yu-chi, C. L.; Bergeron, N.; Rodriguez, N.; Schwarz, J.-M., Gas chromatography/mass spectrometry method to quantify blood hydroxycitrate concentration. *Anal. Biochem* **2001,** *292* (1), 148-154.
222. Soni, M.; Burdock, G.; Preuss, H.; Stohs, S.; Ohia, S.; Bagchi, D., Safety assessment of (−)-hydroxycitric acid and Super CitriMax®, a novel calcium/potassium salt. *Food Chem. Toxicol.* **2004,** *42* (9), 1513-1529.

223. Dara, L.; Hewett, J.; Lim, J. K., Hydroxycut hepatotoxicity: a case series and review of liver toxicity from herbal weight loss supplements. *World J. Gastroenterol.* **2008,** *14* (45), 6999.
224. Mozersky, D.; Klonz, K.; Katz, L., The Problem: Liver toxicity following consumption of dietary supplement, Hydroxycut. *Health Hazard Review Board Food and Drug Administration* **2009**.
225. Chuah, L. O.; Yeap, S. K.; Ho, W. Y.; Beh, B. K.; Alitheen, N. B., In vitro and in vivo toxicity of garcinia or hydroxycitric Acid: a review. *J. Evid. Based Complementary Altern. Med.* **2012,** *2012*.
226. Clouatre, D. L.; Preuss, H. G., Hydroxycitric acid does not promote inflammation or liver toxicity. *World J. Gastroenterol.* **2013,** *19* (44), 8160.
227. Lunsford, K. E.; Bodzin, A. S.; Reino, D. C.; Wang, H. L.; Busuttil, R. W., Dangerous dietary supplements: Garcinia cambogia-associated hepatic failure requiring transplantation. *World J Gastroenterol* **2016,** *22* (45), 10071.
228. Kothadia, J. P.; Kaminski, M.; Samant, H.; Olivera-Martinez, M., Hepatotoxicity Associated with Use of the Weight Loss Supplement Garcinia cambogia: A Case Report and Review of the Literature. *Case reports in hepatology* **2018,** *2018*.
229. Cody, A.; Cody, R., Calcium oxalate trihydrate phase control by structurally-specific carboxylic acids. *J. Cryst. Growth* **1994,** *135* (1-2), 235-245.
230. Qin, L.; Wang, L.; Wang, B., Role of alcoholic hydroxyls of dicarboxylic acids in regulating nanoscale dissolution kinetics of dicalcium phosphate dihydrate. *ACS Sustain. Chem. Eng.* **2017,** *5* (5), 3920-3928.
231. Chen, C.-L.; Qi, J.; Tao, J.; Zuckermann, R. N.; DeYoreo, J. J., Tuning calcite morphology and growth acceleration by a rational design of highly stable protein-mimetics. *Sci. Rep.* **2014,** *4* (1), 1-11.
232. Chung, J.; Taylor, M. G.; Granja, I.; Asplin, J. R.; Mpourmpakis, G.; Rimer, J. D., Factors Differentiating the Effectiveness of Polyprotic Acids as Inhibitors of Calcium Oxalate Crystallization in Kidney Stone Disease. *Crystal Growth & Design* **2018,** *18* (9), 5617-5627.
233. Politi, Y.; Arad, T.; Klein, E.; Weiner, S.; Addadi, L., Sea urchin spine calcite forms via a transient amorphous calcium carbonate phase. *Science* **2004,** *306* (5699), 1161-1164.
234. Gong, Y. U. T.; Killian, C. E.; Olson, I. C.; Appathurai, N. P.; Amasino, A. L.; Martin, M. C.; Holt, L. J.; Wilt, F. H.; Gilbert, P., Phase transitions in biogenic amorphous calcium carbonate. *Proc. Natl. Acad. Sci. U.S.A* **2012,** *109*, 6088.
235. De Yoreo, J. J.; Gilbert, P. U.; Sommerdijk, N. A.; Penn, R. L.; Whitelam, S.; Joester, D.; Zhang, H.; Rimer, J. D.; Navrotsky, A.; Banfield, J. F., Crystallization by particle attachment in synthetic, biogenic, and geologic environments. *Science* **2015,** *349* (6247), aaa6760.
236. Kellermeier, M.; Gebauer, D.; Melero-García, E.; Drechsler, M.; Talmon, Y.; Kienle, L.; Cölfen, H.; García-Ruiz, J. M.; Kunz, W., Colloidal stabilization of calcium carbonate prenucleation clusters with silica. *Adv. Funct. Mater.* **2012,** *22* (20), 4301-4311.

237. Finney, A. R.; Rodger, P. M., Probing the structure and stability of calcium carbonate pre-nucleation clusters. *Faraday Discuss.* **2012,** *159* (1), 47-60.
238. Sun, S.; Gebauer, D.; Cölfen, H., A solvothermal method for synthesizing monolayer protected amorphous calcium carbonate clusters. *Chem. Commun.* **2016,** *52* (43), 7036-7038.
239. Wiener, S. V.; Ho, S. P.; Stoller, M. L., Beginnings of nephrolithiasis: insights into the past, present and future of Randall's plaque formation research. *Curr. Opin. Nephrol. Hypertens.* **2018,** *27* (4), 236-242.
240. Evan, A. P.; Lingeman, J. E.; Coe, F. L.; Parks, J. H.; Bledsoe, S. B.; Shao, Y.; Sommer, A. J.; Paterson, R. F.; Kuo, R. L.; Grynpas, M., Randall's plaque of patients with nephrolithiasis begins in basement membranes of thin loops of Henle. *J. Clin. Investig.* **2003,** *111* (5), 607-616.
241. Hsi, R. S.; Ramaswamy, K.; Ho, S. P.; Stoller, M. L., The origins of urinary stone disease: upstream mineral formations initiate downstream Randall's plaque. *BJU Int.* **2017,** *119* (1), 177.
242. Marimuthu, A.; O'Meally, R. N.; Chaerkady, R.; Subbannayya, Y.; Nanjappa, V.; Kumar, P.; Kelkar, D. S.; Pinto, S. M.; Sharma, R.; Renuse, S., A comprehensive map of the human urinary proteome. *J. Proteome Res.* **2011,** *10* (6), 2734-2743.
243. Bouatra, S.; Aziat, F.; Mandal, R.; Guo, A. C.; Wilson, M. R.; Knox, C.; Bjorndahl, T. C.; Krishnamurthy, R.; Saleem, F.; Liu, P., The human urine metabolome. *PLoS ONE* **2013,** *8* (9), e73076.
244. Teng, H. H.; Dove, P. M.; Orme, C. A.; De Yoreo, J. J., Thermodynamics of calcite growth: baseline for understanding biomineral formation. *Science* **1998,** *282* (5389), 724-727.
245. Olafson, K. N.; Rimer, J. D.; Vekilov, P. G., Early onset of kinetic roughening due to a finite step width in hematin crystallization. *Phys. Rev. Lett.* **2017,** *119* (19), 198101.
246. Jena, B.; Jayaprakasha, G.; Singh, R.; Sakariah, K., Chemistry and biochemistry of (−)-hydroxycitric acid from Garcinia. *J. Agric. Food Chem.* **2002,** *50* (1), 10-22.
247. Bushinsky, D. A.; Grynpas, M. D.; Nilsson, E. L.; Nakagawa, Y.; Coe, F. L., Stone formation in genetic hypercalciuric rats. *Kidney Int.* **1995,** *48* (6), 1705-1713.
248. Bushinsky, D. A.; Asplin, J. R.; Grynpas, M. D.; Evan, A. P.; Parker, W. R.; Alexander, K. M.; Coe, F. L., Calcium oxalate stone formation in genetic hypercalciuric stone-forming rats. *Kidney Int.* **2002,** *61* (3), 975-987.
249. Lupulescu, A. I.; Rimer, J. D., Tailoring Silicalite-1 Crystal Morphology with Molecular Modifiers. *Angew. Chem. Int. Ed.* **2012,** *124* (14), 3401-3405.
250. Farmanesh, S.; Chung, J.; Sosa, R. D.; Kwak, J. H.; Karande, P.; Rimer, J. D., Natural Promoters of Calcium Oxalate Monohydrate Crystallization. *J. Am. Chem. Soc.* **2014,** *136* (36), 12648-12657.
251. Rimer, J. D.; An, Z.; Zhu, Z.; Lee, M. H.; Goldfarb, D. S.; Wesson, J. A.; Ward, M. D., Crystal Growth Inhibitors for the Prevention of l-Cystine Kidney Stones Through Molecular Design. *Science* **2010,** *330* (6002), 337-341.
252. Ma, W.; Balta, V. A.; West, R.; Newlin, K. N.; Miljanić, O. Š.; Sullivan, D. J.; Vekilov, P. G.; Rimer, J. D., A second mechanism employed by artemisinins to

suppress Plasmodium falciparum hinges on inhibition of hematin crystallization. *J. Biol. Chem.* **2021,** *296*, 100123.
253. Kumar, M.; Luo, H.; Román-Leshkov, Y.; Rimer, J. D., SSZ-13 Crystallization by Particle Attachment and Deterministic Pathways to Crystal Size Control. *J. Am. Chem. Soc.* **2015,** *137* (40), 13007-13017.
254. Zahn, D., Thermodynamics and Kinetics of Prenucleation Clusters, Classical and Non-Classical Nucleation. *Chemphyschem* **2015,** *16* (10), 2069-75.
255. Markov, I. V., *Crystal Growth for Beginners. Foundations of Nucleation, Crystal Growth and Epitaxy*. 2nd Edition ed.; World Scientific: Singapore, 2003.
256. De Yoreo, J. J.; Vekilov, P. G., Principles of crystal nucleation and growth. In *Biomineralization*, Dove, P. M.; DeYoreo, J. J.; Weiner, S., Eds. 2003; Vol. 54, pp 57-93.
257. Park, J.; da Silveira, K. C.; Sheng, Q.; Wood, C. D.; Seo, Y., Performance of poly (N-isopropylacrylamide)-based kinetic hydrate inhibitors for nucleation and growth of natural gas hydrates. *Energy Fuels* **2017,** *31* (3), 2697-2704.
258. Grases, F.; Rodriguez, A.; Costa-Bauza, A., Efficacy of mixtures of magnesium, citrate and phytate as calcium oxalate crystallization inhibitors in urine. *J. Urol.* **2015,** *194* (3), 812-819.
259. Thieme, K.; Rüssel, C., Nucleation inhibitors—the effect of small concentrations of Al2O3, La2O3 or TiO2 on nucleation and crystallization of lithium disilicate. *J. Eur. Ceram. Soc.* **2014,** *34* (15), 3969-3979.
260. Nudelman, F.; Pieterse, K.; George, A.; Bomans, P. H.; Friedrich, H.; Brylka, L. J.; Hilbers, P. A.; de With, G.; Sommerdijk, N. A., The role of collagen in bone apatite formation in the presence of hydroxyapatite nucleation inhibitors. *Nat. Mater.* **2010,** *9* (12), 1004-1009.
261. Münch, G.; Mayer, S.; Michaelis, J.; Hipkiss, A. R.; Riederer, P.; Müller, R.; Neumann, A.; Schinzel, R.; Cunningham, A. M., Influence of advanced glycation end-products and AGE-inhibitors on nucleation-dependent polymerization of β-amyloid peptide. *Biochim. Biophys. Acta. Mol. Basis Dis.* **1997,** *1360* (1), 17-29.
262. Worcester, E. M., Inhibitors of stone formation. *Semin. Nephrol.* **1996,** *16* (5), 474-486.
263. Wesson, J. A.; Worcester, E. M.; Kleinman, J. G., Role of anionic proteins in kidney stone formation: interaction between model anionic polypeptides and calcium oxalate crystals. *J. Urol.* **2000,** *163* (4), 1343-1348.
264. Hess, B.; Nakagawa, Y.; Parks, J. H.; Coe, F. L., Molecular abnormality of Tamm-Horsfall glycoprotein in calcium oxalate nephrolithiasis. *Am. J. Physiol. Renal Physiol.* **1991,** *260* (4), F569-F578.
265. Scurr, D.; Robertson, W., Modifiers of calcium oxalate crystallization found in urine. III. Studies on the role of Tamm-Horsfall mucoprotein and of ionic strength. *J. Urol.* **1986,** *136* (2), 505-507.
266. Mo, L.; Liaw, L.; Evan, A. P.; Sommer, A. J.; Lieske, J. C.; Wu, X.-R., Renal calcinosis and stone formation in mice lacking osteopontin, Tamm-Horsfall protein, or both. *Am. J. Physiol. Renal Physiol.* **2007,** *293* (6), F1935-F1943.

267. Millan, A.; Sohnel, O.; Grases, F., The influence of crystal morphology on the kinetics of growth of calcium oxalate monohydrate. *J. Cryst. Growth* **1997,** *179* (1-2), 231-239.
268. Asplin, J.; DeGanello, S.; Nakagawa, Y. N.; Coe, F. L., Evidence that nephrocalcin and urine inhibit nucleation of calcium oxalate monohydrate crystals. *Am. J. Physiol. Renal Physiol.* **1991,** *261* (5), F824-F830.
269. Grohe, B.; O'Young, J.; Ionescu, D. A.; Lajoie, G.; Rogers, K. A.; Karttunen, M.; Goldberg, H. A.; Hunter, G. K., Control of Calcium Oxalate Crystal Growth by Face-Specific Adsorption of an Osteopontin Phosphopeptide. *J. Am. Chem. Soc.* **2007,** *129* (48), 14946-14951.
270. Steitz, S. A.; Speer, M. Y.; McKee, M. D.; Liaw, L.; Almeida, M.; Yang, H.; Giachelli, C. M., Osteopontin inhibits mineral deposition and promotes regression of ectopic calcification. *Am. J. Pathol.* **2002,** *161* (6), 2035-2046.
271. Grohe, B.; Chan, B. P.; Sørensen, E. S.; Lajoie, G.; Goldberg, H. A.; Hunter, G. K., Cooperation of phosphates and carboxylates controls calcium oxalate crystallization in ultrafiltered urine. *Urol. Res.* **2011,** *39* (5), 327-338.
272. Aiello, D.; Cardiano, P.; Cigala, R. M.; Gans, P.; Giacobello, F.; Giuffre, O.; Napoli, A.; Sammartano, S., Sequestering ability of oligophosphate ligands toward Al3+ in aqueous solution. *J. Chem. Eng. Data* . **2017,** *62* (11), 3981-3990.
273. Bollyn, J.; Nijsen, M.; Baken, S.; Joye, I.; Waegeneers, N.; Cornelis, G.; Smolders, E., Polyphosphates and fulvates enhance environmental stability of PO4-bearing colloidal iron oxyhydroxides. *J. Agric. Food Chem.* **2016,** *64* (45), 8465-8473.
274. Grases, F.; Ramis, M.; Costa-Bauza, A., Effects of phytate and pyrophosphate on brushite and hydroxyapatite crystallization - Comparison with the action of other polyphosphates. *Urological Research* **2000,** *28* (2), 136-140.
275. Tarayre, C.; Nguyen, H. T.; Brognaux, A.; Delepierre, A.; De Clercq, L.; Charlier, R.; Michels, E.; Meers, E.; Delvigne, F., Characterisation of Phosphate Accumulating Organisms and Techniques for Polyphosphate Detection: A Review. *Sensors-Basel* **2016,** *16* (6).
276. Pinto, A.; Saad, F.; Leite, C.; Aquino, A.; Alves, M.; Pereira, D., Sodium tripolyphosphate and sodium hexametaphosphate in preventing dental calculus accumulation in dogs. *Arq. Bras. Med. Vet. Zoo.* **2008,** *60* (6), 1426-1431.
277. Stookey, G.; Warrick, J.; Miller, L., Effect of sodium hexametaphosphate on dental calculus formation in dogs. *Am. J. Vet. Res.* **1995,** *56* (7), 913-918.
278. Liu, J. Y.; Huang, W.; Pang, Y.; Yan, D. Y., Hyperbranched polyphosphates: synthesis, functionalization and biomedical applications. *Chemical Society Reviews* **2015,** *44* (12), 3942-3953.
279. Kore, A. R.; Yang, B.; Srinivasan, B.; Conrad, R., Chemical and Enzymatic Synthesis of Nucleoside Tetraphosphates. *Curr Org Chem* **2014,** *18* (12), 1621-1650.
280. Kornberg, A.; Rao, N. N.; Ault-Riche, D., Inorganic polyphosphate: A molecule of many functions. *Annu Rev Biochem* **1999,** *68*, 89-125.
281. Maechling, C.; Ball, V., Exothermic–Endothermic Transition in the Titration of Poly (allylamine chloride) with Sodium Hexametaphoshate Associated with a Change in the Proton Release Regime. *J. Phys. Chem. B* **2016,** *120* (20), 4732-4741.

282. Carracedo, G.; Crooke, A.; Guzman-Aranguez, A.; de Lara, M. J. P.; Martin-Gil, A.; Pintor, J., The role of dinucleoside polyphosphates on the ocular surface and other eye structures. *Prog. Retin. Eye Res.* **2016,** *55*, 182-205.
283. Best, M. D.; Zhang, H.; Prestwich, G. D., Inositol polyphosphates, diphosphoinositol polyphosphates and phosphatidylinositol polyphosphate lipids: structure, synthesis, and development of probes for studying biological activity. *Nat. Prod. Rep.* **2010,** *27* (10), 1403-1430.
284. Zhu, J.; Cheng, W. D.; Zhang, H.; Wu, D. S.; Zhao, D., Syntheses and structures of alkali metal rare earth polyphosphates CsLn(PO3)(4) (Ln = La, Ce). *Chinese J. Struc. Chem.* **2008,** *27* (4), 471-476.
285. Fueredi-Milhofer, H.; Sikirić, M.; Tunik, L.; Filipović-Vinceković, N.; Garti, N., Interactions of organic additives with ionic crystal hydrates: the importance of the hydrated layer. *Int. J. Mod. Phys. B* **2002,** *16* (01n02), 359-366.
286. Liu, J.; Huang, W.; Pang, Y.; Yan, D., Hyperbranched polyphosphates: synthesis, functionalization and biomedical applications. *Chem. Soc. Rev.* **2015,** *44* (12), 3942-3953.
287. Grases, F.; Ramis, M.; Costa-Bauza, A., Effects of phytate and pyrophosphate on brushite and hydroxyapatite crystallization. *Urol. Res.* **2000,** *28* (2), 136-140.
288. Sarig, S.; Raphael, M., Inhibiting Effect of Polyphosphates on Crystallization of Strontium Sulfate. *Journal of Crystal Growth* **1972,** *16* (3), 203-208.
289. Mijowska, S.; Polishchuk, I.; Lang, A.; Seknazi, E.; Dejoie, C.; Fermani, S.; Falini, G.; Demitri, N.; Polentarutti, M.; Katsman, A., High Amino Acid Lattice Loading at Nonambient Conditions Causes Changes in Structure and Expansion Coefficient of Calcite. *Chem. Mater.* **2020,** *32* (10), 4205-4212.
290. Williams Jr, J. C.; Zarse, C. A.; Jackson, M. E.; Witzmann, F. A.; McAteer, J. A., Variability of protein content in calcium oxalate monohydrate stones. *J. Endourol.* **2006,** *20* (8), 560-564.
291. Boyce, W. H.; Garvey, F. K., The amount and nature of the organic matrix in urinary calculi: a review. *J. Urol.* **1956,** *76* (3), 213-227.
292. Dyer, R.; Nordin, B., Urinary crystals and their relation to stone formation. *Nature* **1967,** *215* (5102), 751-752.
293. Elliot, J. S.; Rabinowitz, I. N., Calcium oxalate crystalluria: crystal size in urine. *J. Urol.* **1980,** *123* (3), 324-327.
294. Kok, D. J.; Blomen, L. J.; Westbroek, P.; Bijveot, O. L., Polysaccharide from coccoliths (CaCO3 biomineral) Influence on crystallization of calcium oxalate monohydrate. *Eur. J. Biochem.* **1986,** *158* (1), 167-172.
295. Chan, B. P.; Vincent, K.; Lajoie, G. A.; Goldberg, H. A.; Grohe, B.; Hunter, G. K., On the catalysis of calcium oxalate dihydrate formation by osteopontin peptides. *Colloids Surf. B.* **2012,** *96*, 22-28.
296. Liu, J.; Jiang, H.; Liu, X.-Y., How does bovine serum albumin prevent the formation of kidney stone? A kinetics study. *J. Phys. Chem. B* **2006,** *110* (18), 9085-9089.
297. Cerini, C.; Geider, S.; Dussol, B.; Hennequin, C.; Daudon, M.; Veesler, S.; Nitsche, S.; Boistelle, R.; Berthézène, P.; Dupuy, P., Nucleation of calcium oxalate

crystals by albumin: involvement in the prevention of stone formation. *Kidney Int.* **1999,** *55* (5), 1776-1786.
298. Zhang, C.-Y.; Wu, W.-H.; Wang, J.; Lan, M.-B., Antioxidant properties of polysaccharide from the brown seaweed Sargassum graminifolium (Turn.), and its effects on calcium oxalate crystallization. *Mar. Drugs* **2012,** *10* (1), 119-130.
299. Akyol, E.; Öner, M., Controlling of morphology and polymorph of calcium oxalate crystals by using polyelectrolytes. *J. Cryst. Growth* **2014,** *401*, 260-265.
300. Jung, T.; Kim, W.-S.; Choi, C. K., Crystal structure and morphology control of calcium oxalate using biopolymeric additives in crystallization. *J. Cryst. Growth* **2005,** *279* (1-2), 154-162.
301. Chen, Z.; Wang, C.; Zhou, H.; Sang, L.; Li, X., Modulation of calcium oxalate crystallization by commonly consumed green tea. *CrystEngComm*

2010, *12* (3), 845-852.
302. Abd-El-Khalek, D. E.; Abd-El-Nabey, B. A., Evaluation of sodium hexametaphosphate as scale and corrosion inhibitor in cooling water using electrochemical techniques. *Desalination* **2013,** *311*, 227-233.
303. Konietzny, U.; Greiner, R., PHYTIC ACID | Properties and Determination. In *Encyclopedia of Food Sciences and Nutrition (Second Edition)*, Caballero, B., Ed. Academic Press: Oxford, 2003; pp 4546-4555.
304. Zhu, T.; Wang, L.; Sun, W.; Yang, Z.; Wang, S.; Zhou, Y.; He, S.; Wang, Y.; Liu, G., Corrosion-Induced Performance Degradation of Phosphorus-Containing Scale Inhibitors at Carbon Steel–Water Interface. *Ind. Eng. Chem. Res.* **2018,** *57* (14), 5183-5189.
305. Brady, A. G.; Williams, L. E.; Haught, D.; Abee, C. R., Use of the feed additive sodium hexametaphosphate to prevent dental calculus in squirrel monkeys (Saimiri spp.). *J. Am. Assoc. Lab. Anim. Sci.* **2000,** *39* (2), 27-29.
306. Robinson, T. E.; Hughes, E. A.; Wiseman, O. J.; Stapley, S. A.; Cox, S. C.; Grover, L. M., Hexametaphosphate as a potential therapy for the dissolution and prevention of kidney stones. *J. Mater. Chem. B* **2020,** *8* (24), 5215-5224.
307. Grases, F.; Perelló, J.; Isern, B.; Costa-Bauzá, A., Myo-inositol hexakisphosphate (phytate) inhibits calcium carbonate crystallisation in hard water. *Water SA* **2007,** *33* (5).
308. Fakier, S.; Rodgers, A.; Jackson, G., Potential thermodynamic and kinetic roles of phytate as an inhibitor of kidney stone formation: theoretical modelling and crystallization experiments. *Urolithiasis* **2019,** *47* (6), 493-502.
309. Wang, F.; Devine, C. L.; Edwards, M. A., Effect of corrosion inhibitors on in situ leak repair by precipitation of calcium carbonate in potable water pipelines. *Environ. Sci. Technol.* **2017,** *51* (15), 8561-8568.
310. Trueman, B. F.; Krkošek, W. H.; Gagnon, G. A., Effects of ortho-and polyphosphates on lead speciation in drinking water. *Environ. Sci. Water Res. Technol.* **2018,** *4* (4), 505-512.
311. Jung, T.; Sheng, X. X.; Choi, C. K.; Kim, W. S.; Wesson, J. A.; Ward, M. D., Probing crystallization of calcium oxalate monohydrate and the role of macromolecule additives with in situ atomic force microscopy. *Langmuir* **2004,** *20* (20), 8587-8596.

312. Qiu, S. R.; Wierzbicki, A.; Salter, E. A.; Zepeda, S.; Orme, C. A.; Hoyer, J. R.; Nancollas, G. H.; Cody, A. M.; De Yoreo, J. J., Modulation of calcium oxalate monohydrate crystallization by citrate through selective binding to atomic steps. *J. Am. Chem. Soc.* **2005,** *127* (25), 9036-9044.
313. Cho, K. R.; Salter, E. A.; De Yoreo, J. J.; Wierzbicki, A.; Elhadj, S.; Huang, Y.; Qiu, S. R., Growth inhibition of calcium oxalate monohydrate crystal by linear aspartic acid enantiomers investigated by in situ atomic force microscopy. *CrystEngComm*

2013, *15* (1), 54-64.
314. Chi, J.; Zhang, W.; Putnis, C. V.; Wang, L., Face-Specific Occlusion of Lipid Vesicles within Calcium Oxalate Monohydrate. *Cryst. Growth Des.* **2021,** *21* (4), 2398-2404.
315. Wang, L.; Ruiz-Agudo, E.; Putnis, C. V.; Putnis, A., Direct observations of the modification of calcite growth morphology by Li+ through selectively stabilizing an energetically unfavourable face. *CrystEngComm*

2011, *13* (12), 3962-3966.
316. Land, T. A.; Martin, T. L.; Potapenko, S.; Palmore, G. T.; De Yoreo, J. J., Recovery of surfaces from impurity poisoning during crystal growth. *Nature* **1999,** *399* (6735), 442-445.
317. Ristic, R. I.; DeYoreo, J. J.; Chew, C. M., Does Impurity-Induced Step-Bunching Invalidate Key Assumptions of the Cabrera− Vermilyea Model? *Cryst. Growth Des.* **2008,** *8* (4), 1119-1122.
318. Farmanesh, S.; Chung, J.; Chandra, D.; Sosa, R. D.; Karande, P.; Rimer, J. D., High-throughput platform for design and screening of peptides as inhibitors of calcium oxalate monohydrate crystallization. *J. Cryst. Growth* **2013,** *373*, 13-19.
319. Tomazic, B.; Nancollas, G., A study of the phase transformation of calcium oxalate trihydrate-monohydrate. *Invest. Urol.* **1979,** *16* (5), 329-335.
320. Weber, P. C., Cessation of growth and crystal disorder. In *Advances in protein chemistry, C*, Anfinsen, D. B.; Edsall, J. T.; Richards, F. M.; Eisenber, D. S., Eds. Academic press, lnc: 1991; Vol. 41, p 19.
321. Whitaker, A. t.; Jeffery, J., X-ray evidence for a single-bonded rotating ammonium ion in struvite. *Acta Crystallogr., Sect. B: Struct. Sci., Cryst. Eng. Mater.* **1970,** *26* (10), 1440-1444.
322. Sosa, R. D.; Geng, X.; Agarwal, A.; Palmer, J. C.; Conrad, J. C.; Reynolds, M. A.; Rimer, J. D., Acidic Polysaccharides as Green Alternatives for Barite Scale Dissolution. *ACS Appl. Mater. Interfaces* **2020,** *12* (49), 55434-55443.

APPENDICES

APPENDIX A

CHAPTER 2 SUPPLEMENTARY INFORMATION

Note A1. Calculation of Relative Supersaturation

Corresponding relative supersaturation values, σ, for growth solutions of varying ionic strengths, species concentrations and pH were calculated using the speciation program PhreeqC, using the experimentally determined thermodynamic solubility product of struvite at 25°C with 150 mM NaCl ionic strength, $K_{sp} = 5.49$ x 10^{-14} (Parkhurst and Appelo, 1999; Bouropoulos and Koutsoukos, 2000; Wang and Song, 2006). PhreeqC has an in-built calculator for solubility products of various relevant phases and additional equilibrium constants used for the equilibrium study.

Table A1. Additional equilibrium constants used for PhreeqC simulation

Solution Species	Log K_{sp}
$Mg^{2+} + PO_4^{3-} \Leftrightarrow MgPO_4^-$	4.8
$Mg^{2+} + HPO_4^{2-} \Leftrightarrow MgHPO_4$	2.8
$Mg^{2+} + H_2PO_4^- \Leftrightarrow MgH_2PO_4^+$	0.45
$Mg^{2+} + NH_3 \Leftrightarrow MgNH_3^{2+}$	0.24
$Mg^{2+} + 2NH_3 \Leftrightarrow Mg(NH_3)_2^{2+}$	0.2
$Mg^{2+} + 3NH_3 \Leftrightarrow Mg(NH_3)_3^{2+}$	-0.3
$Mg^{2+} + OH^- \Leftrightarrow MgOH^+$	2.6
Phases	**Log K_{sp}**
$MgNH_4PO_4{:}6H_2O \Leftrightarrow 6H_2O + Mg^{2+} + NH_4^+ + PO_4^{3-}$	-13.26
$Mg_3(PO_4)_2{:}8H_2O \Leftrightarrow 8H_2O + 3Mg^{2+} + 2PO_4^{3-}$	-25.2
$Mg_3(PO_4)_2{:}22H_2O \Leftrightarrow 22H_2O + 3Mg^{2+} + 2PO_4^{3-}$	-23.1
$Mg(OH)_2{:}6H_2O \Leftrightarrow 6H_2O + Mg^{2+} + 2OH^-$	-10.9
$MgHPO_4{:}3H_2O \Leftrightarrow 3H_2O + HPO_4^{2-} + Mg^{2+}$	-5.8

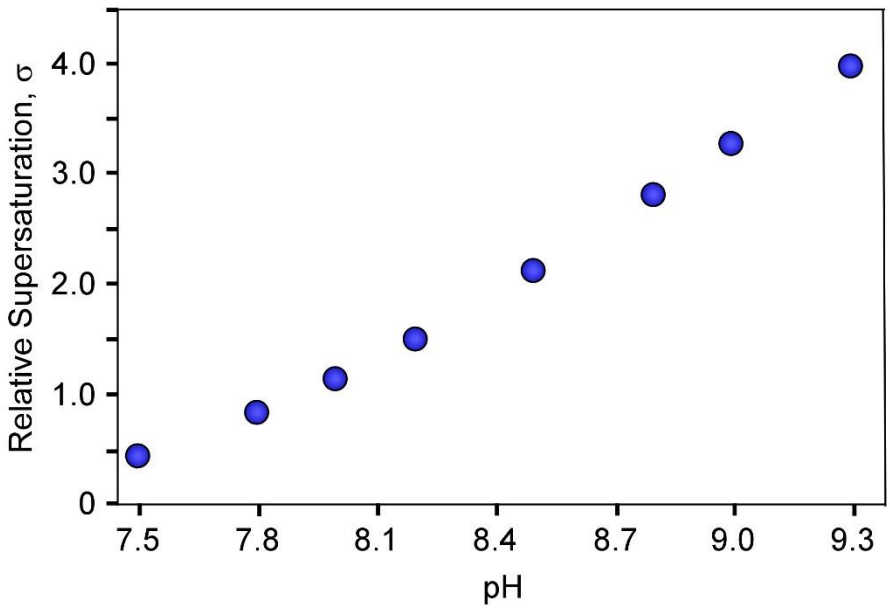

Figure A1. Relative supersaturation (σ) of the 7 mM $MgCl_2 \cdot 6H_2O$:7 mM $NH_4H_2PO_4$:150 mM NaCl synthesis solutions at pH values ranging from pH 7.5 to pH 9.3.

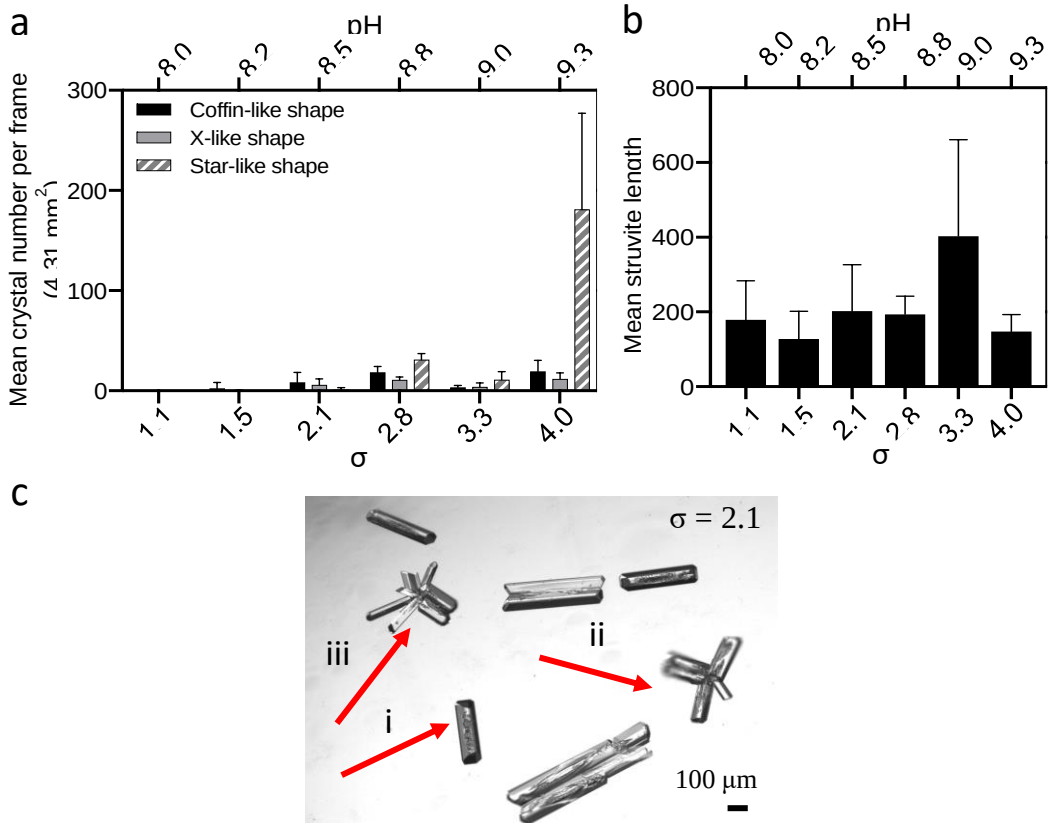

Figure A2. (a) Mean crystal number per frame at different σ values rangingfrom 1.1 –4.0. (b) Mean length of coffin-like struvite crystals at (101) direction at different σ values ranging from 1.1 – 4.0. (c) Optical microscopy images of the crystals.

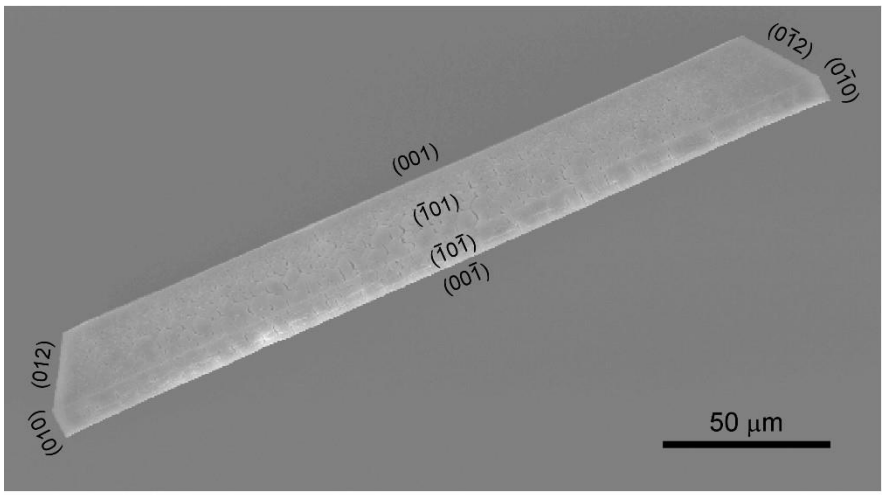

Figure A3. Scanning electron micrograph (SEM) of struvite crystal reveal $(001), (00\bar{1}), (012), (0\bar{1}2), (101)$, and $(\bar{1}01)$ faces

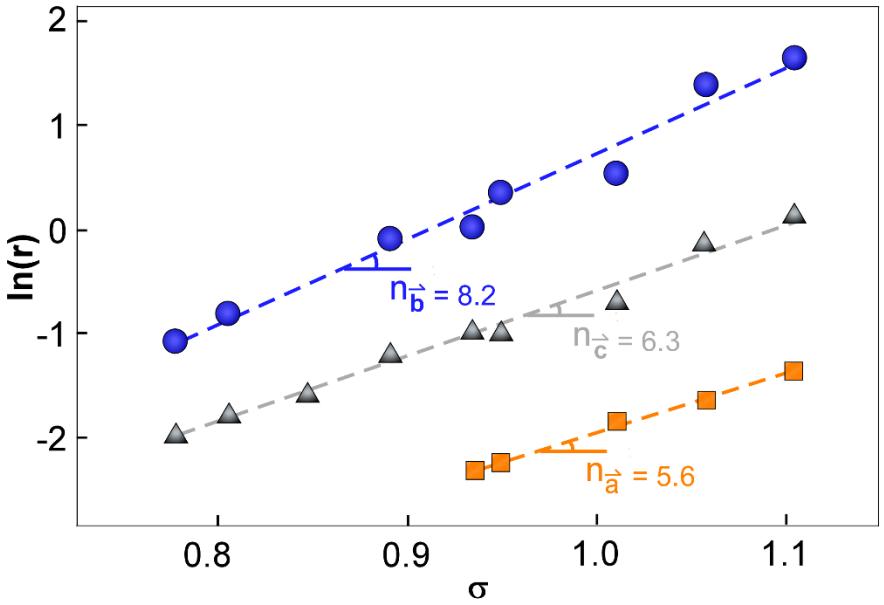

Figure A4. Linearized plot of growth rate (r) data plotted as ln r versus σ reveals an exponential dependence indicating growth governed by 2D nucleation at this supersaturation range (ca. σ >0.8).

APPENDIX B

CHAPTER 3 SUPPLEMENTARY INFORMATION

Note B1. Calculation of Extent of Reaction

In the crystallization of struvite, the reaction involves the deprotonation of HPO_4^{2-} via the following equation

$$Mg^{2+} + NH_4^+ + HPO_4^{2-} + 6H_2O \leftrightarrow MgNH_4PO_4 \cdot 6H_2O + H^+. \quad \text{(B1)}$$

Struvite crystallization proceeds with release of a proton, triggering a reduction in solution pH[1,2]. Hence, the pH change in the growth solution was used as an indicator of struvite crystallization (including the effects of both nucleation and crystal growth). The extent of reaction, ξ, in the absence and presence of 50 μg mL^{-1} of additives was assessed according to the following equation

$$\xi = \frac{(pH_i - pH_t)}{(pH_i - pH_{c,eq})} \times 100 \quad \text{(B2)}$$

where pH_i is the initial pH (8.6), pH_t is the pH at time *t*, and $pH_{c,eq}$ is the final equilibrium pH (pH 7.42) achieved by struvite formation free of additive (control).

Note B2. Phosphoric Acid Speciation as a Function of pH

Table S1 lists the equilibrium equations and corresponding dissociation constants (pK_a) for phosphoric acid (H_3PO_4). We calculated the percentage of neutral and charged species as a function of solution pH for phosphoric acid using a speciation model using the equations in Table B1.

Species fraction of phosphoric acid is presented in Figure B1. To highlight model calculations, we selected phosphoric acid with its three dissociation constants:

$$K_{a1} = \frac{[H_2PO_4^-][H^+]}{[H_3PO_4]}, \quad \text{(B3)}$$

$$K_{a2} = \frac{[HPO_4^{2-}][H^+]}{[H_2PO_4^-]}, \text{ and} \quad \text{(B4)}$$

$$K_{a3} = \frac{[PO_4^{3-}][H^+]}{[HPO_4^{2-}]}. \quad \text{(B5)}$$

All experiments were performed in aqueous solution, thus we accounted for water dissociation

$$K_w = [H^+][OH^-]. \quad \text{(B6)}$$

The ionic strength was set to 150 mM using NaCl. The net charge of electrolytes in solution is neutral,

$$0 = [H^+] - [OH^-] - [H_2PO_4^-] - 2[HPO_4^{2-}] - 3[PO_4^{3-}] + [Na^+] - [Cl^-]. \quad \text{(B7)}$$

Or if we simplify the equation by substituting the phosphoric acid and water dissociation constants,

$$0 = [H^+] - \frac{K_w}{[H^+]} - K_{a1}\frac{[H_3PO_4]}{[H^+]} - 2K_{a1}K_{a2}\frac{[H_3PO_4]}{[H^+]^2} - 3K_{a1}K_{a2}K_{a2}\frac{[H_3PO_4]}{[H^+]^3} + [Na^+] - [Cl^-]. \quad \text{(B8)}$$

Total amount of phosphoric acid in solution equals the sum of all the species in solution,

$$[H_3PO_4]_{tot} = [H_3PO_4] + K_{a1}\frac{[H_3PO_4]}{[H^+]} + K_{a1}K_{a2}\frac{[H_3PO_4]}{[H^+]^2} + K_{a1}K_{a2}K_{a2}\frac{[H_3PO_4]}{[H^+]^3}. \quad \text{(B9)}$$

All concentrations were replaced by activity, $a = \gamma C$. The activity coefficients γ were calculated with the Davis equation,

$$\log(\gamma) = -0.5z^2\left(\frac{\sqrt{\mu}}{1+\sqrt{\mu}} - 0.2\mu\right) \quad \text{(B10)}$$

where z is the ion charge and μ is the ionic strength. Combination of these equations yield equations for the fraction of each species with one unknown: $[H^+]$. For each pH

(or $[H^+]$ value) we can calculate the fraction of each phosphoric acid species. The ionic strength was set equal to the experimental condition (150 mM NaCl) used for bulk crystallization assays.

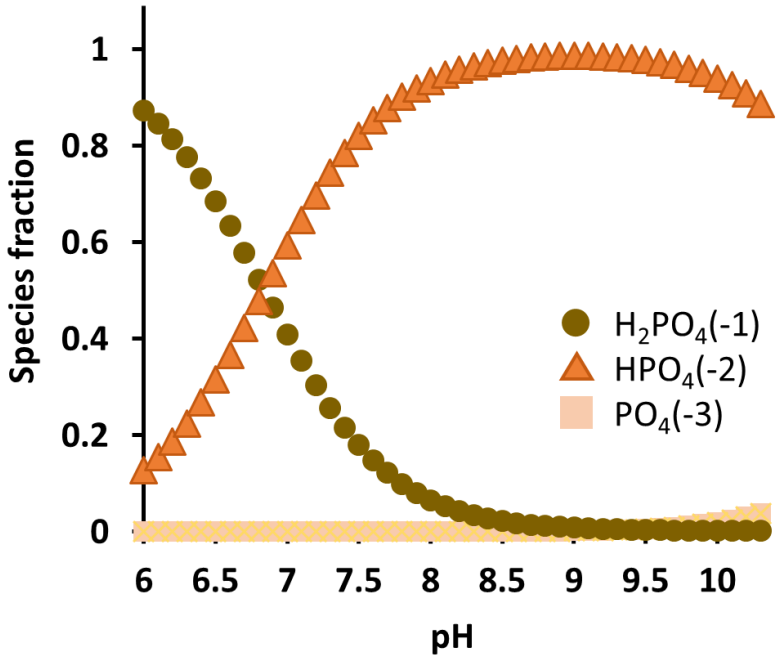

Figure B1. Ion speciation curves for phosphoric acid (H_3PO_4) as a function of pH.

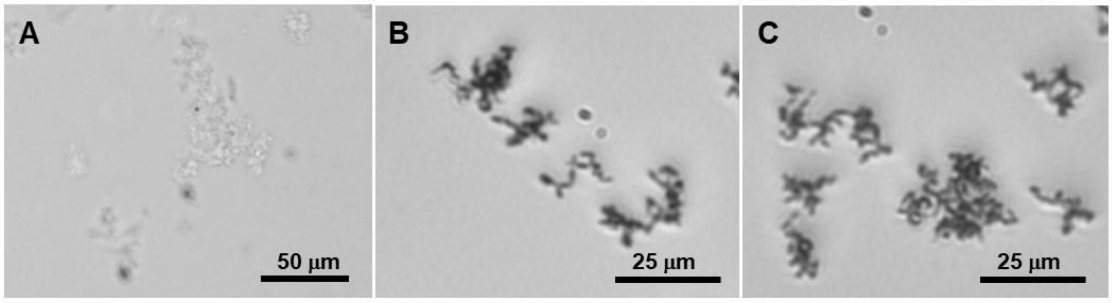

Figure B2. Optical micrographs from bulk crystallization assays in solutions containing 50 µg mL^{-1} of (A) PA, (B) P45, and (C) HMP. The images were collected after 24 hours of continuous stirring at 1200 rpm.

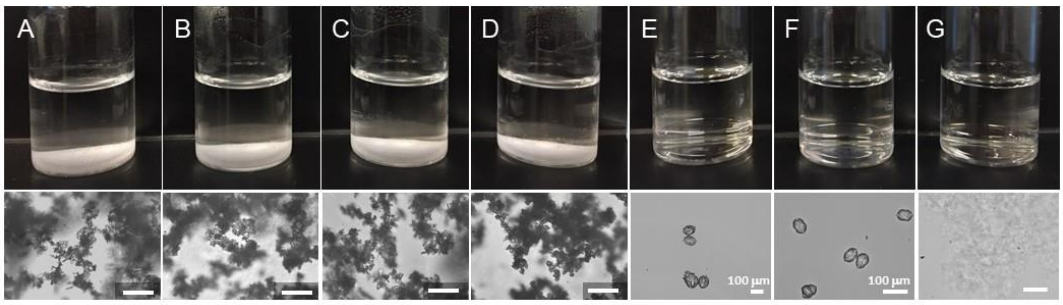

Figure B3. Synthesis vials (top) and optical micrographs (bottom) from bulk crystallization assays in solutions without (A) and with 50 μg mL^{-1} of PP (B), TMP (C), TP (D), HMP (E), P45 (F), and PA (G).

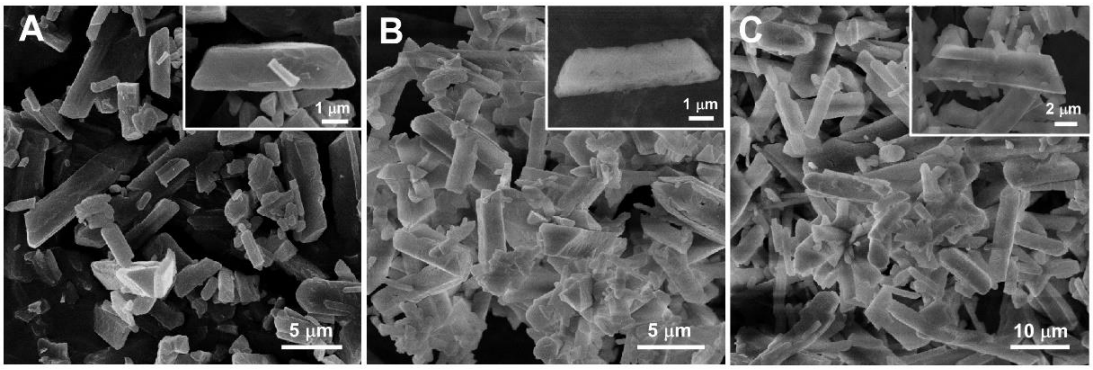

Figure B4. SEM of struvite crystals synthesized in solutions containing no additives (control) (A) and 50 μg mL^{-1} of (B) PP and (C) TMP. Insets are high magnification images of representative crystals in each batch.

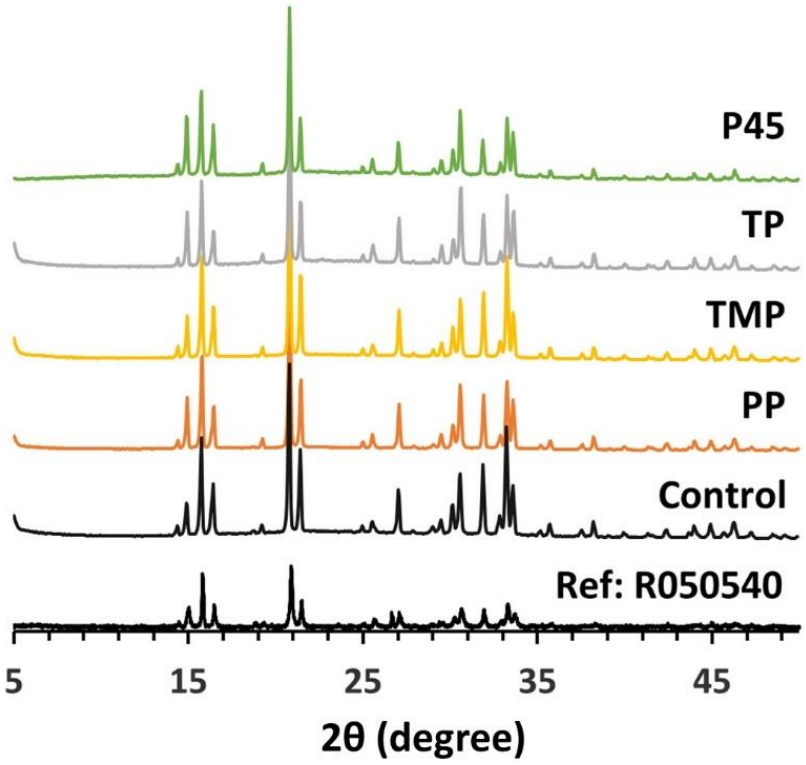

Figure B5. PXRD patterns of crystals synthesized in the presence and absence of inhibitors in comparison to a struvite reference pattern (Ref: R050540). Samples were prepared with 50 μg mL^{-1} of additives and pH 8.6.

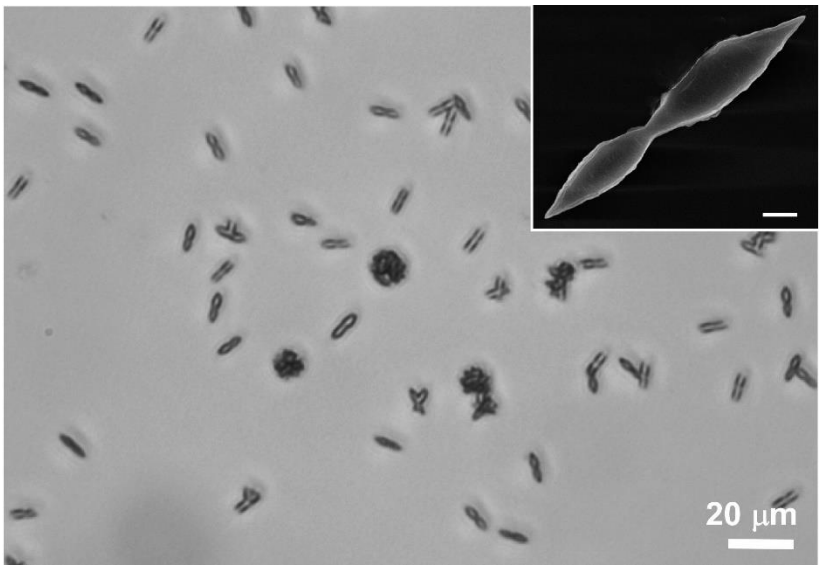

Figure B6. Struvite crystals formed 4 hours into bulk crystallization assays (under quiescent conditions) in the presence of 50 μg mL^{-1} P45. Inset: Scanning electron micrograph of a representative crystal (scale bar = 2 μm).

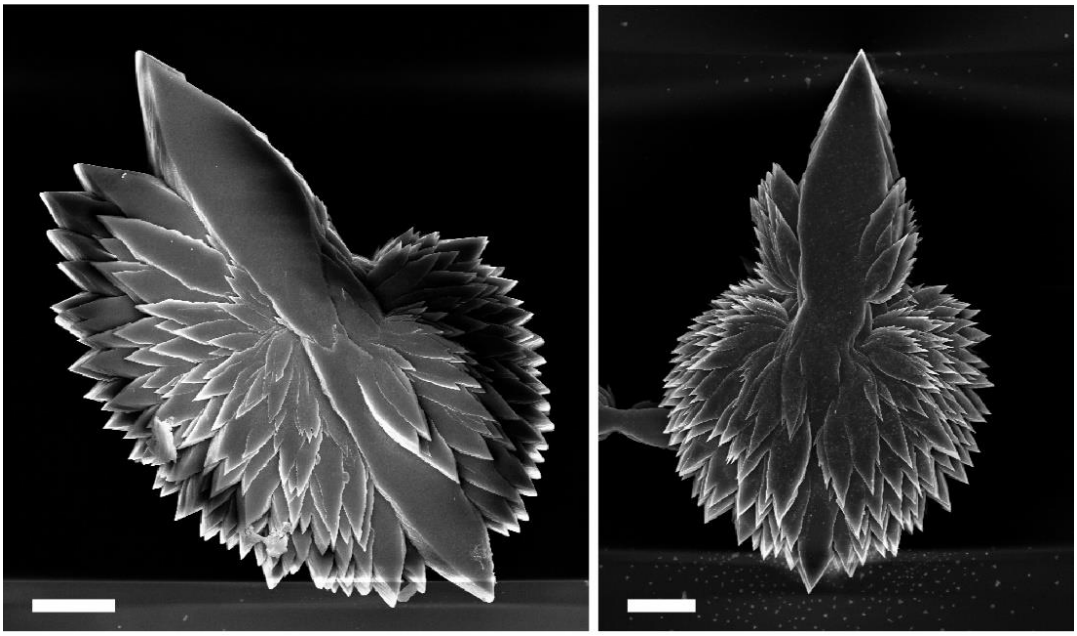

Figure B7. Examples of asymmetrical hierarchical struvite crystals formed in the presence of 50 μg mL^{-1} HMP. Scale bars equal 10 μm.

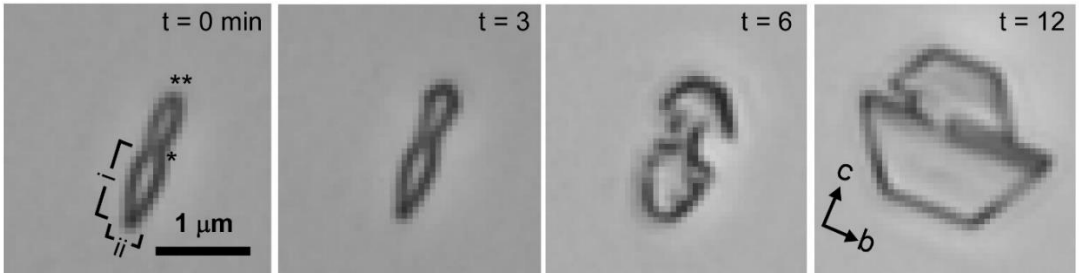

Figure B8. Time-resolved optical micrographs showing the growth of HMP seed crystals.

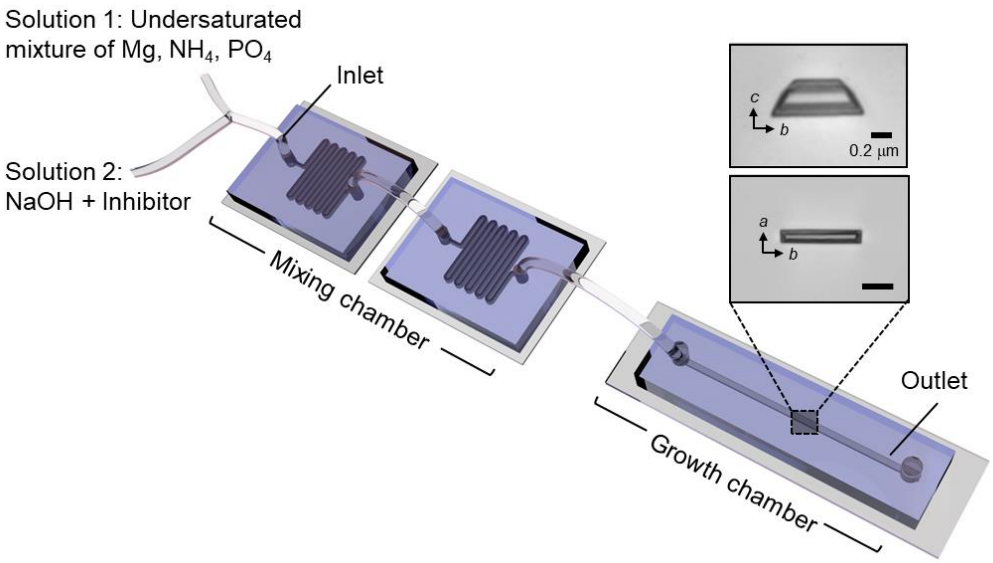

Figure B9. Schematic of the microfluidic device (not drawn to scale) used to assess anisotropic rates of growth during bulk crystallization.

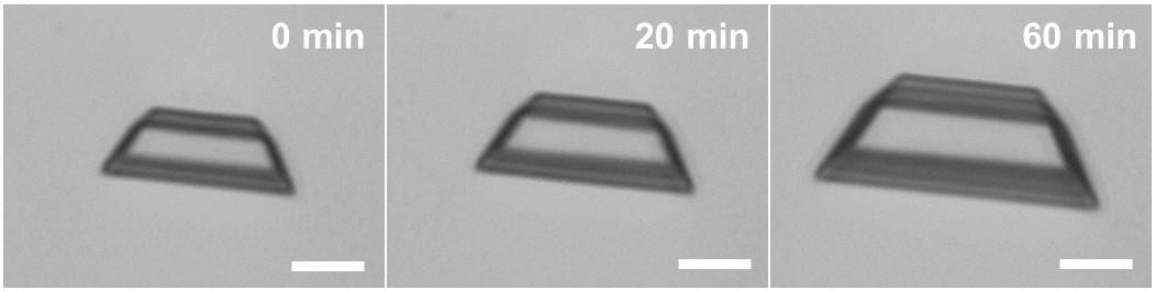

Figure B10. Time-resolved optical micrographs of struvite crystals growing in a microfluidics channel in the presence of 5 μg mL^{-1} TMP. Scale bars equal 10 μm.

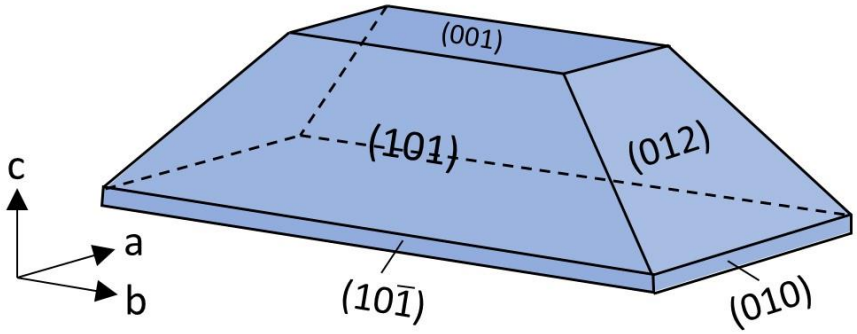

Figure B11. Illustration of a typical struvite crystal morphology with indexed facets and principal growth directions according to Kim et al.

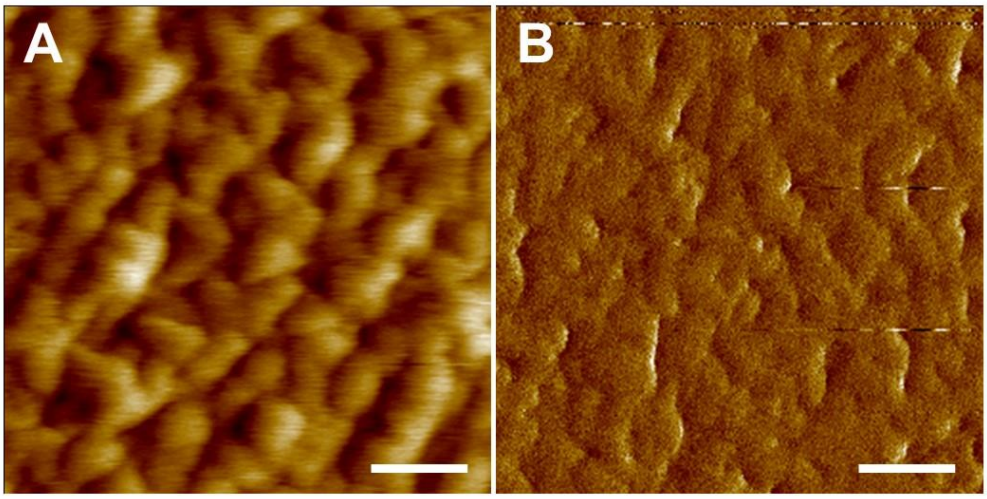

Figure B12. P45 and PA both induce the formation of roughened struvite (101) surfaces. Images are snapshots taken during in situ AFM measurements in a growth solution with 3 μg mL^{-1} of (A) P45 and (B) PA. Scale bars equal 100 nm.

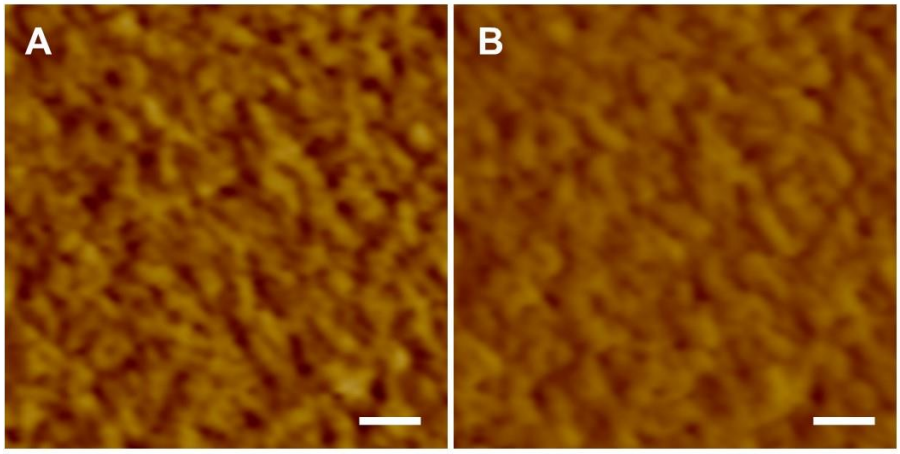

Figure B13. Rough surface features remain relatively constant in size without continuous scanning in a growth solution containing 3 μg mL^{-1} HMP after (A) 10 min and (B) 60 min. Scale bars equal 100 nm.

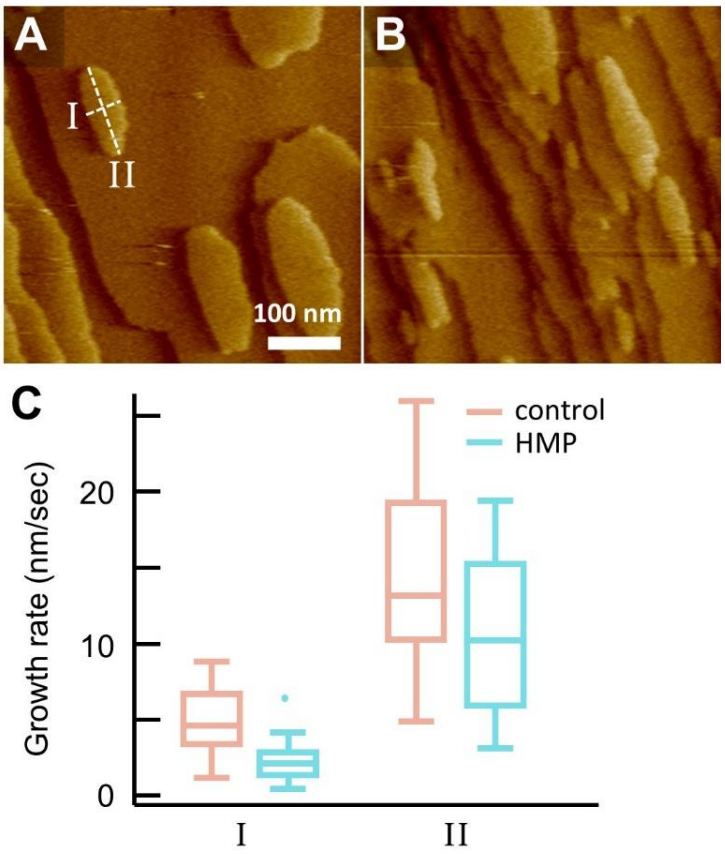

Figure B14. (A and B) In situ AFM imaging of layered growth on (101) surfaces in the (A) absence and (B) presence of 0.25 μg mL^{-1} HMP. (C) Growth rates in the absence (control) and presence of 0.25 μg mL^{-1} HMP.

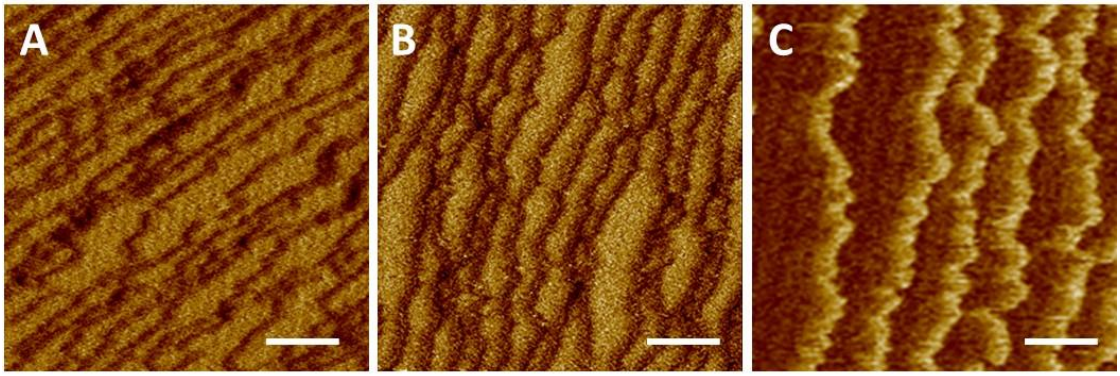

Figure B15. In situ AFM deflection mode image of a struvite (101) surface exposed to solutions containing 10 μg mL^{-1} of (A) PP, (B) TMP, and (C) TP. Scale bars equal 500 nm.

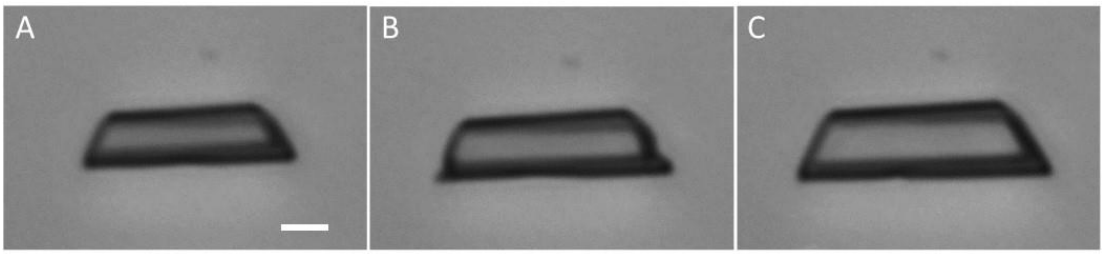

Figure B16. Struvite growth after its suppression in solution containing 3 μg mL^{-1} HMP at (A) t = 0 min, (B) t = 10 min, and (C) t = 20 min after replacing the solution with a HMP-free growth. Scale bar equals 10 μm.

Table B1. Speciation reactions and dissociation constants for phosphoric acids.

Equation	Phosphoric acid reactions	$_{P}K_a$
S11	$H_3PO_4 \rightarrow H^+ + H_2PO_4^-$	2.16
S12	$H_2PO_4^- \rightarrow H^+ + HPO_4^{2-}$	7.21
S13	$HPO_4^{2-} \rightarrow H^+ + PO_4^{3-}$	12.32

APPENDIX C

CHAPTER 3 SUPPLEMENTARY INFORMATION

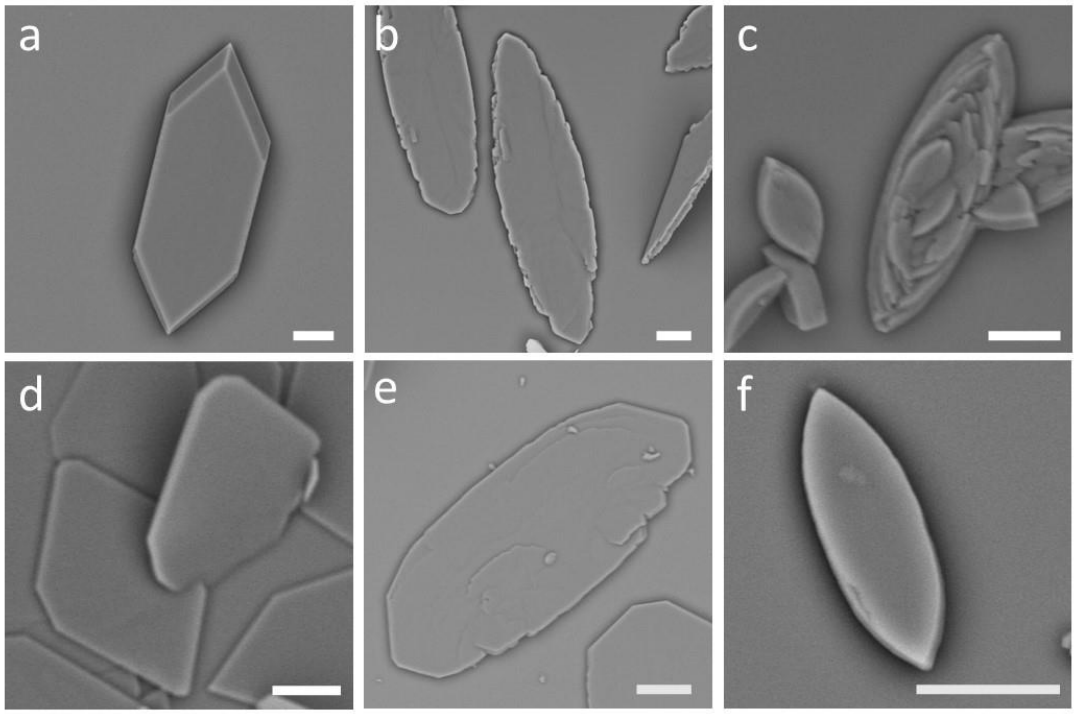

Figure C1. SEM of COM crystals synthesized in the presence of additives: (a) CTMP (20 μg mL^{-1}), (b) LTPP (5 μg mL^{-1}), (c) LTPP (10 μg mL^{-1}), (d) HMP (5 μg mL^{-1}), (e) HMP (10 μg mL^{-1}), (f) HMP (20 μg mL^{-1}). Scale bars, 10 μm.

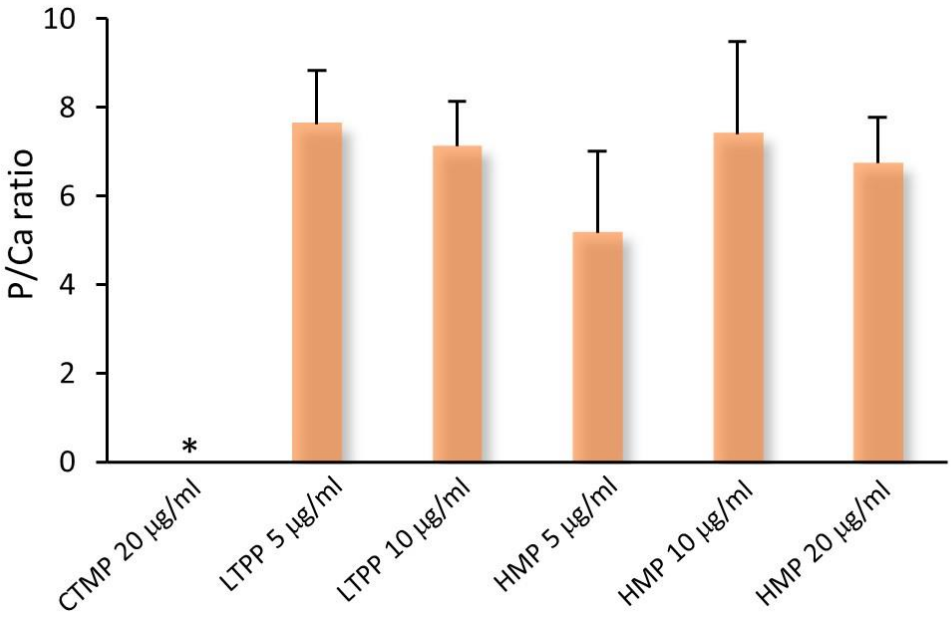

Figure C2. Energy-dispersive X-ray (EDX) analysis of potassium-to-calcium ratios of COM crystals synthesized in the presence of CTMP (20 μg mL^{-1}), LTPP (5 and 10 μg mL^{-1}), HMP (5, 10, and 20 μg mL^{-1}).

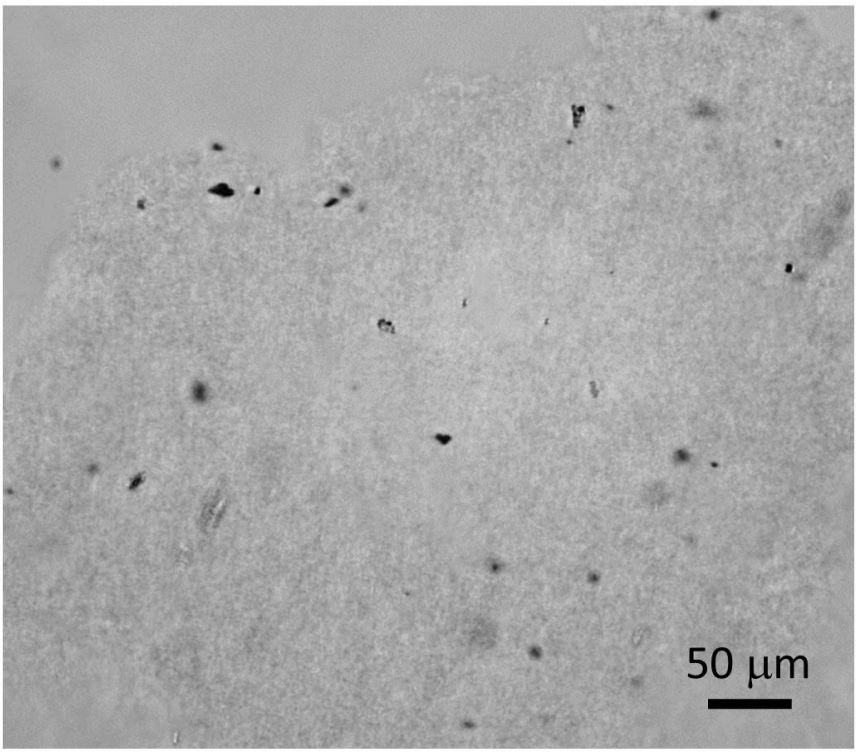

Figure C3. Optical micrograph of amorphous precipitate formed in the presence of 5 μg mL^{-1} phytate (PA).

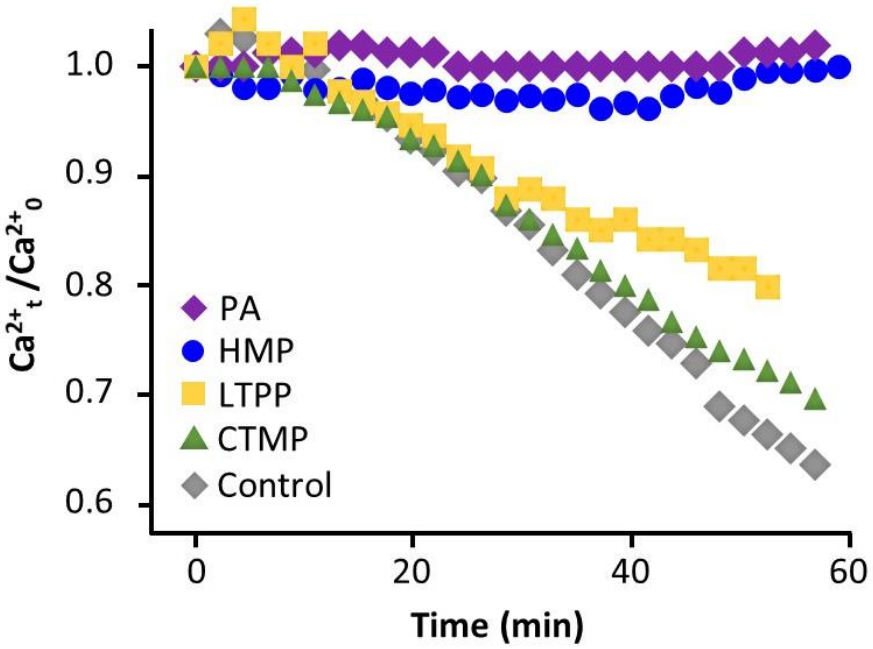

Figure C4. ISE measurements in the absence and presence of 5 μg mL^{-1} additives.

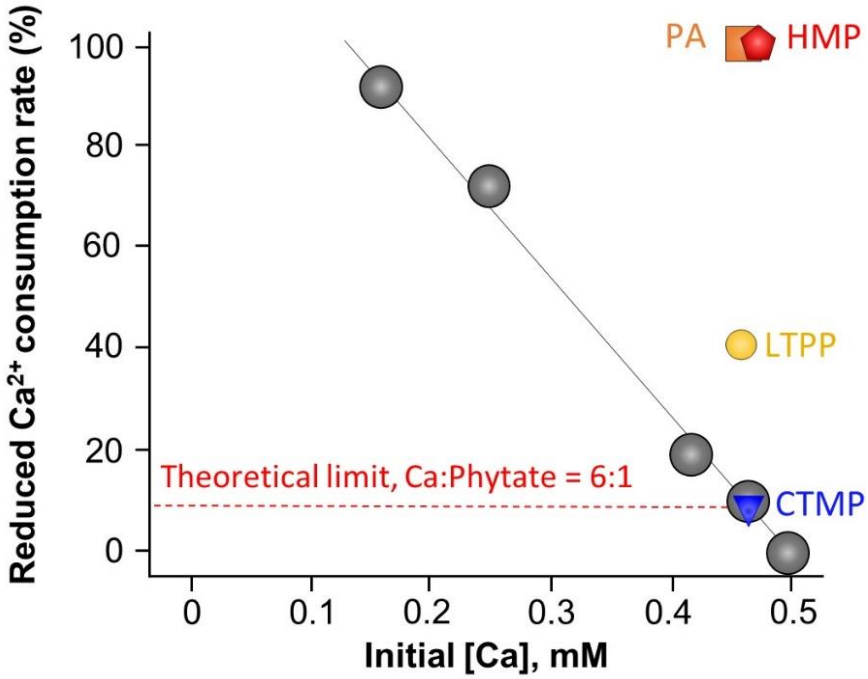

Figure C5. Percentage reduction in free calcium ion consumption rate at reduced initial [Ca].

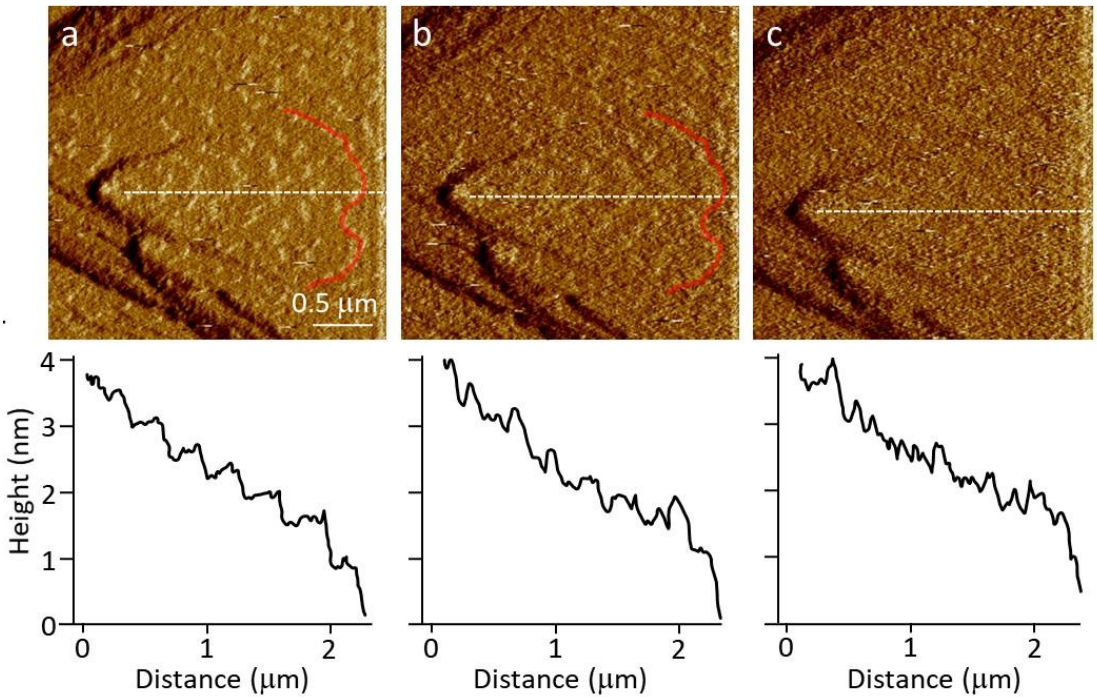

Figure C6. AFM image and height profile of COM surface in the presence of PA after (a) 10 min, (b) 27 min, and (c) 48 min of exposure to a constant flow of growth solution containing 1 µg mL^{-1} PA.

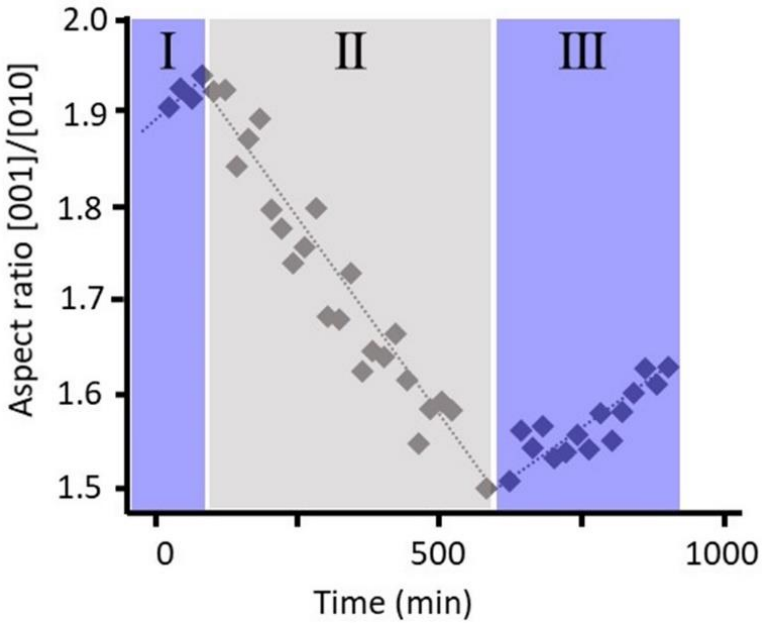

Figure C7. Measurements of COM crystal aspect ratio, length [001] to width [010], during microfluidics experiments. Growth in the absence (I and III), presence (II) of LTPP 1 μg mL^{-1}.

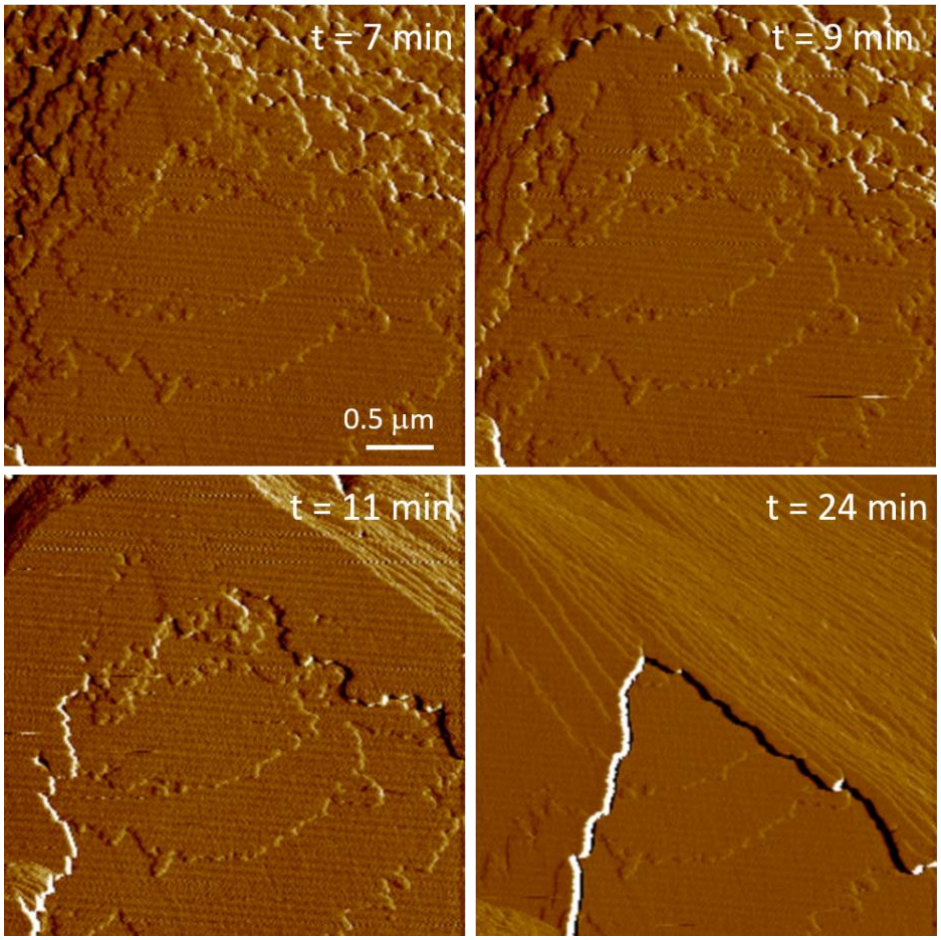

Figure C8. Time-resolved AFM images showing growth of a COM (100) surface under flow of growth solution without any additives after exposure to 1 µg mL^{-1} LTPP.

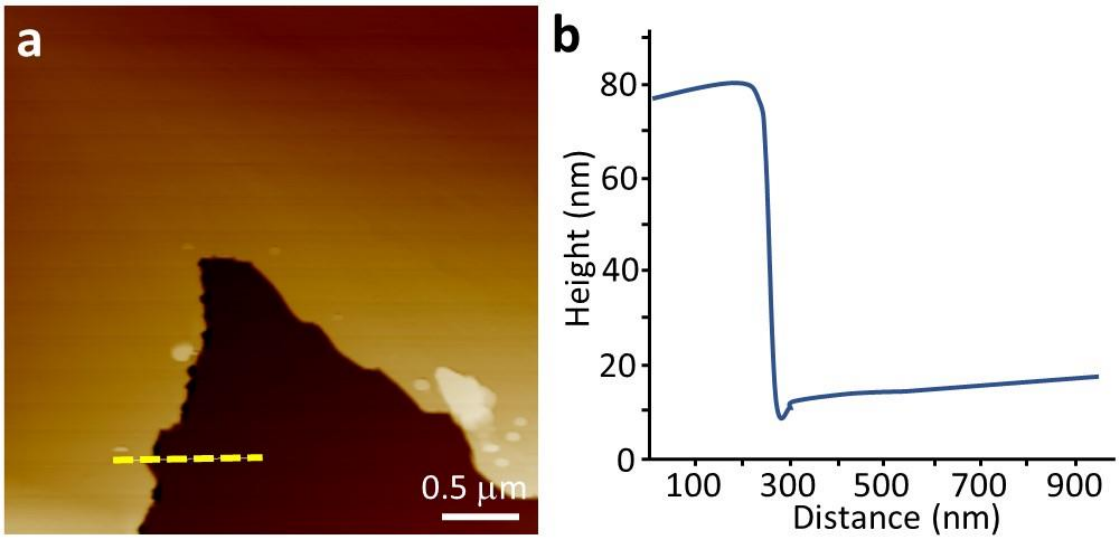

Figure C9. AFM height mode image (a) and the corresponding height profile (b) of a representative macrostep on a regenerated COM (100) surface after exposure to 1 µg mL^{-1} LTPP.

Table C1. Composition of solutions tested with OIM.

Supersaturation	[Ca]=[Ox] (mM)	Modifier	[NaCl], (mM)	pH	Time (hr)	Cluster?
4.08	0.5	0	150	6.1	0, 2, 20	X
3.67	0.45	0	150	6.1	0, 2, 20	X
3.26	0.4	0	150	6.1	0, 2, 20	X
2.86	0.35	0	150	6.1	0, 2, 20	X
2.45	0.3	0	150	6.1	0, 2, 20	X
2.04	0.25	0	150	6.1	0, 2, 20	X
1.63	0.2	0	150	6.1	0, 2, 20	X
1.23	0.15	0	150	6.1	0, 2, 20	X
1.06	0.13	0	150	6.1	0, 2, 20	X
0.82	0.1	0	150	6.1	0, 2, 20	X
4.08	0.5	5 ug/mL CTMP	150	6.1	0, 2, 20	X
4.08	0.5	5 ug/mL LTPP	150	6.1	0, 2, 20	X
4.08	0.5	5 ug/mL HMP	150	6.1	0, 2, 20	X
4.08	0.5	5 ug/mL PA	150	6.1	0, 2, 20	X
4.08	0.5	5 ug/mL Citrate	150	6.1	0, 2, 20	X
2.04	0.5	5 ug/mL CTMP	150	6.1	0, 2, 20	X
2.04	0.5	5 ug/mL LTPP	150	6.1	0, 2, 20	X
2.04	0.5	5 ug/mL HMP	150	6.1	0, 2, 20	X
2.04	0.5	5 ug/mL PA	150	6.1	0, 2, 20	X
2.04	0.5	5 ug/mL Citrate	150	6.1	0, 2, 20	X

Table C2. Conditions tested for AFM measurements on Mica surface.

Supersaturation	[Ca]=[Ox] (mM)	Modifier	[NaCl], (mM)	pH	Time (hr)	Cluster?
4.08	0.5	0	150	6.1	0, 2, 20	X
3.26	0.4	0	150	6.1	0, 2, 20	X
2.04	0.25	0	150	6.1	0, 2, 20	X
4.08	0.5	5 ug/mL HMP	150	6.1	0, 2, 20	X
4.08	0.5	5 ug/mL PA	150	6.1	0, 2, 20	X
2.04	0.5	5 ug/mL HMP	150	6.1	0, 2, 20	X
2.04	0.5	5 ug/mL PA	150	6.1	0, 2, 20	X

APPENDIX D

CHAPTER 7 SUPPLEMENTARY INFORMATION

Note D1. Experimental section

Materials. The following reagents were purchased from Sigma Aldrich (St. Louis, MO, USA): magnesium chloride hexahydrate (BioXtra, 99.0%), ammonium dihydrogen phosphate (99.999% trace metals basis), and sodium hydroxide (98.0%). Millex 0.22 μm membrane filters were purchased from Millipore Ltd (Cork, Ireland). Deionized (DI) water used in all experiments was purified with an Aqua Solutions RODI water purification system (18.2 MΩ). All reagents were used as received without further purification.

Synthesis. Struvite crystals were prepared by a seeded growth method. Struvite seeds were synthesized in a 20-ml glass vial by adding 0.8 ml of each 50 mM $NH_4H_2PO_4$ and 50 mM $MgCl_2{\cdot}6H_2O$ stock solutions. The alkalinity of the solution was adjusted to pH 8.5 by adding an appropriate volume of 1 M NaOH solution. The solution prepared to the final composition 4 mM $MgCl_2{\cdot}6H_2O$:4 mM $NH_4H_2PO_4$ (pH 8.5) was then mixed with a stir bar at 600 rpm for a short time (ca. 30 sec) resulting in the precipitation of struvite seed crystals (< 0.03 mm in size). A 50-ml aliquot of this solution containing struvite seeds was transferred to another 20-ml glass vial containing growth solutions prepared at 2.3 mM $MgCl_2{\cdot}6H_2O$:2.3 mM $NH_4H_2PO_4$ (pH 8.5). A growth solution supersaturation σ of 0.75 (where $\sigma = (IAP/Ksp)^{1/}3\text{-}1$ where IAP = ion activity product and $pK_{sp} = 13.26$ at 25 °C)[34] was selected below the metastable zone to allow the growth of seeds without the nucleation of new crystals. The growth solution with seeds was then stored at room temperature. After 3 hours the solution was removed from the vial

via pipette carefully to not disturb the crystals that settled on the bottom of the glass vial. The vial was replenished with new growth solution prepared at $\sigma = 0.75$. Replacement of growth solution was repeated 3 times every 3 hours after which the solution was stored at room temperature overnight. Optical microscope images of crystals in the solution revealed that after overnight incubation, struvite crystals in the vials ranged from 0.10 to 0.40 mm in length. Crystals of sufficiently large size (approximately 0.30 mm) were selected for single-crystal X-ray diffraction measurements.

X-ray Experiment. The single crystal X-ray diffraction data was collected using Mo-Kα radiation ($\lambda = 0.710173$ Å), on a Bruker Apex-II diffractometer equipped with CCD detector, controlled using APEX3 software. Data integration and reduction were performed using the SAINT software.[i] The data were scaled, and an absorption correction was applied using SADABS [36]. The symmetry equivalent reflections were merged prior to structure solution. Crystal structures were solved by direct methods using the program SHELXS,[ii] and subsequent Fourier calculations and least-squares refinements were performed on F^2 using the program CRYSTALS.[iii] All non-hydrogen atoms were refined with anisotropic displacement parameters. Protons were located directly via inspection of difference Fourier maps and were refined isotropically.

Table D1. Crystallographic data for struvite.

	Struvite
Empirical formula	$H_8 N_{0.5} O_5 Mg_{0.5} P_{0.5}$
formula weight	122.70
Temperature/K	293
Crystal system	Orthorhombic
Space group	$Pmn2_1$
a/Å	6.945700(14)
b/Å	6.133300(10)
c/Å	11.203000(17)
α/°	90
β/°	90
γ/°	90
Volume/$Å^3$	477.2485(14)
Z	4
$\rho_{calc}g/cm^3$	1.708
μ/mm^{-1}	0.389
F(000)	260.5
Crystal size/mm^3	0.200 × 0.120 × 0.110
Radiation	Mo Kα (λ = 0.71073)
2θ range for data collection/°	6.644 to 80.472
Index ranges	$-12 \leq h \leq 12$, $-11 \leq k \leq 11$, $-20 \leq l \leq 20$
Reflections collected	36024
Independent reflections	3181 [R_{int} = 0.0275, R_{sigma} = 0.0133]
Data/restraints/parameters	3181/17/107
Goodness-of-fit on F^2	0.952
Final R indexes [I>=2σ (I)]	R_1 = 0.0232, wR_2 = 0.0596
Final R indexes [all data]	R_1 = 0.0256, wR_2 = 0.0616
Largest diff. peak/hole / e $Å^{-3}$	0.20/-0.23

Table D2. Bond Lengths of struvite structure without disorder.

Atom	Atom	Length/Å	Atom	Atom	Length/Å
P001	O7	1.5366(5)	Mg02	$O1^2$	2.0742(6)
P001	$O7^1$	1.5366(5)	Mg02	$O3^2$	2.0488(7)
P001	O6	1.5406(7)	Mg02	O3	2.0488(7)
P001	O5	1.5432(7)	Mg02	O2	2.1001(10)
Mg02	O1	2.0742(6)	Mg02	O4	2.1099(10)

Table D3. Bond Angles of struvite structure without disorder.

Atom	Atom	Atom	Angle/°	Atom	Atom	Atom	Angle/°
O7[1]	P001	O7	110.68(4)	O3[2]	Mg02	O3	91.13(4)
O6	P001	O7	108.88(3)	O2	Mg02	O1	90.03(4)
O6	P001	O7[1]	108.88(3)	O2	Mg02	O1[2]	90.03(4)
O5	P001	O7	109.54(3)	O2	Mg02	O3	88.69(4)
O5	P001	O7[1]	109.54(3)	O2	Mg02	O3[2]	88.69(4)
O5	P001	O6	109.29(4)	O4	Mg02	O1	91.57(3)
O1[2]	Mg02	O1	93.9	O4	Mg02	O1[2]	91.57(3)
O3[2]	Mg02	O1[2]	178.13(4)	O4	Mg02	O3	89.67(3)
O3	Mg02	O1[2]	87.48(3)	O4	Mg02	O3[2]	89.67(3)
O3	Mg02	O1	178.13(4)	O4	Mg02	O2	177.65(5)
O3[2]	Mg02	O1	87.48(3)				

***** - the superscripts 1 & 2 are used to indicate symmetry equivalent atoms.

[i] Bruker APEX2 and SAINT; Bruker AXS Inc.: Madison, Wisconsin, USA, 2009.
[ii] G. M. Sheldrick, Acta Crystallogr., Sect. C: Struct. Chem. 2015, 71, 3−8.
[iii] P. W. Betteridge, J. R. Carruthers, R. I. Cooper, K. Prout, D. J. Watkin, J. Appl. Cryst. 2003, 36, 1487.